# Synthesis of workable, strong and acid-resistant N-A-S-H geopolymers incorporating dry-water

by

Chaofan Yi

A thesis submitted in partial fulfillment of the requirements for the degree of

Doctor of Philosophy

in

Structural Engineering

Department of Civil and Environmental Engineering
University of Alberta

## Abstract

The production of cement-based materials releases numerous greenhouse gases into the atmosphere and therefore, accelerates global warming. The search for an alternative to Portland cement systems has thrown up the family of alkali-activated geopolymers as a potential choice. In civil engineering, workability, setting time, strength and durability are the most important demands as they determine the quality of construction, engineering performance and the service life of structures. To boost the widespread application of N-A-S-H geopolymers in civil engineering, developing mature mix design guidelines is strongly necessary. The mechanical performance of N-A-S-H geopolymers has been found to rely on the $SiO_2/Al_2O_3$, $Na_2O/Al_2O_3$ and $H_2O/Na_2O$ ratios. Despite that, there so far has not been a systematic investigation on their attendant role upon workability, setting and durability. How to optimize these properties, without sacrificing the strength remains a challenge that limits the widespread use of locally available precursors for geopolymers in practice. In the meantime, the search for an effective additive that can enhance geopolymerization, without sacrificing the fresh paste rheology or the subsequent setting and durability, also continues into the present study. A preliminary review led to a water-in-air Pickering emulsion, specifically known as dry water, as a potential choice. Its promising characteristic in the present context is that it renders the nano silica as enlarged particles through the physical reorganization, while it retains the amorphous property of $SiO_2$.

Accordingly, this doctoral study aims to explain the mechanisms that underlie the mutual interaction between oxide components and dry water led enhancement in geopolymerization and thus, develop the mix design guidelines for making the workable, strong and durable N-A-S-H geopolymers incorporating dry water.

The results show that an increase in any of $SiO_2/Al_2O_3$, $Na_2O/Al_2O_3$, and $H_2O/Na_2O$ ratios, automatically increased the liquid-to-solid ratio and therefore, raised the flowability of the system. The setting process of N-A-S-H geopolymers was most sensitive to the $SiO_2/Al_2O_3$ ratio, as this ratio essentially dominated the degree of geopolymerization. By contrast, the other two oxide ratios, i.e., $Na_2O/Al_2O_3$ and $H_2O/Na_2O$, caused the relatively minor influence on setting. A deficient $SiO_2/Al_2O_3$ ratio and an excessive $Na_2O/Al_2O_3$ ratio reduced the amorphocity and boosted the significant formation of crystalline zeolite. These, therefore, reduced the mechanical strength and acid resistance. Although a value of $H_2O/Na_2O$ ratio at the lower end may slightly depress the geopolymerization, the attendant high alkalinity improved the acid resistance. For generally used N-A-S-H geopolymers, a satisfactory combination of compositional ratios to simultaneously achieve the desired workability, final set and strength may fall within $SiO_2/Al_2O_3$ = 2.8-3.6, $Na_2O/Al_2O_3$ = 0.75-1.0 and $H_2O/Na_2O$ = 9-10. When subjected to the acid-rich environment, the $SiO_2/Al_2O_3$ ratio could be suitably narrowed to 3.1-3.4, and the $H_2O/Na_2O$ slightly shifts to 8-10.

Moreover, depending on the unique combination of characteristics of size coarsening, micro-filling, supplementary silica source and temporary water encapsulation, the nano silica stabilized dry water resolved the “trade-off” between the fresh and hardened properties. An optimal ratio was found at 15% nanoparticles-to-emulsion ratio to yield the most satisfactory combination of high flow diameter, quick set, high strength and superior acid resistance simultaneously.

Overall, this thesis provides a guideline to synthesize the workable, strong and acid-resistant N-A-S-H geopolymer incorporating dry water. The findings are very promising to boost the widespread application of N-A-S-H geopolymers with locally available precursors, in both the ordinary condition and an acid-rich environment.

## Preface

This thesis is an original work by Chaofan Yi. The N-A-S-H geopolymer systems with varying principal compositional ratios and nano silica stabilized dry water were synthesized to develop a mix design guideline for producing the sustainable, workable, strong and acid-resistant alternative to conventional Ordinary Portland cement systems. This thesis contains both experimental and modelling work and is developed from a couple of journal papers that are either published or drafted for the consideration for publication.

Chapter 3 of this thesis has been published as **Yi, C**., Boluk, Y., & Bindiganavile, V. (2022). Experimental Characterization and Multi-Factor Modelling to Achieve Desired Flow, Set and Strength of N-A-S-H Geopolymers. *Materials*, 15(16), 5634.

A journal paper and a manuscript have been developed from Chapter 4. The first paper has been published as **Yi, C.**, Boluk, Y., & Bindiganavile, V. (2020). Enhancing alkali-activation of metakaolin-based geopolymers using dry water. *Journal of Cleaner Production*, 258, 120676. Another independent manuscript has been submitted for peer review as **Yi, C.**, Boluk, Y., & Bindiganavile, V. (2022). Aluminosilicates Geopolymerized with Dry Water Stabilized by Hydrophobic Nanosilica: Mechanisms underlying its Rheology, Microstructure and Strength. *Construction and Building Materials*.

Chapter 5 of this thesis has been submitted for peer review as **Yi, C.**, Boluk, Y., & Bindiganavile, V. (2022), Characterizing Mechanisms Underlying Effects of Compositional Oxide Ratios on Performances of N-A-S-H Geopolymers Subjected to Sulphuric Acid Attack. *Cement and Concrete Composites*.

Chapter 6 of this thesis has been drafted for submission as **Yi, C.**, Boluk, Y., & Bindiganavile, V. (2022), Potential Benefits of Hydrophobic Nano Silica Stabilized Dry Water for N-A-S-H Geopolymers Against Sulphuric Acid Attack. *Cement and Concrete Composites*.

Chapter 7 of this thesis is related to multi-factor modelling. The main results have been published together with the results shown in Chapter 3, as **Yi, C**., Boluk, Y., & Bindiganavile, V. (2022). Experimental Characterization and Multi-Factor Modelling to Achieve Desired Flow, Set and Strength of N-A-S-H Geopolymers. *Materials*, 15(16), 5634. Besides, this concept has also been used to contribute to additional two journal papers as (i) Li J., Tao Y., …, Boluk Y., Bindiganavile V., Chen Z., **Yi C. (corresponding author)** (2022). Optimal Amorphous Oxide Ratios and Multifactor Models for Binary Geopolymers from Metakaolin Blended with Substantial Sugarcane Bagasse. *Journal of Cleaner Production*, 377, 134215; (ii) Li, J., **Yi, C.**, Chen, Z., Cao, W., Yin, S., Huang, H., ... & Yu, Q. (2022) Relationships between Reaction Products and Carbonation Performance of Alkali-activated Slag with Similar Pore Structure. *Journal of Building Engineering*, 45, 103605.

In this thesis, my work includes conceptualization, experiment design and operation, data collection, model establishment, formal analysis, writing and editing. Dr. Vivek Bindiganavile and Dr. Yaman Boluk are my academic supervisors, who were involved in conceptualization, supervision, resources, founding acquisition, review, and editing. Dr. Rajender Gupta is my supervisory committee member, also contributed to the review of this thesis.

## DEDICATION

*This thesis is dedicated to my beloved family.*

**Acknowledgement**

First and foremost, I would like to express my sincere gratitude to my principal supervisor, Dr. Vivek Bindiganavile for his invaluable supervision, continuous guidance and warm encouragement throughout my Ph.D. program. My sincere thanks are also extended to my co-supervisor, Dr. Yaman Boluk, for sharing the exciting concept of Pickering emulsion and also his expertise in nanomaterials. It is absolutely my huge pleasure to work under their supervision. Their immense knowledge and plentiful experience constantly inspire me to grow into a better scientific researcher. Besides, I would also like to acknowledge Dr. Rajender Gupta, for his constructive and helpful comments on this doctoral program. Equally, my sincere gratitude is extended to professors Dr. Luca Sorelli, Dr. Rick Chalaturnyk, Dr. Wei Viktor Liu and Dr. Carlos Cruz Noguez for their valuable comments and suggestions on this thesis.

My deepest appreciation also goes to the technical staff of several laboratories at University of Alberta, as follows: (i) Mr. Rizaldy Mariano for his invaluable and unconditional technical assistance during the specimen preparation and various tests conducted at the Concrete Research Laboratory; (ii) Mr. Nathan Gerein and Mr. Guibin Ma for their professional help on carrying out the microstructural investigation at the Scanning Electron Microscope Laboratory; (iii) Dr. Peng Li, Dr. Nancy Zhang, Dr. Shihong Xu and Dr. Anqiang He from NanoFAB for helping and training me to perform morphological and chemical characterizations; (iv) Mr. Greg Miller and Mr. Cameron West for their technical support on the Material Test System. Without the technical assistance provided by these gentlemen and ladies mentioned above, this research program would not be completed.

I would like to extend my thanks to my colleagues and friends Dr. Jose Roberto Albuquerque Goncalves, Dr. Muhammad Mamun, Dr. Guangping Huang and Dr. Linping Wu for their kind

help and suggestions during my doctoral program. As well, I wish to express my appreciation to my former supervisor Dr. Zheng Chen from Guangxi University, who is also a research collaborator in Dr. Vivek Bindiganavile's team, for his warm and selfless support and assistance in my career development.

This acknowledgement would not be complete without expressing my endless love and gratitude to my dear wife Xiaoyu Lu, my beloved parents Zeming Yi and Hongchun Liang and parents-in-law Yanjie Lu and Yi Huang, for their unconditional love, support, encouragement and guidance during this important and challenging chapter in my life. I sincerely appreciate them for understanding my temporary absence from their daily lives when pursuing my dreams.

## Table of contents

## List of tables

## List of figures

## List of abbreviations

| | |
|---|---|
| A | Anatase |
| AFt | Ettringite |
| $Al_2O_3$ | Aluminium oxide or alumina |
| $AlO_4$ | Tetrahedral aluminum |
| ASTM | American Society for Testing and Materials |
| AVPV | Apparent volume of permeable voids |
| C | Na-Chabazite |
| CaO | Calcium oxide |
| C-A-S-H | Calcium aluminosilicate hydrate |
| $CO_2$ | Carbon dioxide |
| C-S-H | Calcium silicate hydrate |
| CS | Compressive strength |
| CSL | Compressive strength loss |
| DL | Dimension loss |
| DTG | Derivative of thermogravimetric |
| $DW^a$ | Dry water made with 10% nano silica and 90% water |
| $DW^b$ | Dry water made with 15% nano silica and 85% water |

| | |
|---|---|
| $DW^c$ | Dry water made with 20% nano silica and 80% water |
| EDS | Energy Dispersive X-ray Spectroscope |
| F | Faujasite |
| FTIR | Fourier-transform infrared spectroscopy |
| H/Na | $H_2O/Na_2O$ |
| $H_2O$ | Water |
| L/S | Liquid-to-solid ratio |
| MIP | Mercury intrusion porosimetry |
| ML | Mass loss |
| Na/Al | $Na_2O/Al_2O_3$ |
| $Na_2O$ | Sodium oxide |
| $Na_2SiO_3$ | Sodium silicate |
| NaOH | Sodium hydroxide |
| N-A-S-H | $NaO_2$-$Al_2O_3$-$SiO_2$-$H_2O$ |
| NBO | Nonbridging oxygen |
| NS | Nano-$SiO_2$ |
| OPC | Ordinary Portland cement |

| | |
|---|---|
| Q | Quartz |
| S | Hydroxysodalite |
| SEM | Scanning electron microscopy |
| Si/Al | $SiO_2/Al_2O_3$ |
| $SiO_2$ | Silicon dioxide or silica |
| $SiO_4$ | Tetrahedral silicon |
| SSS | Sodium silicate solution |
| TGA | Thermogravimetric analysis |
| STS | Splitting tensile strength |
| XRD | X-ray diffraction |

# Chapter 1. Introduction

## 1.1. Background

Cement-based materials now represent one of the most consumed commodities in the world, second only to potable water (Aïtcin, 2000), however, the production of cement-based materials releases a large number of greenhouse gases into the atmosphere. This issue has of late attracted global attention. Also, Canada has joined over 120 countries to commit to net-zero emissions by 2050. In the meantime, Alberta plans to invest $131 million in projects designed to help prevent carbon emissions from entering the atmosphere. The popularity of Portland cement concrete serving as a building material in the last 150 years is mainly associated with the success of its primary binder: Ordinary Portland cement (OPC). OPC possesses a host of traits with practical value, such as high plasticity, satisfactory compressive strength and stiffness, outstanding fire resistance and, when suitably designed, even excellent durability. At the same time, its raw materials may be sourced widely, with relatively low cost across its applications (Juenger et al., 2011). On the other hand, its environmental cost is high as its production releases a large number of pollutants into the atmosphere and especially, it adds to the carbon footprint of the construction industry (Gartner, 2004; Taylor et al., 2006; Damtoft et al., 2008; Ali et al., 2011). Specifically, manufacturing one tonne of ordinary Portland cement releases 0.8~0.9 tonnes of $CO_2$ emission (Gartner, 2004). This has triggered a wide range of scientific efforts towards finding an alternative to Portland cement.

The family of alkali-activated geopolymers has emerged as a potential choice. Past studies conducted on their development have confirmed that the corresponding greenhouse gas emissions are significantly lower in alkali-activated materials than for Portland cement (Duxson et al., 2007;

Pacheco-Torgal et al., 2008a; Pacheco-Torgal et al., 2008b; Li et al., 2010). Davidovits et al. (1990) found that producing one tonne of binder as required for geopolymerization would generate only 0.184 tonnes of $CO_2$, while McLellan et al. (2011) recorded a 64% reduction in the associated carbon emission in comparison with an equal volume of concrete. Their findings are further corroborated by Habert et al. (2011) using the Life Cycle Assessment method. In addition, manufacturing geopolymers is reported to consume much less energy (Kumar and Kumar, 2014). Statistically, the embodied energy has been reported as 4000~4400 MJ/ton for Portland cement, whereas the corresponding value drops down to 2200~2400 MJ/ton, equivalent to about a 50% reduction (Kumar and Kumar, 2014).

In general, the synthesis of alkali-activated geopolymer systems consists of activating an aluminosilicate using strong alkali solutions, such as sodium hydroxide and/or sodium silicate, to form a three-dimensional poly-condensed network, N-A-S-H (N: $Na_2O$, A: $Al_2O_3$, S: $SiO_2$ and H: $H_2O$), comprising the tetrahedral $SiO_4$ and $AlO_4$ units. A wide range of aluminosilicates sourced mostly as industrial by-products is proven to be suitable precursors. These include calcined clays (Kong et al., 2007; Yunsheng et al., 2010), fly ash (Olivia and Nikraz, 2012; Zhuang et al., 2016), other ashes (Chindaprasirt et al., 2009; Hardjito and Fung, 2010; Temuujin et al., 2010) and some artificial aluminosilicates such as zeolite (Villa et al., 2010), pure $Al_2O_3$-$2SiO_2$ powder (Zheng et al., 2015), magnesium-containing minerals (MacKenzie et al., 2013) and red mud (Hu et al., 2018).

As a potential alternative to Portland cement concrete, excellent workability and setting are important for in-situ construction, while compressive strength and durability are essential throughout its service life. In this regard, it has been widely confirmed that when suitably designed, the geopolymer system displays satisfactory workability, with a flow diameter ranging from 150 mm to 250 mm (Huseien et al., 2016; Ghosh and Ghosh, 2012a). Huseien et al. (2016) reported

the geopolymerized mixture comprising granulated blast furnace slag (GBFS), fly ash (FA) and palm oil fuel ash (POFA) could quickly set within 1 hour. The alkali-activated metakaolin geopolymer is also able to finish its final setting within 6 hours (De Silva et al., 2007), which is equivalent to the required setting time for various types of Portland cement specified in ASTM C150/C150M-19a. Prior research observed that the compressive strength of alkali-activated systems was at least as much as that obtained with Portland cement (Glukhovsky, 1981; Duxson et al., 2005; Chindaprasirt et al., 2007). Of particular note, the former is reported to rapidly achieve structural integrity and acquire high early strength (Rovnaník, 2010). Besides their mechanical performance, alkali-activated geopolymers are resistant to common durability concerns which have been widely reported upon cement-based systems, including sulphate attack, other acids and chloride-induced corrosion of embedded rebar (Shi and Stegemann, 2010; Bakharev, 2003; Fernando, 2010; El-Sayed et al., 2011).

However, when conducting the mixture design for N-A-S-H based geopolymers, the interaction between compositional ratios namely, $SiO_2/Al_2O_3$, $Na_2O/Al_2O_3$ and $H_2O/Na_2O$, triggers mutual sacrifice, or "trade-off", between the above equally important properties. So that, there remains no mix design guideline for the practitioner to regulate and then optimize the proportions of the raw materials, in order to simultaneously achieve satisfactory workability, quick final set, high compressive strength and excellent durability. The above scientific gap must be filled, with the aim to boost the widespread application of N-A-S-H geopolymers.

The merits of nanomaterials have been attracting intensive scientific attention, with the potential to enhance the fresh and hardened properties of both conventional OPC and alkali-activated systems. Adding nanoparticles is one of the most popular means. And in N-A-S-H geopolymers, nano-$SiO_2$ is the most commonly used nanoparticle to improve mechanical strength, considering

its silica composition and the amorphous characteristic. However, their nano-size has been found to cause local agglomeration, which in turn frequently reduces the workability and sometimes extends the setting process (Gao et al., 2015). Clearly, these shortcomings must be resolved to derive maximum benefits from nano additives for N-A-S-H geopolymers. According to the literature, solid particles of nanometric size (or sub-micron, ~100 nm) allow the stabilization of droplets as large as a few micrometers in diameter or even larger (Chevalier and Bolzinger, 2013). The resulting emulsion, also called water-in-air Pickering emulsion or dry water, could then range in size from 10 μm to 300 μm. This offers a possibility to offset the damage led by the agglomeration of nanoparticles on the workability of the fresh mixture due to its nano-size effect. However, its potential application in the field of cementitious materials has never been explored.

In view of the foregoing, the present doctoral study is directed to synthesize N-A-S-H geopolymer mixtures with nano-$SiO_2$ stabilized dry water and understand the mechanisms that govern geopolymerization in order to optimize the design for wider application of N-A-S-H geopolymer concrete systems. Accordingly, the following aspects will be investigated: (a) The mechanisms underlying effects of various oxide ratios on workability, setting, compressive strength and acid resistance of N-A-S-H geopolymers will be studied; (b) Nano-$SiO_2$ stabilized dry water will be used to improve the four aforementioned properties, and the associated enhancement mechanisms will be clarified; (c) Multi-factor models will be proposed and validated based on the generated experimental data, to predict these fundamental engineering properties and so, provide a design guideline for N-A-S-H geopolymers. These models could be used further by practitioners to conduct and validate their mix design in practice.

## 1.2. Problem Statement

After reviewing the available literature, geopolymer is known as a potential alternative to Portland cement concrete with comparable engineering properties and much lower carbon emissions and energy consumptions during its manufacture. As compared to the well-designed OPC systems, there so far lacks mature mix design techniques for N-A-S-H geopolymer systems. Prior studies confirmed that the compositional oxide ratios, namely $SiO_2/Al_2O_3$, $Na_2O/Al_2O_3$ and $H_2O/Na_2O$, dominate the compressive strength of geopolymer systems. However, the following challenges are still existing and require to be solved to promote its further application in the building industry:

(1) There is no current mixture design guideline available for N-A-S-H geopolymers. A conventional mix design on the lines of Portland cement concrete quantifies the binder, water and aggregates. However, unlike Portland cement, the oxide composition of the precursor, itself usually an agro-industrial waste, is not standardized.

(2) In addition to compressive strength, the mechanisms underlying the effects of oxide ratios on other basic and equally important properties, e.g., workability, setting and acid resistance, have not been revealed clearly. Besides, the mutual interactions between the compositional oxide ratios result in a trade-off for practical engineering benefits. Therefore, a flexible mixture design for N-A-S-H geopolymers is indeed required, when the priority of the above properties varies in practice.

(3) There so far lacks predictive models that could be used by practitioner to conduct and validate their mix design for N-A-S-H geopolymers.

(4) Nano-$SiO_2$ is known to impart greater compressive strength in N-A-S-H geopolymers, but at the cost of workability and often, delayed setting. Nano-$SiO_2$ stabilized dry water powders (Water-in-air Pickering emulsions) potentially offer a resolution to this trade-off between the desired

engineering properties due to the unique combination of characteristics: (i) the size coarsening effect; (ii) the amorphous of stabilizing nano-$SiO_2$ and (iii) the temporarily encapsulated water droplet. However, this has never been explored.

### 1.3. Scope and objectives

N-A-S-H geopolymer is essentially made from the aluminosilicate precursor with extremely low calcium content, alongside the sodium-involved alkali activator. Due to the wide clay resource and the rich amorphous $SiO_2$ and $Al_2O_3$ contents, metakaolin is used as the most popular aluminosilicate precursor to be activated by the combination of sodium hydroxide and sodium silicate solutions to produce N-A-S-H geopolymers. Thus, the focus is limited to metakaolin-based geopolymers in this project. Other types of aluminosilicate precursor and alkali activator are currently not considered. In addition, as a potential alternative to the OPC system, the N-A-S-H geopolymer must ensure satisfactory workability, quick final set and excellent compressive strength, simultaneously. So that, the mixture design guidelines developed for N-A-S-H geopolymers will be aimed at the above engineering properties. Besides, due to the low calcium content contained in N-A-S-H geopolymers, some classic durability concerns such as chloride and sulphate attacks may not threaten the durability that much and therefore, will not be examined in this study, Instead, the acid attack will significantly reduce the alkaline condition inside N-A-S-H geopolymers and then depolymerize the associated structure. Accordingly, the acid resistance of N-A-S-H geopolymers will be one of the scientific focuses in this doctoral project. With regard to the water-in-air Pickering emulsion, dry water, prior studies have reported that any hydrophobic nanoparticles are promising to produce it with varying application purposes. For the N-A-S-H geopolymer, the higher $SiO_2/Al_2O_3$ molar ratio essentially boosts the geopolymerization and then improves the engineering properties. Thus, the dry water powders stabilized by amorphous nano-

$SiO_2$ will be investigated in this study, as a reinforcing additive to enhance the engineering properties of N-A-S-H geopolymers.

The overall objective of this doctoral project is to understand the geopolymerization in N-A-S-H geopolymers made with varying compositions alongside the potential enhancement led by dry water, and in turn, promote the widespread application of N-A-S-H geopolymers in the Canadian region. To achieve this, three primary goals are set accordingly:

(1) To clarify the mechanisms underlying the effects of principal compositional ratios namely, $SiO_2/Al_2O_3$, $Na_2O/Al_2O_3$ and $H_2O/Na_2O$ ratios, on workability, final set, compressive strength and acid resistance of N-A-S-H geopolymers.

(2) To develop N-A-S-H geopolymers incorporating nano-$SiO_2$ stabilized dry water and investigate the enhancing mechanism of this dry water upon geopolymerization as well as the ensuing properties of N-A-S-H geopolymers.

(3) To establish multi-factor models that will be used as a predictive tool to help design a workable, strong and acid-resistant N-A-S-H geopolymer system to meet different engineering requirements in the Canadian region.

### 1.4. Significance

As a promising alternative to Portland cement systems, the successful and widespread application of N-A-S-H geopolymers alongside nano-$SiO_2$ stabilized dry water will significantly offset the huge use of conventional Portland cement and concrete in building engineering. This will in turn impart excellent engineering properties to built infrastructures and also contribute to global sustainability. However, as aforementioned, there so far lacks mature mixture design techniques to guide the production of N-A-S-H geopolymers incorporating nano-$SiO_2$ stabilized dry water

and, achieve great workability, final set, strength and durability simultaneously. Also, very few related articles could be found in the current literature to resolve the above scientific gap. Thus, this Ph.D. study may be deemed novel and significant.

### 1.5. Thesis organization

The present Chapter namely, Chapter 1, briefly introduces the background of the topic and states the existing problems related to this research. Besides, this Chapter also highlights the main objectives and significance of this doctoral study. Finally, the outline of this thesis is listed.

Chapter 2 gives a comprehensive literature review upon the issues approached by this research. Along with the mechanism underlying the geopolymerization of aluminosilicate, the effects of compositional oxides upon properties of geopolymers, mainly compressive strength, are reviewed critically. And, both advantages and disadvantages of using conventional nano-$SiO_2$ particles in alkali-activated geopolymers are discussed. In addition, the methodology to evaluate and characterize the performance of geopolymers is introduced in detail.

Chapter 3 investigates the effects of principal oxide ratios namely, $SiO_2/Al_2O_3$, $Na_2O/Al_2O_3$ and $H_2O/Na_2O$ ratios, on workability, final set and strength of N-A-S-H geopolymers. In the regard, N-A-S-H geopolymers with varying oxide compositions are produced, and tested for flow diameter, final setting time, splitting tensile strength and compressive strength. Alongside, the companion rheological, thermal, morphological, chemical, and microstructural characterizations are carried out to help understand the underlying mechanisms.

Chapter 4 aims to examine the potential benefit of nano-$SiO_2$ stabilized dry water upon enhancing the fresh and hardened properties of N-A-S-H geopolymers. In this Chapter, various dry water powders are produced and added to the geopolymer mixture, followed by the combination of

workability, final set and strength tests. The reference mixtures respectively made without any nano additive and with lone nano silica are prepared as well, to compare with those dry water-involved mixtures. Further, the rheological, thermal, morphological, chemical, and microstructural characterizations are conducted to clarify the mechanism of enhancement led by dry water upon N-A-S-H geopolymers.

Chapter 5 explores the effects of principal oxide ratios namely, $SiO_2/Al_2O_3$, $Na_2O/Al_2O_3$ and $H_2O/Na_2O$, on the acid-resistance of N-A-S-H geopolymers. In this manner, the produced specimens are immersed in the sulphuric acid solution with a pH value of 1 for up to 12 weeks. During this continuous chemical attack, a couple of physical and mechanical properties are monitored, including the pH evolution of sulphuric acid solution, mass and diameter variations, strength changes, and penetration depth. In the meantime, the companion characterizations of morphology, chemistry, porometry and microstructure are evaluated for N-A-S-H geopolymer specimens right before and after the acid attack, in order to understand the underlying mechanisms.

Chapter 6 examines the potential enhancement led by nano-$SiO_2$ stabilized dry water upon the acid-resistance of N-A-S-H geopolymers. Three variants of dry water, respectively containing 10%, 15% and 20% nano silica, are prepared and then added to the N-A-S-H system. Besides, the plain reference mixture and the other one incorporating lone nano silica are produced as well, to compare with the associated dry water-involved sample. The testing protocols in this Chapter are same as the previous Chapter 5.

Chapter 7 establishes multi-factor models for predicting flow diameter, final setting time, compressive strength and acid penetration of N-A-S-H geopolymers, by taking the principal mixing ratios namely, $SiO_2/Al_2O_3$, $Na_2O/Al_2O_3$, $H_2O/Na_2O$ and liquid-to-solid ratios, into account. These models are validated against untrained data, and the satisfactory accuracy proves that they

may be used as the predictive tool for practitioners to conduct and validate their mix design for N-A-S-H geopolymers in practical projects.

In Chapter 8, the significant findings and concluding remarks generated from Chapter 3~7 are condensed. Besides, this Chapter also states the limitation of the present study and recommendations for ongoing and further studies on this topic.

# Chapter 2. Literature review

## 2.1. Introduction

As widely reported, alkali-activated geopolymer systems are recognized as a promising alternative to conventional OPC systems. Besides the merits in terms of low carbon emissions and energy consumption, they also display comparable engineering properties, including high workability, quick final set, great strength, and even superior durability when served in some aggressive conditions. Table 2.1 compares the geopolymer and conventional OPC systems to highlight the applicability of the former (Kumar and Kumar, 2014). As seen therein, besides environmental merits, the geopolymer displays much superior performance on both fresh and hardened properties. However, there exists limited application of geopolymers in practice. One of the most important factors behind this is that there currently is no design guideline available for practitioners to help them design a geopolymer mixture to meet the various performance requirements. Also, the durability of geopolymers, for example, under acid penetration, resistance to shrinkage, chloride and sulphate attack, have not been investigated as systematically as the OPC systems. Consequently, some of the above issues have been taken up here as the objectives of this thesis, with the view to promoting the widespread application of geopolymers in Canada.

Table 2.1 Comparison between conventional Portland cement and geopolymer systems.

| Properties | Portland cement | Geopolymer |
|---|---|---|
| Physical-mechanical properties | | |
| Setting time | 30~300 mins | 60~120 mins |
| Compressive strength | 33~53 MPa after 28 days | 30~120 MPa after 7 days |
| Durability | Moderate | More durable than Portland cement |
| Environmental impact | | |
| $CO_2$ emission | 800~900 kg/ton | 150~200 kg/ton |
| Embodied energy | 4000~4400 MJ/ton | 2200~2400 MJ/ton |
| Water requirement | ~600 liters/ton | ~450 liters/ton |

The N-A-S-H geopolymer is commonly produced by activating the solid aluminosilicate precursor with the blended alkaline solution of sodium hydroxide and sodium silicate. According to prior studies, the performance of N-A-S-H geopolymers is strongly dependent upon the chemical compositions, chiefly the ratio of the component oxides and especially the $Si_2O/Al_2O_3$, $Na_2O/Al_2O_3$ and $H_2O/Na_2O$ molar ratios. Therefore, this chapter will firstly present a detailed review of the mechanisms of geopolymerization, alongside the effects of oxide compositions on fresh and hardened properties of N-A-S-H geopolymers. In addition, although dry water has not been examined in the available literature, its raw material, i.e., nano-$SiO_2$ itself, has been widely used as an additive to enhance the mechanical property of geopolymer systems, depending on its nano size and amorphous characteristic. So that, the application of nano-$SiO_2$ particles in this topic will be reviewed as well. Finally, the relevant experimental techniques that are widely used to characterize geopolymer systems will be introduced in detail.

### 2.2. Mechanism of geopolymerization

In the last a few decades, intensive scientific efforts have been carried out to understand the mechanism of geopolymerization, and it has been widely recognized that the formation of

geopolymer systems may be summarized as follows: (i) Dissolution and hydrolysis of aluminosilicate precursor in the alkali activator solution, mainly comprising alkali hydroxides and/or silicates; (ii) Physical transportation of dissolved Si and Al complexes; (iii) Chemical polycondensation between the tetrahedral $SiO_4$ and $AlO_4$ units to form the oligomeric aluminosilicate in the gel phase, which may continuously transform into a more rigid gel phase; (iv) Final hardening of formed N-A-S-H gels (Provis and Van Deventer, 2007). The formed N-A-S-H geopolymer network is typically expressed as $M_n[-(Si-O_2)_z-Al-O]_n \cdot wH_2O$ (Davidovits, 1988; Palomo and Glasser, 1992; Davidovits et al., 1994; Van Jaarsveld et al., 1997), wherein M means the alkali metal ions such as $K^+$, $Na^+$, and $Ca^{2+}$, which play a significant role in balancing the negative charge (Khale and Chaudhary, 2007; Juengsuwattananon et al., 2019). Here, n indicates the polycondensation degree while z represents the amount of silicon atoms contained in each oligomer and may variously be 1, 2 and 3, depending on the type of the silicate-aluminate structure (Palomo and Glasser, 1992). The above process has further been expressed by Davidovits (2008) in a couple of chemical equations, as now replotted and shown in Figure 2.1.

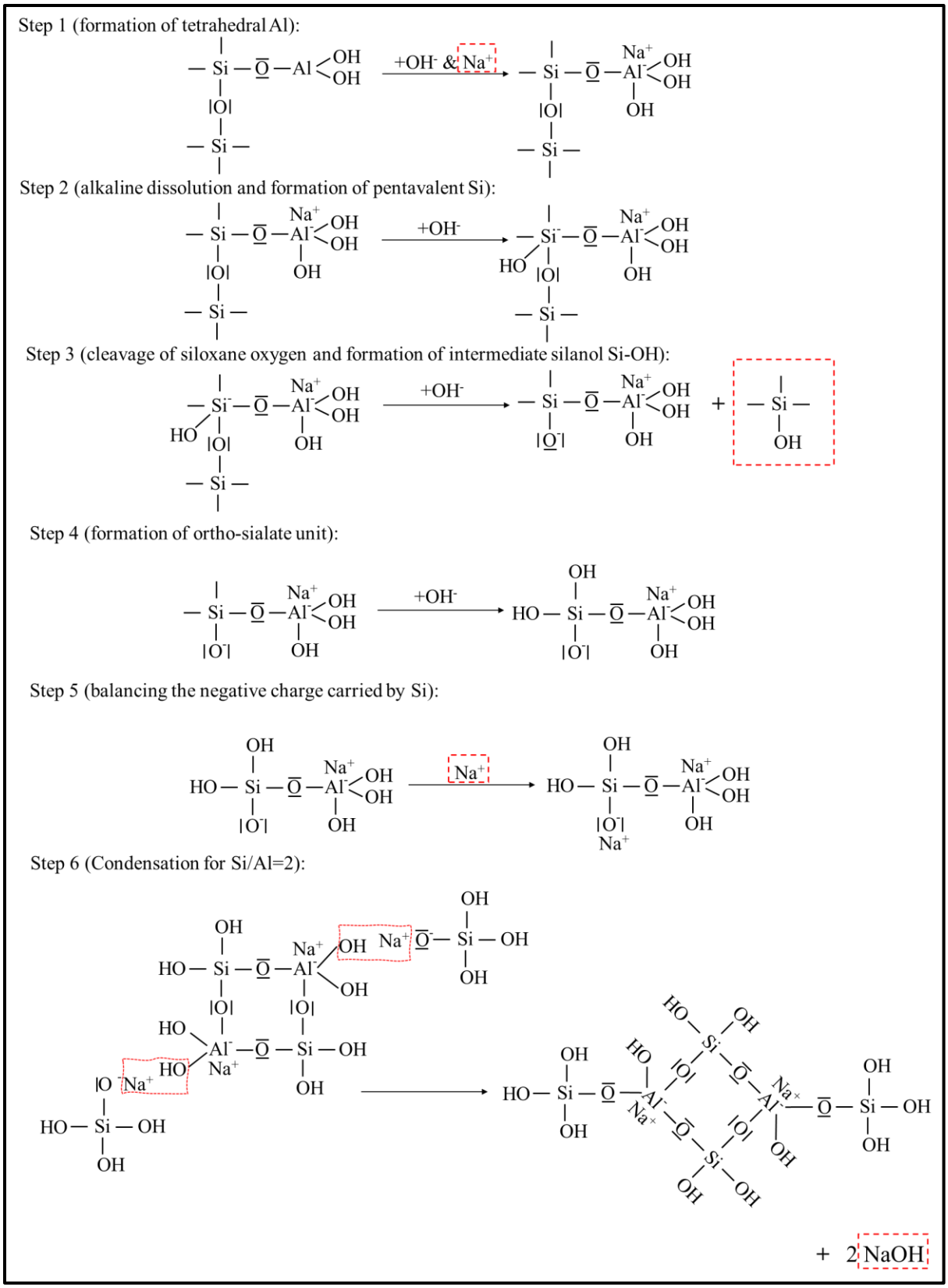


Figure 2.1 The chemical mechanism of geopolymerization.

It is clear to see that the tetrahedral $SiO_4$ and $AlO_4$ groups mutually connect with each other by sharing the oxygen atom, forming the skeleton of the oligomeric chain. And, the additional silica species appear to extend the length of the polymerized aluminosilicate framework. This in turn manifests in an improvement in the degree of geopolymerization. Notice also that the last step namely, the condensation, is a process of $Na^+$ and $OH^-$ regenerations. This may imply the amount of alkali may need to be controlled within a suitable range, in order to ensure adequate activation efficiency on the one hand and avoid the depression of condensation on the other hand.

### 2.3. Effect of oxide ratios on fresh and hardened properties of geopolymer

#### 2.3.1. Compressive strength

Compressive strength is one of the most significant properties of cementitious systems when serving as a structural material. The main responsibility of a cement-based system is to sustain the compressive load. Being a potential alternative to conventional Portland cement concrete, geopolymer systems must display adequate compressive strength, which could be determined as per ASTM C39 (2018).

In general, the amount of amorphous $SiO_2$ and $Al_2O_3$ determines the polycondensation degree while the metal cations and hydroxyl ions control the dissolution and hydrolysis. This could also be confirmed, according to the mechanism of the geopolymerization shown in Figure 2.1. Hence, a large number of studies have been conducted to investigate the effect of compositional ratios on the compressive strength of the N-A-S-H geopolymer. In particular, Davidovits et al. (1994) recommended the following range for each compositional ratio to achieve a satisfactory compressive strength: $SiO_2/Al_2O_3$=3.5~4.5, $Na_2O/Al_2O_3$=0.8~1.2 and $H_2O/Na_2O$=10~25.

The $SiO_2/Al_2O_3$ ratio carries priority in the polycondensation. Stevenson and Sagoe-Crentsil (2005) reported that the highest strength was witnessed when the $SiO_2/Al_2O_3$ ratio was between 3.5-3.8. This finding was partially supported by Duxson et al. (2007). It was seen that regardless of the alkaline solution, the compressive strength of the N-A-S-H-based geopolymer increased linearly as the $SiO_2/Al_2O_3$ ratio increased from 2.3 to 3.8. However, any further increase in this ratio beyond 3.8 led to a noticeable decrease in compressive strength. The above phenomenon may be explained through the following: (i) A higher $SiO_2/Al_2O_3$ molar ratio promotes the formation of sialate siloxo, i.e., $M_n(\text{-Si-O-Al-O-Si-O-})_n$, and sialate disiloxo i.e., $M_n(\text{-Si-O-Al-O-Si-O-Si-O})_n$, which both have stronger bonds between the silicon compounds themselves. The Si-O bond is long recognized as much stronger than the Al-O bond, and therefore, the resulting aluminosilicate framework involving more Si-O bonds will exhibit better structural integrity. In as much as the structure being tighter, this densification results in a higher compressive strength (Kong et al., 2007); (ii). On the other hand, an over-high $SiO_2/Al_2O_3$ ratio (beyond 4.0) may hinder the corresponding strength development since the rate of condensation between the silicate species is substantially slower than that between silicon and aluminum oxides (Chindaprasirt et al., 2009; Hardjito and Fung, 2009; Temuujin et al., 2010); (iii) Further, the $SiO_2/Al_2O_3$ ratio in N-A-S-H geopolymers is commonly adjusted by the sodium silicate solution. And, the higher $SiO_2/Al_2O_3$ ratio usually corresponds to the greater liquid content brought into the mixture, which in turn plants a potential risk for the degradation of the microstructure and accordingly, damages the eventual strength.

As for the $Na_2O/Al_2O_3$ molar ratio, a few studies were conducted to investigate its effect on alkali-activated geopolymers. Kovalchuk et al. (2008) examined the fly ash-based geopolymer and found that both flexural and compressive strength increased as this molar ratio rose from 0.5 to 1.0. A

similar tendency was witnessed elsewhere (Thakur and Ghosh, 2009; Adam, 2009; Ghosh and Ghosh, 2012b). On the other hand, Kani and Allahverdi (2003) reported the optimum $Na_2O/Al_2O_3$ molar ratio of 0.92 to achieve the greatest compressive strength. Based on the statistical analysis, Lahoti et al. (2017) found that the optimum range of $Na_2O/Al_2O_3$ for metakaolin-based geopolymer to yield the greatest strength was between 0.8 and 1.2, which coincided with the one recommended by Davidovits et al. (1994). Note however that, while the preceding studies reported the effect of the $Na_2O/Al_2O_3$ molar ratio upon compressive strength, the underlying mechanism has not been described clearly yet and therefore requires further clarification.

The $H_2O/Na_2O$ molar ratio essentially indicates the alkalinity within the geopolymer mixture, and it plays a significant role in the dissolution of aluminosilicate precursors as well as the subsequent activation (Heah et al., 2013; Xu and Van Deventer, 2000). Some studies reported that this ratio would not affect the nature of the formed geopolymer network namely, the type and the degree of polycondensation in the geopolymer network (Rahier et al., 1997). Recall earlier, the acceptable $H_2O/Na_2O$ molar ratio was recommended as 10-25 by Davidovits to produce geopolymer systems with acceptable strength (Davidovits et al., 1994). However, many studies claimed that the above range might be too broad. While a value of 10 in this ratio resulted in adequate compressive strength, the value close to the upper bound, i.e., 25, may not be able to trigger sufficient geopolymerization (Barbosa et al., 2000; Kirschner and Harmuth, 2004; Yusuf et al., 2014). Also, a continuous increase in the $H_2O/Na_2O$ molar ratio beyond 10 has been noted to cause a decrease in compressive strength for N-A-S-H geopolymers (Hardjito et al., 2004a; Šulc, 2009).

### 2.3.2. Workability and setting

As compared to compressive strength, there exists very little literature to clarify how the oxide ratios impact other equally vital properties such as workability, setting time and durability.

Workability defines the ability of concrete and other cementitious materials to be placed and compacted without any segregation. It also determines how easily the fresh mixture could fill in the mould with different shapes during the in-situ construction. For cementitious paste mixtures, the corresponding workability is usually evaluated as per ASTM C230/C230M (2008), expressing in the average flow diameter on the flow table.

There so far is no specific study directed to investigate the effect of $SiO_2/Al_2O_3$ molar ratio on the rheology of geopolymer. Considering this ratio is mainly adjusted by the silicate-based activator, such as sodium silicate, the higher this ratio, therefore, raises the liquid-to-solid ratio in the mixture (Yi et al., 2020). Based on the knowledge of conventional OPC systems, an increase in the liquid-to-solid ratio could reduce the inter-particle friction (Meng et al., 2019). Given this, increasing the $SiO_2/Al_2O_3$ molar ratio is expected to enhance the workability of N-A-S-H geopolymers. But this speculation has not been verified experimentally. Therefore, further experimental investigations are indeed required and also the underlying mechanism must be clarified.

The final setting time refers to the moment at which the fresh mixture completely loses its plasticity and starts to gain strength. This parameter could be determined by using a Vicat Needle apparatus, conforming to ASTM C191 (2008).

De Silva et al. (2007) examined the final setting time of N-A-S-H geopolymers made with a $SiO_2/Al_2O_3$ molar ratio ranging from 2.5 to 5.01. A considerably exponential increase in the final setting time was witnessed when raising the $SiO_2/Al_2O_3$ molar ratio continuously. This phenomenon was supported by another related study (Tajunnisa et al., 2017). It is recognized that the rate of condensation between the silica species is substantially slower than that between silica and alumina (Hardjito and Fung, 2009). As a result, the higher the $SiO_2/Al_2O_3$ molar ratio, the

longer the final setting time. However, it should be pointed out here that the examination of the $SiO_2/Al_2O_3$ molar ratio below 2.5 is rarely conducted. The initial $SiO_2/Al_2O_3$ molar ratio in some aluminosilicate precursors, such as metakaolin, is only about 1.8~2.0 and therefore, the range close to the lower end also deserves detailed investigations. Besides, the underlying mechanisms must be clarified.

In general, the aluminosilicate precursor is the sole $Al_2O_3$ source of N-A-S-H geopolymers, and the $Na_2O$ content is related to the alkaline activator. Hence, the larger $Na_2O$ content usually corresponds to the greater liquid content (Huseien et al., 2016), which is in turn expected to improve the workability of the fresh geopolymer mixture. However, very limited experimental studies were carried out to justify this. Besides, the mechanism underlying the effect of $Na_2O/Al_2O_3$ molar ratio on workability is not revealed yet.

According to Davidovits et al. (1994), while the alkali metal ion is required to balance the charge during the synthesis of N-A-S-H geopolymers, the associated geopolymerization is also a regeneration process of $Na^+$ and $OH^-$, see Figure 2.1. Given this, either an excessive or a deficient $Na_2O$ content may deter the process of geopolymerization and in turn, hinder the further setting process. However, the above speculation has not been verified in any experimental study and therefore, requires further detailed investigations.

The liquid phase effectively enlarges the inter-particle distance and then, enhances the flowability of the fresh geopolymer mixture. This determines that the $H_2O/Na_2O$ molar ratio is able to affect the workability of N-A-S-H geopolymer mixtures strongly. According to Sathonsaowaphak et al. (2009), the flowability of the fresh mixture increased significantly as the $H_2O/Na_2O$ ratio rose from 12.27 to 19.08. This tendency was then corroborated by Berger et al. (2009) who evaluated the

workability of fresh geopolymer mixture within the $H_2O/Na_2O$ molar ratio range of 10~15. Once again, the higher the $H_2O/Na_2O$ molar ratio, the greater the flowability.

As for the final set, although an increase in this molar ratio is recognized to dilute the alkali concentration and in turn depress the alkali-activation efficiency (Kirschner and Harmuth, 2004), there is limited information in the available literature to clarify the influence of the $H_2O/Na_2O$ molar ratio on the setting process of geopolymers. Also, the underlying mechanism of this ratio on final setting time is not clarified yet.

### 2.3.3. Summary

As summarized above, the influence of the $SiO_2/Al_2O_3$ molar ratio on the strength of geopolymer systems has been well documented. However, the underlying mechanisms, that detail the role of $Na_2O/Al_2O_3$ and $H_2O/Na_2O$, have not been comprehensively revealed. Besides, their effects upon other equally vital properties such as workability, setting and even durability have not been systematically examined, and therefore require further investigations. Notwithstanding the active research on N-A-S-H geopolymers, there exists very limited information to guide the mixture design to guarantee all of these attributes namely, workability, setting, strength and durability simultaneously. It should be noted here that due to the mutual interactions between mixing design ratios, the best performance of one property, e.g. strength, is likely to be achieved by sacrificing other engineering properties. Besides, there currently is no set of accurate and explicit models for practitioners to operate a flexible mix design for N-A-S-H geopolymers, per varying engineering demands.

## 2.4. Acid resistance

As a potential alternative to OPC, geopolymers should register not only superior strength but also enough resistance to durability concerns. Depending on the low calcium content, N-A-S-H geopolymers are recognized to be durable, against some typical durability issues such as chloride and sulphate attacks. This is mainly because these chemical attacks essentially require adequate calcium to form the respective corrosion product namely, Friedel's salt for chloride attack and ettringite (Aft) for sulphate attack. However, due to the highly alkaline nature, both OPC and N-A-S-H geopolymer systems are susceptible to an acid-rich environment. As broadly reported, the acid attack occurring in OPC and geopolymer systems will cause irreversible deteriorations, manifesting as significant stiffness and strength losses (Miyamoto et al., 2014; Aiken et al., 2018). Accordingly, the acid resistance of geopolymers essentially governs the lifespan of structural members when served in such a harsh environment (Gutberlet et al., 2015). Also, the maintenance of these structures increases additional costs on the one hand and, is harmful to the ecological environment and resource conservation on the other hand (Gutberlet et al., 2015).

Although the excellent acid resistance of N-A-S-H geopolymers is widely confirmed, acid-induced degradation has still been observed during continuous exposure to an acid-rich environment. Allahverdi and Šlvára (2001; 2005) proposed the mechanism underlying the acid attack in geopolymer systems, which has been widely accepted by other researchers (Gao et al., 2013a). The mechanism of this durability issue in geopolymers mainly involves the following two steps: Firstly, the metal cations constituting the N-A-S-H framework, i.e., $Na^+$, will be replaced by the penetrating $H^+$, which in turn causes the dealumination of the geopolymerized structure. Then, an imperfect siliceous structure will be formed, due to the framework vacancies. In the meantime, the

released aluminum species will be substantially leached out toward the external environment. The above process has now been schematically plotted by the author and shown in Figure 2.2.

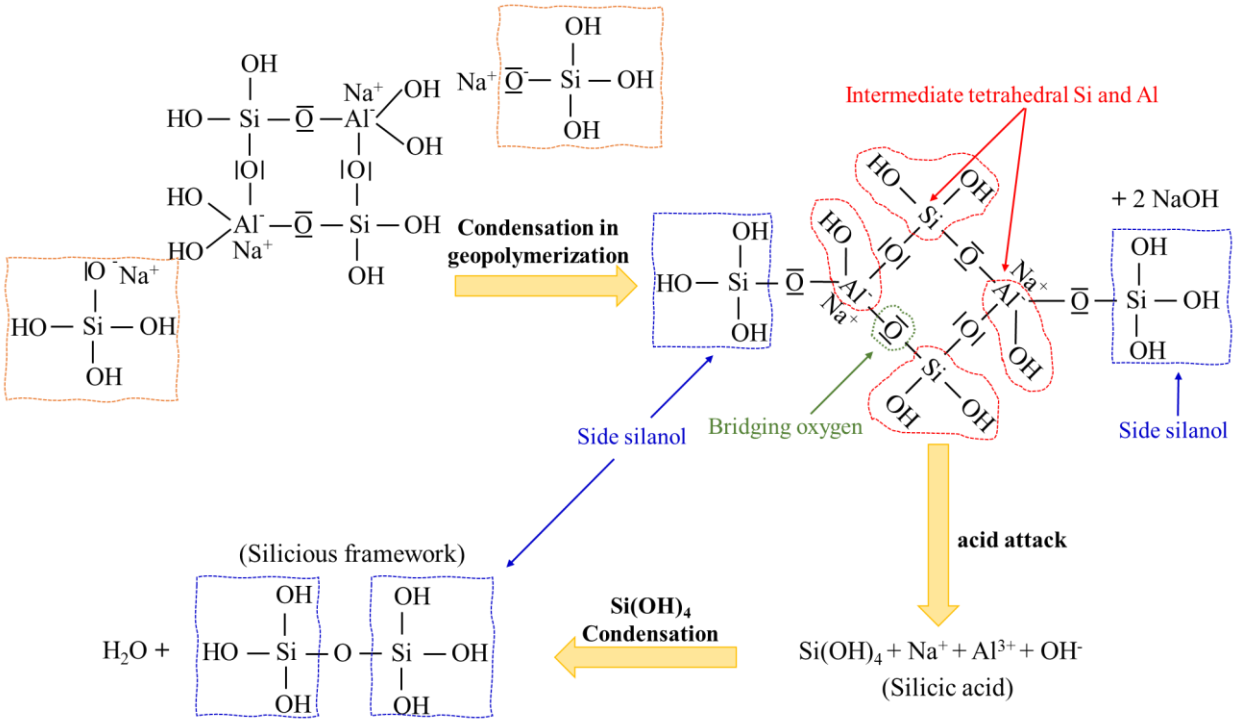


Figure 2.2 The chemical mechanism of acid attack in N-A-S-H geopolymer systems.

In the current literature, factors in terms of precursor and alkali activator have been broadly investigated. For instance, Thokchom et al. (2009) found that although increasing the alkali dosage caused a rise in the mass loss for geopolymers subjected to sulphuric acid attack, the residual compressive strength was increased. Aiken et al. (2018) examined the acid resistance of binary slag-fly ash geopolymers, and the result revealed that the porosity of geopolymer specimens was refined gradually with an increasing slag content. However, the resultant reaction products became more susceptible to sulfuric acid attack. A similar result was noticed by Lee and Lee (2016). In addition, Vogt et al. (2021) noted that the N-A-S-H geopolymer made from metakaolin with a 7.5%~9% silica fume replacement displayed the enhanced acid resistance, attributed to the boosted

formation of silicate-rich geopolymerized structures. Bouguermouh et al. (2017) examined the effect of activator type on the acid resistance of metakaolin-based geopolymers, and the potassium-based and sodium-based activators were employed, respectively. It was found that the former helped alleviate the mass loss led by the acid attack. The reason behind this may be the presence of secondary minerals such as quartz and muscovite in the case of the potassium-based activator. These crystals acted as the filler in pores and thereafter, hindered the penetration of hydrogen ions.

Although the acid-induced degradation of the N-A-S-H geopolymer framework is strongly dependent upon the principal oxide components, very limited information exists in the current literature to clarify the effects of $SiO_2/Al_2O_3$, $Na_2O/Al_2O_3$ and $H_2O/Na_2O$ ratios on this topic. Therefore, further investigations along this line must be conducted, to develop the mixture design guideline for acid-resistant N-A-S-H geopolymers.

### 2.5. Benefits of nano-$SiO_2$

As aforementioned, amorphous $SiO_2$ and $Al_2O_3$ are the two most important sources of geopolymerization, and the higher $SiO_2/Al_2O_3$ ratio essentially corresponds to a higher degree of polycondensation. Therefore, nano-$SiO_2$ is the most commonly used nanoparticle to strengthen the mechanical strength of geopolymer systems. It has been found that Prior studies reported that a 1%~3% (w./w.) addition of nano silica to geopolymer mixtures was able to improve the compressive strength by 10%~55% (Gao et al., 2013b; Gao et al., 2015; Deb et al., 2016; Rashad and Ouda, 2019; Rashad, 2019). The reasons behind this are firstly attributed to that the supplementary silica source of nano-$SiO_2$ promotes the degree of geopolymerization. Secondly, depending upon the nature of the nanoscale in particle size, nanoparticles may act as a filler to alleviate the microcrack propagation inside geopolymer systems.

Besides mechanical properties, adding nanoparticles has also been reported to improve the durability of geopolymer systems. Some studies reported that the presence of nanoparticles alleviated the leaching behaviour inside the geopolymer and in turn, strengthened the resistance of geopolymers against chloride and sulphate attacks (Çevik et al., 2018; Nuaklong et al., 2018). Also, the geopolymer system made with nano-$SiO_2$ displayed a stronger resistance to acid attack, manifesting as the higher remaining compressive and splitting strength after various acid exposures (Sumesh et al., 2017). The detected enhancement upon acid resistance is likely linked to that the addition of nanoparticles reduces the pore size, porosity and sorptivity of geopolymers (Duan et al., 2016). As a result, the penetration of external chemicals may be depressed effectively.

In spite of the potential enhancement upon mechanical property and durability, the presence of nano-$SiO_2$ was widely found to sacrifice other equally important engineering properties, i.e., reducing the workability and extending the final set, due to the significantly large surface area of nanoparticles and in turn the increasing water demand (Gao et al., 2015). Some representative studies are summarized in Table 2.1. The above disadvantages also become the important reasons for its limited application in cementitious systems.

Table 2.2 Effect of nano-$SiO_2$ on workability and setting of geopolymer systems.

| Reference | Nano-$SiO_2$ | Nano size | Precursor | Positive |
|---|---|---|---|---|
| Workability | | | | |
| Deb et al. (2016) | 0.5%~3% | 15 nm | Fly ash | No |
| Gao et al. (2015) | 1%~3% | - | Fly ash/slag | No |
| Luo et al. (2017) | 1%~3% | 20~50 nm | Metakaolin/slag | No |
| Shahrajabian and Behfarnia | 1%~3% | 11~13 nm | Slag | No |
| Nuaklong et al. (2018) | 1%~3% | 40 nm | Fly ash | No |
| Rashad and Ouda (2019) | 0.5%~4% | 240 $m^2/g$ | Metakaolin | No |
| Ramezanianpour and Moeini | 2%~4% | 12 nm | Slag | No |
| Setting time | | | | |
| Luo et al. (2017) | 1%~3% | 20~50 nm | Metakaolin/slag | No |
| Lo et al. (2017) | 1%~2% | 10 nm | Metakaolin | No |
| Gao et al. (2015) | 1%~3% | - | Fly ash/slag | No |

### 2.6. Water-in-air Pickering emulsion (Dry water)

Pickering emulsions are emulsions of any type, either oil-in-water (o/w), water-in-oil (w/o), or air-in-water (a/w), water-in-air (w/a), stabilized by solid particles in place of surfactants (Binks and Horozov, 2006). Pickering emulsions retain the basic properties of classical emulsions stabilized by surfactants (emulsifiers), so that a Pickering emulsion can be substituted for a classical emulsion in most applications of emulsions. In general, solid stabilizing particles are necessarily smaller than emulsion droplets. Solid particles of nanometric size (or sub-micron, ~100 nm) allow for the stabilization of droplets as large as a few micrometres in diameter or even larger (Chevalier and Bolzinger, 2013). The resulting emulsion could then range in size from 10 μm to 300 μm. This offers a possibility to offset the damage led by the agglomeration of nanoparticles on the workability of the fresh mixture due to its nano-size effect.

Dry water is a water-in-air (w/a) Pickering emulsion, which is usually produced by stabilizing 90%~95% water droplets with 5%~10% predominantly hydrophobic nanoparticles under the highly shearing stirring process (Binks and Murakami, 2006; Forny et al., 2009). The obtained dry water will exist in the form of soft powder with the water droplet encapsulated inside. Recall that, amorphous $SiO_2$ and $Al_2O_3$ are the two most important sources for the formation of N-A-S-H frameworks, and the higher $SiO_2/Al_2O_3$ ratio essentially leads to a greater degree of geopolymerization and in turn, the stronger structural integrity. Therefore, nano-$SiO_2$ is the most suitable stabilizer to produce the eligible Pickering emulsions. According to relevant literature, the hydrophilic particles are used to produce the air-in-water emulsion, viz. foam, whereas the hydrophobic stabilizer could successfully yield the particle-stabilized water-in-air powders, namely dry water (Dieter et al., 1968; Aussillous and Quéré, 2001). In the civil engineering field, foam has been widely reported to magnify the porous character of OPC as well as geopolymer systems. This causes a significant decrease in density and a considerable increase in the porosity of the hardened structure. Eventually, the mechanical properties are poor (Bindiganavile and Hoseini, 2019). Given this, the water-in-air emulsion namely, dry water, is thus more suitable to be used as a functional material in N-A-S-H geopolymers. However, this topic has not been touched.

## 2.7. Characterizations on geopolymers

### 2.7.1. Viscosity

Viscosity is an important rheological property. It essentially indicates the resistance of the fresh mixture to a change in dimension, or the movement of neighbouring portions relative to one another. As the fresh mixture is forced to move and carry along to some extent adjacent parts, viscosity is considered as internal friction between the molecules. Viscosity also controls the

flowable mixture in such processes as spraying, shaping, and surface coating. Thus, this parameter could be used to explain the flowability of alkali-activated geopolymer mixtures made with varying oxide compositions. In general, the distilled water has a viscosity of 1 mPa.s at room temperature, and that of sodium hydroxide and sodium silicate solutions is 70 mPa.s and 200~400 mPa.s, respectively. This, therefore, determines the viscous nature of alkali-activated geopolymer mixtures. In addition, the flowability of the fresh mixture could also be affected by the liquid-to-solid ratio (Mu et al., 2017). Usually, the larger the liquid-to-solid ratio, the smaller the internal friction and in turn the lower viscosity. Viscosity is commonly measured with various types of viscometers and rheometers. For instance, the Brookfield DV-II+ Programmable Viscometer that is fitted with a SC4-27 spindle can capture the viscosity within the range of 0~1250 mPa·s, as shown in Figure 2.3. It must be emphasized here that while determining the viscosity of fresh geopolymer mixtures, close temperature control must be ensured, as the temperature change may cause a significant error upon the measurement.

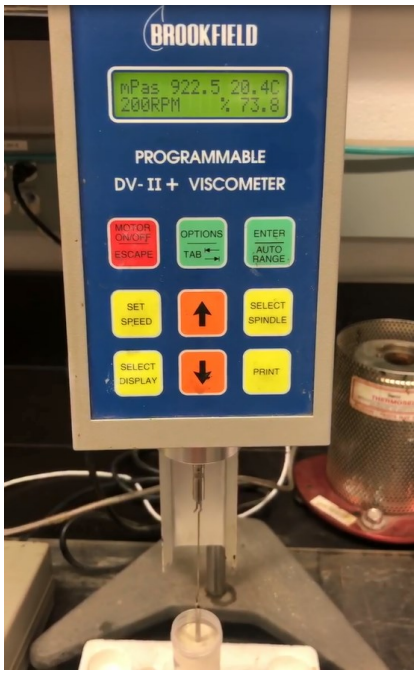


Figure 2.3 Brookfield DV-II+ Programmable Viscometer employed to determine viscosity.

### 2.7.2. Temperature evolution

Thermodynamically, geopolymerization is found as exothermic, mainly attributed to the following two processes namely, (i) the dissolution of solid aluminosilicate precursor and (ii) the condensation between tetrahedral $SiO_4$ and $AlO_4$ units as well as the subsequent polycondensation between formed oligomeric aluminosilicate chains. The above two processes both release an amount of heat. The enthalpy changes during the first process, i.e., dissolution, is found as $\Delta H_1$= -208.3 kJ/mol (Zhang et al., 2013), according to Equation (2-1). However, the polymerization products are too complex to enable us to perform the thermodynamic calculation for the second process of polymerization. In addition, it is often difficult to attribute the overlapping thermal peaks to each of the reactions as the above two processes are usually taking place in parallel. (Zhang et al., 2014). Therefore, some thermodynamic parameters, such as temperature evolution and heat release, are used to better analyze the exothermicity of geopolymerization.

$$Al_2O_3 \bullet 2SiO_2 + 5H_2O + 4OH^- \rightarrow 2Al(OH)_4^- + 2SiO(OH)_3^- \quad (2\text{-}1)$$

One commonly used method to evaluate the exothermic geopolymerization is called the thermal-graph method, as recommended by Davidovits (2008). In this way, the temperature evolution during the geopolymerization is monitored against time. As illustrated in Figure 2.4, there is a slow temperature rise, attributed to the progressive dissolution of solid precursor. As time elapses, the temperature may increase intensively and reach the maximum after the condensation begins. But it should be mentioned here that, the peak temperature during the geopolymerization is strongly dependent upon the composition of geopolymers. Further, the moment for reaching the maximum temperature is usually close to the final set of the associated geopolymer mixture. Therefore, the thermal graph is very helpful for understanding the setting process of various geopolymers.

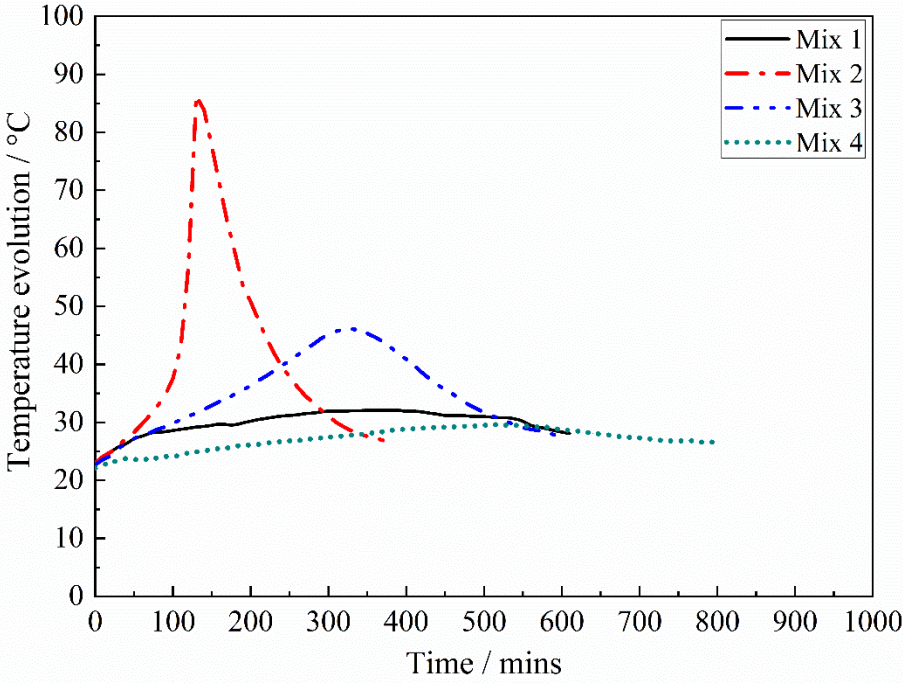


Figure 2.4 Thermal graph of geopolymer mixtures made with various compositions.

### 2.7.3. X-ray diffraction (XRD)

X-ray diffraction (XRD) is a rapid analytical technique primarily used for the phase identification of crystalline materials. The degree of disorder in a geopolymer can be inferred by observations of the way it diffracts X-rays, usually resulting in a broad diffuse halo positioned at 25°~35° in 2θ. In general, the mineral phases that constitute the geopolymer samples are assessed through X-ray Diffraction, using a Copper-Kα radiation beam (operated at 40kV and 44mA), with a step size of 0.02°/s, from 10° to 60° diffraction angle (2θ).

According to Yuan et al. (2016), the value of 2θ corresponding to the diffuse peak will vary slightly for various geopolymer mixtures, which is usually treated as an indicative of the varying amorphicity of the geopolymerized system. And, such a change will further manifest in a variation in mechanical performance. In addition, numerous crystalline phases including Faujasite (F), Anatase (A), Hydroxysodalite (S), Na-Chabazite (C) and Quartz (Q) could be detected when the

aluminosilicate is not well activated, see Figure 2.5. These crystal impurities may be detrimental to the ensuing strength development of the hardened geopolymer system (Cundy and Cox, 2003).

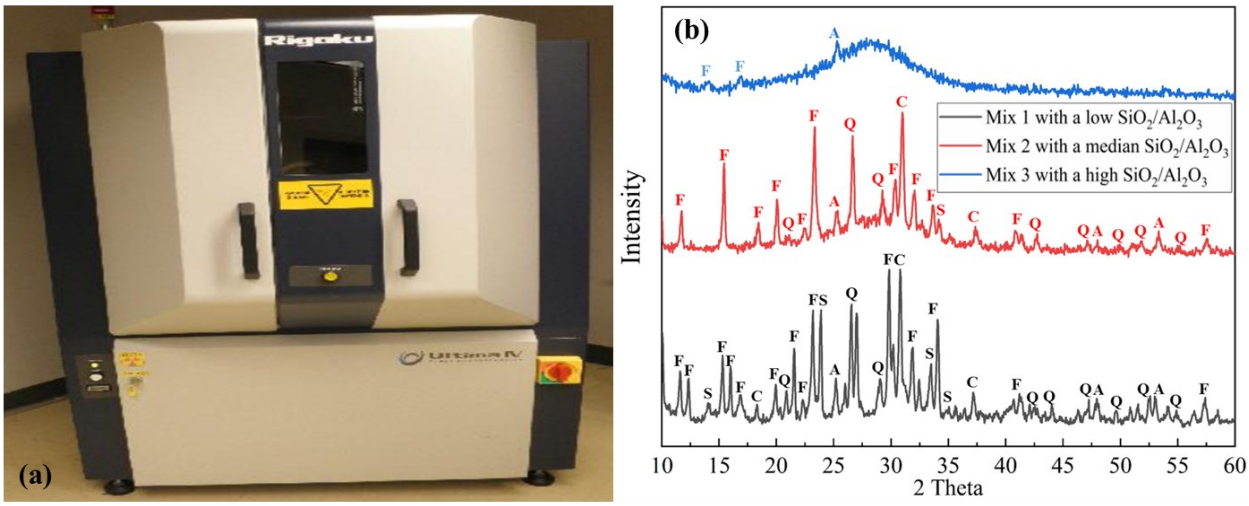


Figure 2.5 The Rigaku XRD Ultima IV and (b) representative XRD spectra for N-A-S-H geopolymers.

### 2.7.4. Thermogravimetric analysis (TGA)

Thermogravimetric analysis (TGA) allows for identifying the type and amount of reaction products in geopolymer systems, based on the weight loss during heating. Thermogravimetric analysis is usually carried out using the TGA instrument that functions in a temperature range of 20~1000°C and at a heating rate of 10 °C/min under a nitrogen atmosphere. The most weight loss for N-A-S-H geopolymers usually occurs between 100~300 °C, and this is attributed to the evaporation of chemically bound water constituting geopolymer, led by the dehydroxylation of the N-A-S-H phase (Tchakouté et al., 2017). Besides, the differential thermogravimetry (DTG) peak assigned to the principal N-A-S-H framework has been found to slightly shift toward the larger end of heating temperature (Yi et al., 2022). This is possibly due to the presence of crystal impurities, i.e., Na-substituted zeolites. According to Davidovits (2008), the associated DTG peak

of Na-substituted zeolites appears at a slightly higher temperature (~170 °C) than the oligomeric aluminosilicate chain (-Si-O-Al-O-Si-O-) that constitutes the N-A-S-H framework (~125 °C).

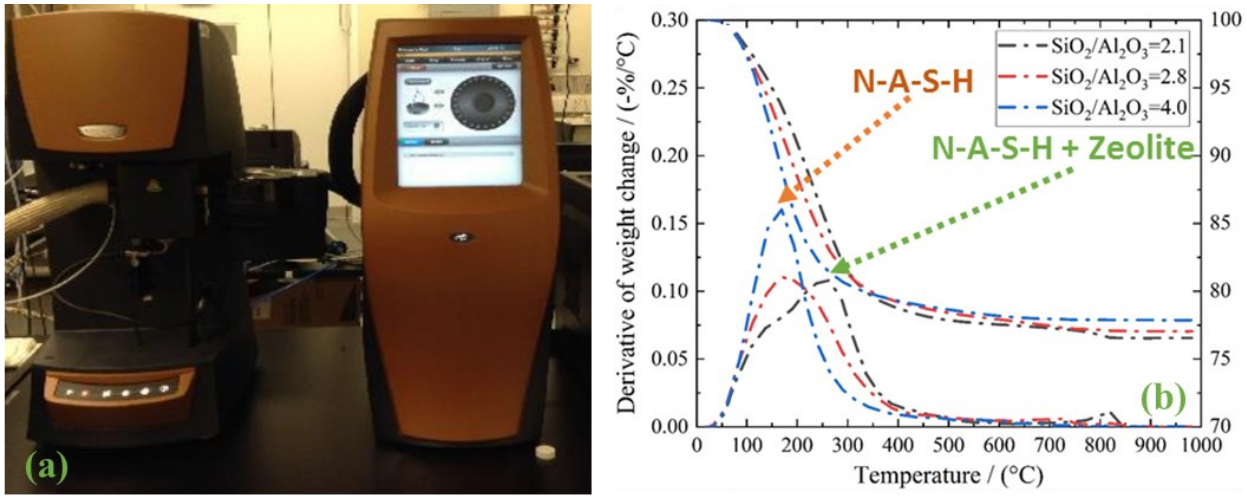


Figure 2.6 The Discovery TGA instrument and (b) typical TG/DTG curves for N-A-S-H geopolymers.

### 2.7.5. Fourier transform infrared spectroscopy (FTIR)

The Fourier-transform infrared spectroscopy (FTIR) spectra for geopolymer associated with its precursor consist of the strongest vibration found in all aluminosilicates, which is mainly assigned to internal vibrations of Si-O-T in the three-dimensional N-A-S-H framework (T: tetrahedral Si or Al) and is found at 800-1250 $cm^{-1}$. More importantly, the shift of the Si-O-T band towards the higher wavenumber is widely recognized as an indication of the higher geopolymerization degree (Li et al., 2019).

In general, the iS50 FTIR system coupled with a build-in ATR module is used to obtain the eligible FTIR spectra. Besides analyzing the aforementioned shift in terms of the overall Si-O-T band, a quantitative assessment could be carried out by deconvoluting the Si-O-T band within the wavenumber of 800-1250 $cm^{-1}$ (Zhang et al., 2012; Li et al., 2019). According to prior studies

(Cortes et al., 2021), the following sub-peaks are frequently considered in this analysis (see Figure 2.7):

Peak I (850~860 $cm^{-1}$) to Si-OH bending; Peak II (930 $cm^{-1}$) to Si-O-T in $Q^2$; Peak III (950~960 $cm^{-1}$) to asymmetric stretching vibrations of nonbridging oxygen (NBO) sites; Peak IV (990~1000 $cm^{-1}$) to Si-O-T in a three-dimensional N-A-S-H network; Peak V (1080~1090 $cm^{-1}$) to Si-O-Si of silica gels; and Peak VI (1150~1160 $cm^{-1}$) to Si-O-T of unreacted precursor. Also, it should be emphasized here that a reduced area proportion for Peak III but an increased fraction for Peak IV together indicates a greater degree of gopolymreization (Cortes et al., 2021).

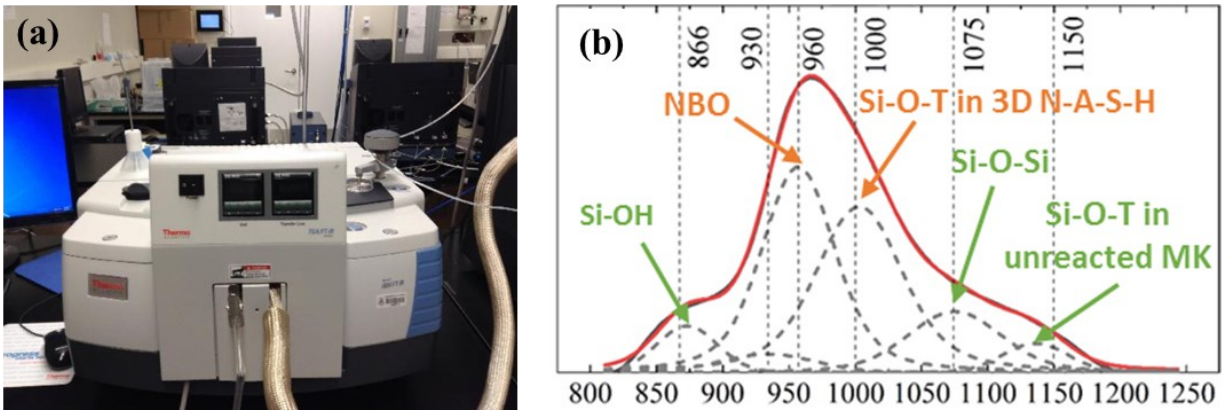


Figure 2.7 (a) The FTIR-iS50 system and (b) the typical FTIR spectrum of N-A-S-H geopolymers within the range of 800-1250 $cm^{-1}$ alongside the deconvolution.

### 2.7.6. Scanning electron microscope and energy dispersive X-ray spectroscope (SEM-EDS)

Both OPC and geopolymer systems are porous building materials and involve a few micro-cracks even after hardening. The intrinsic cracks associated with the compactness of the microstructure strongly determine the corresponding mechanical property and durability. Adopting the Scanning Electron Microscope (SEM) technique allows us to evaluate the microstructure of the hardened N-A-S-H geopolymer (Nath and Kumar, 2020). As well, the coupled Energy Dispersive X-ray

Spectroscope (EDS) could yield the chemical element compositions constituting the examined geopolymer network.

Further, the generated SEM images can be binarized to show the voids and microcracks as the black area and the solid geopolymer gel as fully white. A sample image is now shown in Figure 2.8. The compactness of the geopolymer microstructure may thus be quantified as the area fraction of the flaws, by counting the black pixels out of the total.

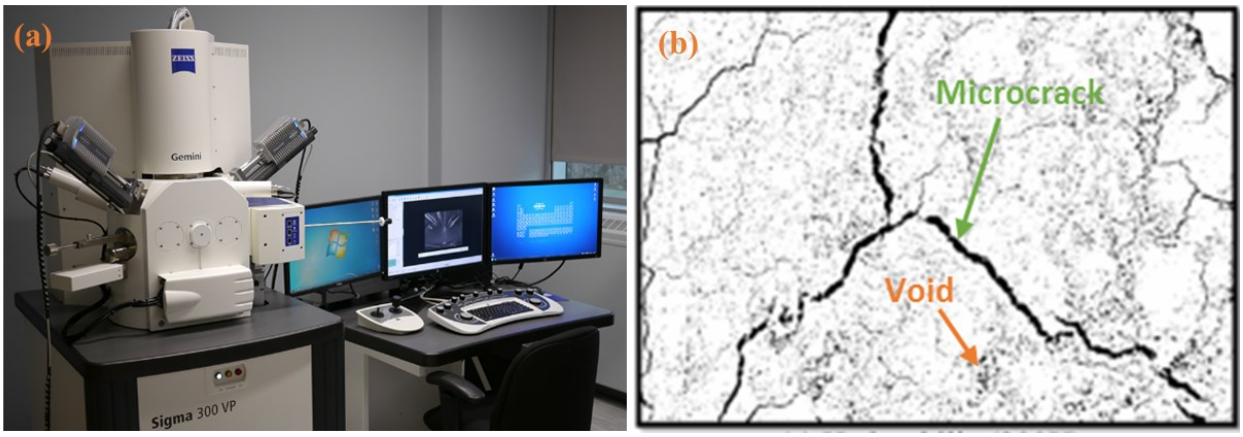


Figure 2.8 (a) The Zeiss Sigma 300 VP-FESEM and (b) the binarized SEM images with microcracks and voids displayed in black pixels.

## 2.8. Conclusion

After reviewing the relevant literature, it is noted that several aspects in terms of mix design for N-A-S-H geopolymers were scarcely investigated. For starters, although the influence of the $SiO_2/Al_2O_3$ molar ratio on the strength of geopolymer systems has been well documented, the underlying mechanisms, that detail the role of $Na_2O/Al_2O_3$ and $H_2O/Na_2O$, have not been comprehensively revealed. Besides, their effects upon other equally vital properties such as the rheology, setting and acid resistance have not been systematically examined, and therefore require further investigations. Secondly, there exists very limited information to guide the mixture design

to guarantee all of these attributes namely, workability, setting, strength and acid resistance simultaneously. Even though some studies recommended a workable range for N-A-S-H geopolymers to achieve satisfactory compressive strength, based on the technique of neural network, there currently is no set of accurate and explicit models for practitioners to operate and validate their mix design for N-A-S-H geopolymers, in order to meet varying engineering demands. Furthermore, the water-in-air Pickering emulsion, also called dry water, is a promising resolution to solve the "trade-off" between workability, setting and strength, when introducing nanoparticles into cementitious and geopolymerized systems. However, this topic has not been investigated.

# Chapter 3. Characterizing effects of compositional oxide ratios on workability, setting and strength of N-A-S-H geopolymers

## 3.1. Introduction

It is well-established that the manufacturing of Portland cement results in inordinately high carbon emissions and is recognized as a significant contributor to global warming (Gartner, 2004; Damtoft t al., 2008; Ali et al., 2011). Hence, in recent decades, it has become an absolute necessity to reduce the use of Portland cement and natural aggregates, aiming to alleviate the associated carbon footprint (Hrabova et al., 2020; Horňáková et al., 2022). More recently, alkali-activated systems have been identified as potential substitutes for Portland cement, due to the significantly low carbon emissions during manufacturing and their satisfactory mechanical performance. Specifically, a reduction in $CO_2$ emissions up to 70~80% can be achieved (Davidovits et al., 1990; McLellan et al., 2011). Furthermore, while the strength is comparable with that of conventional Portland cement-based systems, alkali-activation often assures high early strength as well (Duxson et al., 2007). The $Na_2O$-$Al_2O_3$-$SiO_2$-$H_2O$ (N-A-S-H) geopolymer is a subset of the family of alkali-activated systems, which is usually produced with a precursor that is rich in silica and alumina but low in calcium content (Davidovits et al., 1990; Hrabova et al., 2020). The alkaline environment required for its activation may be generated with either sodium hydroxide or potassium hydroxide in combination with their respective silicate in an aqueous solution (Liew et al., 2016). The latter serves as a secondary source of silica to extend the oligomeric aluminosilicate chain (Yi et al., 2020). The first step in the synthesis of alkali-activated systems is the dissolution of the solid aluminosilicate precursor in a strongly alkaline environment. This forms the tetrahedral $AlO_4$ unit, which is thereafter linked to the tetrahedral $SiO_4$ unit, through sharing an oxygen atom. The negatively charged $[OH]^-$ ion supplied by the alkali-activating solution will attach to the oligomeric

aluminosilicate chain, which extends the valence sphere. In this manner, the system achieves polycondensation (Noll, 2012). On the other hand, although the tetrahedral $AlO_4$ group is preferentially formed in the prevailing alkaline environment, it still carries a unit negative charge due to the donation of an electron from the shared oxygen atom. Thus, the alkali metal ions are essentially needed to balance this negative charge in order to attain chemical equilibrium (Barbosa et al., 2000; Zakka et al., 2021). Eventually, the oligomeric aluminosilicate framework will self-condense and form a more complex and stronger network, which may be expressed chemically as $M_n[-(Si\text{-}O_2)_z\text{–}Al\text{–}O]_n \cdot wH_2O$ (Palomo and Glasser, 1992; Davidovits et al., 1994; Van Jaarsveld et al., 1997). Here, M is the alkali metal ion sourced from the activator, and n represents the eventual degree of polycondensation. Additionally, w is the number of chemically bound water molecules, while z is the number of silicon atoms that constitute a single oligomeric aluminosilicate chain. The latter depends, in turn, upon the molar ratio of $SiO_2/Al_2O_3$ contained in the raw materials. The choice of this ratio varies according to the desired setting time and strength (Davidovits et al., 2008). As this value progressively increases from 1 to 3, a sialate, i.e., $M_n(\text{-Si-O-Al-O-})_n$, a sialate-siloxo, i.e., $M_n(\text{-Si-O-Al-O-Si-O-})_n$, or a sialate disiloxo, i.e., $M_n(\text{-Si-O-Al-O-Si-O-Si-O})_n$, will be formed, respectively.

It is widely reported that the engineering properties of N-A-S-H geopolymer systems are strongly dependent upon their chemical compositions and other mixing proportions. Among the compositional ratios, the role of $SiO_2/Al_2O_3$ has been examined extensively. A higher $SiO_2/Al_2O_3$ molar ratio usually promotes the polycondensation degree and, in turn, yields a higher compressive strength (Panagiotopoulou et al., 2015). However, the higher $SiO_2/Al_2O_3$ molar ratio makes the self-condensation between silicon compounds more difficult than that occurring between silica and alumina and, therefore, the corresponding condensation rate is relatively slow (Sadat et al.,

2016). Since the oligomeric aluminosilicate chain carries a single negative charge due to the tetrahedral $AlO_4$ unit, the molarity of alkali metal ions should theoretically be equivalent to that of the aluminum species contained in the mixture in order to attain chemical equilibrium (Mozumder and Laskar, 2015). However, excessive alkali metal ions will hinder the geopolymerization (Rovnaník et al., 2010). Prior studies also indicate that both an excess and a deficit in the $H_2O/M_2O$ molar ratio may be detrimental to the properties of the evolving geopolymer. Whereas very low ratios adversely affect the stability of the aluminosilicate (Rovnaník et al., 2010), an excessively high ratio hinders the structural integrity due to insufficient activation (Kirschner and Harmuth, 2004). Besides the experimental investigations, some numerical studies have been conducted to predict the compressive strength of geopolymers. At present, the artificial neural network method is most frequently used to forecast compressive strength (Kamalloo et al., 2010; Nazari and Torgal, 2013; Ghanbari et al., 2017; Shahmansouri et al., 2021). For instance, Kamalloo et al. (2010) optimized $SiO_2/Al_2O_3$, $M_2O/Al_2O_3$ and $H_2O/M_2O$ ratios as 3.6–3.8, 1.0–1.2, and 10–11, respectively, to achieve the maximum compressive strength, whereas the optimal combination was predicted as $SiO_2/Al_2O_3 = 2.90$, $Na_2O/Al_2O_3 = 0.58$, $H_2O/Na_2O = 13.75$ by Ghanbari et al. (2017).

As summarized above, the influence of the $SiO_2/Al_2O_3$ molar ratio on the strength of geopolymer systems has been well-documented. However, the underlying mechanisms that detail the role of $Na_2O/Al_2O_3$ and $H_2O/Na_2O$ have not been comprehensively revealed. Additionally, their effects upon other equally vital properties such as the rheology and setting have not been systematically examined and, therefore, require further investigations. Notwithstanding the active research on N-A-S-H geopolymers, there exists very limited information to guide the mixture design to guarantee all of these attributes, namely, workability, setting and strength, simultaneously. It should be noted here that due to the mutual interactions between mixing design ratios, the best performance of one

property, e.g., strength, is likely to be achieved by sacrificing other engineering properties. Accordingly, this study proposed multi-factor models to predict workability, final set and compressive strength based on the compositional ratios, i.e., the liquid-to-solid, $SiO_2/Al_2O_3$, $Na_2O/Al_2O_3$ and $H_2O/Na_2O$ ratios. In the meantime, a set of experimental characterizations was carried out to clarify the underlying mechanism of these ratios affecting the individual engineering properties of geopolymers. Further, the sensitivities of workability, setting and strength to these compositional ratios are quantified by a variance-based analysis. When serving as a potential alternative to conventional Portland cement concrete used in civil engineering, the outcomes generated in this study are promising to guide the mixture design of N-A-S-H geopolymers for structural members with varying priorities upon workability, setting and strength.

## 3.2. Materials and methods

### 3.2.1. Materials

A combination of sodium silicate and sodium hydroxide was used as the activator. The sodium silicate solution comprised approximately 40% sodium silicate compound and 60% deionized water, and the overall $SiO_2/Na_2O$ modulus (molar ratio) was about 3.22. The sodium hydroxide was sourced as solid pellets with a purity of 99%. The formation of N-A-S-H geopolymer requires high amorphous $SiO_2$ and $Al_2O_3$ content (Davidovits et al., 2008). A commercially sourced metakaolin was selected to serve as the aluminosilicate precursor. Its chemical composition, determined by X-ray fluorescence (XRF), is listed in Table 3.1. As seen therein, this metakaolin is composed of 53.8% $SiO_2$ and 43.8% $Al_2O_3$ by mass. Considering the molar mass of these two oxides, namely, 60 and 102, respectively, the corresponding $SiO_2/Al_2O_3$ molar ratio may be calculated as approximately 2.1. The associated XRD and FTIR spectra for this precursor are presented in Figure 3.1. Notice the smooth hump in Figure 3.1(a), centre at $2\theta = 22.5°$, alongside

minor crystals identified as anatase and quartz. Three prominent peaks were detected in the FTIR spectrum at 1060 $cm^{-1}$, 792 $cm^{-1}$ and 434 $cm^{-1}$; see Figure 3.1(b). These are identified as the Si–O bonds in amorphous $SiO_2$, tetrahedral $AlO_4$ and T-O-T (T: Si or Al), respectively.

Table 3.1 Chemical composition of employed metakaolin.

| $SiO_2$ | $Al_2O_3$ | $TiO_2$ | $Fe_2O_3$ | $P_2O_5$ | $Na_2O$ | $K_2O$ | CaO |
|---|---|---|---|---|---|---|---|
| 53.8% | 43.8% | 0.9% | 0.5% | 0.4% | 0.3% | 0.2% | 0.1% |

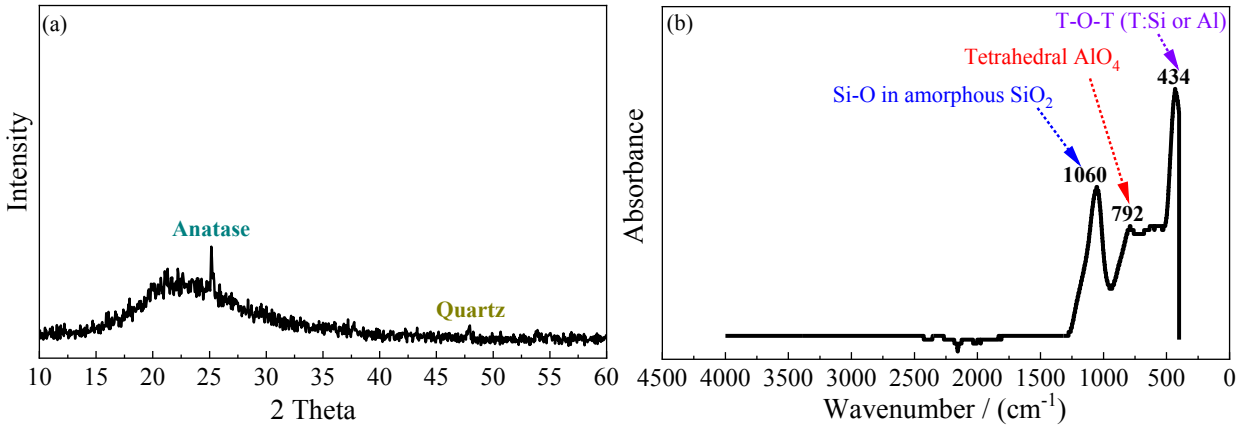


Figure 3.1 (a) XRD and (b) FTIR spectra of the metakaolin precursor.

### 3.2.2. Preparation of geopolymer samples

Three series of mixtures incorporating varying $SiO_2/Al_2O_3$, $Na_2O/Al_2O_3$ and $H_2O/Na_2O$ molar ratios were designed, as listed in Table 3.2. The production of N-A-S-H geopolymer specimens starts with the preparation of the alkali-activating solution. It should be emphasized here that the solubility of sodium hydroxide pellets is about 111 g in 100 mL water under room temperature, here, ~20 °C. Therefore, for those mixtures made with a higher $SiO_2/Al_2O_3$ molar ratio, such as 3.6 and 4.0, the water is predominantly sourced from the sodium silicate solution. Hence, a very small amount of extra water needs to be added manually. More importantly, the heat that evolves in the process of preparing the alkaline solution, especially for higher concentrations, poses

potential risks of causticity. Thus, the sodium hydroxide pellets were blended with the sodium silicate solution along with extra distilled water to produce the alkali activator in solution. The beaker containing the blended activator solution was sealed and placed in a fume hood for 24 h, allowing the contents to cool down to room temperature. On the following day, the alkali activator in solution was first poured into the mixer and stirred for 60 s to ensure its homogeneity. Next, the solid precursor was added gradually to let it blend with the activator solution for 3~5 min until a homogeneous slurry was obtained. This mixture was then cast into plastic cylindrical moulds with dimensions of Φ50 mm × 100 mm height. The specimens, after demoulding, were cured in air-tight plastic bags under ambient conditions to reach 28 days of maturity.

Table 3.2 Mix proportions of N-A-S-H geopolymers with varying oxide ratios.

| $SiO_2$/ $Al_2O_3$ (molar ratio) | $Na_2O/Al_2O_3$ (molar ratio) | $H_2O/Na_2O$ (molar ratio) | Metakaolin (g) | $Na_2SiO_3$ (g) | NaOH (g) | Water (g) | Liquid-to-solid |
|---|---|---|---|---|---|---|---|
| 2.1 | 1.15 | 11 | 500 | 6.63 | 196.86 | 484.96 | 1.377 |
| 2.8 | 1.15 | 11 | 500 | 320.98 | 160.76 | 400.76 | 1.540 |
| 3.6 | 1.15 | 11 | 500 | 680.23 | 119.50 | 63.96 | 1.727 |
| 4.0 | 1.15 | 11 | 500 | 837.41 | 104.89 | 0 | 1.885 |
| 2.8 | 0.75 | 11 | 500 | 320.98 | 92.02 | 118.37 | 1.063 |
| 2.8 | 1.00 | 11 | 500 | 320.98 | 134.98 | 224.70 | 1.361 |
| 2.8 | 1.30 | 11 | 500 | 320.98 | 186.54 | 352.29 | 1.720 |
| 2.8 | 1.00 | 8 | 500 | 320.98 | 134.98 | 108.71 | 1.129 |
| 2.8 | 1.00 | 9 | 500 | 320.98 | 134.98 | 147.37 | 1.207 |
| 2.8 | 1.00 | 10 | 500 | 320.98 | 134.98 | 186.04 | 1.284 |
| 2.8 | 1.00 | 11 | 500 | 320.98 | 134.98 | 224.70 | 1.361 |
| 2.8 | 1.00 | 12 | 500 | 320.98 | 134.98 | 263.37 | 1.439 |
| 2.8 | 1.00 | 14 | 500 | 320.98 | 134.98 | 340.70 | 1.593 |

**Note:** Liquid components include $Na_2SiO_3$ solution and dissolved NaOH in water; Solids means metakaolin.

### 3.2.3. Test protocols

The engineering properties were evaluated for produced geopolymers. In this manner, the workability and setting time were tested as per ASTM C230/C230M-08 (2008) and ASTM C191-

08 (2008), respectively. The compression test was conducted for geopolymer specimens aged 28 days, conforming to ASTM C39/C39M-18 (2018). The tensile strength was measured, as per ASTM C496/C496M-17 (2017). The employed machines and apparatus are shown in Figure 3.2.


Figure 3.2 View of employed machines and apparatus for measuring fresh and hardened properties of N-A-S-H geopolymers: (a) mixer, (b) flow table, (c) Vicat needle apparatus, (d) grinder, compression machine for (e) modulus and (f) compressive alongside splitting tensile strength.

Further characterizations were also conducted in order to understand the mechanisms underlying the attendant effects of each oxide ratio on the above engineering properties. In this regard, the rheology of fresh mixtures was investigated using a Brookfield DV-II+ Programmable Viscometer that was fitted with a SC4-27 spindle. This viscometer operates within a specified range of

viscosity between 0 to 1250 mPa·s with a constant rotation of 200 rpm. The temperature evolution during the setting process was investigated using the thermography method (Davidovits et al., 2008). For each mixture, the fresh paste was first poured into a mould chamber (Φ50 mm × 100 mm) that could be closed with a tightly secured lid. The lid was bored with a hole in its centre to accommodate the thermometer with a functioning range of 50~300 °C. Once secure, the thermometer was inserted through the lid and the real-time temperature was recorded against time. The mineral phases constituting the hardened composite were assessed through X-ray diffraction (XRD), of representative samples, using a copper Kα radiation beam (operated at 40 kV and 44 mA) with a step size of 2°/min, from 10° to 60° diffraction angle (2θ). A thermogravimetric analysis (TGA) was carried out using the Leco TGA 701 instrument that functions in a temperature range of 20~800°C and at a heating rate of 10 °C/min under a nitrogen atmosphere. The chemical bonds involved in geopolymers were examined by using the iS50 Fourier transform infrared (FTIR) spectrometer coupled with a built-in attenuated total reflection (ATR) module. The micro-structure of representative paste samples was examined under a field emission scanning electron microscope (FE-SEM) with a 15 kV accelerating voltage. The generated images were then binarized to show the voids and cracks as black and the solid geo-polymer gel as fully white. The compactness of the geopolymer microstructure may, thus, be quantified by counting the black pixels.

### 3.3. Experimental characterizations

#### 3.3.1. Rheology of fresh geopolymer mixtures

The rheological parameters of fresh geopolymer mixtures help explain the associated workability. We recall that the functional range of the rotational viscometer used here is 0~1250 mPa·s. However, all the mixtures listed in Table 3.2 exceeded this upper bound during the experimental trials, due to the viscous nature of alkali-activated geopolymer. Hence, an independent batch of

mixtures with suitably higher $NaO_2/Al_2O_3$ and $H_2O/Na_2O$ ratios was prepared, as shown in Table 3.3, and their rheological outcomes are presented in Figure 3.3. Notice that as the $SiO_2/Al_2O_3$ molar ratio increases from 2.4 to 3.6, both the viscosity and the yield shear stress drop at first, reaching a minimum at 3.2; see Figure 3.3(a) and 3.3(d). This is followed by a recovery for higher values of this ratio. Recall that the $SiO_2$ content was raised through an increase in the $Na_2SiO_3$ and, as such, it increases the liquid content. Whereas the $Na_2SiO_3$ used here has a viscosity of 200~400 mPa·s at 20 °C, that of the NaOH and water is only 70 mPa.s and 1 mPa.s, respectively. Therefore, an increase in the viscosity and the yield shear stress may now be explained through the "competition" between the increased content of sodium silicate solution and the enlarged liquid-to-solid ratio. On the one hand, an increase in sodium silicate solution raises the overall viscosity of the alkali-activator solution since the viscosity of sodium silicate solution is significantly higher than NaOH and water. In turn, the viscosity of the fresh geopolymer slurry is also higher. On the other hand, the more sodium silicate solution also leads to a greater liquid-to-solid ratio, which has long been recognized to make the slurry more flowable by alleviating the inter-particle friction (Lei et al., 2016). The smaller mutual friction is supposed to reduce the viscosity of the slurry. Given the above, there may exist a competition between the above two effects. Based on these results, when increasing the $SiO_2/Al_2O_3$ molar ratio from 2.4 to 3.2, the effect led by the increase in the liquid-to-solid ratio governs the rheology of the geopolymer mixture, as the content of sodium silicate is relatively small. However, with a further increase in $SiO_2/Al_2O_3$ beyond 3.2, the sodium silicate content dominates over the presence of water alone; see Table 3.3. For the $Na_2O/Al_2O_3$ and $H_2O/Na_2O$ molar ratios, any change in their value is independent of the content of sodium silicate solution in the mixture. As a result, increasing either one of them simply raises

the liquid-to-solid ratio. This, in turn, lowers both the viscosity and the yield shear stress of the fresh geopolymer mixture.

Table 3.3 Proportioning the N-A-S-H paste mixtures for rheology test.

| $SiO_2/Al_2O_3$ (molar ratio) | $Na_2O/Al_2O_3$ (molar ratio) | $H_2O/Na_2O$ (molar ratio) | Metakaolin (g) | $Na_2SiO_3$ (g) | NaOH (g) | Water (g) | Liquid-to-solid |
|---|---|---|---|---|---|---|---|
| 2.4 | 1.40 | 16 | 50 | 14.14 | 22.43 | 77.77 | 2.287 |
| 2.8 | 1.40 | 16 | 50 | 32.10 | 20.37 | 66.55 | 2.380 |
| 3.2 | 1.40 | 16 | 50 | 50.06 | 18.31 | 55.32 | 2.474 |
| 3.5 | 1.40 | 16 | 50 | 63.53 | 16.76 | 46.90 | 2.544 |
| 3.6 | 1.40 | 16 | 50 | 68.02 | 16.25 | 44.09 | 2.556 |
| 2.8 | 1.10 | 16 | 50 | 32.10 | 15.22 | 47.99 | 1.906 |
| 2.8 | 1.25 | 16 | 50 | 32.10 | 17.79 | 57.27 | 2.143 |
| 2.8 | 1.40 | 16 | 50 | 32.10 | 20.37 | 66.55 | 2.380 |
| 2.8 | 1.40 | 12 | 50 | 32.10 | 20.37 | 44.90 | 1.947 |
| 2.8 | 1.40 | 14 | 50 | 32.10 | 20.37 | 55.72 | 2.164 |
| 2.8 | 1.40 | 16 | 50 | 32.10 | 20.37 | 66.55 | 2.380 |

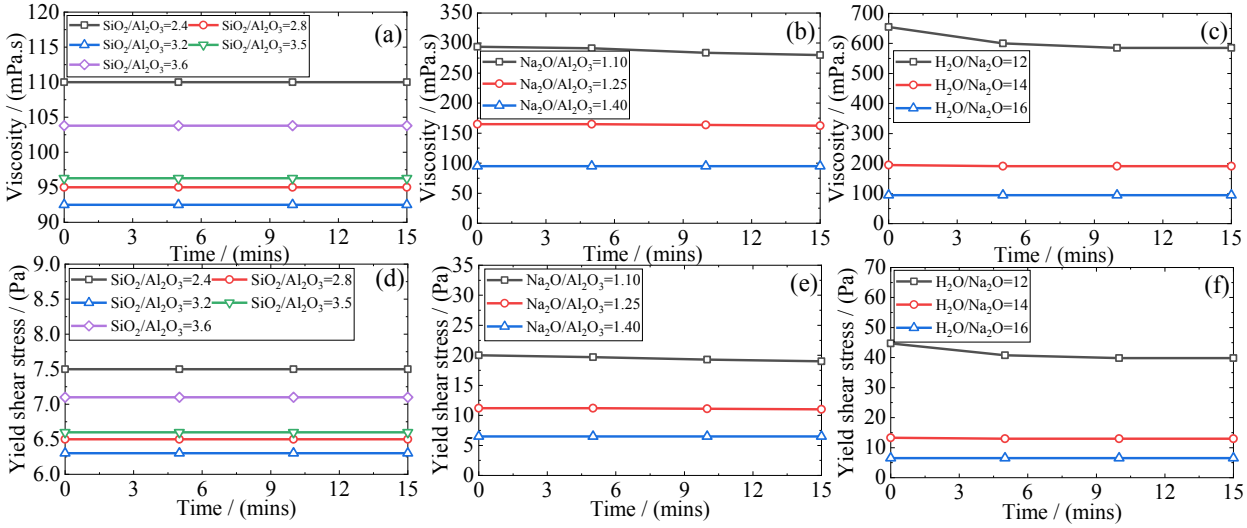


Figure 3.3 Rheological properties of fresh geopolymer mixtures made with varying compositional ratios: (a-c) viscosity and (d-f) yield shear stress.

### 3.3.2. Temperature evolution

N-A-S-H geopolymer mixtures show strong exothermicity and, therefore, the associated temperature changes are related to the reaction rate and degree (Davidovits et al., 2008). Accordingly, the temperature–time history for each geopolymer mixture here is presented in Figure 3.4. To begin with, a significant difference, not only in the peak temperatures but also in its rate of rise, was witnessed for the series made with varying the $SiO_2/Al_2O_3$ molar ratio. The mixture registering the quickest rate of increase, as well as the highest peak temperature (see Figure 3.4(a)), was that made with a $SiO_2/Al_2O_3$ molar ratio of 2.8. However, both an increase and a decrease in this ratio led to progressively lower peaks and a slower rate of temperature rise. This indicates that the $SiO_2/Al_2O_3$ molar ratio must be in an optimum range, otherwise, it will slow down the geopolymerization. It is likely due to the competition in the dissolution between the solid silica and alumina, in the precursor. At the lower end, the raw precursor is the sole source of aluminosilicate, and the progress of subsequent chemical reactions is dominated by the availability of dissolved silica and alumina. However, as the $SiO_2/Al_2O_3$ molar ratio increases through the addition of sodium silicate, the dissolved alumina will quickly react with the liquid silicon groups from the activator to form the (-Si-O-Al-O-) chain (Davidovits et al., 2008). On the other hand, when this molar ratio exceeds a certain value (here, 2.8) any further rise triggers a more complex polycondensation, i.e., the formation of (-Si-O-Al-O-Si-O-) (Davidovits et al., 2008). This extends the reaction time and manifests in a slower temperature rise. Note that Davidovits (2008) reported a geopolymerization thermograph for N-A-S-H geopolymers made with different sources of metakaolin having varied chemical compositions. Specifically, the one made with the larger $SiO_2$-to-$Al_2O_3$ mass fraction also displays slower temperature evolution. However, this result is not comparable with the data generated in the present study, as the former was examined in an oven

with the curing temperature set to 80 °C. For mixtures made with different $Na_2O/Al_2O_3$ molar ratios, the generated peak temperatures differed slightly from one another; see Figure 3.4(b). Of the values chosen in this study, the mixture made with a $Na_2O/Al_2O_3$ = 1.0 showed a faster temperature evolution with a slightly higher peak than the rest. As mentioned earlier, each (-Si-O-Al-O-) or (-Si-O-Al-O-Si-O-) chain contains a single $AlO_4$ unit and carries a negative charge. Therefore, an equivalent amount of $Na^+$ is required in order to maintain the chemical equilibrium. This accounts for the slowing down of the geopolymerization process at lower $Na_2O/Al_2O_3$ molar ratios. Additionally, at the higher range of this ratio, the excessive $Na^+$ may deter polycondensation as per the reaction kinetics, since this reaction is also a NaOH regeneration process (Davidovits, 2008), see Figure 3.5. Similarly, it also explains the slightly depressed geopolymerization in the case of a low $H_2O/Na_2O$ ratio, manifesting in the reduction in both the rise and the peak temperature. On the other hand, at ratios higher than a threshold, there is too much water, which will dilute the alkali and lower the activation efficiency. Once again, this will reduce the exothermicity. Thus, as seen in Figure 3.4(c), the rate of temperature raises, and its peak is maximum for a $H_2O/Na_2O$ ratio of 9.

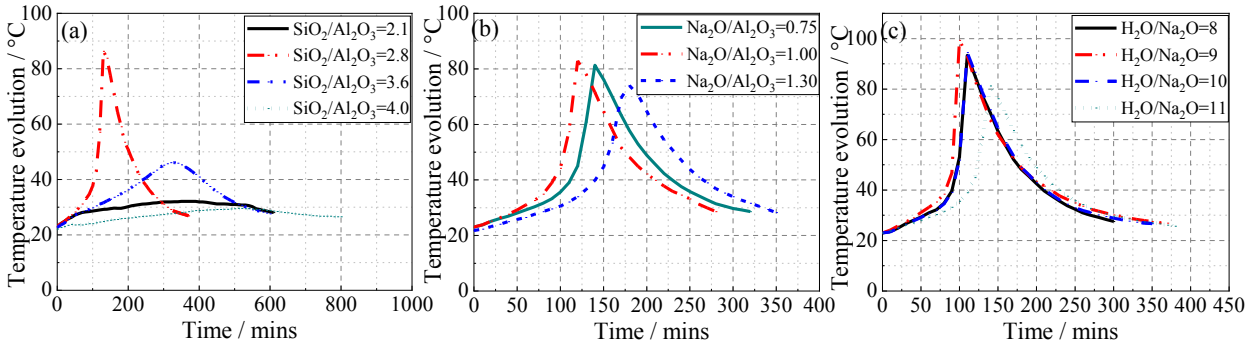


Figure 3.4 Temperature evolution as a function of time for fresh geopolymer mixture made with varying (a) $SiO_2/Al_2O_3$, (b) $Na_2O/Al_2O_3$, (c) $H_2O/Na_2O$ molar ratios.

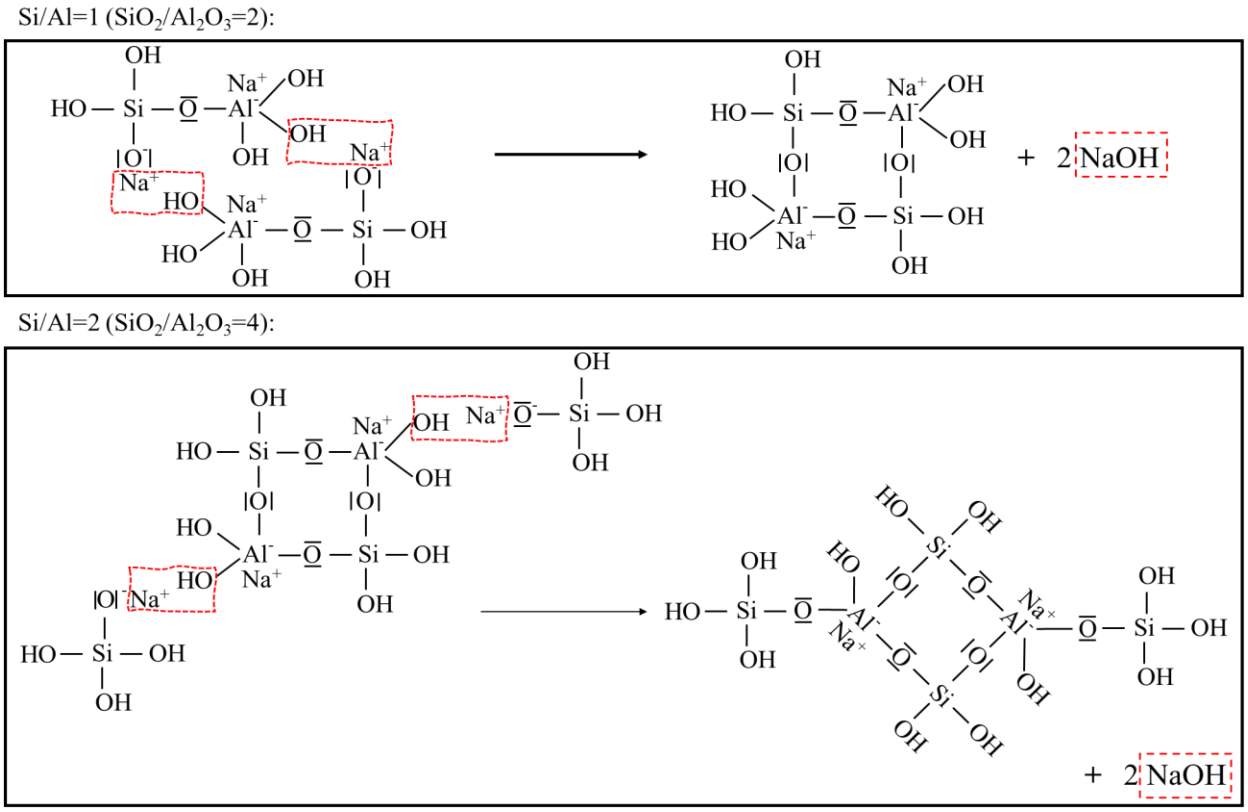


Figure 3.5 NaOH regeneration during the polycondensation of N-A-S-H geopolymer.

### 3.3.3. X-Ray diffraction (XRD) and thermogravimetric analysis (TGA)

The XRD diffractograms and TG/DTG curves of the hardened geopolymer systems are shown in Figure 3.6(a–c) and (d–f), respectively. One can see from Figure 3.6(a) that when $SiO_2/Al_2O_3$ molar ratio is 2.1, numerous crystalline phases including faujasite, anatase, hydroxysodalite, Na-chabazite and quartz show up. This clearly indicates that for lower $SiO_2/Al_2O_3$ molar ratios, geopolymerization is suppressed, forming Na-substituted zeolites instead (Cundy and Cox, 2003). Now, as this ratio rises through 2.8 and to 4, the peaks in the XRD trace that represent the crystalline phases reduce substantially. Simultaneously, a broad and clear diffuse hump appears, implying a greater degree of amorphicity. Connecting with the amorphous character of N-A-S-H networks, an increase in the $SiO_2/Al_2O_3$ molar ratio favours this geopolymerization. Interestingly,

the mixture displaying the better amorphicity also registers a sharper and taller differential thermogravimetry (DTG) peak positioned at 100~300 °C. These taller peaks are mainly connected to the dehydroxylation of the sodium aluminosilicate hydrate phase (N-A-S-H) (Tchakouté et al., 2017). As the $SiO_2/Al_2O_3$ molar ratio drops through 2.8 and to 2.1, this peak becomes flatter and lower. It also shifts towards the higher end of the testing temperature. Whereas these Na-substituted zeolites lose their chemically bound water when raised from 100 °C to 300 °C, the associated DTG peak appears at a slightly higher temperature (~170 °C) than the (-Si-O-Al-O-Si-O-) chain that constitutes the N-A-S-H framework (~125 °C) (Davidovits et al., 2008). Clearly, this is attributed to other crystalline "impurities", as noted in the XRD spectra in Figure 3.6(a–c), namely, faujasite, anatase, Na-chabazite and hydroxysodalite.

For the $Na_2O/Al_2O_3$ molar ratio, the two mixtures at the lower end of the $Na_2O/Al_2O_3$ molar ratio registered fewer crystalline phases and displayed the tell-tale hump of amorphous constituents, as evident from Figure 3.6(b). On the other hand, the mixture containing a $Na_2O/Al_2O_3$ ratio of 1.3 displays significant crystalline phases, an outcome of the formation of zeolite at high alkali content (Juengsuwattananon et al., 2019). This agrees well with the TGA findings presented in Figure 3.6(e). As seen therein, the mixture exhibiting the superior amorphicity, once again, registers the sharper DTG peak assigned to the de-hydroxylation of the N-A-S-H network. Furthermore, the corresponding DTG peak shifts towards the lower end of the temperature scale as the $Na_2O/Al_2O_3$ ratio decreases down to 0.75.

Figure 3.6(c) maps the XRD trace for mixtures made with varying the $H_2O/Na_2O$ ratio. All three traces show only limited crystalline phases. Nevertheless, a small yet significant difference is observed by locating the centre of the diffuse hump in each trace. When the $H_2O/Na_2O$ ratio moves from either extreme of 9 and 12 to the median 10, the value of 2θ corresponding to the diffuse

peak increases from 28.43° and 28.49°, respectively, to a local maximum of 29°. According to Yuan et al. (2016), such a shift is indicative of an increase in the amorphicity of the geopolymerized system despite a limited presence of crystals. In the case of the $H_2O/Na_2O$ ratio, it is evident that this has no bearing upon the nature of the reaction products formed in N-A-S-H geopolymers. The corresponding TGA data shown in Figure 3.6(f) illustrate that, regardless of the $H_2O/Na_2O$ ratio, identical DTG plots were obtained, especially at 100–300 °C, associated with the dehydroxylation of the N-A-S-H framework.

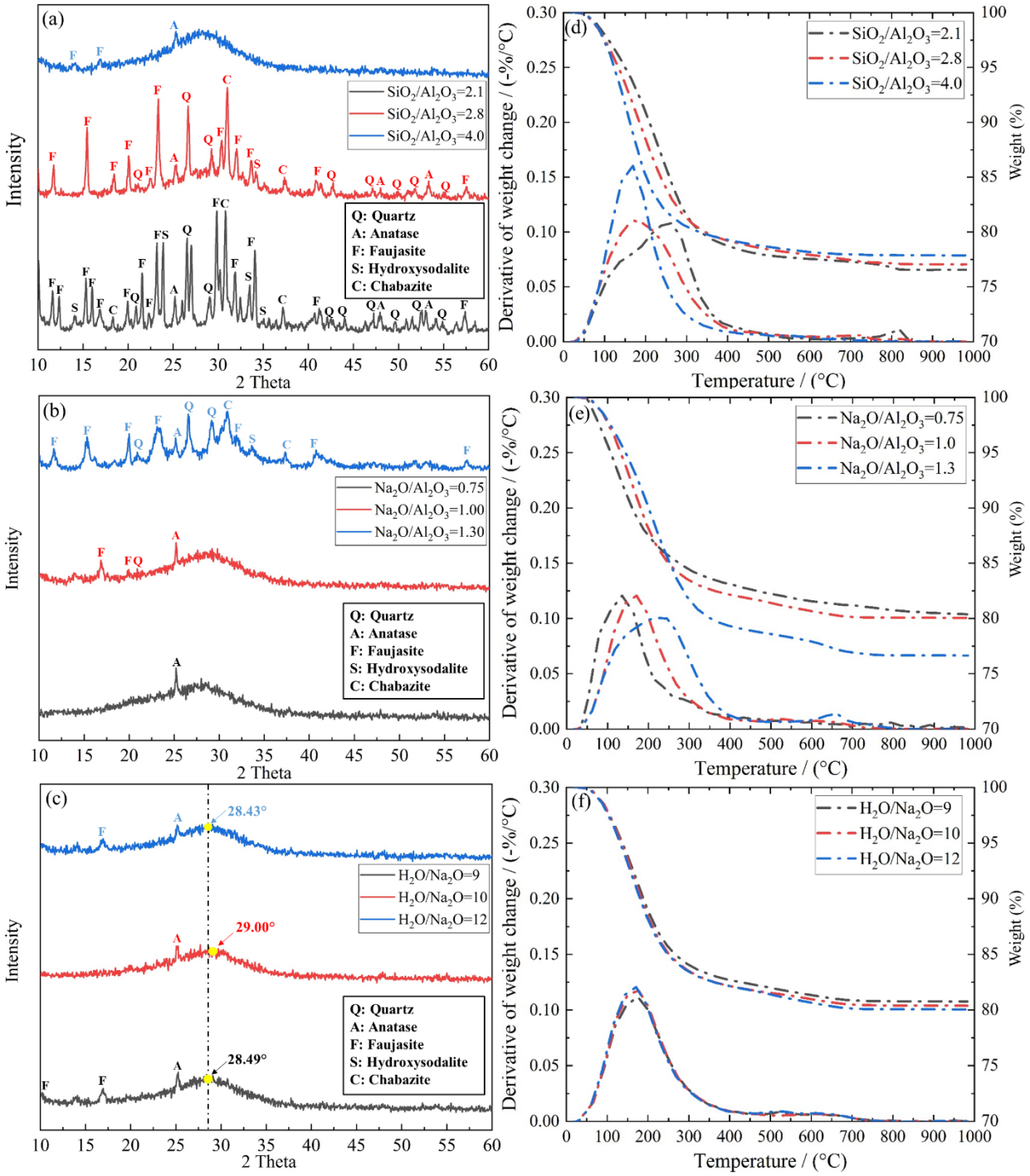


Figure 3.6 (a–c) XRD and (d–f) TGA outcomes of hardened geopolymers made with varying $SiO_2/Al_2O_3$, $Na_2O/Al_2O_3$ and $H_2O/Na_2O$ molar ratios.

### 3.3.4. Fourier transform infrared spectroscopy (FTIR)

In their mature state, the geopolymerized samples were examined through FTIR, as presented in Figure 3.7. As seen therein, a small band located around 560~570 $cm^{-1}$ is ascribed to the external linkage vibrations of the $TO_4$ in the double rings of zeolite (Zhang et al., 2013; Moudio et al., 2021). In addition, it has been widely reported that the most significant signal, assigned to the asymmetric stretching vibrations of the geopolymer band Si-O-T, is usually found between 850~1250 $cm^{-1}$ (Chen et al., 2019; Li et al., 2019). Here, T is the 4-coordinated atom, Si or Al. More importantly, the degree of geopolymerization is associated with the shift of this main band (Chen et al., 2019; Li et al., 2019). Further, the band positioned at ~1645 $cm^{-1}$ is attributed to the bending vibrations H-O-H, implying the presence of structural water in the reaction products (Zhang et al., 2013). Now, as seen from Figure 3.7(a), the mixture made with a $SiO_2/Al_2O_3$ ratio of 4.0 registered the highest wavenumber associated with the Si-O-T band; in turn, the weakest signal was assigned to the $TO_4$ in the double rings of zeolite. This was followed by those for $SiO_2/Al_2O_3$ of 2.8 and 2.1, respectively. From the above, it is clear that an increase in the $SiO_2/Al_2O_3$ ratio promotes geopolymerization and simultaneously depresses the formation of zeolites. This agrees well with the XRD traces in Figure 3.6(a). A continuous increase in the $Na_2O/Al_2O_3$ molar ratio was seen to deter the associated geopolymerization, as evident from the principal Si-O-T bands shifting towards the smaller wavelength in the FTIR spectra; see Figure 3.7(b). As expected, the wavelength ascribed to the zeolite formation increases as this ratio rises from 0.75 to 1.3. Assuming a perfectly activated system, the optimum $Na_2O/Al_2O_3$ ratio is theoretically calculated as 1.0 in order to achieve the charge balance. However, in practice, the raw aluminosilicate precursor may not be completely activated. The XRD traces and the detected $TO_4$ band assigned to zeolites in the FTIR spectrum also lead to the same inference. Thus, it is not

surprising that the actual optimum $Na_2O/Al_2O_3$ is, in fact, a bit lower than the predicted value of 1. As opposed to the variation in the S-O-T band seen with varying the $SiO_2/Al_2O_3$ or $Na_2O/Al_2O_3$ molar ratio, the FTIR spectra for the series prepared with varying the $H_2O/Na_2O$ molar ratio do not register a significant change; see Figure 3.7(c). Nevertheless, the mixture made with a $H_2O/Na_2O$ ratio of 10 is seen to register the highest wavenumber for the Si-O-T band among the three values of this molar ratio. Once again, when the $H_2O/Na_2O$ molar ratio is excessive, it deters geopolymerization. When it is too low, the excessive alkalinity in the mixture depresses polycondensation, as explained through Figure 3.5.

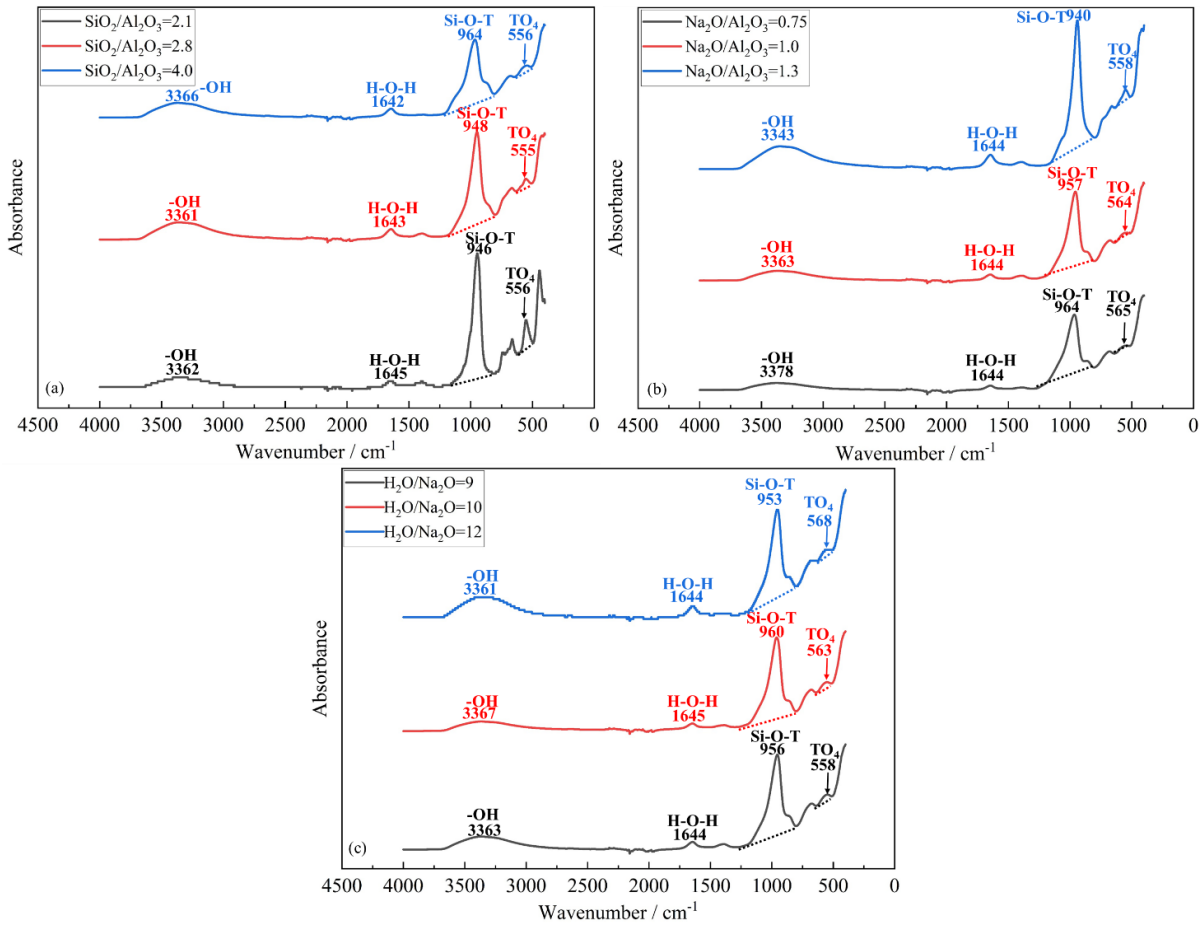


Figure 3.7 FTIR spectra of hardened geopolymers made with varying (a) $SiO_2/Al_2O_3$, (b) $Na_2O/Al_2O_3$ and (c) $H_2O/ Na_2O$ molar ratios.

In order to interpret the structural changes referred to above, the FTIR spectra were deconvoluted for the range of 800~1250 $cm^{-1}$ with Gaussian peak shapes that correspond to the Si-O-T band (Zhang et al., 2013). The associated fitting procedure was performed in accordance with the related literature (Zhang et al., 2013; Cortes et al., 2021). The following peaks are considered: Peak I (850~860 $cm^{-1}$) to Si-OH bending; Peak II (930 $cm^{-1}$) to Si-O-T in $Q_2$; Peak III (950~960 $cm^{-1}$) to asymmetric stretching vibrations of nonbridging oxygen (NBO) sites; Peak IV (990 ~1000 $cm^{-1}$) to Si-O-T in a 3-dimentional N-A-S-H network; Peak V (1080~1090 $cm^{-1}$) to Si-O-Si of silica gels; and Peak VI (1150~1160 $cm^{-1}$) to Si-O-T of unreacted metakaolin. The FTIR deconvolution peaks for each mixture are now presented in Figure 3.8, with a regression coefficient $R^2$ beyond 0.997. In addition, the relative peak areas are quantified in Figure 3.9. It is evident that an increase in the $SiO_2/Al_2O_3$ ratio from 2.1 to 4.0 leads to a reduced area for Peak III but an increase in areas for both Peaks IV and V. Clearly, this corresponds to a greater degree of geopolymerization (Cortes et al., 2021). Further, a slight increase is also seen in the area of Peak VI for $SiO_2/Al_2O_3 = 4.0$, i.e., in the unreacted metakaolin particles. This implies a slight increase in the unreacted metakaolin for an increase in the sodium silicate content. This is not surprising, since adding more sodium silicate solution will lower the relative amount of sodium hydroxide in the mixture and, thus, slow the dissolution of the precursor due to the slightly reduced alkalinity (Hajimohammadi et al., 2008). Nevertheless, the rise in unreacted metakaolin is minor when compared to the rise in the areas of Peaks IV and V. In sum, therefore, a rise in the $SiO_2/Al_2O_3$ ratio favours a higher degree of geopolymerization.

On the other hand, a continuous increase in $Na_2O/Al_2O_3$ leads to a drop in areas of both Peaks IV and V. Further, a noticeable rise is witnessed for Peak II when this ratio increases to 1.3. This corresponds to an increase in the $Q_2$ silicate. Together, they imply a depressed degree of

geopolymerization. Finally, in the case of the $H_2O/Na_2O$ ratio, the highest area for Peaks IV and V is noticed for the mixture with $H_2O/Na_2O = 10$. As noted in Figure 3.6(c and f), it confirms that there exists an optimum alkali concentration to yield the maximum degree of geopolymerization.

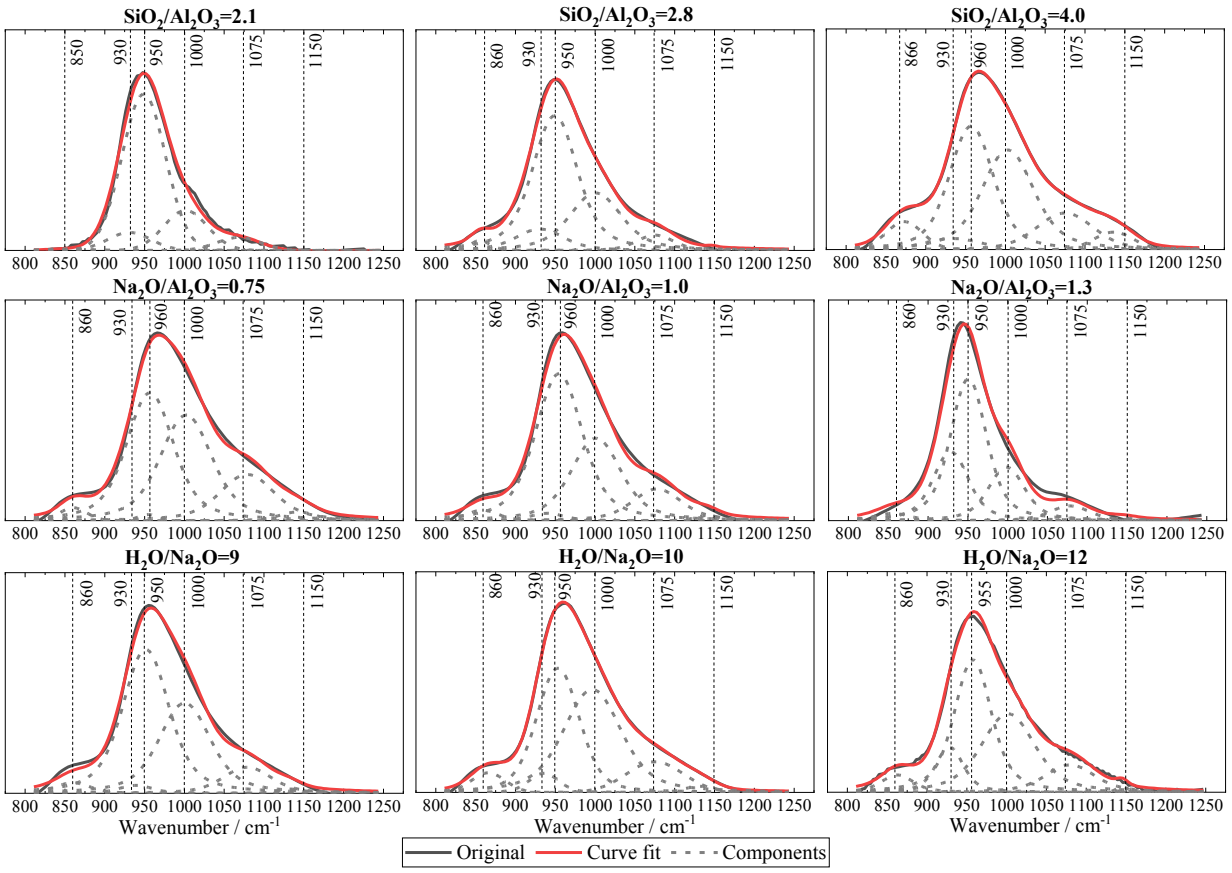


Figure 3.8 FTIR spectral deconvolutions of the main Si-O-T stretching band positioned at 800~1250 $cm^{-1}$ for geopolymers reported in Figure 3.7.

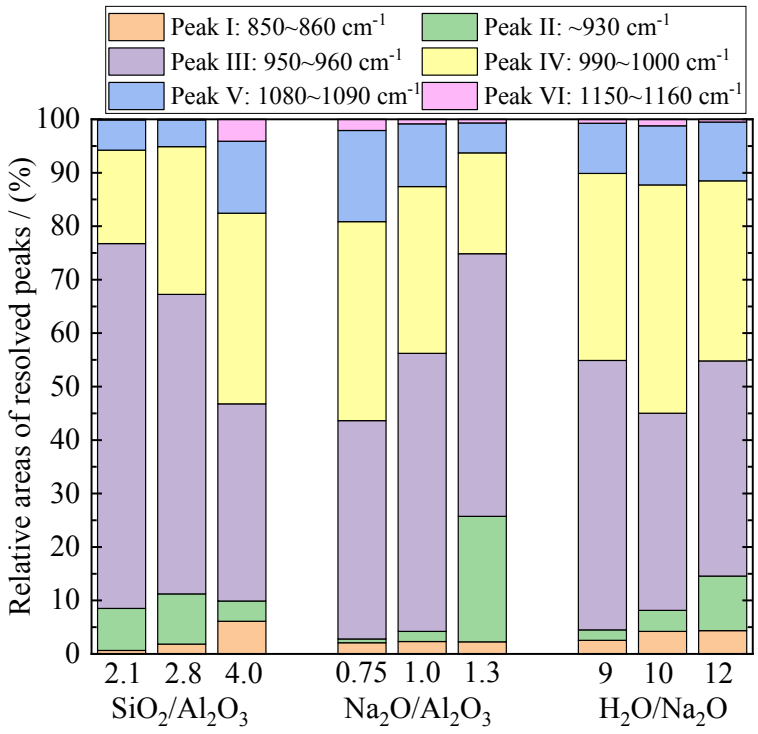


Figure 3.9 Relative areas of the deconvoluted component peaks within the main Si-O-T band.

### 3.3.5. Scanning electron microscope (SEM)

The microstructure of representative mixtures from the three series was examined under SEM. The images captured at 300X magnification are shown in Figure 3.10. Those mixtures prepared with varying the $SiO_2/Al_2O_3$ ratio are illustrated in Figure 3.10(a–c). From a ratio of 2.1 through 4.0, while microcracks are visible, it is wider in the former, progressively becoming narrow in the latter. The higher the $SiO_2/Al_2O_3$ ratio, the more compact and the more homogenous the microstructure. This illustrates that the condensed structure, resulting from the higher degree of geopolymerization, has the greater structural integrity.

Figure 3.10(d–f) represents mixtures made with varying the $Na_2O/Al_2O_3$ molar ratio. While microcracks appear in the sample made with the $Na_2O/Al_2O_3$ of 0.75, the corresponding crack widths are significantly smaller than in the other two mixtures containing the higher $Na_2O/Al_2O_3$

ratios. Particularly, the mixture containing a $Na_2O/Al_2O_3$ of 1.3 displays the widest microcrack in this series. This may be attributed to the following: (i) the continuous increase in this ratio depresses the geopolymerization degree, as confirmed in previous XRD and FTIR outcomes. Note here that the lower degree of geopolymerization usually indicates the lower structural integrity of formed N-A-S-H networks; (ii) the larger $Na_2O/Al_2O_3$ corresponds to a greater liquid-to-solid ratio (see Table 3.1), and the increased liquid content may degrade the texture of hardened geopolymer networks. Given these, it may not be surprising to note the widest microcracks appear in the case of $Na_2O/Al_2O_3 = 1.3$.

Figure 3.10(g–i) shows the variation in the $H_2O/Na_2O$ molar ratio. Clearly, the mixture made with the $H_2O/Na_2O = 10$ registers the best microstructure, as evident from the smallest microcracks. Both a decrease and an increase in this ratio appear to degrade the microstructure of N-A-S-H geopolymers, due to the depressed degree of geopolymerization. The former may be led by an excessive alkali concentration, as the geopolymerization is a regeneration process of $Na^+$ and $OH^-$ (see Figure 3.5), while the latter is simply due to the inefficient alkali activation.

The raw SEM images shown in Figure 3.10 are binarized to highlight the voids and microcracks, as now updated in Figure 3.11. It is then followed by a quantification upon these flaws by counting the black pixels. According to Figure 3.12, the lowest area fraction of cracks and voids is found for $SiO_2/Al_2O_3 = 4.0$, $Na_2O/Al_2O_3 = 0.75$ and $H_2O/Na_2O = 10$, respectively, across each series. This quantitatively validates their densest microstructure.

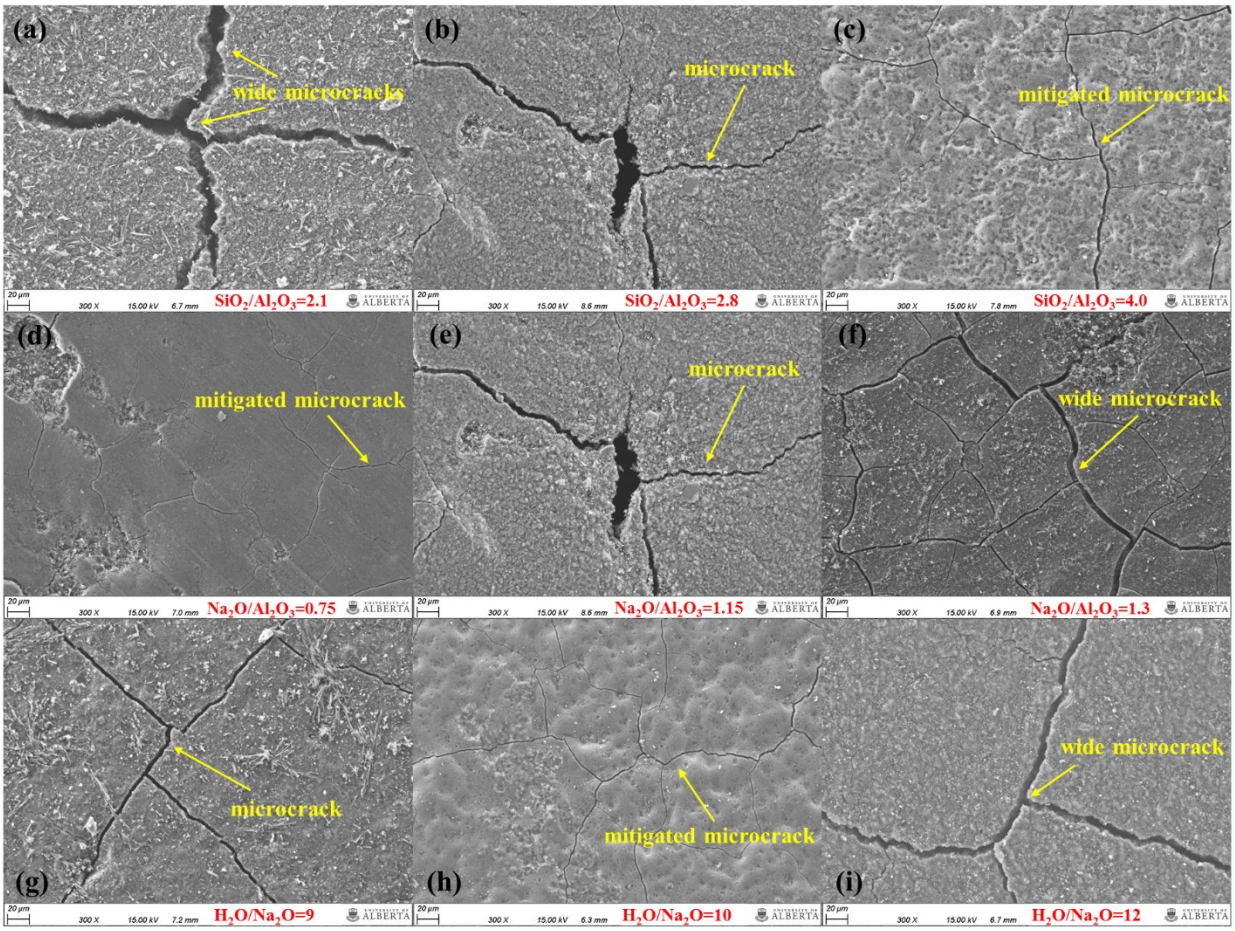


Figure 3.10 SEM images of geopolymer mixture made with varying (a–c) $SiO_2/Al_2O_3$, (d–f) $Na_2O/Al_2O_3$ and (g–i) $H_2O/Na_2O$.

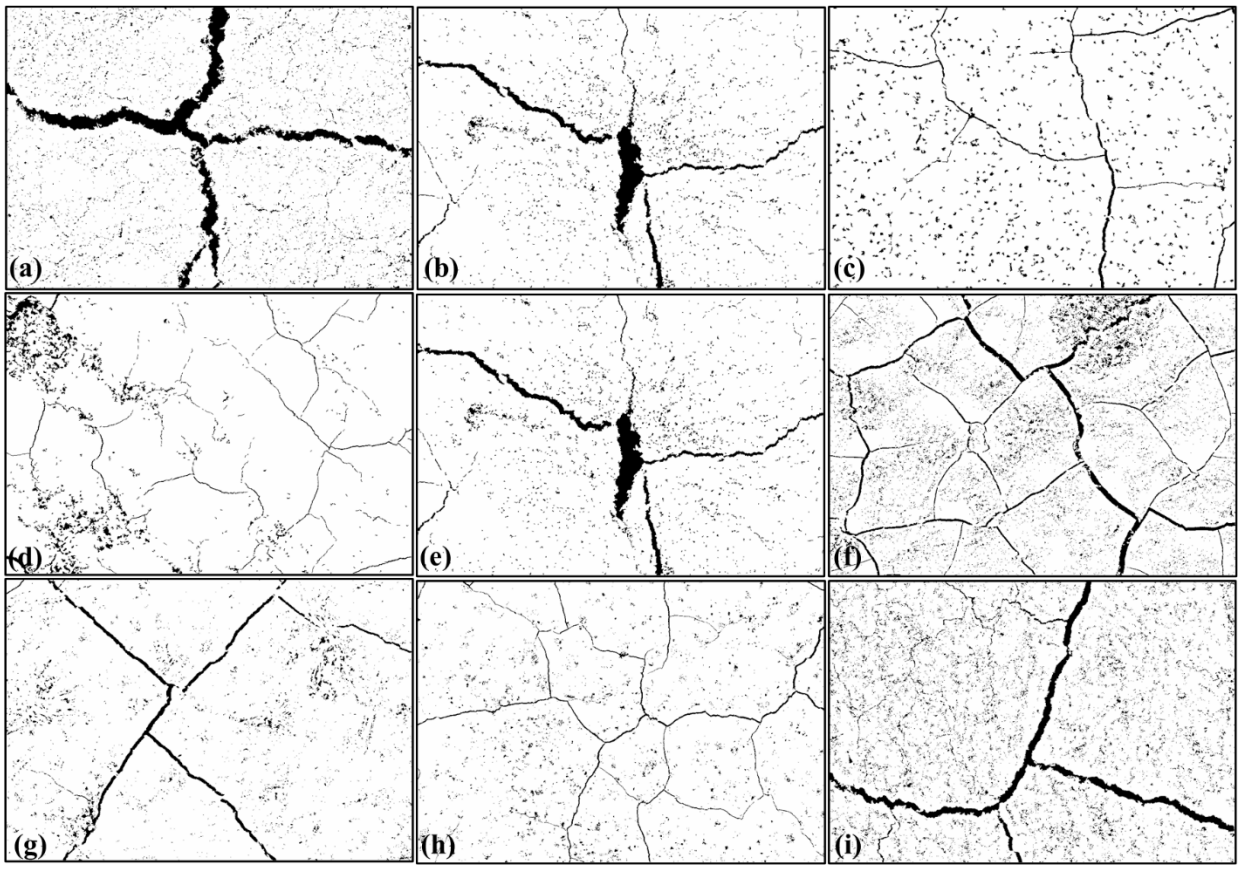


Figure 3.11 Binarized SEM images generated from Figure 3.10.

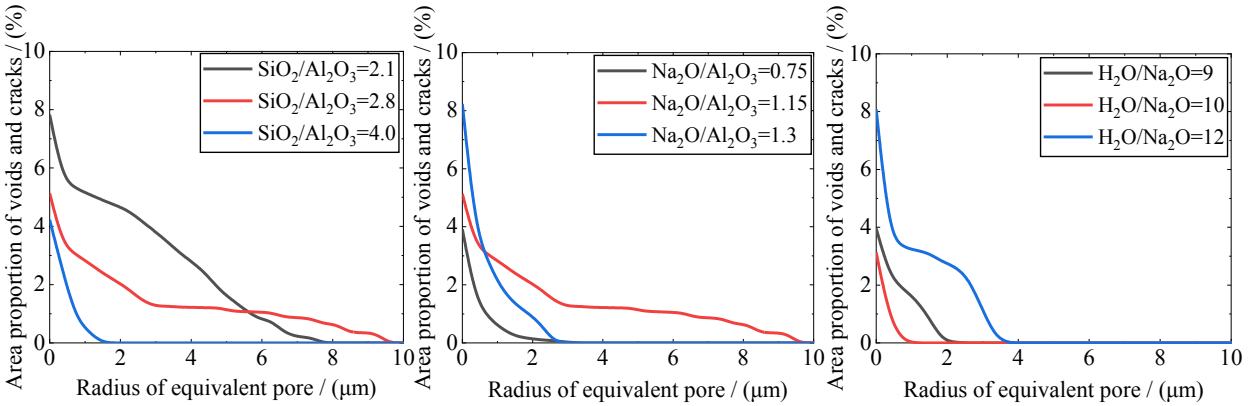


Figure 3.12 The quantified area fraction of voids and cracks in various N-A-S-H geopolymers.

### 3.4. Fresh and hardened properties

#### 3.4.1. Workability

The workability is expressed here in the form of flow diameter. As seen in Figure 3.13(a), the workability increases substantially with an increase in any of the three compositional ratios. While it is clear that an increase in the $H_2O/Na_2O$ ratio directly implies a higher water content, an increase in the $SiO_2/Al_2O_3$ or $Na_2O/Al_2O_3$ ratios also, indirectly, implies a higher liquid-to-solid fraction. This is because the $SiO_2$ and $Na_2O$ may only be varied by changing the activator, which in this case is introduced as a solution. It is illustrated in Figure 3.13(b), wherein an increase in any of these three oxide ratios leads to an increase in the liquid-to-solid ratio. For a fixed amount of dry powder in the mixture, a higher liquid-to-solid ratio will act as a lubricant (Hajimohammadi et al., 2008) and, thus, lead to a greater flowability. Recall that for the rheological parameters presented in Figure 3.3, an increase in the $Na_2O/Al_2O_3$ or $H_2O/Na_2O$ ratio corresponds to a decrease in the viscosity and yield shear stress of the fresh mixture. This agrees well with the superior flow seen in Figure 3.13(a). As explained earlier, it is due to the $Na_2SiO_3$ being substantially more viscous, in comparison with NaOH or water, at 20 °C. Beyond a critical $SiO_2/Al_2O_3$ ratio, found earlier as 3.2, the geopolymer slurry turns more viscous due to a higher sodium silicate content, despite an associated increase in the liquid-to-solid ratio. However, for an increase in the $SiO_2/Al_2O_3$ ratio, the flow is governed by the liquid-to-solid ratio, and eventually manifests as a continuous improvement in flow diameter.

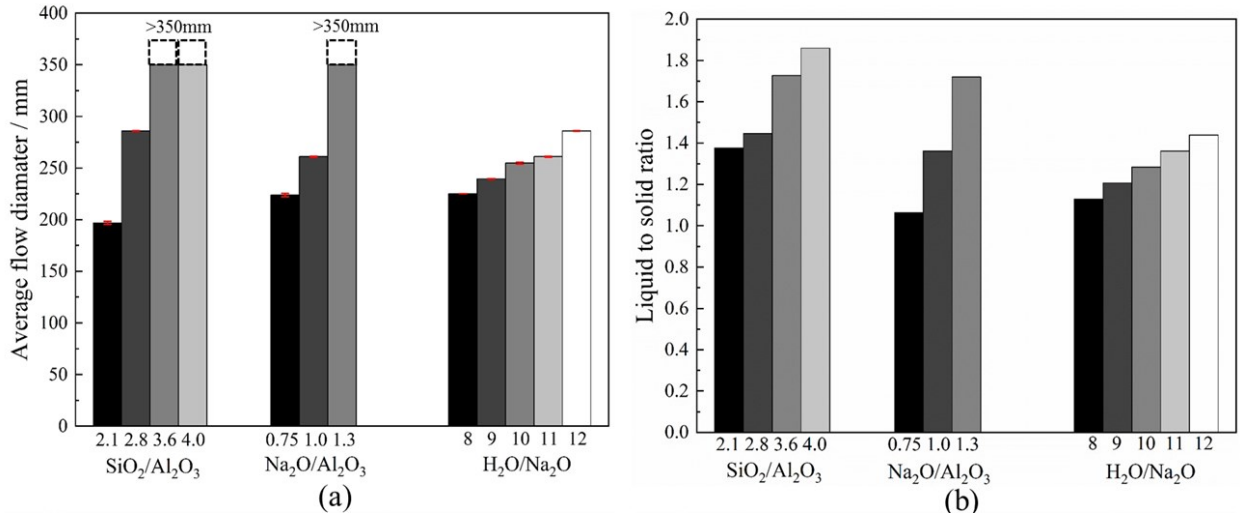


Figure 3.13 (a) Workability and (b) liquid-to-solid ratio of various N-A-S-H geopolymer pastes (>350 mm indicates that the diameter of mixture is more than 350 mm after 25 blows on flow table).

### 3.4.2. Setting

The effect of the compositional ratios in the mixture components upon the setting time is shown in Figure 3.14. It is seen that at a low $SiO_2/Al_2O_3$ ratio, i.e., 2.1, the setting process is delayed because all the silica originates from the metakaolin, and so it takes time to allow the aluminosilicate to dissolve and then be activated. On the other hand, an excess of $SiO_2/Al_2O_3$ ratio, as noticed beyond 2.8 in this series, implies a transformation of the product from the relatively simple sialate (-Si-O-Al-O-) structure to the more complex sialate-siloxo (-Si-O-Al-O-Si-O-) framework. The latter is a more interconnected network that requires some time to form and so, once again, extends the setting time so that there exists an optimum range for the $SiO_2/Al_2O_3$ ratio to ensure the minimum final setting time. In Figure 3.4, the mixture made with the optimum $SiO_2/Al_2O_3$ ratio may be taken as that which displays the highest peak temperature and the quickest temperature evolution.

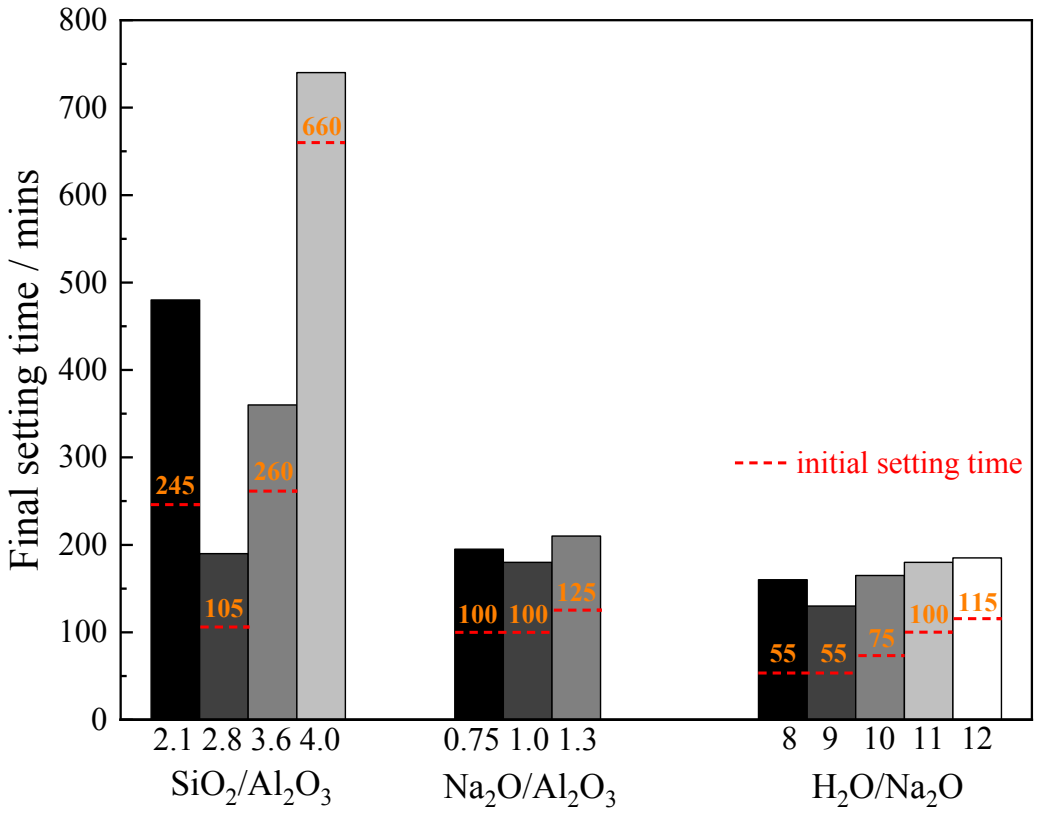


Figure 3.14 Setting time of various N-A-S-H geopolymer pastes.

The $H_2O/Na_2O$ ratio directly reflects the alkalinity of the system. So, under very high alkalinity, the excessive $Na^+$ and $OH^-$ will deter the polycondensation (see Figure 3.5), manifesting as a delayed final set. In contrast, the excessive $H_2O/Na_2O$ ratio dilutes the alkali concentration and, thus, reduces the activation efficiency. An optimum range for the $H_2O/Na_2O$ ratio is found around 8~10 to ensure the shortest duration for the final set. Nevertheless, any further increase in this ratio only causes minor extension, likely due to the slightly diluted alkalinity. As for the initial setting, an increase in this ratio extends the initial setting time, possibly due to the higher liquid-to-solid ratio. The effect seen for the $Na_2O/Al_2O_3$ ratio upon the final setting time was also minor. Nevertheless, a value of about 1.0 makes both initial and final set occur somewhat sooner. A deficit in the $Na_2O/Al_2O_3$ ratio leads to insufficient $Na^+$ required to balance the negative charge carried

by $AlO_4^-$. On the other hand, earlier characterizations reported that an excess in this ratio is likely to depress the N-A-S-H formation and even cause the transformation into various crystals. This, thereafter, corresponds to a delay in the set of mixture. Note that all these final setting outcomes agree well with the temperature evolution curves presented in Figure 3.4.

### 3.4.3. Compressive strength

As seen from Figure 3.15, within the examined range of 2.1~4.0, an increase in the $SiO_2/Al_2O_3$ ratio boosts the associated strength. Recall that the mixture made with a lower $SiO_2/Al_2O_3$ ratio witnessed a substantial presence of crystalline phases, namely, various Na-substituted zeolites, in the XRD trace. The same mixture also registered fewer peak areas ascribed to the Si-O-T band in 3-D N-A-S-H network under FTIR inspection. These together confirm that increasing the $SiO_2/Al_2O_3$ ratio restricts the formation of other crystalline impurities (principally the Na-substituted zeolites) and also improves the compactness of the N-A-S-H framework. This eventually manifests as higher mechanical strength. An increase in the $Na_2O/Al_2O_3$ ratio implies a lower compressive strength, with the associated optimum range lying between 0.75~1.0, according to Figure 3.15(b). Note that a continuous increase in $Na_2O$ will result in the formation of other zeolite crystals, which strongly depresses the polycondensation of N-A-S-H geopolymers, as evident from the associated XRD, TGA and FTIR outcomes. Furthermore, the alumina contained in the raw precursor may not completely be associated with the geopolymer. Thus, the optimum value for the $Na_2O/Al_2O_3$ molar ratio was somewhat lower than the theoretical value, viz. 1.0. In the case of the $H_2O/Na_2O$ ratio, where a lower value denotes a stronger alkalinity, excessive alkali concentration may also suppress the regeneration of NaOH and, in turn, hinder the geopolymerization progress, according to the aspect of reaction kinetics (see Figure 3.5). On the other hand, when this ratio is too high, it deters activation efficiency and restricts the associated

geopolymerization. As such, the compressive strength was highest for a $H_2O/Na_2O$ ratio of 10, as found in this series. It is worth noting here that unlike the $SiO_2/Al_2O_3$ and $Na_2O/Al_2O_3$ ratios, varying the $H_2O/Na_2O$ ratio has minimal impact upon the products resulting in the N-A-S-H geopolymer, and the resulting impact of this ratio may be achieved through the microstructural aspect.

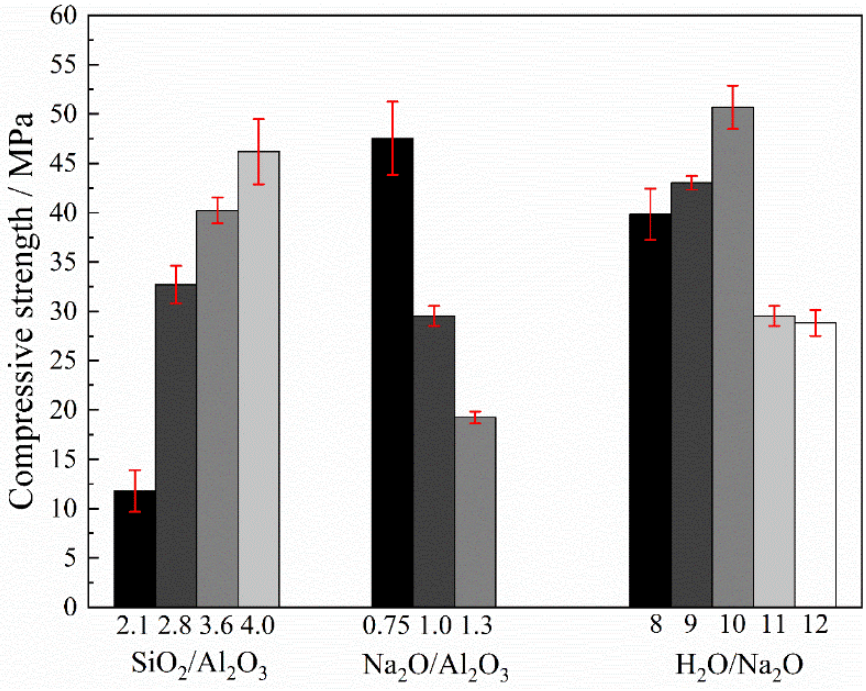


Figure 3.15 Compressive strength of various N-A-S-H geopolymer pastes.

### 3.4.4. Tensile strength

Figure 3.16 presents the tensile strength of N-A-S-H geopolymers, made with varying compositional oxide ratios. As expected, these specimens displayed a similar tendency, as noted for compressive strength in Figure 3.15. In this regard, the mixtures $SiO_2/Al_2O_3$=4.0, $Na_2O/Al_2O_3$=0.75 and $H_2O/Na_2O$=10 registered the highest tensile strength across the respective

series. The reason behind this should be the same as those discussed in Section 3.4.3 earlier, namely, the greatest degree of geopolymerization alongside the densest microstructure.

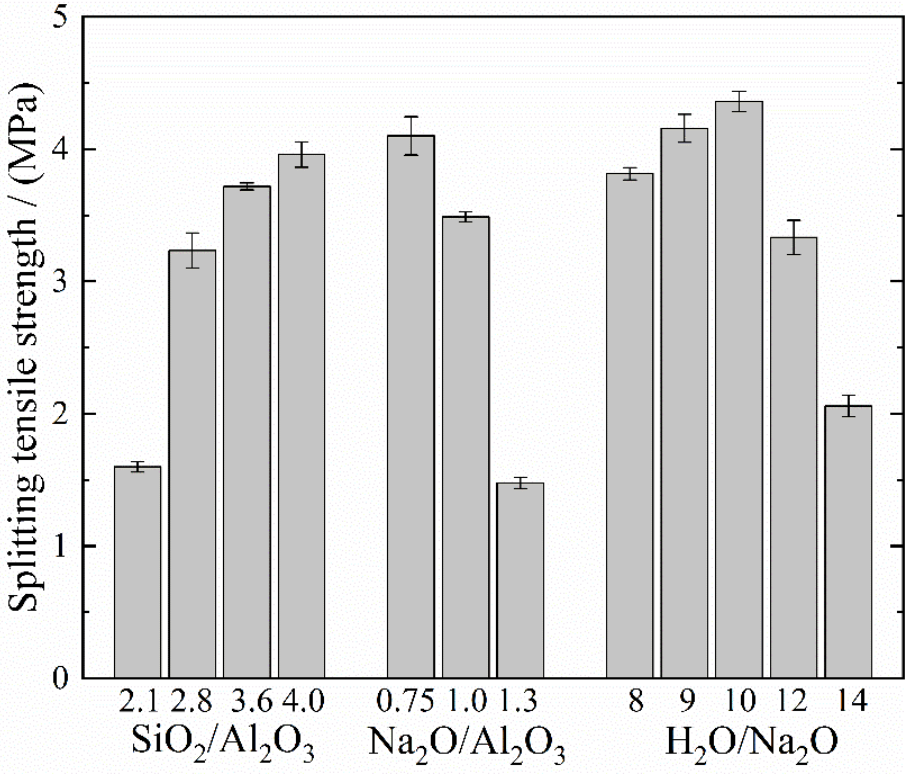


Figure 3.16 Tensile strength of various N-A-S-H geopolymers.

Further, the correlation between compressive and tensile strength is investigated in this study, based on the obtained experimental data. For conventional OPC systems, there exist a few models proposed in prior studies. Among them, the power function model is widely recognized and used (Albidah t al., 2021). For instance, Equations (3.1) and (3.2) are recommended by AS 3600 (2009) and ACI 318 (2008), respectively. Based on this, the correlation between compressive and tensile strength of N-A-S-H geopolymers is explored in this study. A similar model, in the form of a power function, is firstly presented in Equation (3.3). Besides, considering the value of tensile

strength usually falls into the range of 8%~15% of its compressive strength (confirmed by Figure 3.17 as well), another model including both power and linear forms are proposed in Equation (3.4).

$$f_t = 0.4\sqrt{f_c} \tag{3.1}$$

$$f_t = 0.56\sqrt{f_c} \tag{3.2}$$

$$f_t = a_1 f_c^{a_2} \tag{3.3}$$

$$f_t = a_1 f_c^{a_2} + a_3 f_c \tag{3.4}$$

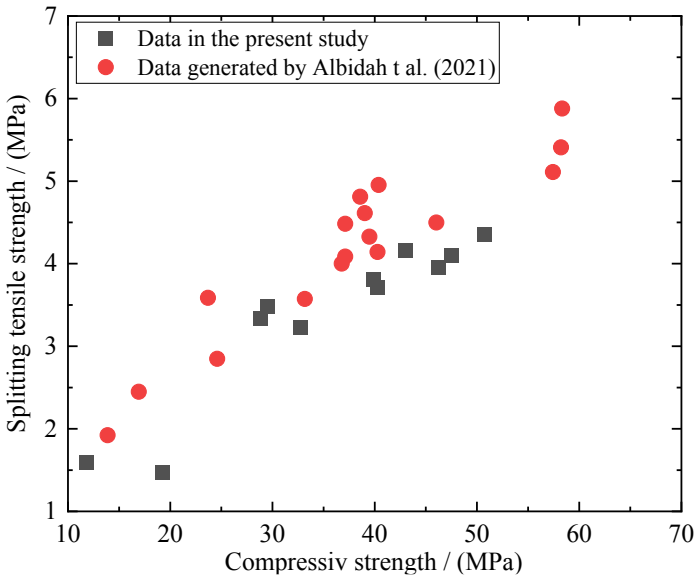


Figure 3.17 Correlation between tensile and compressive strength.

The optimum solution to the coefficient vector in these two sets of models could be determined, using the nonlinear recession analysis based on Ordinary Square Method. The models are now updated in Equations (3.5) ~ (3.8), which are respectively determined based on the dataset generated in this study only and after combining with the data from Albidah t al. (2021). It is seen from Figure 3.18 that the two sets of models considering the power form both display satisfactory predicting efficiency ($R^2$=0.835~0.86). However, considering the linear form on the basis of the above models (Equations (3.5) and (3.6)), does not contribute to the accuracy, as evident from the

slightly reduced coefficient of determination ($R^2$=0.80~0.85). This may indicate that there predominantly exists a power correlation between compressive and tensile strength.

$$f_t = 0.2042 f_c^{0.7885} \tag{3.5}$$

$$f_t = 0.2578 f_c^{0.7517} \tag{3.6}$$

$$f_t = 0.2794 f_c^{0.7855} - 0.0343 f_c \tag{3.7}$$

$$f_t = 0.3288 f_c^{0.7517} - 0.0179 f_c \tag{3.8}$$

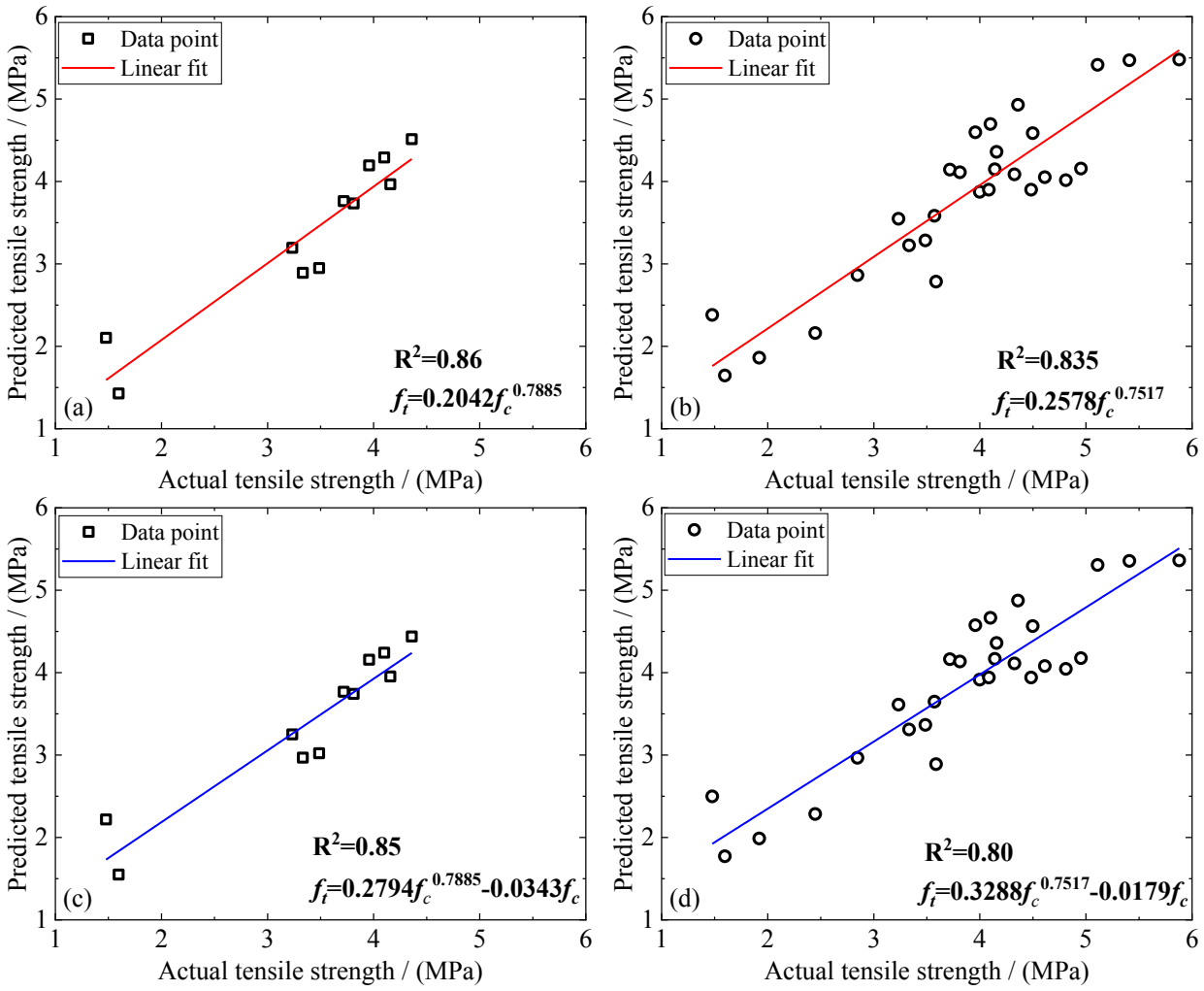


Figure 3.18 Comparison between actual and predicted tensile strength based on different models: (a, c) dataset in this study, (b, d) dataset in this study and the one generated by Albidah t al. (2021).

### 3.4.5. Elastic modulus

The elastic modulus of N-A-S-H geopolymers made with various compositional ratios is presented in Figure 3.19. As seen therein, an increase in the $SiO_2/Al_2O_3$ ratio or a decrease in the $Na_2O/Al_2O_3$ ratio leads to a rise in the associated elastic modulus. And, the mixture made with $H_2O/Na_2O$=10 is found to register the largest modulus across the respective series. Once again, the above findings coincide with their outcomes of compressive and tensile strength. This may also indicate that the optimized mixture will not only show the highest strength but also the best resistance to deformation during the elastic stage, due to the improved geopolymerization and microstructure.

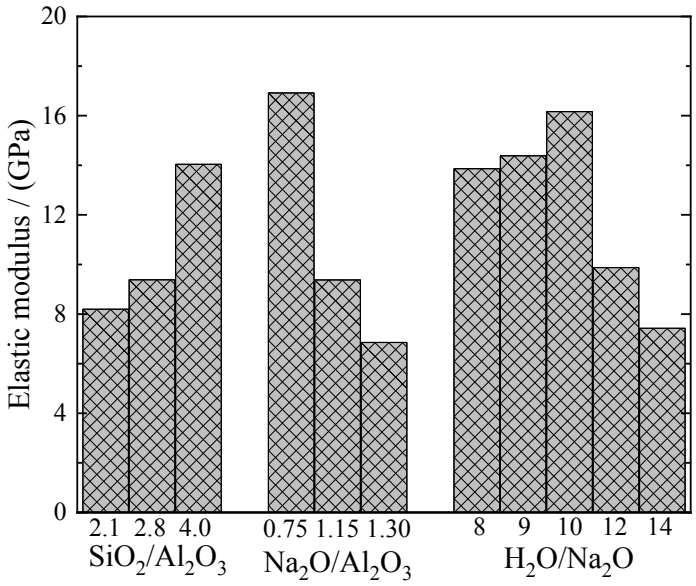


Figure 3.19 Elastic modulus of various N-A-S-H geopolymer mortars.

According to prior studies (Hardjito et al., 2004b; Thomas and Peethamparan, 2015; Azarsa and Gupta, 2020), a similar power correlation may also exist between compressive strength and elastic modulus. Hence, two sets of models that are composed of a similar form as Equations (3.3) and (3.4) are assumed here. Then, the least square method alongside the nonlinear regression analysis is adopted again to determine the optimum coefficients based on the dataset generated in this study.

Now, the two sets of models correlating the elastic modulus to compressive strength are updated in Equations (3.9) and (3.10). Seen from Figure 20, these two models both register acceptable prediction efficiency, as evident from the coefficient of determination ($R^2$) beyond 0.8. However, once again, the consideration of linear form on the basis of the power model does not improve the accuracy significantly.

$$E = 1.4233 f_c^{0.596} \tag{3.9}$$

$$E = 0.8481 f_c^{0.596} + 0.1389 f_c \tag{3.10}$$

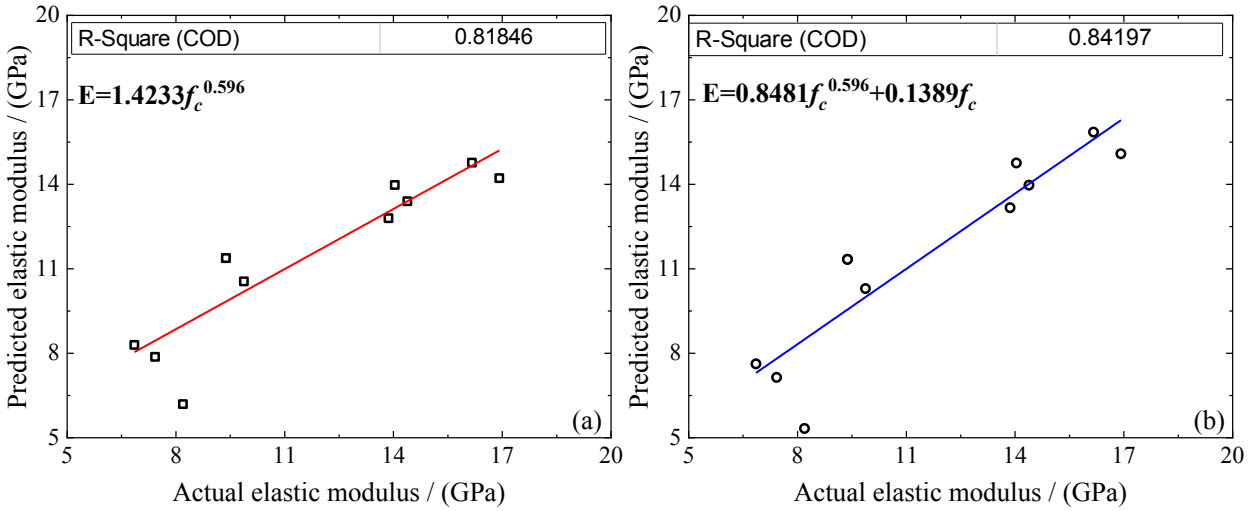


Figure 3.20 Comparison between actual and predicted elastic modulus based on different models.

### 3.5. Sensitivity analysis

An effective variance-based sensitivity analysis (Yi et al., 2019) is conducted here to quantify the influence of these oxide ratios on workability, final set and compressive strength. It is illustrated mathematically by Equations (3.11) and (3.12). The sensitivity index, $S_i$, for each factor is defined as the proportion of the effective partial variance, $V_{ei}$, in the total effective variance, $V_{te}$. An increment coefficient, $\alpha_{ij}$, is introduced to eliminate the disturbance and normalize the traditional variance. The oxide ratio, $x$, and the engineering property, $y$, are the input and output variables,

respectively. In this study, the engineering property denotes either the flow, the setting time or the compressive strength. *n* denotes the size of the dataset, with *m* being the median value of each factor. The data used for this analysis are listed in Table 3.4, and the resulting sensitivity indices are illustrated in Figure 3.21. As seen therein, among this specific series of mixes, the workability of the fresh mixture is most sensitive to the $H_2O/Na_2O$ molar ratio, while the compressive strength of N-A-S-H geopolymers is more dependent upon, firstly, the $H_2O/Na_2O$ and secondly, the $SiO_2/Al_2O_3$ molar ratios. Further, the $SiO_2/Al_2O_3$ molar ratio dominates the setting process, as evident from its sensitivity index beyond 95%.

Table 3.4 Dataset used for sensitivity analysis.

| $SiO_2/Al_2O_3$ (molar ratio) | $Na_2O/Al_2O_3$ (molar ratio) | $H_2O/Na_2O$ (molar ratio) | Flow diameter (mm) | Final setting time (mins) | Compressive strength (MPa) |
|---|---|---|---|---|---|
| 2.1 | 0.95 | 11 | 152.3 | - | - |
| 2.4* | | | 203.5 | - | - |
| 2.8 | | | 257.3 | - | - |
| 3.1 | | | 261.0 | - | - |
| 2.1 | 1.15 | 11 | - | 480 | 11.78 |
| 2.8* | | | - | 190 | 32.71 |
| 3.6 | | | - | 360 | 40.23 |
| 4.0 | | | - | 740 | 46.19 |
| 2.1 | 0.75 | 11 | 101.5 | - | - |
| | 0.95* | | 152.3 | - | - |
| | 1.15 | | 196.9 | - | - |
| | 1.25 | | 247.7 | - | - |
| 2.8 | 0.75 | 11 | - | 195 | 47.54 |
| | 1.00* | | - | 180 | 29.53 |
| | 1.15 | | - | 190 | 32.71 |
| | 1.30 | | - | 210 | 19.24 |
| 2.8 | 1.00 | 8 | 225.1 | 160 | 39.83 |
| | | 9* | 239.5 | 130 | 43.03 |
| | | 10 | 254.7 | 165 | 50.68 |
| | | 11 | 261.0 | 180 | 29.53 |

**Note:** * denotes the median value.

$$V_{ei} = \frac{1}{n\text{-}1}\sum_{j=1}^{n}\frac{\left(y_{ij} - y_{im}\right)^2}{\alpha_{ij}} \quad \text{with} \quad \alpha_{ij} = \frac{x_{ij} - x_{im}}{x_{im}} \tag{3.11}$$

$$S_i = \frac{V_{ei}}{V_{te}} = \frac{V_{ei}}{\sum_{i=1}^{l} V_{ei}} \in [0,1] \tag{3.12}$$

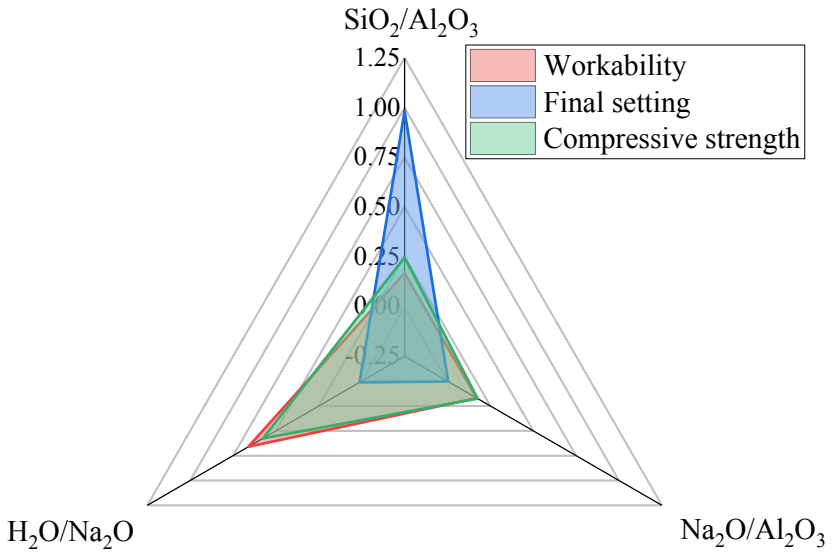


Figure 3.21 Sensitivities of workability, final set and compressive strength to compositional ratios.

### 3.6. Further discussion

The present study shows that the interaction between these oxides triggers mutual sacrifice between workability, setting time and strength of N-A-S-H geopolymers. For example, although a continuous increase in the $SiO_2/Al_2O_3$ molar ratio boosts the compressive strength of N-A-S-H geopolymers, it extends the final set considerably once this ratio exceeds a threshold. Furthermore, an increase in $H_2O/Na_2O$ molar ratio beyond an upper bound appears to damage the structural integrity and strength while it contributes to the workability. As per ASTM C150/C150M-19a (2019), the final setting time requested for Portland cement should not exceed 375 min. Additionally, going by the workability criterion for geopolymers (Ghosh and Ghosh, 2012a), a fresh geopolymer mixture with a median flow diameter larger than 180 mm may be viewed as

highly workable. The experimental observations in this study show that those mixtures produced with a liquid-to-solid ratio beyond 1.1 could easily achieve this diameter. Further, extreme oxide ratios may hinder the strength development even though the corresponding mixture registered satisfactory workability and setting time, e.g., $Na_2O/Al_2O_3 = 1.3$ ($SiO_2/Al_2O_3 = 2.8$ and $H_2O/Na_2O = 11$). Taking this together, it is recognized that the mix design for N-A-S-H geopolymers must simultaneously guarantee the desired workability, setting and strength. As seen in Figures 3.13~3.16, when the $SiO_2/Al_2O_3$ ratio falls within 2.8~3.6, it results in satisfactory strength alongside acceptable final setting time and workability. When the actual $Na_2O/Al_2O_3$ ratio falls slightly below the theoretical value of unity, it achieves a quicker final set and a higher strength. The optimum range for this ratio was found to lie in 0.75~1.0 in the pre-sent study. A $H_2O/Na_2O$ ratio between 9~10 guarantees a great flowability for the N-A-S-H mixture without undermining the other two engineering properties. Together, the above range of oxide ratios offers a guideline for N-A-S-H geopolymers to achieve the most practical combination of workability, final set and compressive strength. If a specific application puts a premium on only one of three properties, the sensitivity results now provide an insight into the design strategy. Adjusting the $H_2O/Na_2O$ ratio is the most effective means to improving workability, while controlling the $SiO_2/Al_2O_3$ ratio imparts the greatest efficiency towards a shorter setting time. The mechanical strength may be adjusted by regulating the above two ratios simultaneously.

### 3.7. Conclusion

This Chapter mainly investigated the mechanisms that underlie the effects of compositional oxide ratios on the fresh and hardened properties of N-A-S-H geopolymers. The experimental observations demonstrate that, when suitably designed, the N-A-S-H geopolymer displays

excellent workability, setting and strength. Based on the results, the following specific conclusions may be drawn:

(1) An increase in the $Na_2O/Al_2O_3$ or $H_2O/Na_2O$ ratio reduces the viscosity of the fresh geopolymer mixture due to a corresponding increase in the liquid-to-solid ratio. There was an accompanying drop in the yield shear stress. Together, this leads to a greater flowability. However, there exists an optimum $SiO_2/Al_2O_3$ ratio to obtain the lowest viscosity. Whereas, at lower values, the system is dominated by sodium silicate, once this ratio exceeds 3.2, the liquid-to-solid ratio dominates and eventually raises the flowability of the system.

(2) In N-A-S-H geopolymers, the setting time is associated with the exothermicity during the geopolymerization, which was found most sensitive to the $SiO_2/Al_2O_3$ ratio. When the other two ratios were fixed as $Na_2O/Al_2O_3$=1.15 and $H_2O/Na_2O$=11, the mixture made with a $SiO_2/Al_2O_3$ ratio of about 2.8 registered the highest peak temperature and the fastest temperature rise, both of which coincide with its fastest setting time.

(3) A deficient $SiO_2/Al_2O_3$ ratio and an excessive $Na_2O/Al_2O_3$ ratio will, in either case, deter geopolymerization. Additionally, they promote significant zeolite formation. This was evident from the reduced amorphicity in XRD, a wider but much lower DTG peak assigned to depolymerization of N-A-S-H in TGA, and also a smaller peak area ascribed to the Si-O-T band in the N-A-S-H framework in FTIR. These together reduce the mechanical strength and elastic modulus. The $H_2O/Na_2O$ ratio at its optimum value, found to be 9~10 here, led to the highest degree of geopolymerization and eventually, the best mechanical performance.

(4) A satisfactory combination of compositional ratios to simultaneously achieve the desired workability, final set and strength may fall within $SiO_2/Al_2O_3$ = 2.8~3.6, $Na_2O/Al_2O_3$ = 0.75~1.0

and $H_2O/Na_2O$ = 9~10. The workability of the fresh N-A-S-H mixture is most sensitive to the $H_2O/Na_2O$ ratio, while the setting time is predominantly governed by the $SiO_2/Al_2O_3$ ratio.

(5) There predominantly exists a power correlation between the compressive and tensile strength and between the compressive strength and elastic modulus of N-A-S-H geopolymers. Considering an additional linear form on the basis of the power model does not contribute to the predicting accuracy.

# Chapter 4. Potential benefits of nano silica stabilized dry water on fresh and hardened properties of N-A-S-H geopolymers

## 4.1. Introduction

Geopolymers have been widely confirmed as a promising alternative to conventional OPC systems. More importantly, the properties of geopolymer systems are strongly dependent upon the compositional ratios that make up the raw materials. Among the principal oxide ratios, the varying $SiO_2/Al_2O_3$ ratio triggers poly-condensation to various degrees. De Silva et al. (2007) noted that within a certain range, a continuous increase in the $SiO_2/Al_2O_3$ molar ratio improves the strength of geopolymer systems, principally attributed to the formation of a highly condensed aluminosilicate structure. Since the main oxides comprising the aluminosilicate precursor are $SiO_2$ and $Al_2O_3$, recent studies have found merit in adding nano silica (Rashad, 2019). The additional silica supplied by the nanoparticles promotes the geopolymerization process. Specifically, adding about 1%~3% nanoparticles to the system manifests in an increase of strength of between 10% to 55% (Gao et al., 2013b; Gao et al., 2015; Deb et al., 2016; Sumesh et al., 2017). Secondly, as seen in cementitious systems, the nanoparticles may also act as a physical filler and densify the microstructure (Nazari and Riahi, 2011). However, due to the nature of extremely small particle size, those prior studies have widely reported that for a given mixture proportion, the improvement through nanoparticles on strength are frequently achieved by sacrificing workability (Gao et al., 2015; Deb et al., 2016). A smaller particle size distribution, and therefore a greater specific surface area, understandably raises the liquid demand and in turn drops the slump. As for the effect of nanoparticles on the setting process, there is no consensus in the literature; some studies report a reduction in the setting time in presence of nanoparticles (Phoo-ngernkham et al., 2014), whereas others argue that these nanoparticles prolong the setting (Lo et al., 2017). Given the above, the

"trade-off" between the desired engineering properties when introducing nanoparticles must be resolved, in order to promote the widespread application of both geopolymer and nanomaterials in building engineering field.

Emulsion is the mixture consisting of multiple liquids that are chemically immiscible. Conventionally, amphophilic surfactants are frequently used as the emulsifier to produce different emulsions. However, these conventional emulsions show an instability, mainly manifesting as coalescence, flocculation, creaming and sedimentation as time elapses. Considering this, solid particles with a nanometric or micrometric size begun to attract more scientific attentions and, the produced emulsion was noted to register much stronger stability, depending on the partial wetting of the employed solid particles. Amorphous silica nanoparticles, when they are predominantly hydrophobic, can be used to stabilize a water-in-air Pickering emulsion, often called "dry water". More importantly, such a novel material usually registers a micrometric size after the physical re-organization and in the meantime, retains the properties of stabilizer (Aveyard et al., 2003; Binks, 2002; Binks and Murakami, 2006; Chevalier and Bolzinger, 2013). This offers a possible resolution to the witnessed "trade-off" between fresh and hardened properties when employing nanoparticles alone. Developed in 1964, such Pickering emulsions are more stable against coalescence and have found application in biomedicine, food processing, fire extinguishing, fine chemical synthesis and cosmetics (Yang et al., 2017; Wang et al., 2021). However, the application of Pickering emulsions in building engineering has not been seen, and the corresponding mechanisms underlying its potential enhancement upon rheology, geopolymerization and the ensuing reaction products are still not clear enough. Therefore, further systematic characterizations are required. Also, the comparison between this Pickering emulsion and conventional silica

nanoparticles needs to be conducted when added as a supplementary admixture to geopolymers. However, there so far exists no information in this regard.

The present study describes the mechanisms underlying this interaction between dry water and the geopolymer system. The dry water, itself formed with the varying content of hydrophobic nano silica, was added to an aluminosilicate geopolymerized system. Further, the geopolymer systems, respectively reinforced by nano silica and the associated dry water, were compared in this Chapter. Besides a plain reference mixture without any nanoparticle, two others were also prepared, one with hydrophilic silica nanoparticles, and the other with hydrophobic silica nanoparticles. These systems were examined under a suite of rheological, thermal, physical, chemical and morphological analyses. The findings were matched with results from macro-scale tests that measured the strength, flowability and setting time. Accordingly, a schematic model is proposed here to convey how dry water powders enhance the geopolymerization involved in the aluminosilicate geopolymer.

## 4.2. Materials and methods

### 4.2.1. Materials

A commercially sourced metakaolin was employed as the aluminosilicate precursor. Its chemical composition as determined through X-ray Fluorescence (XRF) has been presented in Table 3.1 in the previous Chapter 3. As seen therein, the corresponding $SiO_2$ and $Al_2O_3$ contents together account for about 97% of the total and have a $SiO_2/Al_2O_3$ molar ratio equal to 2.1 approximately. The alkaline activator was a sodium silicate solution with a mass fraction of $W_{Na2O+\ SiO2} \approx 40\%$, blended with sodium hydroxide pellets (NaOH, 99% purity). Hydrophobic silica nanoparticles are a hexamethyldisilazane treated version of hydrophilic nanoparticles and contain methylated silicon

surface groups. The physicochemical characteristics of fumed silica nanoparticles are listed in Table 4.1.

Table 4.1 Physicochemical properties of fumed silica nanoparticles.

| Properties and test method | Unit | Hydrophobic | Hydrophilic |
|---|---|---|---|
| Average particle diameter | nm | 7 | 7 |
| Specific surface area (BET) | $m^2/g$ | 195-245 | 270-330 |
| Contact angle against water | $^o$ | 118 | 14 |
| pH value (in 4% dispersion) | - | 5.5-9.0 | 3.7-4.5 |
| Loss on drying (2 hours at 105 °C) | % | $\leq 0.5$ | $\leq 1.5$ |
| C content (as methyl groups) | % | 3.0-4.0 | - |
| $SiO_2$ content (based on ignited) | % | $\geq 99.8$ | $\geq 99.8$ |

### 4.2.2. Preparation of dry water

As introduced earlier, dry water is an air-water Pickering emulsion, stabilized by nano particles of hydrophobic silica. The procedure employed in producing dry water in this study is schematically shown in Figure 4.1. Nanoparticles of hydrophobic fumed silica were mixed with water in a blender that had a stirring rate approximately ranging from 1,000 to 30,000 rpm. It must be noted here that whereas hydrophobic silica produces the desired dry water, hydrophilic nano silica resulted in a foam and was deemed unsuitable for this study. Note that the blender was stirred at close to the upper limit of 30,000 rpm in producing the dry water for the present study. Aside from the hydrophobicity of the encapsulating particles, the water-to-solid ratio also plays an important part when stabilizing such water-in-air Pickering emulsions: the more the amount of nano silica particles, the drier the resulting powder.

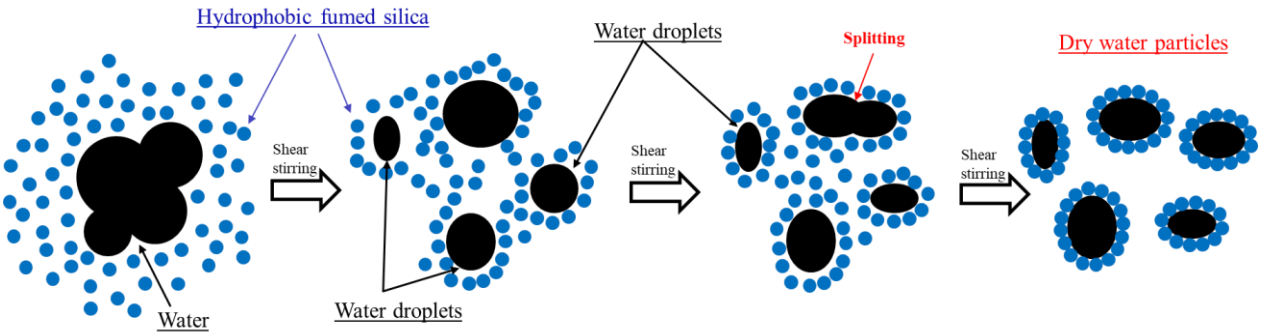


Figure 4.1 Schematic showing the mechanism of dry water formation.

Typically, a maximum of about 96% deionized water can be encapsulated by 4% of such highly hydrophobic particles of nano silica. Note that the encapsulated water is gradually released into the alkali-activated mixture, so that it should be deducted from the batched amount in the design mix. Based on prior studies, it is suggested that a secondary source of silica in the form of the nanoparticles when added between 1%~2%, improves mechanical performance (Gao et al., 2014). Taking this into account, three dry water compositions were prepared such that the solid-to-dry water ratio ranged from 10% to 20%. Prior reports note that the mixing time required to produce a fully encapsulated dry water sample in a standard blender range from a minimum of 10 seconds up to a maximum of 5 minutes (Forny et al., 2009). Complete encapsulation is confirmed by a visual examination of the dry water produced here. When there was insufficient encapsulation, the individual water droplets were distinctly seen inside the blender. Through trial-and-error, a blending time of 1~2 minutes was chosen in this study. The hydrophobic nano silica and the resulting dry water are shown in Figure 4.2.

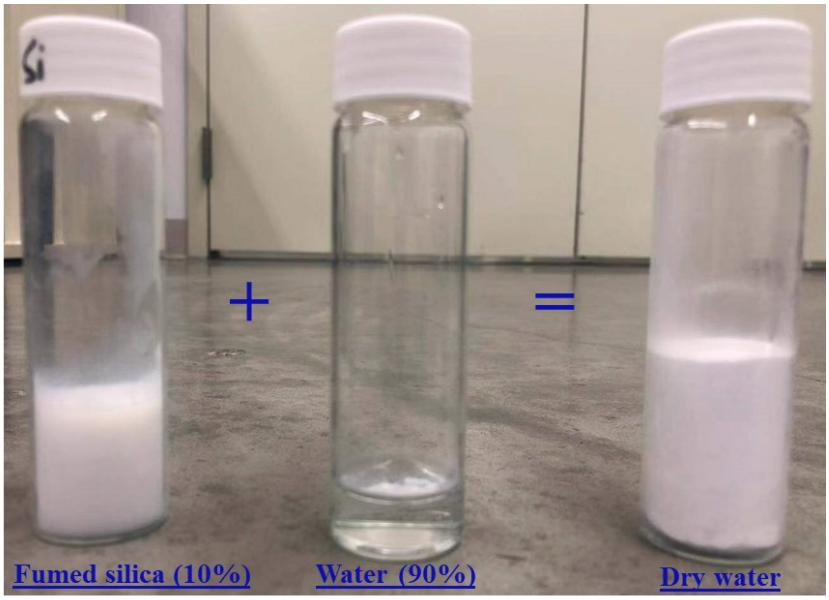


Figure 4.2 Fumed silica powder, distilled water and dry water powder.

Fourier transform infrared spectroscopy (FTIR) was applied to confirm the successful encapsulation of water droplets by the hydrophobic silica nanoparticles. As well, this technique identifies the nature of the various bonds resulting in the dry water powders. It is seen from Figure 4.3 that the peak at 1080 $cm^{-1}$ and the relatively weak peaks at 459 $cm^{-1}$ and 811 $cm^{-1}$ were detected upon the hydrophobic fumed silica. They are essentially attributed to the asymmetric stretching and bending bands of Si-O-Si. As for the dry water samples, apart from the above peaks, two fresh peaks occurring at 1636.92 $cm^{-1}$ and 3380.48 $cm^{-1}$ were observed, which respectively reflect the bending vibration of H-O-H and the stretching vibration of -O-H or H-O-H. In addition, the dry water samples were observed under optical microscopy, as shown in Figure 4.4. Note that, this silica-stabilized water-in-air Pickering emulsion registers irregular shapes in a micro-scale size ranging from 10 to 100 μm. Such was reported by prior studies as well (Forny et al., 2009). The non-spherical shape of dry water is attributed mainly to the mechanical entanglement between the branched silica nanoparticles promoted by high shearing forces (Forny et al., 2009, Golkhou &

Haghtalab, 2019). The angle of repose was measured to confirm the physical state of the resultant dry water, as presented in Figure 4.5. It is worth pointing out that wet sand has a lower angle of repose than does dry sand (Glover, 1995). In the present instance however, the dry water has an angle of repose of 34.77°, which is higher than that for the original hydrophobic nanoparticles of fumed silica (26.36°). This may be attributed to the transformation in the mean particle size, going from the nano-scale in the latter to the micro-scale of the newly formed particles of the Pickering emulsion.

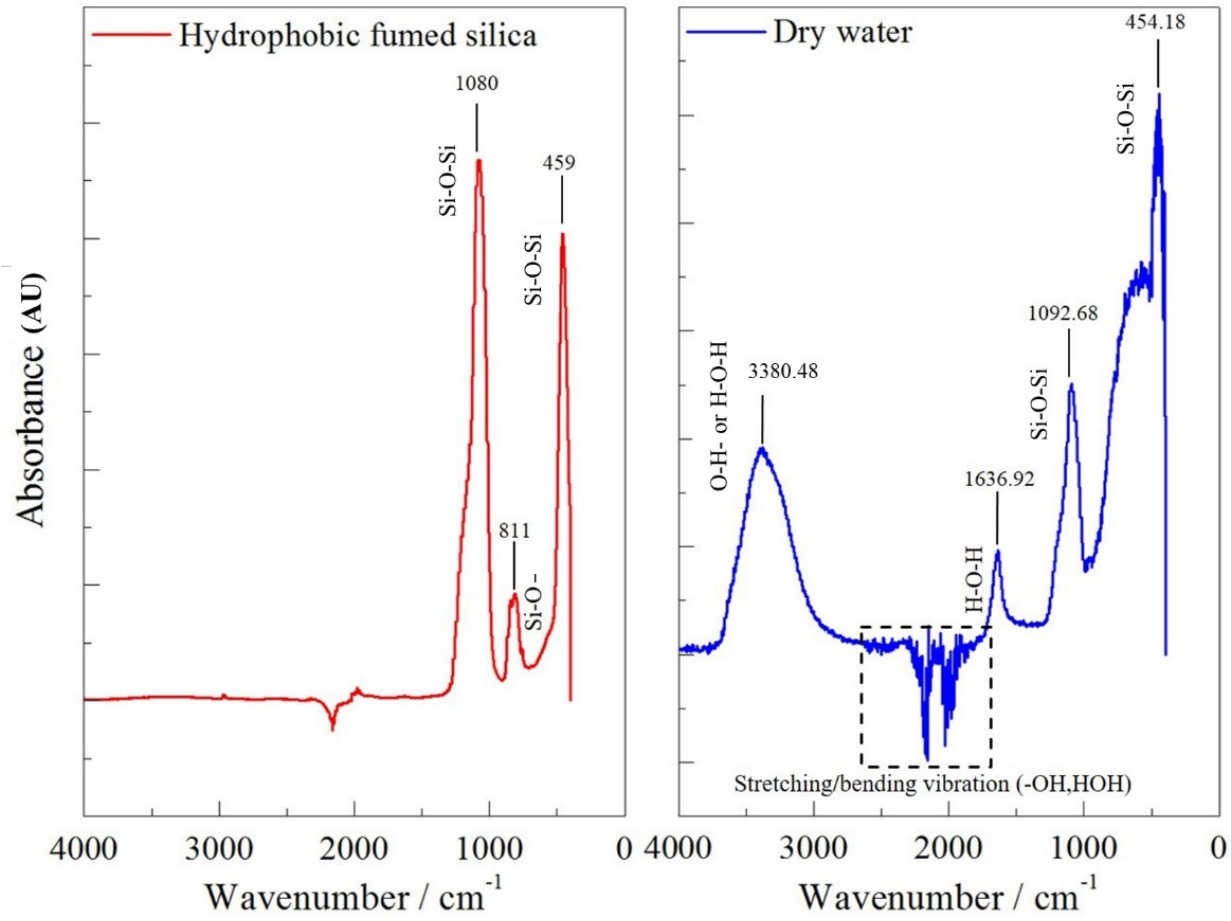


Figure 4.3 FTIR of the hydrophobic fumed silica and resulting dry water.

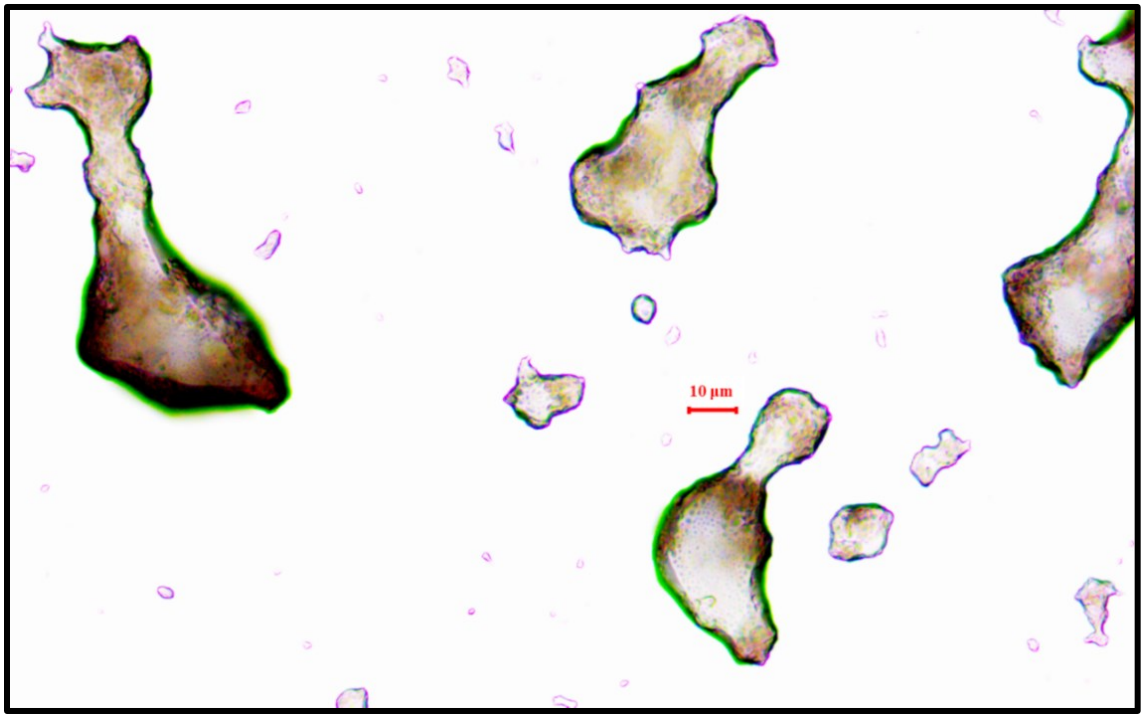


Figure 4.4 The particles of dry water observed under optical microscopy.

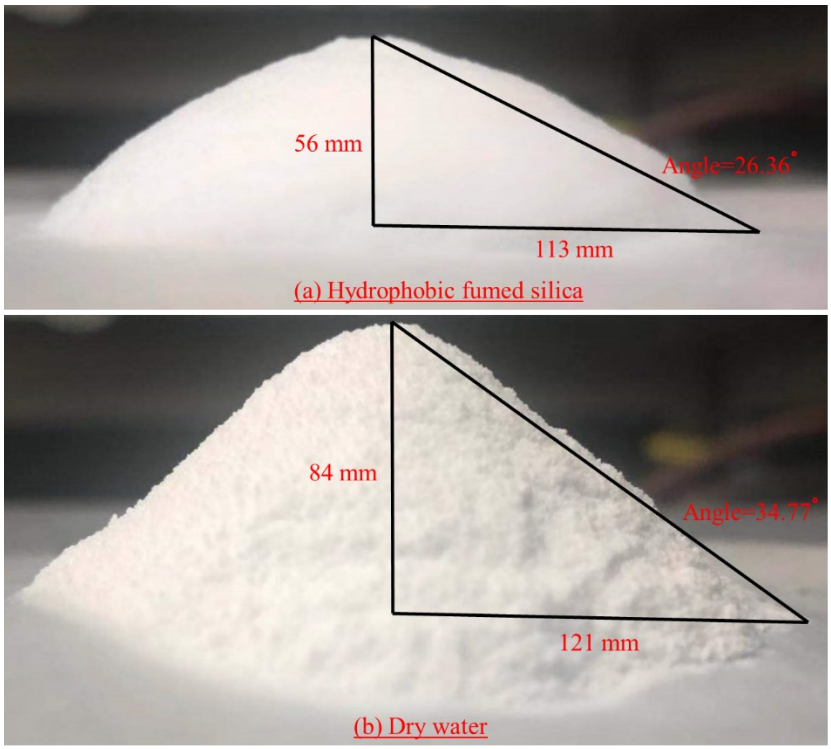


Figure 4.5 Angle of repose for (a) hydrophobic fumed silica and (b) dry water.

### 4.2.3. Preparation of geopolymer samples

Two independent batches of mixtures were prepared in this Chapter. In the first batch, three variants of dry water were produced, with the nano-$SiO_2$ content in dry water varying from 10% to 20% (corresponding to 1%~2% when the dry water was added at 10% of precursor). This batch of specimens was used to preliminarily investigate the optimum composition of dry water. Secondly, another independent batch was cast to conduct a comparative study between the lone nano silica and the associated dry water. In this regard, a reference mixture of geopolymer system was produced first, followed by variously introducing the predominantly hydrophilic silica nanoparticles, the predominantly hydrophobic silica nanoparticles and the dry water. Now, the mixing proportions of various geopolymers are shown in Table 4.2.

Table 4.2 Mix proportions of various N-A-S-H geopolymers.

| Mixture designation | Metakaolin (g) | SSS (g) | NaOH (g) | Water (g) | Dry water (g) | NS (g) | $SiO_2$/ $Al_2O_3$ | $Na_2O$/ $Al_2O_3$ | $H_2O$/ $Na_2O$ |
|---|---|---|---|---|---|---|---|---|---|
| Ref. | 500 | 545.51 | 100.61 | 99.83 | 0 | 0 | 3.3 | 0.95 | 12 |
| Hydrophobic | 500 | 545.51 | 100.61 | 99.83 | 0 | 7.5 | 3.3 | 0.95 | 12 |
| Hydrophilic | 500 | 545.51 | 100.61 | 99.83 | 0 | 7.5 | 3.3 | 0.95 | 12 |
| Dry Water | 500 | 545.51 | 100.61 | 57.33 | 50[b] | 0 | 3.3 | 0.95 | 12 |
| Ref. (0%) | 500 | 389.73 | 122.74 | 125.1 | 0 | 0 | 3.0 | 1.0 | 10 |
| 10% | 500 | 389.73 | 122.74 | 80.19 | 50[a] | 0 | 3.0 | 1.0 | 10 |
| 15% | 500 | 389.73 | 122.74 | 82.69 | 50[b] | 0 | 3.0 | 1.0 | 10 |
| 20% | 500 | 389.73 | 122.74 | 85.19 | 50[c] | 0 | 3.0 | 1.0 | 10 |

Note here that [*a], [*b] and [*c] represent the dry water comprising 10%, 15% and 20% of nano-$SiO_2$, respectively; Prior to demolding, the first batch was cured under ambient condition for 28 days,

while the second batch was placed in an oven to cure at 40 °C for 24 hours and then under ambient condition for up to 7 days (thermal curing).

When preparing the activator solution, the pre-determined NaOH pellets were dissolved in the sodium silicate solution and extra water was then added as needed. It was then placed in a fumed hood to cool down to room temperature. To start mixing, this premade activator was poured into a planetary mixer and stirred for 1 minute to ensure its homogeneity. This was followed by mixing with the metakaolin powder for another 3~5 minutes until the homogeneous slurry was formed. At this point, either the nano silica or the dry water was added to the system and the mixture was stirred for a further 3 to 5 minutes. The resulting mixture was cast into plastic moulds of Φ50 mm × 100 mm in size, which were compacted on a vibrating table. The specimens were demolded after 24 hours and cured under ambient conditions.

#### 4.2.4. Test protocols

The workability of the fresh geopolymer paste mixtures was measured per ASTM C230M-08 (2008), while its final setting time was evaluated per ASTM C191-08 (2008). The rheology of these fresh paste samples was investigated using a Brookfield DV-II+ Programmable Viscometer fitted with a SC4-27 spindle. This viscometer operates within a specified range of viscosity between 0 to 1250 mPa·s with a constant spin rate of 150 rpm. The rise in temperature due to the heat generated during the dissolution, hydrolysis and geopolymerization was monitored using an instant-read thermometer with a functioning range of -50~300°C. The compressive and tensile strength were measured on the hardened geopolymer cylinders, as per ASTM C39/C39M-18 (2018) and ASTM C496/C496M-17 (2017), respectively. After the test, some broken samples were ground to yield powder for further characterization. The crystalline phases that constituted the geopolymer were assessed through X-ray Diffraction (XRD), using a Copper-K radiation beam

(operated at 40kV and 44mA) with a step size of 2°/min, from 10° to 60° diffraction angle (2θ). The chemical bonds involved were examined by using the iS50 Fourier-Transform Infrared (FTIR) spectroscopy system coupled with a built-in Attenuated Total Reflection (ATR) module. A Thermogravimetric Analysis (TGA) was carried out using the Leco TGA 701 instrument that functions in a temperature range of 20~800°C and at a heating rate of 10 °C/min under a nitrogen atmosphere. Representative samples from each mixture were obtained from unbroken specimens, after careful slicing, and then placed in a Field Emission Scanning Electron Microscope (FE-SEM) that was coupled with an Oxford Energy Dispersive X-ray Spectroscope (EDS). A 15 kV accelerating voltage was applied to result in the varying magnification scale up to 5000 X. The images obtained were binarized to highlight the pores; voids and cracks (the 'pore fraction') as the black region and the solid geopolymer gel as fully white. This enables quantification of microstructure by counting the black pixels to calculate its fraction of the totality of pixels.

### 4.3. Fresh and hardened properties

#### 4.3.1. Adsorption of nanoparticles at interfaces

The production of dry water depends on the hydrophobic character of silica nanoparticles. The contact angle (θ) of particles against water is the most relevant parameter in dry water formation. The incorporation of silica nanoparticles into water produces either water-in-air aerosols (dry water) or air-in-water foams, and this depends on the surface character of the nanoparticles. As schematically illustrated in Figure 4.6, the hydrophobic particles reside more frequently in air than the hydrophilic samples due to their high contact angle (θ=118$^{o}$). The related energy of particle adhesion onto water surfaces can be calculated per Equation (4.1):

$$\Delta E = -\gamma_{a/w}\pi R_p^2(1+\cos\theta)^2 \tag{4.1}$$

where $\gamma_{a/w}$ is the interfacial tension (72.8 mJ/m$^2$) between water and air, and $R_p$ is the particle radius of silica nanoparticles (7nm). The contact angle θ of hydrophobic and hydrophilic particles against water is 118$^o$ and 14$^o$, respectively. The energy of adhesion is negative in the case of both hydrophobic silica (θ=118$^o$) and hydrophilic silica (θ=14$^o$), with a value of -20.49 mJ/m$^2$ and -282.61 mJ/m$^2$ ($\Delta E/\pi R_p^2$), respectively. Since the free energy of adhesion is negative in those two cases, both hydrophobic and hydrophilic nano silica samples adhere to the water surface spontaneously. Note also that the former case indicates the lower free energy input, which is required for desorption of one particle. When added into water, the hydrophobic nano silica may simply adsorb onto water droplets due to the partial wetting, whereas the hydrophilic nano silica may be dispersed in the water phase.

In order to evaluate the entire state of particles-water systems as illustrated schematically in Figure 4.6, changes in the free energy of particles as a function of their immersion into water could be evaluated:

$$\Delta E(\Delta h) = \pi \Delta h^2 \gamma_L [1 - (1 + \cos\theta)\frac{2R_p}{\Delta h}] \tag{4.2}$$

where $\Delta h$ is the immersion depth of a particle, and a full immersion is defined as $\Delta h \geq 2R_p$. Table 4.3 summarizes the immersion energies of hydrophobic and hydrophilic particles at depths of 1 nm and 7 nm by using Equation (4.2). Despite the spontaneous adhesion of both hydrophobic and hydrophilic silica nanoparticles, hydrophobic particles require a very high immersion energy at full depth of immersion ($\Delta h$=2$R_p$=14nm) compared to the spontaneous immersion of hydrophilic particles. The dry water formation after shear mixing of hydrophobic silica particles in water can now be explained by the adhesion of particles and their shell-like coverage of micrometer size

water droplets. A good flowability of the dry water samples was obtained which showed that the powder consists of individual particulates, with no water bridges between them.

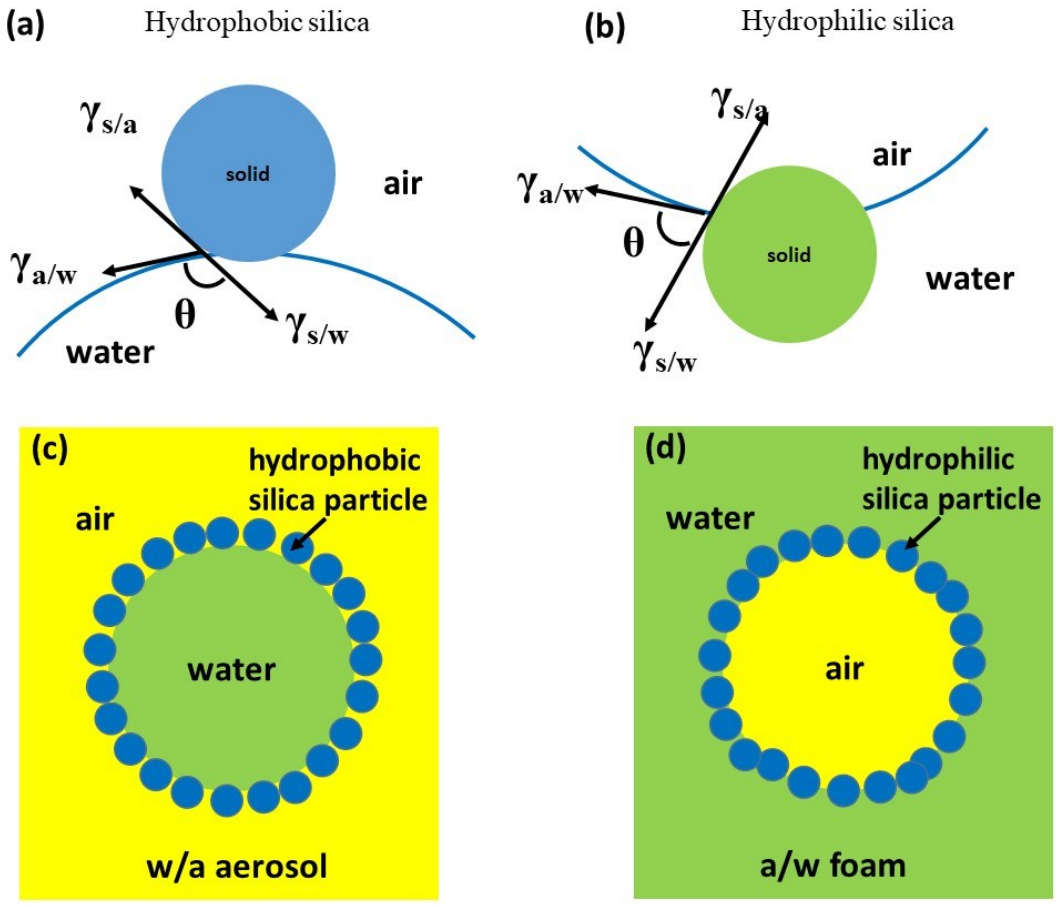


Figure 4.6 Schematic illustrations of silica nanoparticles at air/water interfaces.

Table 4.3 Normalized energies of adhesion and immersion for hydrophilic and hydrophobic silica nanoparticles.

| Properties and test methods | Hydrophobic | Hydrophilic |
|---|---|---|
| Contact angle against water | 118° | 14° |
| Energy of adhesion | -20.49 mJ/m$^2$ | -282.61 mJ/m$^2$ |
| Energy of immersion ($\Delta E/\pi R_p^2$) at Δh=1nm | -9.55 mJ/m$^2$ | -39.49 mJ/m$^2$ |
| Energy of full immersion ($\Delta E/\pi R_p^2$) at | 136.71 mJ/m$^2$ | -282.55 mJ/m$^2$ |

### 4.3.2. Workability

The effect of nano silica and the resulting dry water on workability of N-A-S-H geopolymer mixture is illustrated in Figure 4.7(a). For starters, in comparison to the reference mixture, adding silica nanoparticles as is, led to a drop in the flow diameter. It is as expected, due to the decrease in the mean particle size of the solid precursors as a whole. For, silica nanoparticles given their larger specific surface area, lead to a higher water demand (Gao et al., 2015; Deb et al., 2016). On the other hand, the mixture containing dry water resulted in a minor increase in the workability of fresh paste; indeed, it manifests as the largest flow diameter across all four mixtures. Dry water particles range in size from 10 μm to 300 μm (Binks and Murakami, 2006; Chevalier and Bolzinger, 2013), and this was also confirmed in this study through the optical microscopy (see Figure 4.4). Whereas the metakaolin precursor has an average particle size of 1.3 μm. Silica nanoparticles encapsulate water droplets and increase the interfacial area of the silica nanoparticles powder from the nano-scale to the micro-scale. Therefore, the particle size distribution of the solid powder fraction at the start of geopolymerization shifts to the larger end. As a result, to achieve the same workability as with metakaolin alone, there is a drop in the liquid demand. The dry water likely participates as ball-bearings to lubricate the system. Secondly, as a soft powder, the connection between stabilizing nano particle and water droplet will be easily broken under pressure, which then releases the encapsulated water (Wang et al., 2021). Therefore, as the mechanical mixing progresses, the nano silica gradually unzips to release the water droplets within dry water under the squeezing between solid particles of precursor and also the mechanical pressure from the mixer blade. These water droplets now become a supplement to the existing batched water in the mixture. This supplement functions as an internal source of water entrainment and so restores the liquid-to-solid ratio. So that as the dissolution proceeds, this supplement aids in continued flowability.

The effect of the nano-$SiO_2$-to-water ratio in dry water upon the workability of the resulting mixture is presented in Figure 4.7(b). In all three cases, the alkali-activated systems comprising dry water resulted in a larger flow diameter in comparison with the reference mixture without dry water. On the other hand, and contrary to expectation, one notes that the workability of the systems did not increase commensurately with the water content in dry water particles. This may be attributed to that the difference in water content between these three variants of dry water is extremely minor, particularly after blending with the precursor and activator solution.

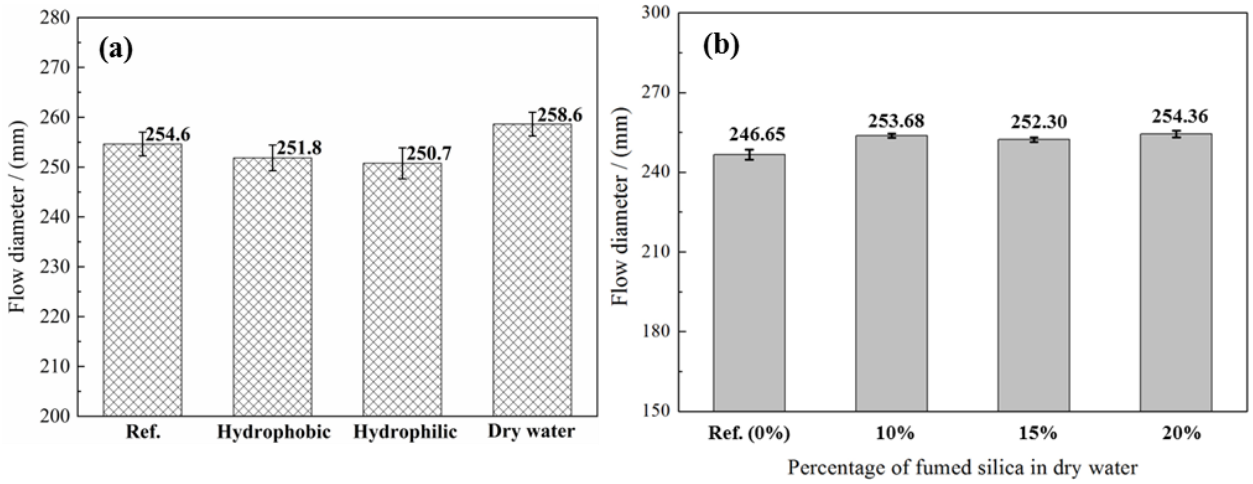


Figure 4.7 Flow diameter of geopolymers incorporating: (a) nano silica in different forms and (b) varying variants of dry water.

### 4.3.3. Final setting time

Figure 4.8(a) shows that adding silica nanoparticles universally led to a drop in the final setting time of geopolymer mixture. Whereas the hydrophobic and hydrophilic silica nanoparticles by themselves led to a reduction of between 15~20 minutes, the final setting time was about 50 minutes shorter in the presence of dry water. The latter corresponds to a 15% decrease in the time to final set when compared with the reference mixture. Although there is no consensus upon the effect of nanoparticles on the setting process of geopolymer systems, some related studies

attributed the resulting reduction in setting time to the surface effect and the associated high surface energy of nanoparticles (Gao et al., 2013b). With regard to nano silica stabilized dry water, besides the above merit of nanoparticles, the shorter final set process is also likely due to the enhanced alkalinity during the early stage. Recall that, a part of batched water was temporarily encapsulated in dry water powder at the outset of mixing, leading to a temporary increase in the ratio of $H_2O/Na_2O$. As a result, the increased alkali concentration promoted the dissolution and activation of solid aluminosilicate precursor. Moreover, the improved flowability in the case of dry water may play a positive part as well.

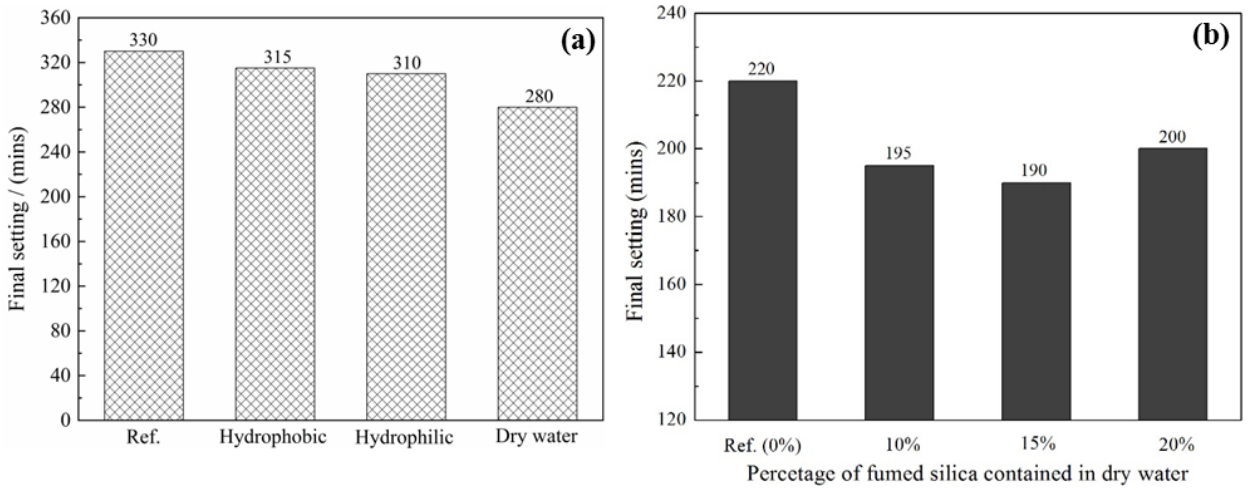


Figure 4.8 Final setting time of geopolymers incorporating: (a) nano silica in different forms and (b) varying variants of dry water.

The three versions of dry water were examined for their effect on final setting time, as shown in Figure 4.8(b) for different nano silica-to-water ratios. Again, the three mixtures made with dry water all registered the shorter final setting time, as compared to the plain reference that was made without dry water. An overall 20~30 mins reduction could be seen in the final setting time upon adding dry-water to the alkali-activated systems. However, the mutual difference between these

three variants of dry water was minor, within 5~10 mins. This may be possibly attributed to the minor difference in terms of their compositions once the dry water was added at 10% of metakaolin by mass to the mixture. This was clearly not enough to substantially alter the setting time. Also, it is widely reported that the setting process in alkali-activated systems is controlled mainly by $Al_2O_3$ (De Silva et al., 2007). In the present study, the proportions of various oxide ratios were kept constant in all mixtures, both with and without dry water.

Note further that attempts were made to produce dry water with nano silica higher than 20%. But, they resulted in excessive unbound nanoparticles, which significantly floats in the air, causing a highly dusty powder with a potential health hazard. Also, prior work on the use of nano silica to promote geopolymerization noticed an optimum dosage of 1~2% nano-$SiO_2$ by mass fraction of the principal precursor (Aly et al., 2012).

### 4.3.4. Compressive strength

Seen from Figure 4.9(a), adding silica nanoparticles to a geopolymer system increases the compressive strength. The two mixtures that contained the silica nanoparticles as is, saw a modest 5% increase in compressive strength. Such an enhancement has been widely attributed to the following two reasons: (i) the chemical effect, in which the added nano silica particles boost the geopolymerization by resulting in formation of extra geopolymerized network or extending the chain length of originally formed aluminosilicate oligomers; (ii) the micro-filling effect, in which the voids and microcracks could be effectively filled by unreacted nanoparticles due to their nano-size (Assaedi et al., 2016); (iii) it is possible that there exist numerous unsaturated bonds and various hydroxy bonding states at the surface of the fumed silica nanoparticles, which are known to improve the speed and degree of polycondensation (De Silva et al., 2007). Comparably, the mixture containing dry water witnessed a 17% increase in compressive strength, which was more

than the case of nano silica as is. Besides the aforementioned merits of nanoparticles, the enhanced alkali concentration led by the temporary encapsulation of water at the early stage should be another important reason, which boosts the dissolution of solid aluminosilicate precursor to yield enough tetrahedral $AlO_4$ and $SiO_4$ groups and form adequate aluminosilicate oligomers for the eventual N-A-S-H framework. Moreover, it is reported that a higher fluid volume may inhibit the dissolution of aluminosilicate (Gao et al., 2013b). However, the presence of dry water decreased the liquid-to-solid ratio at the early stage of geopolymerization, as evident from the mixing proportions shown in Table 4.2 and Figure 4.9(c). And hence, the geopolymerization in the presence of dry water is likely more efficient.

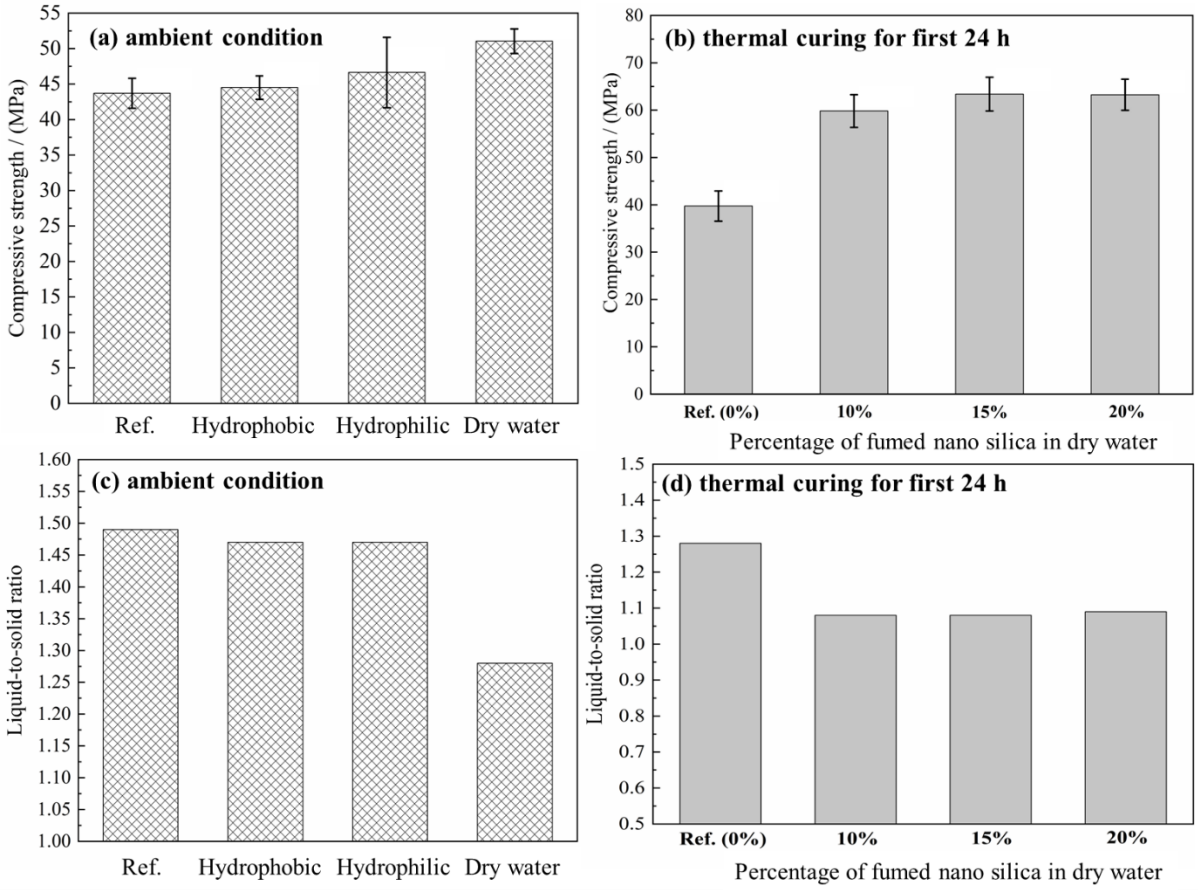


Figure 4.9 Compressive strength of geopolymers incorporating (a) nano silica in different forms, (b) varying variants of dry water, and (c, d) the associated liquid-to-solid ratio.

However, there appears to be a limit to achieve the maximum improvement led by nanoparticles and also its product (i.e., dry water), and its benefit upon the mechanical performance reaches a plateau against an increase in the amount of the silica nanoparticles within the alkali-activated system. Recall that prior studies found this optimum to lie between 1~2% of the principal aluminosilicate precursor, for an excess of unreacted nanoparticles does not contribute to the strength (Gao et al., 2013b). Figure 4.9(b) indicates that there is an optimum percentage of silica nanoparticles within dry water (here, 15% nano-$SiO_2$ with 85% water), for benefits to the compressive strength of the resulting geopolymer. Any further increase in the nanoparticle-to-dry water content beyond 15% led to a plateau. Note that this value translates to 1.5% of nanoparticles with respect to the metakaolin, which supports the previously cited optimal range. Furthermore, it should be emphasized here that the thermal curing was somehow able to cause the appearance of cracks, occasionally at the surface of samples after demoulding. This may lead to some disturbances upon investigating the potential benefits of dry water and also the performance of N-A-S-H geopolymers made with varying compositions. Therefore, the ambient curing was constantly employed in other Chapters in order to avoid this concern.

### 4.4. Characterizations upon geopolymers incorporating dry water

In order to understand the mechanisms underlying the effects of nano-$SiO_2$ and the resulting dry water on fresh and hardened properties of N-A-S-H geopolymers, a combination of rheological, thermal, morphological, chemical and microstructural characterizations was carried out.

#### 4.4.1. Rheology

Recall that, the rheology of cementitious and geopolymerized mixtures is usually connected to their flowability. Hence, the rheological properties of N-A-S-H geopolymer mixture, variously made with nano silica and dry water, were evaluated, as shown in Figure 4.10. Notice that the

system incorporating dry water droplets had a slightly lower viscosity than that of the reference system. As well, there was an associated drop in the yield shear stress. This points to a reduction in inter-particle friction in the fresh geopolymer mixture due to the dry water. On the other hand, note that when the nano silica particles were incorporated as is, there was a detectable increase in the viscosity. It results in an approximately identical rise in the yield shear stress. Furthermore, the changes in these rheological parameters are reflected very closely in the change to the flow diameter shown in Figure 4.7(a).

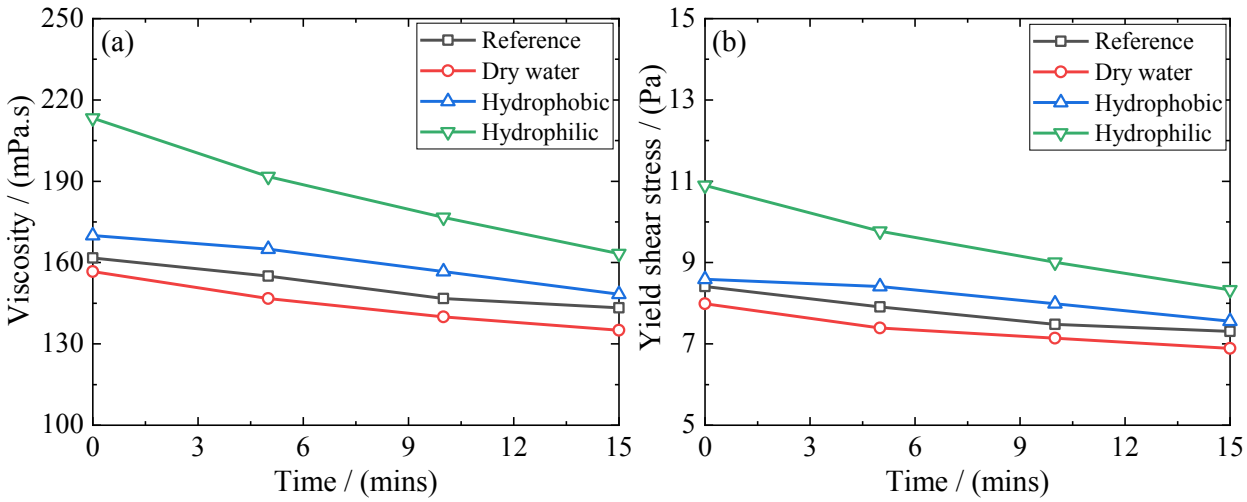


Figure 4.10 Rheological properties of fresh geopolymer systems: (a) viscosity and (b) yield shear stress (Note: Mixtures for rheology test were prepared with the $H_2O/Na_2O$ ratio suitably increased to 20, in order to capture the functional range of the rotational (0~1250 mPa.s)).

### 4.4.2. Temperature evolution

It is widely recognized that the geopolymerization shows a strong exothermicity (Davidovits, 2008). Hence, the accompanying changes in temperature reflect the progress of the associated reaction rate. Figure 4.11 displays the temperature evolution in the first ten hours of geopolymerization. The inset in Figure 4.11 highlights the rise in temperature during the very early

stages of geopolymerization. Note that in this ascending period, the mixture with dry water experienced the most rapid temperature increase. It was followed by the two mixtures containing silica nanoparticles as is. As time progressed, the difference between these three mixtures and the reference mixture continuously increased. This implies that the two silica nano-additives and dry water promote the reaction rate and advance the polycondensation. The benefit from nanoparticles of silica was found to be attributed to the surface effect, namely the significantly small particle size and the considerably high surface energy (Gao et al., 2013b; Sumesh et al., 2017). The specific role of dry water may be explained as follows. As aforementioned, in order to maintain a constant $H_2O/Na_2O$ ratio, the water stabilized in the dry water was deducted from the batched amount. Given that the water droplets temporarily encapsulated by the silica nanoparticles in dry water were not completely released in this early stage, the actual alkalinity in the mixture containing dry water was somewhat higher than in the other three mixtures at early stage. As a result, the system was more alkaline in the presence of dry water, in comparison with the other three mixtures. This stronger alkalinity boosted the early dissolution of solid precursor as well as the associated reactions. The peak in Figure 4.11 also supports the measured final setting time for each mixture shown in Figure 4.8(a).

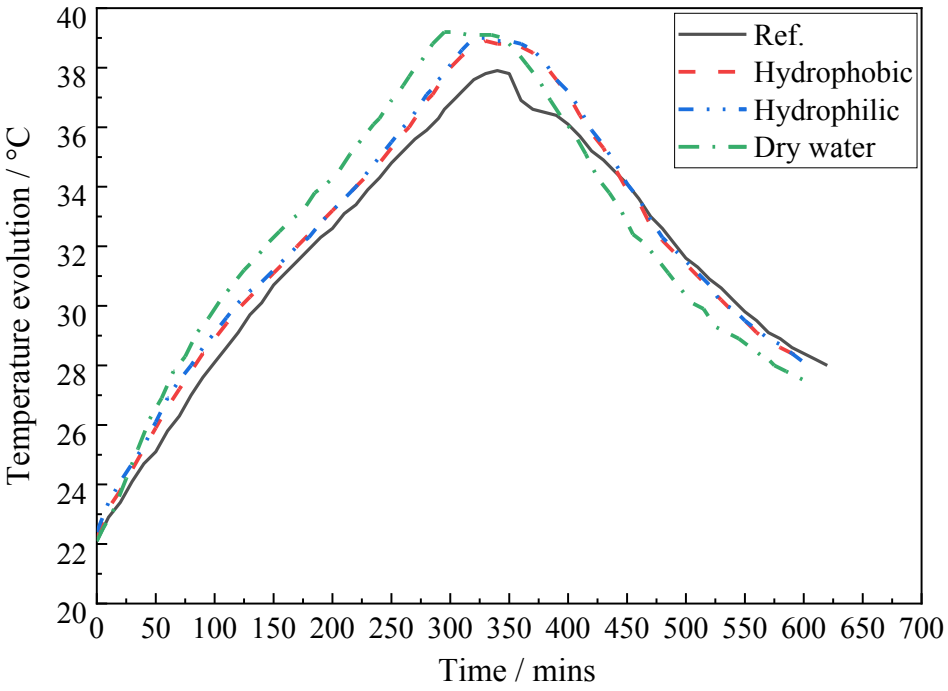


Figure 4.11 Temperature evolution during the setting of the fresh geopolymer mixtures.

### 4.4.3. X-ray diffraction (XRD) and thermogravimetric analysis (TGA)

The XRD traces are shown in Figure 4.12. The geopolymer paste is composed chiefly of amorphous phases and this manifests in the curvilinear shape of each of those four traces, with a broad diffused hump instead of a sequence of sharp diffraction peaks (Davidovits t al., 1990). Prior studies have widely reported that this hump commonly lies within the range of 2θ between 17°~40° with a center approximately at 27°~29° in the generated XRD trace (Chen et al., 2016). The center of this hump is found to shift towards the higher end of 2θ for a greater degree of amorphicity (Williams et al., 2011; Yuan et al., 2016). Figure 4.12 shows that in the reference mixture, the centre of this hump is registered at 2θ = 28.00°. Upon adding hydrophilic silica nanoparticles, the centre shifts slightly to 2θ = 28.15°, whereas hydrophobic silica nanoparticles cause the centre to shift to 2θ = 28.45°. For the mixture dosed with dry water, the center of this tell-tale hump shifts to 2θ = 28.55º. Therefore, it is clear that in all three cases, the additives cause a slightly greater

degree of amorphicity in the hardened paste. It should be emphasized here that although the associated shift may be small in value, this change in 2θ is nevertheless a reliable qualitative measure to assess the variation in the degree of geopolymerization (Saidi et al., 2013; Yuan et al., 2016). For instance, Yuan et al. saw a slight reduction in 2θ from 28° to 27.8°, and this was accompanied by a corresponding 33% drop in the compressive strength of geopolymer system (Yuan et al., 2016). Therefore, the rightward shift in terms of 2θ observed in the present study may be treated as an indicator of enhanced geopolymerization, due to the presence of the silica nanoparticle additives including dry water.

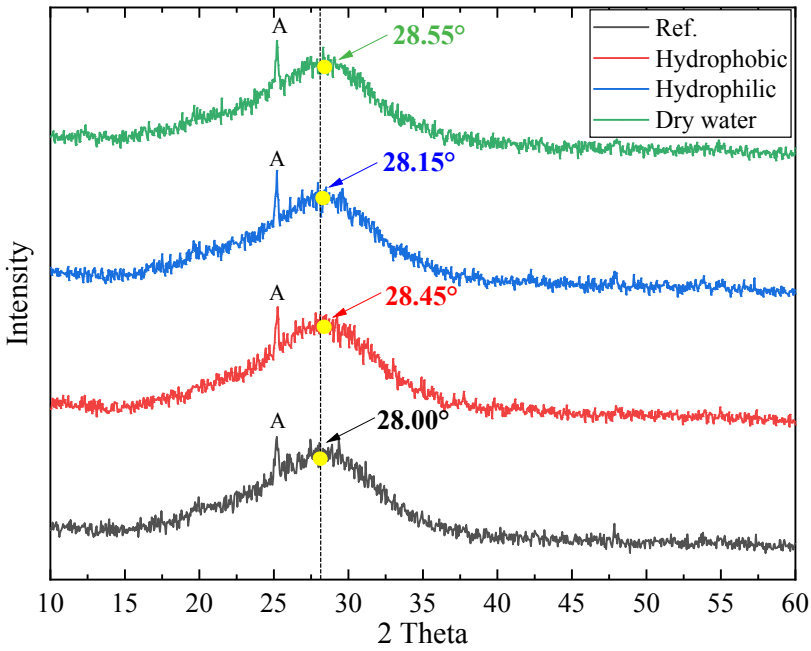


Figure 4.12 XRD spectra for various geopolymer mixtures (A:Anatase).

The TGA curves corresponding to the geopolymer systems are shown in Figure 4.13. The principal weight loss occurs between room temperature (~22 °C) and 300 °C, and this has been widely recognized to be attributed to the evaporation of free water and a part of water chemically bounded to geopolymers (Tchakouté et al., 2017; da Silva Rocha et al., 2018). It is clear from Figure 4.13

that the mixtures incorporating hydrophobic silica nanoparticles and dry water jointly registered the greatest weight loss and the highest peaks associated to the derivative of weight change (DTG) during 22~300 °C. On the other hand, the reference mixture and the one containing the hydrophilic silica nanoparticles saw much less weight loss and the lower DTG peak. This suggests that more water is dehydroxylated from sodium aluminosilicate phases and further, that the structure of geopolymer incorporating dry water or hydrophobic silica nanoparticles likely consists more chemically bound water. This possibly implies a greater chain length for the N-A-S-H network in these two mixtures, since the hydroxyl groups are mainly linked to the silicon atom.

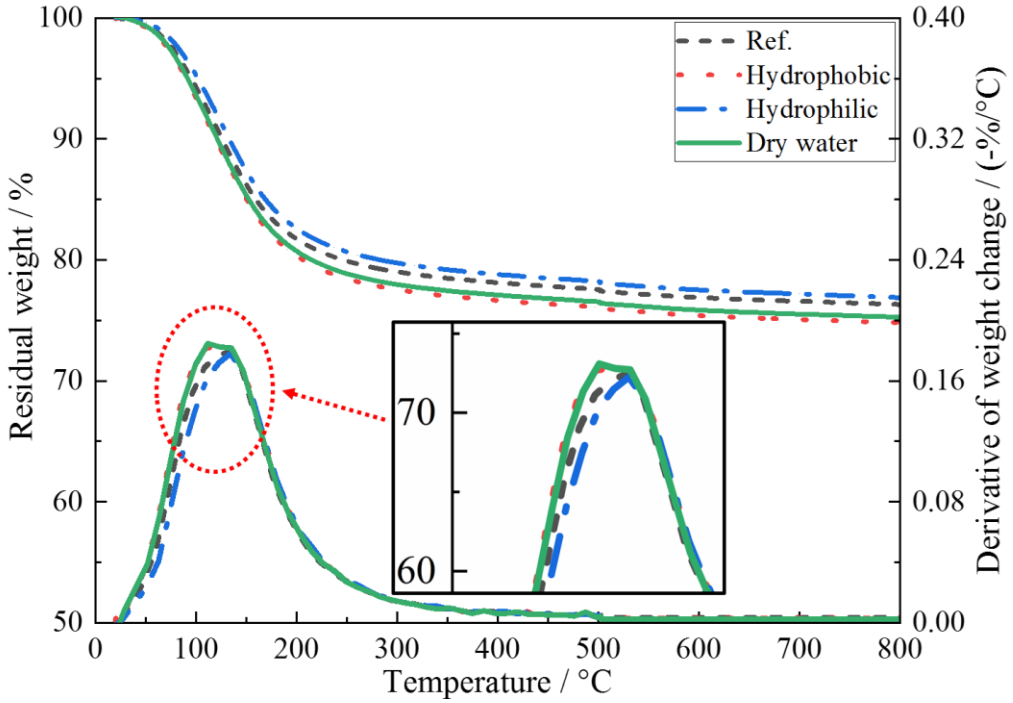


Figure 4.13 TGA outcomes for various geopolymer mixtures.

### 4.4.4. Fourier transform infrared spectroscopy (FTIR)

The FTIR spectra for the four mixtures examined here are shown in Figure 4.14. Note that the small band located around 560~570 $cm^{-1}$ is ascribed to the external linkage vibrations of the $TO_4$

in the double rings of zeolite (Moudio et al., 2021). The strongest absorbance peaks found in fully geopolymerized systems was assigned mainly to the asymmetric stretching vibrations of Si-O-T (T: tetrahedral Si or Al) in the N-A-S-H framework, and is usually found between 800~1250 $cm^{-1}$ in the FTIR spectrum (Chen et al., 2019). Also, a shift in the Si-O-T peak toward the higher wavenumber is an indication of evolving geopolymerization (Li et al., 2019). This shift may be attributed to the increase in the number of tetrahedral Si groups in proportion to the non-activated Si-O-Al within the geopolymer system. The bond between Si and O is much stronger than the corresponding Al-O bond, thus the main geopolymer band (i.e., Si-O-T) shifts towards the higher end (He et al., 2016). Note also that regardless of their water-affinity, the hydrophobic and hydrophilic silica nanoparticles when added as is, produced a spectrum at a slightly higher wavenumber (963.77 $cm^{-1}$) in comparison to the reference mixture (962.8 $cm^{-1}$). Once again, the greatest shift was seen for the mixture made with dry water (966.66 $cm^{-1}$), confirming that this dry water leads to the highest degree of geopolymerization across the four mixtures. The shift in the principal peak toward the higher wavenumber is from the silica nanoparticles, which serve as a secondary silica source and supply more $SiO_4$ groups that are required to form the aluminosilicate framework. Also, since a part of the water in this mixture is encapsulated by silica nanoparticles, until this encapsulating nano silica unzips, the fresh mixture is effectively at a higher alkalinity than the others. As a result, the stronger alkaline condition boosts the evolving geopolymerization (Yuan et al., 2016).

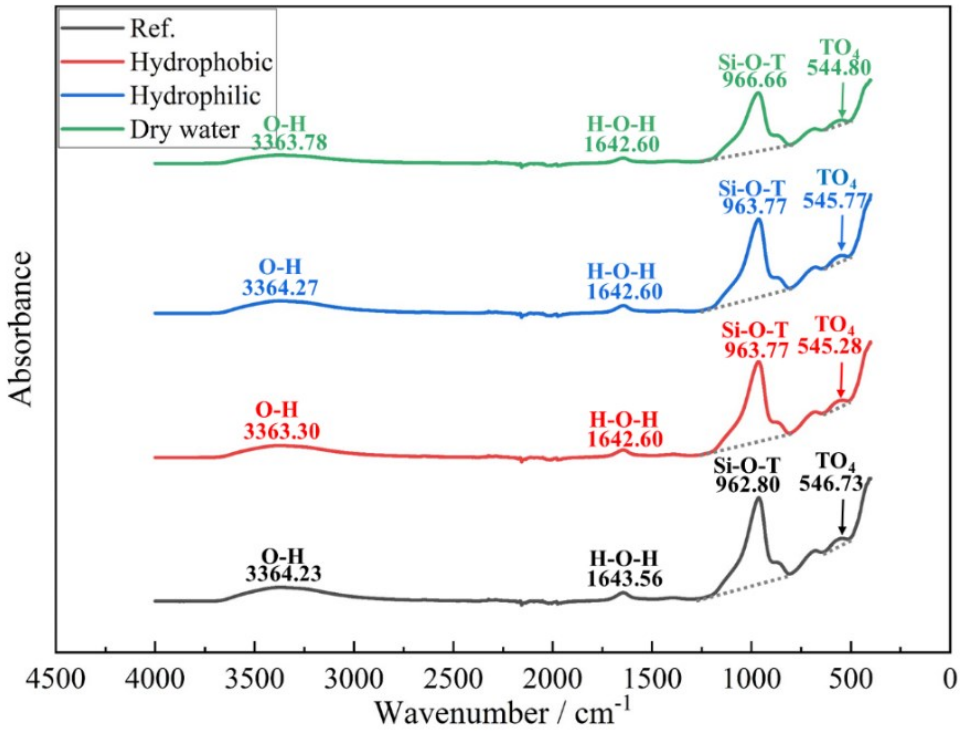


Figure 4.14 FTIR spectra for various geopolymer mixtures.

The FTIR spectra was deconvoluted for the range of 800~1250 $cm^{-1}$, as it corresponds to the Si-O-T band, with Gaussian peak shapes (Zhang et al., 2012). This helps to interpret the structural changes referred to above. The associated fitting procedure was performed in accordance with the related literature (Rattanasak and Chindaprasirt, 2009). The following peaks are considered: Peak I (~860 $cm^{-1}$) to Si-OH bending; Peak II (~930 $cm^{-1}$) to Si-O-T in $Q_2$; Peak III (950~960 $cm^{-1}$) to asymmetric stretching vibrations of nonbridging oxygen (NBO) sites; Peak IV (990~1000 $cm^{-1}$) to Si-O-T in a 3-dimentional N-A-S-H network; Peak V (~1080 $cm^{-1}$) to Si-O-Si of silica gels; and Peak VI (~1150 $cm^{-1}$) to Si-O-T of unreacted metakaolin. The FTIR deconvoluted peaks for each mixture are now presented in Figure 4.15, with a regression coefficient $R^2$ beyond 0.99. In addition, the relative peak areas are quantified in Figure 4.16. It is evident that among all four examined mixtures, the reference registers the maximum area for Peak III and the minimal area for Peak IV.

These together correspond to the lowest degree of polycondensation (Zhang et al., 2012). However, adding nanoparticles, there is a boost in the polycondensation, as evident from an increase in the Peak IV area and a simultaneous drop in the Peak III area. This was true for all three mixtures contained the nano silica additives. Yet, once again, the mixture containing dry water records the lowest Peak III and the highest Peak IV. These together indicates that the associated N-A-S-H framework registers the greatest polycondensation degree.

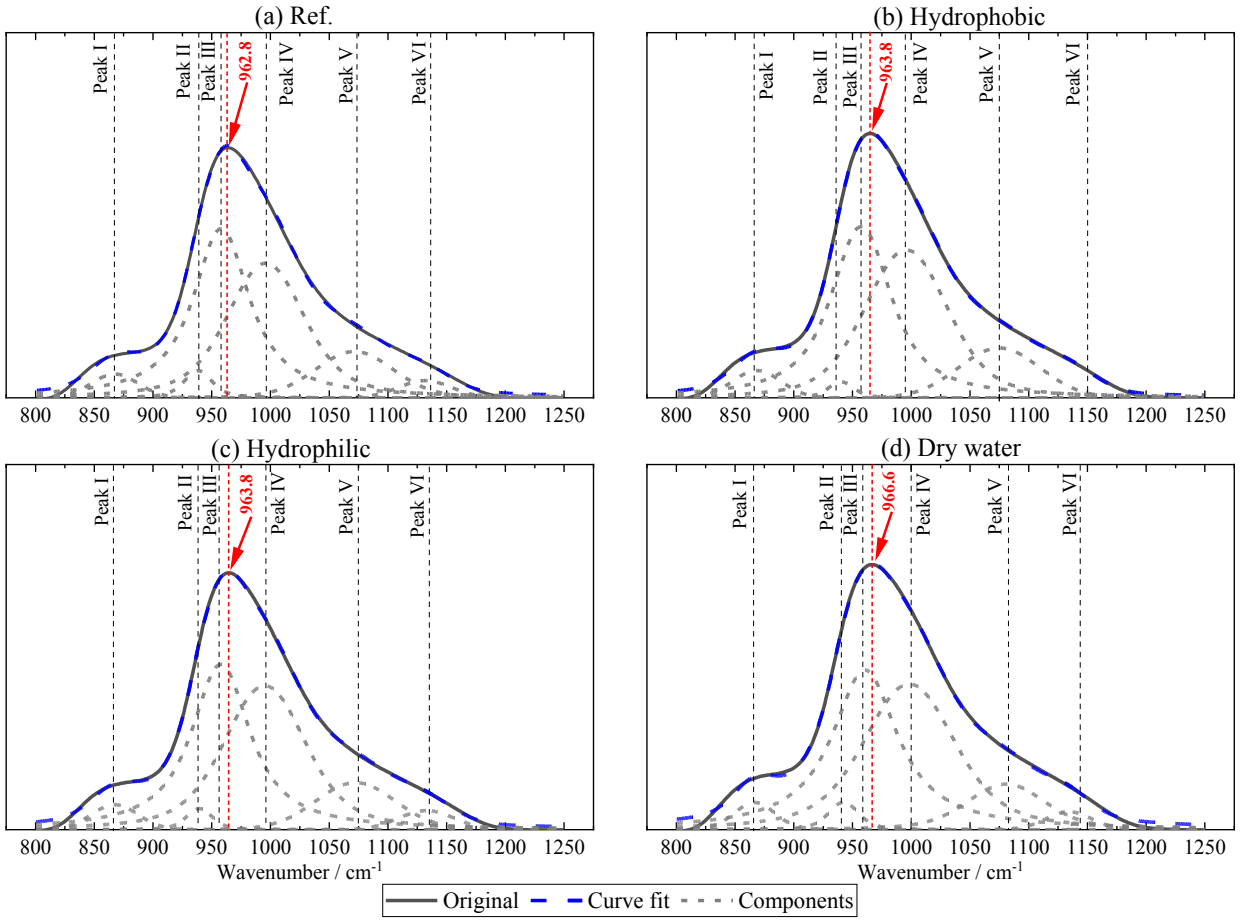


Figure 4.15 FTIR spectral deconvolutions of the main Si-O-T stretching band positioned at 800~1250 $cm^{-1}$ for geopolymers reported in Figure 4.14.

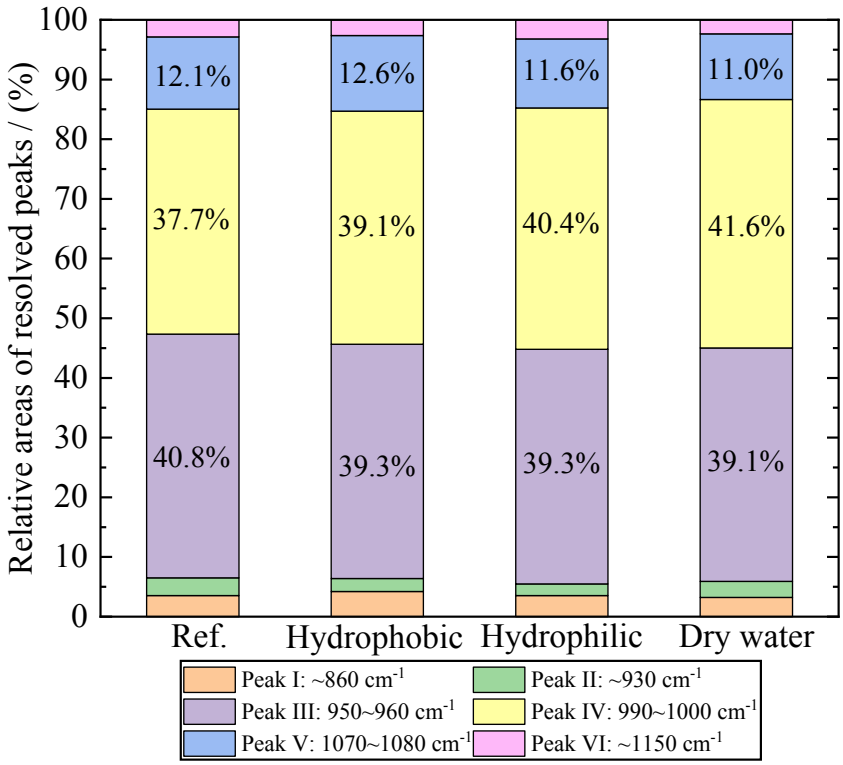


Figure 4.16 Relative areas of the deconvoluted component peaks within the main Si–O-T band.

**4.4.5. Scanning electron microscope and energy dispersive X-ray spectroscope (SEM-EDS)**

Samples from each of the four mixtures were examined under a Field-Emission Scanning Electron Microscope (SEM). Representative images at 200X and 5000X magnifications are presented in Figure 4.17. The images taken under 200X magnification clearly showed the microcracks that appear. The reference mixture displayed the longest and widest microcracks, with a crack width of 10 μm. On the other hand, while microcracks appear in samples made with the other three mixtures, they were much smaller than in the reference mixture, but mutually comparable. Whereas the sample containing hydrophilic silica nanoparticles had a crack width between 6 to 8 μm, the corresponding value in the case of specimens dosed variously with hydrophobic silica nanoparticles or dry water decreased to 2~3 μm. The dense regions from these images at 200X were magnified to 5000X for further investigation. By comparing with the texture of the reference

sample in Figure 4.17, notice that the most compact microstructure once again resulted either by adding hydrophobic silica nanoparticles or by adding dry water. To quantify the porosity and the pore-size distribution, these SEM images were also binarized to express the microcracks, the pores and other flaws (Diamond, 2000). Figure 4.18(a-d) illustrates this binary for images obtained at 200X, while Figure 4.18(e-h) shows the outcome of this operation on images taken at 5000X. The void phase was transformed into its equivalent pore diameter and the associated pore fraction was determined by counting the black and white pixels, as presented in Figure 4.19. The total porosity in the reference sample was beyond 10% under both two magnification scales (200X and 5000X), whereas this value dropped to about 4%~6% in the specimen incorporating dry water. The mixtures variously made with the two nano silica alone also experienced similar refinements, but were smaller than the dry water series. Particularly, the enhancement led by dry water in reducing the fraction of large voids was superior, as evident from Figure 4.19.

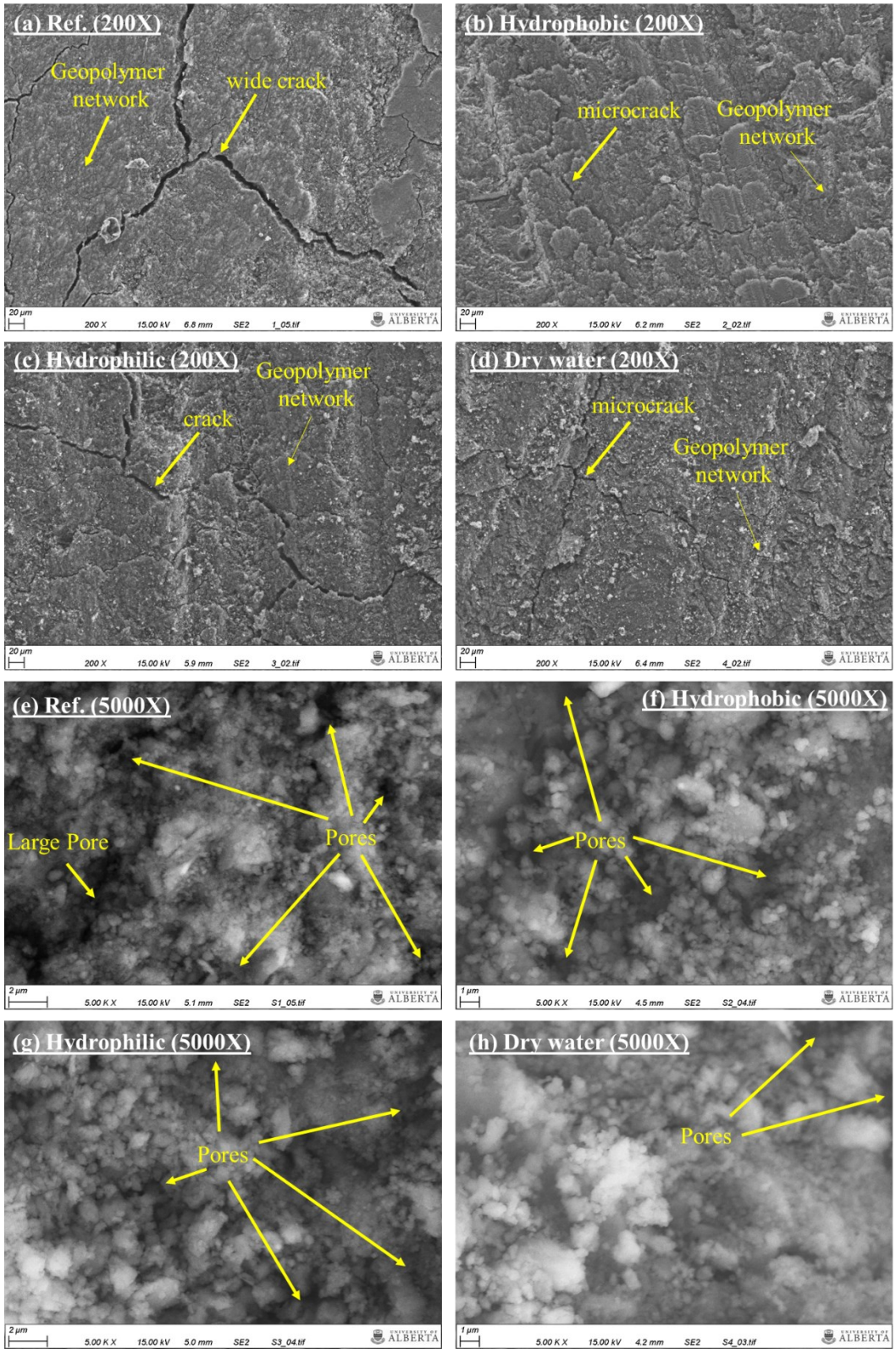


Figure 4.17 SEM images of geopolymer mixtures captured at different magnifications.

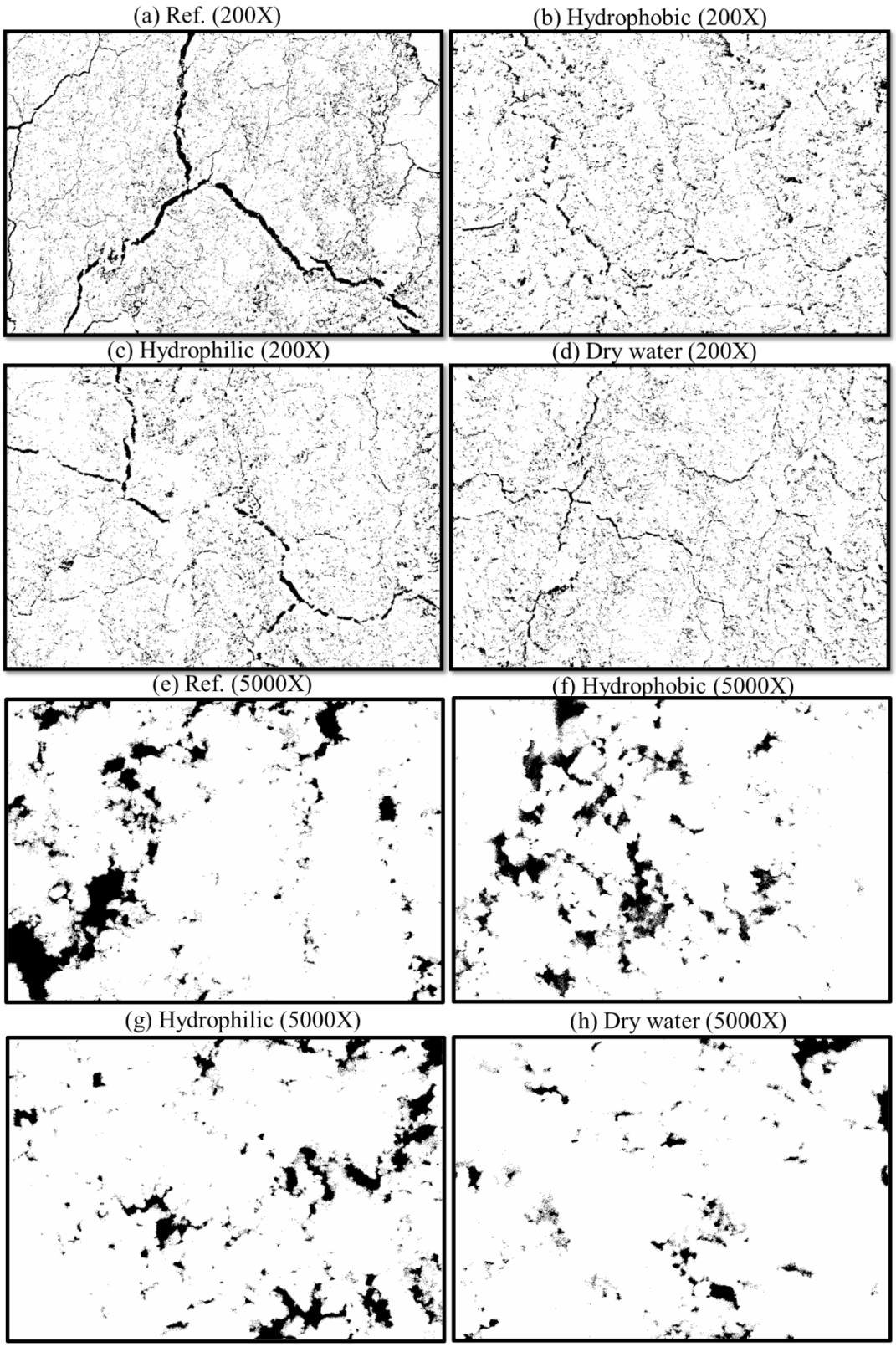


Figure 4.18 SEM images in Figure 4.17 after undergoing binary segmentation.

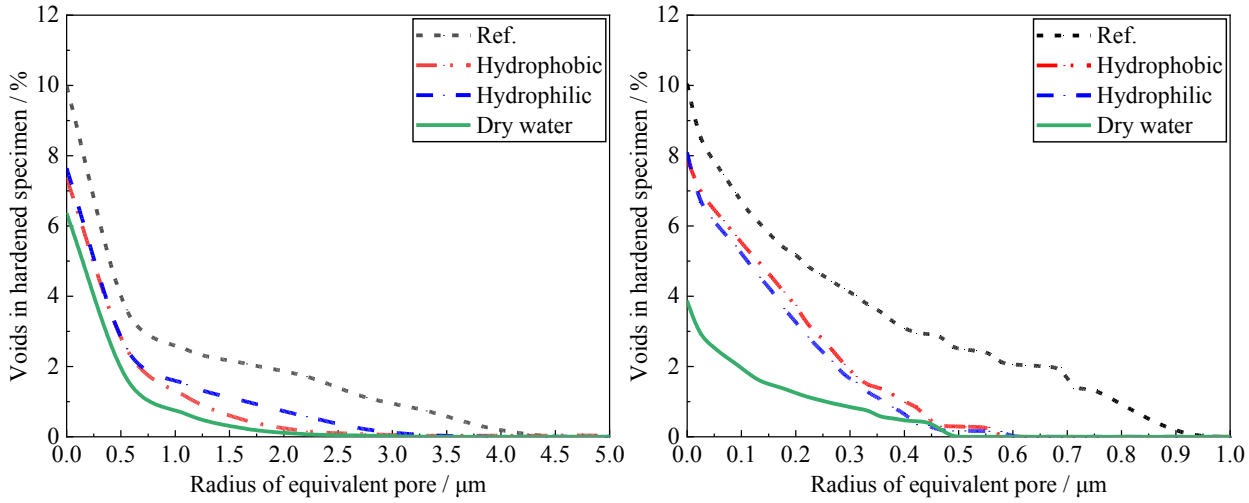


Figure 4.19 Pore size distribution derived from image analysis for images taken at (a) 200X and (b) 5000X.

The images taken at 5000X were analyzed further for elemental composition, using the Energy Dispersive X-Ray Spectroscope (EDS). The elemental mass spectra that result from scanning the entire section are presented in Figure 4.20(a). It is clear that Na, Al, Si and O are the four prominent elements detectable in the geopolymerized solid phase. The three mixtures with a nano-additive display an average of 26.5% Si, which is higher than that for the reference mixture (~24.8%). This difference may principally be attributed to the silica nanoparticles behaving as a secondary source of silica, which then either acts as a micro-filler or participates in the reactions. Also, the mixture containing dry water registered the highest Na amount (~13.1%) across all four mixtures, followed by the two mixtures made with silica nanoparticles as is (~11.8%). All of these were higher than the 10.6% Na detected in the reference mixture. Based on the EDS spectra, the molar atomic ratios, viz. Si/Al and Na/Al, were computed as shown in Figure 4.20(b)**.** It is clear that the three mixtures made with the silica nano-additives had uniformly higher molar Si/Al ratios than the reference mixture. It is well known that a higher Si/Al ratio usually corresponds to a greater geopolymerization degree (De Silva et al., 2007). Moreover, as the designed molar ratio was

$SiO_2/Al_2O_3$ = 3.3, the corresponding element ratio per design was Si/Al = 1.65 across all four mixtures. In Figure 4.20(b), this ratio for the reference mixture was 1.59. On the other hand, across the three mixtures containing the silica nano-additive in one form or another, this ratio was higher than 1.65. That may be, adding silica nanoparticles promotes the activation of the principal aluminosilicate precursor. Similarly, the designed molar ratio Na/Al was 0.95 across all mixtures. The actual ratio of 0.83 was far lower in the reference mixture. Recall that every single Al atom in the geopolymer unit must connect with a Na ion to balance the negative charge carried by the former. A lower Na/Al ratio in situ implies that the principal aluminosilicate precursor was not completely activated, and this is also supported by XRD and FTIR analyses. On the other hand, the two mixtures made with silica nano-additives as is registered a larger Na/Al ratio (~0.93), close to the theoretical value per design. It is noteworthy that the mixture containing dry water saw the highest Na/Al ratio at 1.03. In sum, the in situ microstructural chemistry reveals that the presence of nano silica in general promotes the activation of metakaolin. More importantly, the enhancement led by dry water is notably much stronger than that by the silica nanoparticle as is.

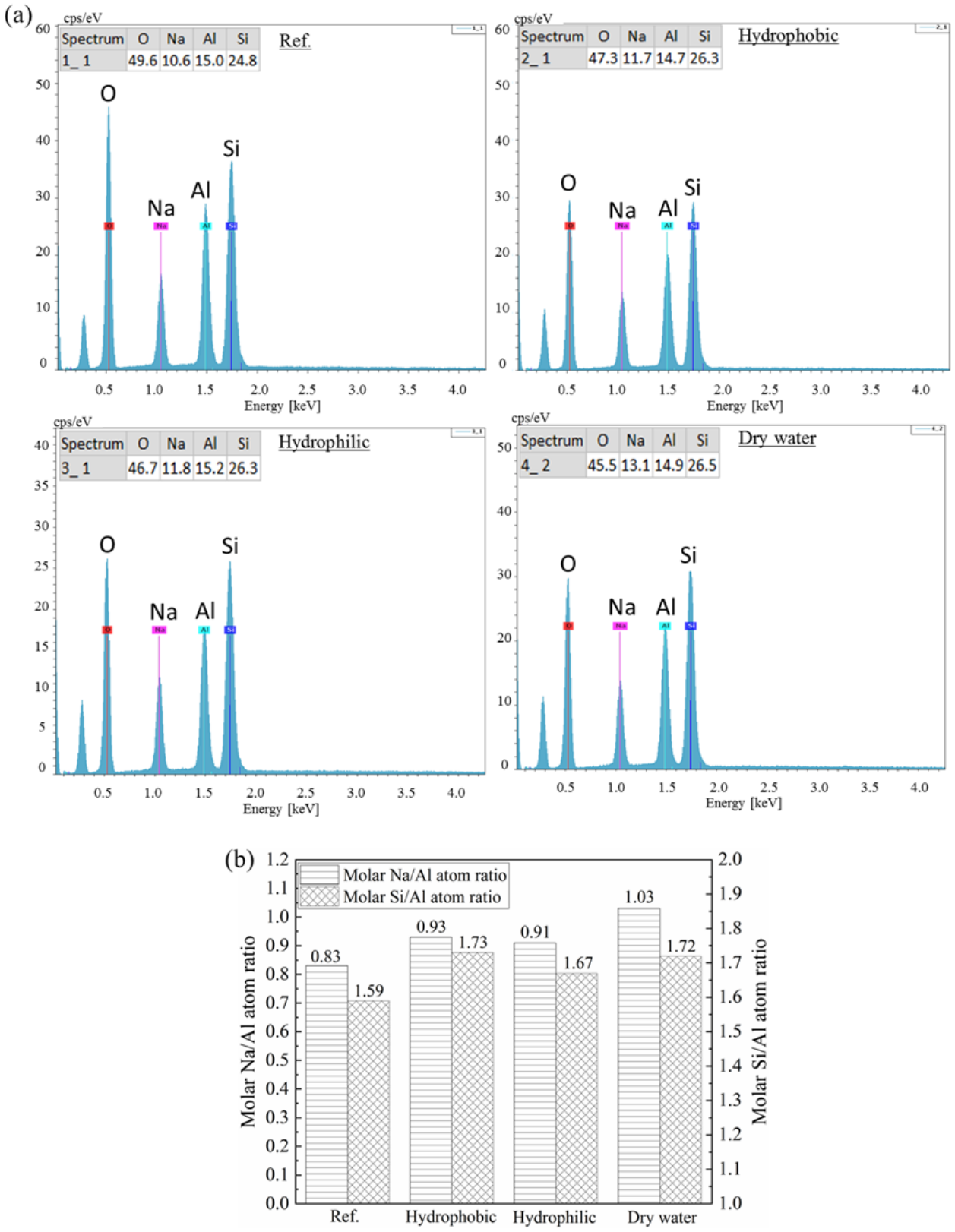


Figure 4.20 (a) EDS patterns and (b) actual molar Si/Al and Na/Al ratios as derived from EDS.

### 4.5. Schematic model of dry water led geopolymerization

Based on the experimental investigations carried out in this study, a schematic model is now proposed to illustrate the enhancement led by dry water upon the alkali-activation of N-A-S-H geopolymer systems. The evolution of a geopolymer system involves a series of physicochemical processes including dissolution, hydrolysis, polycondensation, solidification and hardening. As seen in Figure 4.21, the dry water powders are prepared in advance, by stabilizing water droplets in an encapsulating layer of hydrophobic silica nanoparticles. Due to the particle size coarsening effect in presence of dry water and the excellent flowability of hydrophobic nano silica, the fresh geopolymer system displays superior workability, which in turn makes the fresh mixture homogeneous and aids in its compaction. The water contained in the dry water is deducted from the batched water. As a result, for a fixed compositional ratio, the alkaline concentration in the activator at this stage is temporarily higher than in the design. This higher alkalinity boosts early dissolution of metakaolin, quickly providing the required silicate and aluminate monomers. These processes manifest in a shorter time to final set. Due to their nano-size and amorphous nature, the silica nanoparticles contribute further as the micro-filler to refine the microstructure or/and as the secondary silica source to boost the polycondensation. These are thereafter reflected in the mitigated microcracks, and the higher actual Si/Al and Na/Al ratios reported earlier. All of these processes result in a higher strength and compactness in the hardened system. At the same time, the water gradually released from the dry water restores the alkalinity to the designed value at a later stage. This in turn averts potential damage to the geopolymers formed from excessive alkaline concentration.

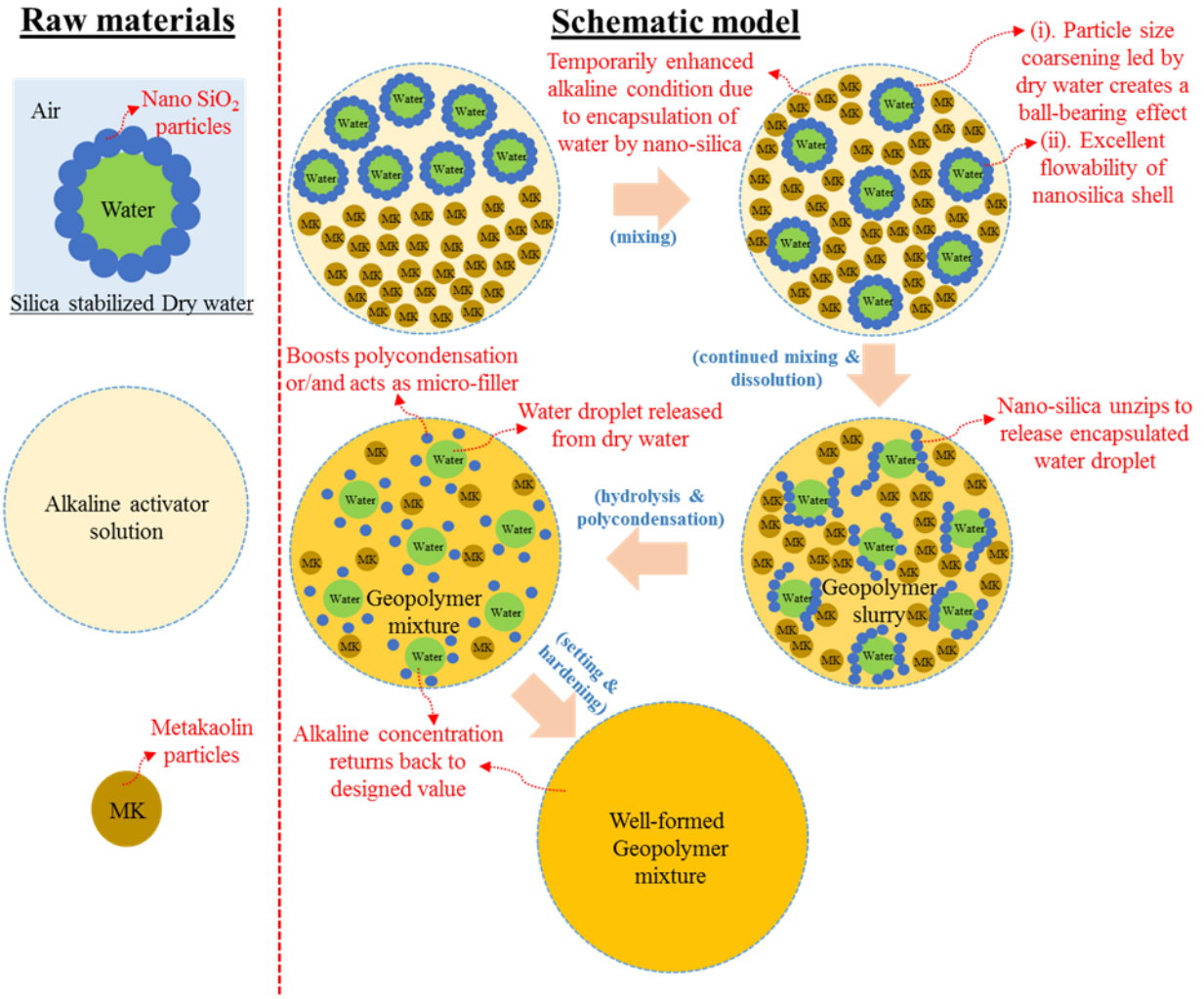


Figure 4.21 Schematic model describing the impact of dry water on the evolving geopolymerization.

### 4.6. Conclusion

This Chapter examined the mechanisms that underlie the geopolymerization of aluminosilicate precursor, as benefiting from the addition of nano silica stabilized dry water. When the silica nanoparticles are added as an admixture to the geopolymer system, the result is higher strength and shorter setting time, but lower flowability. The difference in the water-affinity from the silica nanoparticles has no significant effect on these resulting changes to the geopolymerized system.

On the other hand, only the hydrophobic silica nanoparticles can encapsulate water to form dry water. The dry water acts significantly more favorably upon the geopolymerized system, compared to the silica nanoparticles as is. A combination of thermal, morphological, chemical and microstructural investigations was carried out and a schematic model is presented to explain the enhancement led by dry water upon geopolymerization. Based on the results, the following specific conclusions may be drawn:

(1) Upon stabilizing the water droplets, the hydrophobic silica nanoparticles transform from nanoscale to micron scale particles in dry water. When added to metakaolin, this causes a size coarsening in the precursor. It reduces the water demand, leading to a drop in both viscosity and yield shear stress. This in turn manifests in a superior flow for the fresh paste. Upon continued mixing, the squeezing between solid particles and the mechanical pressure from the mixer result in a gradual release of the encapsulated water, which compensates the liquid-to-solid ratio and leads to a consequent increase in flowability.

(2) Compared with conventional silica nanoparticles when added as is, the silica nanoparticles that accompany dry water, undergo quicker dissolution and boost further polycondensation. Moreover, the encapsulated water droplets in dry water temporarily raise the alkaline concentration, which in turn promotes geopolymerization. Thus, adding dry water shortened the final setting time. This was verified by monitoring the associated rise in temperature, whereby the mixture with dry water showed the highest rate of temperature increase and the highest peak temperature reached throughout the setting process.

(3) It is clear from XRD, TGA and FTIR that, dry water slightly contributes to the amorphicity and the formations of tetrahedral Si as well as Si-O-T band in the N-A-S-H framework. These together impart a higher degree of polycondensation to the geopolymer system. This agrees with

the microstructural chemistry wherein the EDS spectra reveal the highest actual Si/Al and Na/Al ratios for the mixture incorporating dry water. More importantly, adding dry water could yield a superior refinement in microstructure, particularly in reducing the size of microcracks and voids.

(4) Depending on the unique combination of characteristics of size coarsening, micro-filling, supplementary silica source and temporary water encapsulation, the water-in-air Pickering emulsion, also called dry water, resolves the "trade-off" between the fresh and hardened properties of geopolymer systems incorporating nanoparticles.

(5) In preparing the dry water, an optimal ratio was found at 15% nanoparticles-to-emulsion ratio. The resulting dry water led to the most satisfactory combination of high flow diameter, quick final set and superior strength, simultaneously. An excess of silica nanoparticles beyond this optimum did not further benefit these properties significantly.

# Chapter 5. Characterizing effects of compositional oxide ratios on performance of N-A-S-H geopolymers when subjected to sulphuric acid attack

## 5.1. Introduction

As a potential alternative to OPC, geopolymers should register not only superior strength but also adequate resistance to durability concerns. Acid resistance is an important part of durability. As broadly reported, the acid attack occurring in both OPC and geopolymer systems causes irreversible deteriorations, manifesting as significant stiffness and strength losses (Miyamoto et al., 2014; Aiken et al., 2018). Accordingly, the acid resistance of geopolymers essentially governs the lifespan of structural members when served in such a harsh environment (Gutberlet et al., 2015). Also, the maintenance upon these structures increases additional costs on the one hand and, is harmful to the ecological environment and resource conservation on the other hand (Gutberlet et al., 2015). Recently, intensive scientific efforts have been directed to compare the acid resistance of geopolymers with conventional OPC systems. For instance, Vafaei et al. (2018) noted that when subjected to the sulphuric acid condition with a pH of 3, the compressive strength of OPC specimens dropped from 45 MPa to 5 MPa after 12 months, corresponding to a 90% reduction. Whereas the geopolymer system only lost about 48% strength. Qu et al. (2021) also reported that geopolymers even with preloading still performed better than the OPC system. Although the stronger acid resistance has been reported for geopolymers in comparison to conventional OPC systems, chemical-induced deteriorations are still observed. More importantly, such damages appear to evolve with time and accordingly, shorten the service life of structures (Vafaei et al., 2018). This has also become an important factor to constrain the widespread application of geopolymers in practice. Sulphuric acid-induced deterioration is one of the most common issues for cementitious systems. There exist a variety of areas accessible to this aggressive condition,

including sewer systems, industrial estates, mines and backfill areas (Bassuoni et al., 2007; Hewayde et al., 2006; Araghi et al., 2015; Barbhuiya and Kumala, 2017; Wu et al., 2021). Besides, on the walls of geothermal wells, sulphuric acid can also be present through the dissolution of hydrogen sulphide (Pyatina and Sugama, 2016). According to prior studies (Allahverdi and Skvara, 2005; Bakharev, 2005), the sulphuric acid attack occurring in geopolymers starts with the replacement of exchangeable alkali metal ions, i.e., $Na^+$ or $K^+$, by hydrogen ions ($H^+$). Subsequently, the sulphuric acid solution breaks the linkage of principal Si-O-Al bonds that constitute geopolymers, then forming Si-OH and Al-OH groups separately. This process is also named dealumination. As a result, the attacked aluminosilicate network will convert into silicic acid dimers in solution and eventually, manifest in mass and strength losses at the macroscopic level (Bakharev, 2005). In the current literature, a few different variables, such as the source of precursor, the activator type and the alkali content, have been examined when investigating the sulphuric acid resistance of geopolymers. For example, Thokchom et al. noted that although increasing the alkali dosage caused a rise in the mass loss for geopolymers subjected to sulphuric acid attack, the residual compressive strength was increased (Thokchom et al., 2009). Aiken et al. (2018) examined the acid resistance of binary slag-fly ash geopolymers. It was found that the porosity of geopolymer specimens was refined gradually with an increasing slag content, however, the resultant reaction products became more susceptible to sulfuric acid attack. This finding was supported elsewhere (Lee and Lee, 2016). Vogt et al. found that replacing metakaolin with 7.5%~9% silica fume contributed to the formation of silicate-rich geopolymerized structure and in turn, improved the resistance of geopolymers against the sulphuric acid environment (Vogt et al., 2021). Bouguermouh et al. (2017) compared the acid resistance of metakaolin-based (N-A-S-H) geopolymers that were respectively activated by potassium-based and sodium-based activators.

The lowest mass loss was witnessed for the system activated by the potassium-based activator, which was likely attributed to the presence of secondary minerals such as quartz and muscovite. These crystals acted as the filler in the pores and accordingly, hindered the exchange between alkali cations and hydrogen ions.

Despite the superior resistance to acidic conditions frequently being cited as a merit of geopolymers, there remain limitations in understanding the deterioration degree of geopolymers prepared with varying oxide compositions. As aforementioned, the principal reaction product in geopolymers is $Na_n[-(Si-O_2)_z–Al–O]_n \cdot wH_2O$ (N-A-S-H) and more importantly, the degradation of polymerized frameworks under an acidic environment is essentially due to the loss of alkali cations as well as aluminum species. So that, the compositional oxide ratios, i.e., $SiO_2/Al_2O_3$, $Na_2O/Al_2O_3$ and $H_2O/Na_2O$, must play dominant roles in this durability concern. However, there so far exists no information to guide the mixture design to guarantee the maximal acid resistance for N-A-S-H geopolymers. This accordingly constrains the widespread application of geopolymers, particularly in acidic environments. Thus, one primary aim of this study is to clarify the deterioration mechanism of sulphuric acid attack in N-A-S-H geopolymers made with varying chemical compositions. To achieve this objective, three batches of specimens were prepared, with varying $SiO_2/Al_2O_3$, $Na_2O/Al_2O_3$ and $H_2O/Na_2O$ ratios, respectively. In the meantime, a combination of macroscopic, morphological, thermalgravimetric, chemical and microscopic analyses was carried out to experimentally characterize the underlying mechanisms. Moreover, the sensitivities of the sulphuric acid resistance to principal oxide ratios are quantified by a variance-based analysis. It is wished that the outcomes will help guide the mixture design of N-A-S-H geopolymers and in turn, promote its practical application in the acidic environment.

## 5.2. Materials and methods

### 5.2.1. Materials

In this study, a commercially sourced metakaolin was chosen as the aluminosilicate precursor, due to its rich amorphous silica and alumina contents. The detailed chemical compositions are now listed in Table 5.1. Besides, the amorphocity and principal chemical bands were evaluated for this metakaolin, using the X-ray diffractor (XRD) and the Fourier-Transform Infrared spectroscopy (FTIR), respectively. As seen in Figure 5.1(a), a broad and clear hump is centred at $2\theta = 22.5°$, indicating a good amorphocity. Alongside, minor crystals identified as anatase and quartz are detected as well. In the FTIR spectrum shown in Figure 5.1(b), three prominent peaks are observed, which are respectively the Si–O bond in amorphous $SiO_2$ at 1060 $cm^{-1}$, the tetrahedral $AlO_4$ at 792 $cm^{-1}$, and the T-O-T band (T: tetrahedral Si or Al) at 434 $cm^{-1}$.

Table 5.1 The main oxide components of employed metakaolin.

| $SiO_2$ | $Al_2O_3$ | $TiO_2$ | $Fe_2O_3$ | $P_2O_5$ | $Na_2O$ | $K_2O$ | CaO |
|---|---|---|---|---|---|---|---|
| 53.8% | 43.8% | 0.9% | 0.5% | 0.4% | 0.3% | 0.2% | 0.1% |

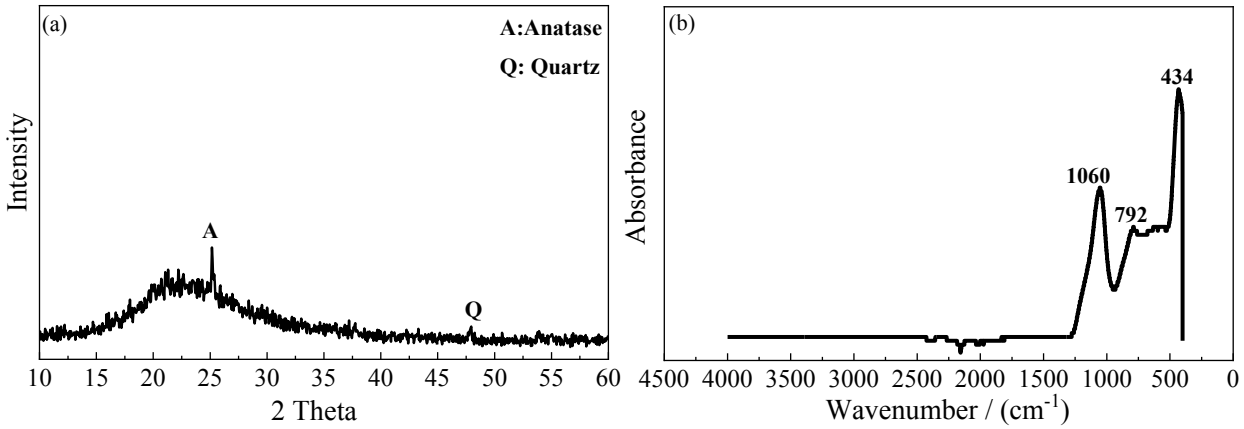


Figure 5.1 (a) XRD and (b) FTIR spectra of employed metakaolin.

The alkali activator was composed of both sodium hydroxide and sodium silicate solution. The sodium hydroxide was sourced as solid pellets with a purity of 99%, while the sodium silicate solution approximately comprised 40% sodium silicate compound and 60% deionized water. The fine aggregates had an oven-dry bulk density of 1570 kg/m$^3$, while the moisture content and water absorption were 0.11% and 1.54%, respectively. The laboratory reagent-grade sulfuric acid containing 95~98% $H_2SO_4$ was blended with deionized water at 1% (w/w) to simulate the acidic environment for the subsequent immersion test. The pH value of the resultant solution was determined using a digital pH meter, corresponding to 0.7 approximately.

### 5.2.2. Sample preparation

In order to satisfy the proposed objectives, three batches of mixtures were designed by adjusting the $SiO_2/Al_2O_3$, $Na_2O/Al_2O_3$ and $H_2O/Na_2O$ molar ratios respectively, as shown in Table 5.2. Note that for each mix, both mortar and paste specimens were produced. The mortar specimens were used to measure the physical and mechanical properties, including the compressive strength, mass and dimension losses, the neutralized depth, and the apparent volume of permeable voids. The respective paste samples were taken for microscopic characterizations such as XRD, TGA, FTIR and SEM-EDS.

Preceding the formal casting, the sodium hydroxide pellets were blended with the sodium silicate solution (SSS) along with extra deionized water to prepare the alkali activator, then followed by 24 hours of cooling in the fume-hood. On the following day, the alkali activator solution was first stirred in the mixing drum for 60 seconds to ensure adequate homogeneity. Then, the solid precursor was added to blend with the activator until the homogeneous paste mixture was observed. Afterwards, the pre-weighed fine aggregates, if needed, were added to produce mortar specimens. The fresh mixture was cast into cylindrical moulds sized as Φ50 mm × 100 mm, then transferred

onto a vibrating table for 30s compaction. 24 hours later, these specimens were demoulded and cured in air-tight plastic bags under ambient conditions for up to 28 days.

Table 5.2 Mix proportions of N-A-S-H geopolymers for sulphuric acid attack.

| $SiO_2$/ $Al_2O_3$ | $Na_2O$/ $Al_2O_3$ | $H_2O$/ $Na_2O$ | Metakaolin (g) | SSS (g) | NaOH (g) | Water (g) | Sand (g) | Liquid/solid | |
|---|---|---|---|---|---|---|---|---|---|
| | | | | | | | | Paste | Mortar |
| 2.2 | 0.9 | 11 | 500 | 51.5 | 148.7 | 350.6 | 1000 | 1.102 | 0.367 |
| 2.8 | 0.9 | 11 | 500 | 321. | 117.8 | 182.2 | 1000 | 1.242 | 0.414 |
| 3.1 | 0.9 | 11 | 500 | 455. | 102.3 | 98 | 1000 | 1.312 | 0.437 |
| 3.4 | 0.9 | 11 | 500 | 590. | 86.9 | 13.8 | 1000 | 1.382 | 0.461 |
| 3.7 | 0.9 | 11 | 500 | 702. | 74.0 | -56.4 | 1000 | 1.441 | 0.480 |
| 3.1 | 0.8 | 11 | 500 | 455. | 85.1 | 55.4 | 1000 | 1.193 | 0.398 |
| 3.1 | 0.9 | 11 | 500 | 455. | 102.3 | 98.0 | 1000 | 1.312 | 0.437 |
| 3.1 | 1.1 | 11 | 500 | 455. | 136.7 | 183.0 | 1000 | 1.551 | 0.517 |
| 3.1 | 1.3 | 11 | 500 | 455. | 171.1 | 268.1 | 1000 | 1.790 | 0.597 |
| 3.1 | 1.0 | 8 | 500 | 455. | 119.5 | 24.5 | 1000 | 1.199 | 0.400 |
| 3.1 | 1.0 | 10 | 500 | 455. | 119.5 | 101.8 | 1000 | 1.354 | 0.451 |
| 3.1 | 1.0 | 12 | 500 | 455. | 119.5 | 179.2 | 1000 | 1.509 | 0.503 |
| 3.1 | 1.0 | 14 | 500 | 455. | 119.5 | 256.5 | 1000 | 1.663 | 0.554 |

### 5.2.3. Sample collections

After reaching 28 days of maturity, the specimens were divided into two series. The first group was tested immediately for various macro-properties and characterizations, serving as the reference. The remaining specimens were immersed in prepared sulphuric acid solutions (1% w/w) for up to 3 months. Note here that the sulphuric acid solution was periodically refreshed every 7 days to ensure sufficient acidity, and the ratio between the solution volume and specimens' surface area was fixed at 10 (Vafaei et al., 2018). At each designed exposure interval, i.e., 4, 8 and 12 weeks, the exposed mortar specimens were retrieved to measure mass, diameter and compressive strength changes, alongside the neutralized depth. To explain the variation observed on the above

macro-properties, powder samples were collected from the respective paste specimens, to conduct further morphological, thermal gravimetric and chemical characterizations.

The exposed specimen was sawn into 6 pieces, as schematically shown in Figure 5.2(a). Then, the 2 endpieces were discarded to eliminate the disturbance from the multi-dimensional penetration. Note here that the later visual inspection upon neutralization also confirmed the degraded depth along one certain direction was significantly smaller than the thickness of 2 endpieces (~20 mm). The remaining 4 slices close to the mid-height plane were used for the subsequent powder collection. To characterize the region where was deteriorated severely, the first layer of powder samples was collected at the region near the exterior edge with a thickness of about 2 mm. Note here that during this powder collection process, 2 slices from the same specimen were placed in a crafted mould. This allows to constrain the slices on the one hand and, avoid unexpected cracking due to the stress concentration during the drilling process on the other hand. The second layer was progressively collected at the deeper location (approximate 4 mm), wherein much less deterioration was expected. The drilling protocol alongside the actual operation is shown in Figure 5.2(b and d).

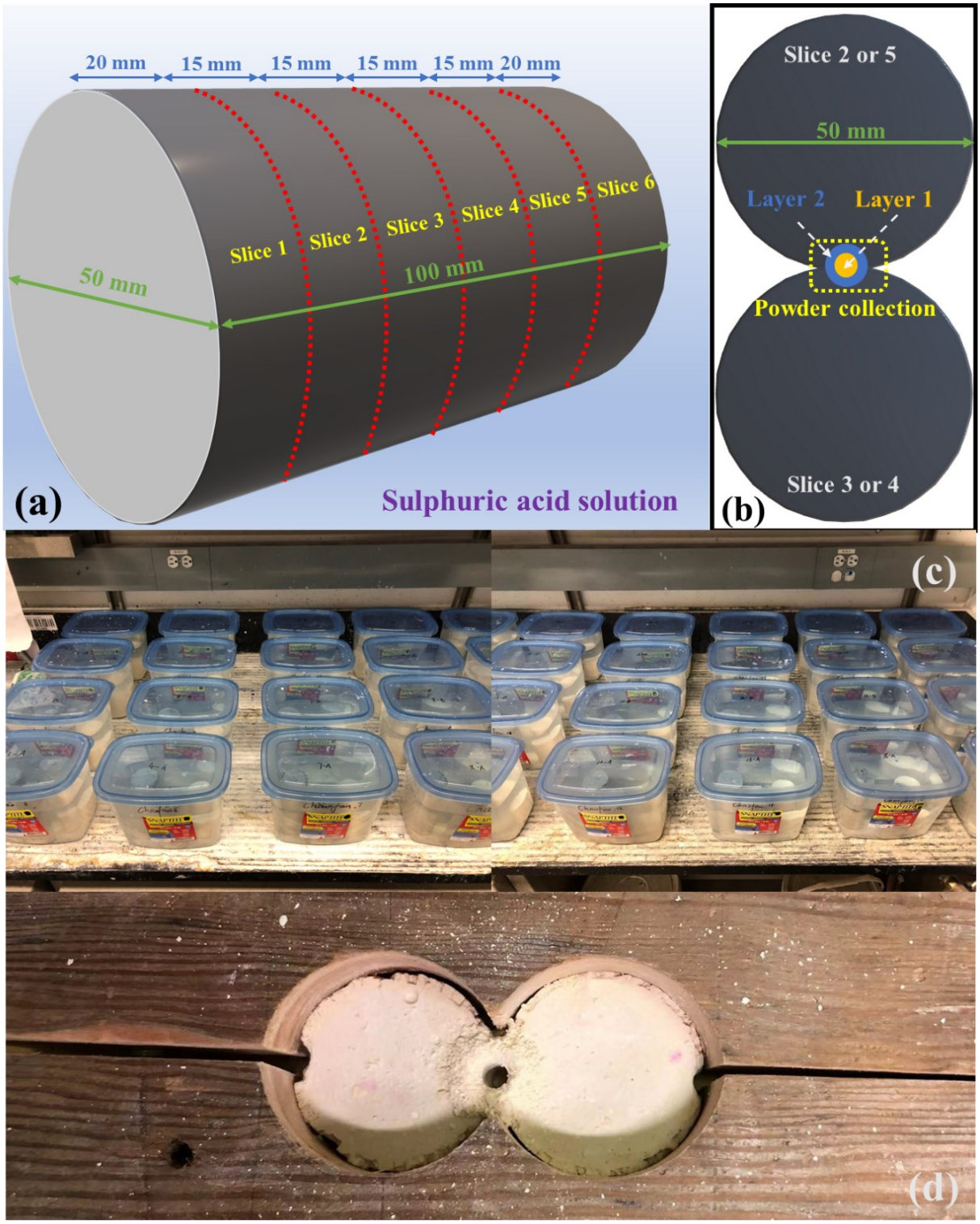


Figure 5.2 Schematic sketches showing (a) slicing, (b) drilling protocols and view of (c) representative specimens immersed in acid solution, and (d) the actual operation for collecting powder samples.

### 5.2.4. Test protocols

The pH value of the external sulphuric acid solution was daily monitored. At each testing interval, i.e., 4, 8 and 12 weeks, the mass and diameter changes were measured immediately, and the compressive strength was tested as per ASTM C39/C39M-18 (2018). The phenolphthalein solution was sprayed onto the surface of the sliced sample, which yielded a deep pink color for the region registering a pH value greater than 9 (Chang and Chen, 2006; Khanet al., 2020). Accordingly, the penetration degree may be computed by dividing the colorless depth by the original diameter. Note here that this value should also consider the part that had fallen off due to the acid-induced deterioration. The alkalinity loss of the geopolymer matrix could also be estimated using the powder suspension method (Räsänen and Penttala, 2004; Khan et al., 2020). In this manner, the powder samples were mixed with distilled water to yield the suspension with a solid-to-liquid ratio of 1. On the following day, the calibrated pH probe was used to measure the pH value of the cooled suspension.

The sulphuric acid attack occurring in cementitious materials is a chemical attack, which essentially involves both diffusion and reaction behaviours. Thus, further characterizations were required, in order to understand the mechanisms underlying the acid-induced deterioration as well as the attendant effects of each oxide ratio on the performance of geopolymers. In this regard, the apparent volume of permeable voids (AVPV) was evaluated, conforming to ASTM C642-13 (2013). In Equation (5.1), $W_s$ refers to the mass of the surface-dry sample in air after immersion and boiling, while $W_a$ indicates the apparent weight of sample in water after immersion and boiling. $W_d$ is the weight of sample after oven-drying at 100 °C for 24 hours.

$$AVPV = \frac{W_s - W_d}{W_s - W_a} \times 100\% \tag{5.1}$$

The X-ray Diffraction (XRD) was carried out to analyze the morphological variation right before and after the sulphuric acid attack, using a Copper-Kα radiation beam (operated at 40kV and 44mA), with a step size of 5°/min, from 10° to 60° diffraction angle (2θ). A Thermogravimetric Analysis (TGA) was conducted in a temperature range of 20~1000°C with a heating rate of 10 °C/min under a nitrogen atmosphere. The chemical bonds constituting geopolymers were examined by the iS50 Fourier-Transform Infrared spectroscopy (FTIR) coupled with a built-in Attenuated Total Reflection (ATR) module. In the following, the obtained FTIR spectra were deconvoluted with Gaussian peak shapes for the range of 800~1250 $cm^{-1}$ (corresponding to the principal Si-O-T band). Representative paste samples from each mixture were placed in a Field Emission Scanning Electron Microscope (FE-SEM) that was coupled with an Oxford Energy Dispersive X-ray Spectroscope (EDS). A 15 kV accelerating voltage resulted in a magnification scale ranging from 300 X to 5000 X. The generated images were then binarized, showing the voids and cracks as the black area and the solid geopolymer gel as fully white. This is subsequently followed by a quantification by counting the black pixels out of the total.

## 5.3. Results and discussion

### 5.3.1. pH evolution of sulphuric acid solution

Figure 5.3 presents the pH evolution of sulphuric acid solution during the immersion of geopolymers made with varying compositional oxide ratios. For all mixes, the pH values of the acid solution increased up to 3.5~4.0 after the first immersion cycle. Over 99% hydrogen ions in sulphuric acid solution had been consumed at this instant. As time elapsed, the maximum pH value at the end of each cycle decreased consecutively, throughout the entire 12 weeks. This implies that the sulphuric acid attack and the attendant leaching behaviour in geopolymers decelerated over time. A similar finding was also observed elsewhere (Aiken et al., 2018; Khan et al., 2020). It is

noted that as compared to the $H_2O/Na_2O$ ratio, varying $SiO_2/Al_2O_3$ and $Na_2O/Al_2O_3$ ratios generate a stronger influence on the neutralization rate of the acid solution. As for the $SiO_2/Al_2O_3$ ratio, an increase from 2.2 to 3.4 was found to alleviate the neutralization obviously. As evident, the neutralization potential decreased from 95.1% (pH=2.01) to 82.6% (pH=1.46) at the end of 12$^{th}$ immersion cycle, as per Equation (5.2). However, the further increase in this ratio from 3.4 to 3.7 did not slow down the neutralization rate significantly, see Figure 5.3(a). With regard to the $Na_2O/Al_2O_3$ ratio, the mixture made with the higher value consumed more hydrogen ions. Up to 12 weeks of exposure, the neutralization potential dropped from 94.6% (pH=1.97) to 81.4% (pH=1.43), as the $Na_2O/Al_2O_3$ ratio decreased from 1.3 to 0.8. This means that increasing the nett amount of alkali cations does not correspond to an absolute improvement in the acid resistance of geopolymers. Decreasing the $H_2O/Na_2O$ ratio from 14 to 8 was observed to favour the resistance to sulphuric acid attack, manifesting as a reduction in the neutralization potential from 89.5% (pH=1.68) to 86.5% (pH=1.57) at the 84$^{th}$ days of exposure.

$$P_n = (1 - 10^{c_1 - c_2}) \times 100\% \tag{5.2}$$

Wherein, $P_n$ represents the neutralization potential. $c_1$ denotes the initial pH value of the sulphuric acid solution, while $c_2$ is the instant pH value of the sulphuric acid solution as the attack progresses.

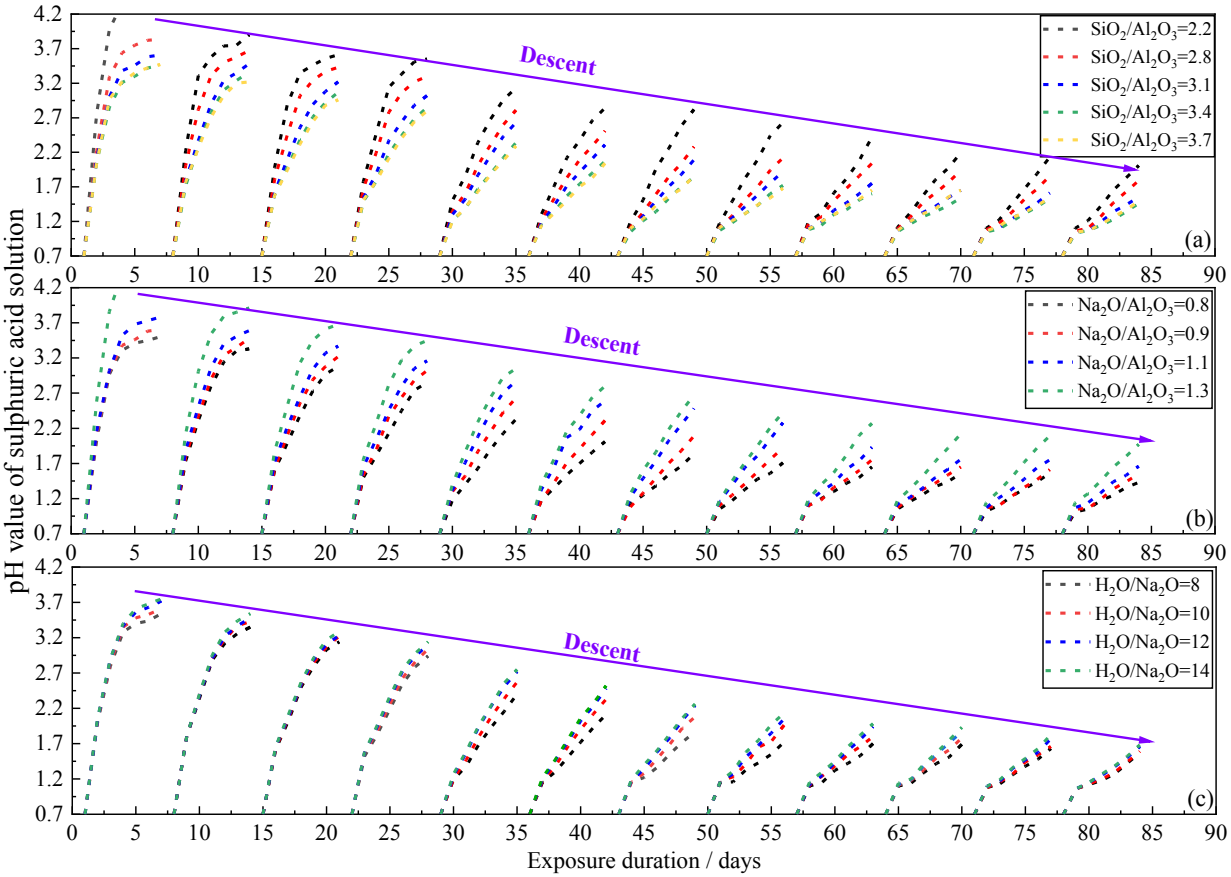


Figure 5.3 pH evolution of the sulphuric acid solution during the immersion of geopolymers made with varying (a) $SiO_2/Al_2O_3$, (b) $Na_2O/Al_2O_3$ and (c) $H_2O/Na_2O$.

### 5.3.2. Alkalinity loss of geopolymers

Strong alkalinity is an important characteristic of cementitious materials, as it maintains the chemical stability of reaction products on the one hand and, avoids the corrosion of embedded reinforcement by forming the passivation film on the other hand (Garcés et al., 2005). In this study, the alkalinity of geopolymer paste was approximately determined, using the powder suspension method. For all mixes, the initial alkalinity of the hardened specimen was found as 12.3±0.2, and this value agreed well with other studies (Khan et al., 2020). After the sulphuric acid attack, the remaining alkalinity at varying depths inside geopolymers was evaluated, as presented in Figure 5.4. Clearly, the alkalinity of all examined geopolymers decreased substantially over time. More

importantly, the corresponding value could drop down to 7 or even shifted toward the acidic range. For a certain depth, increasing the $SiO_2/Al_2O_3$ ratio from 2.2 to 3.4 was found to alleviate the alkalinity loss of the geopolymer matrix, whereas the further increase beyond this value caused an unexpected rise. The higher $SiO_2/Al_2O_3$ ratio has been widely reported to boost the geopolymerization degree by extending the length of aluminosilicate oligomer chains (De Silva et al., 2007). However, a continuous increase in this ratio will also introduce more liquid contents into the mixture, which may be detrimental to the ensuing evolution of the microstructure. Hence, there may exist an optimal $SiO_2/Al_2O_3$ value for geopolymers to achieve the maximal acid resistance. A decrease in both $Na_2O/Al_2O_3$ and $H_2O/Na_2O$ ratios was noted to relieve the alkalinity loss of geopolymers against the acidic environment, as evident from Figure 5.4(b-c). In prior studies, the smaller $Na_2O/Al_2O_3$ ratio was found to yield a higher degree of geopolymerization (Rovnaník, 2010). And, lowering the $H_2O/Na_2O$ ratio essentially corresponds to the enhanced alkalinity of the activator. Also, the lower these two ratios, the smaller the liquid-to-solid ratio and likely, the denser texture of geopolymer networks. Given the above, it may not be surprising to observe the alleviated alkalinity loss when decreasing these two ratios.

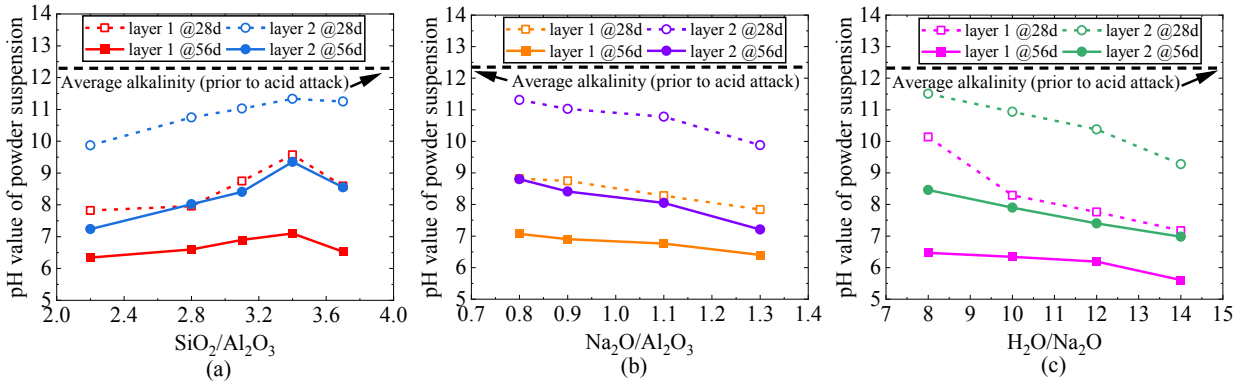


Figure 5.4 Effects of (a) $SiO_2/Al_2O_3$, (b) $Na_2O/Al_2O_3$ and (c) $H_2O/Na_2O$ ratios on the remaining alkalinity of geopolymer powders after sulphuric acid attack.

Phenolphthalein was also used as an indicator to conduct the visual inspection upon geopolymers after sulphuric acid attack. The representative images are presented in Figure 5.5. By computing the proportion of neutralized depth in terms of the original diameter, the effective penetration degree could be determined, as shown in Figure 5.6. Clearly, regardless of exposure durations, the smallest penetration degree was respectively seen on the mixture made with a $SiO_2/Al_2O_3$ of 3.4, a $Na_2O/Al_2O_3$ of 0.8 and a $H_2O/Na_2O$ of 8 in their respective series.

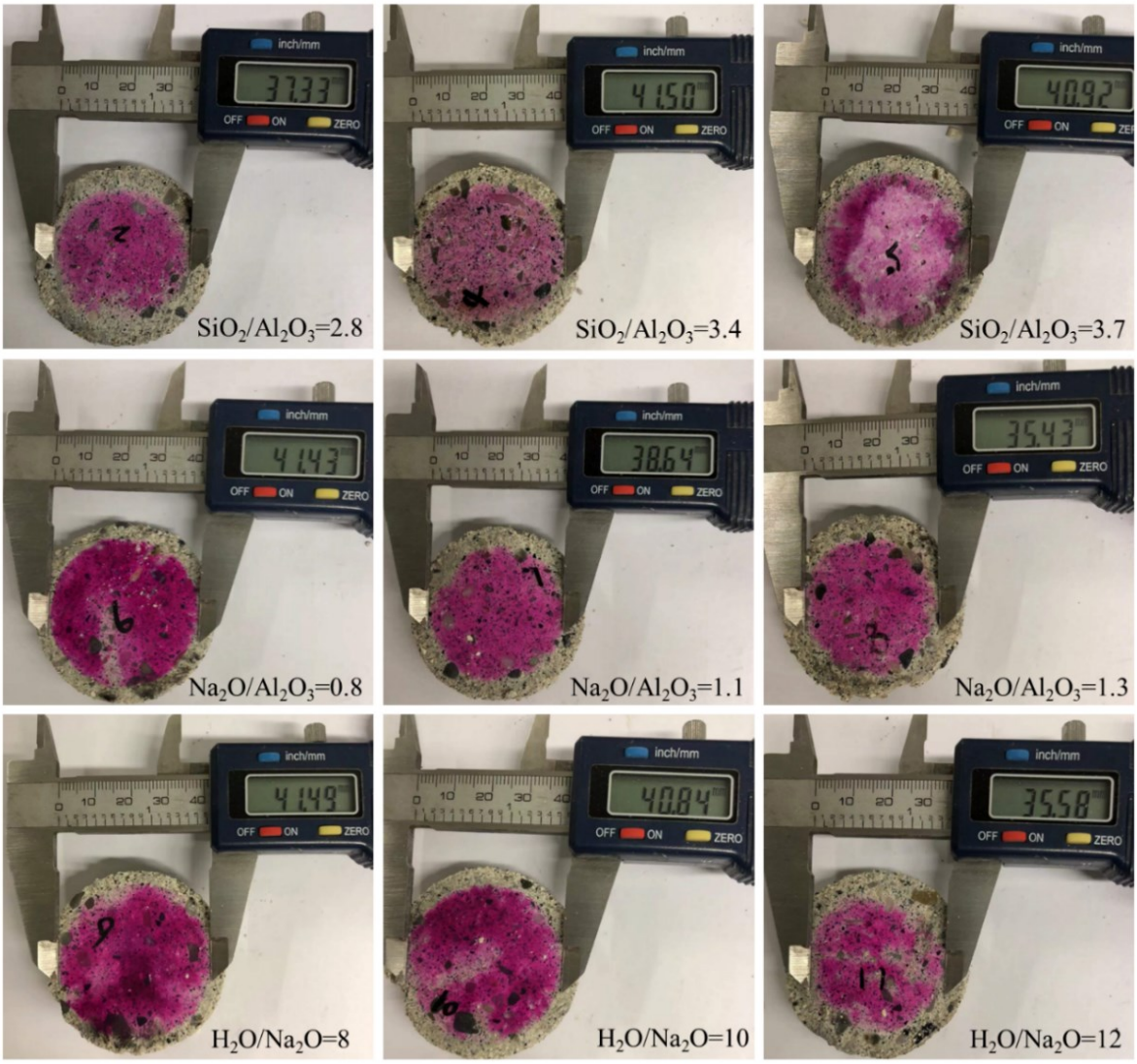


Figure 5.5 Representative images of visual inspection upon geopolymer mortars after 12 weeks of sulphuric acid attack.

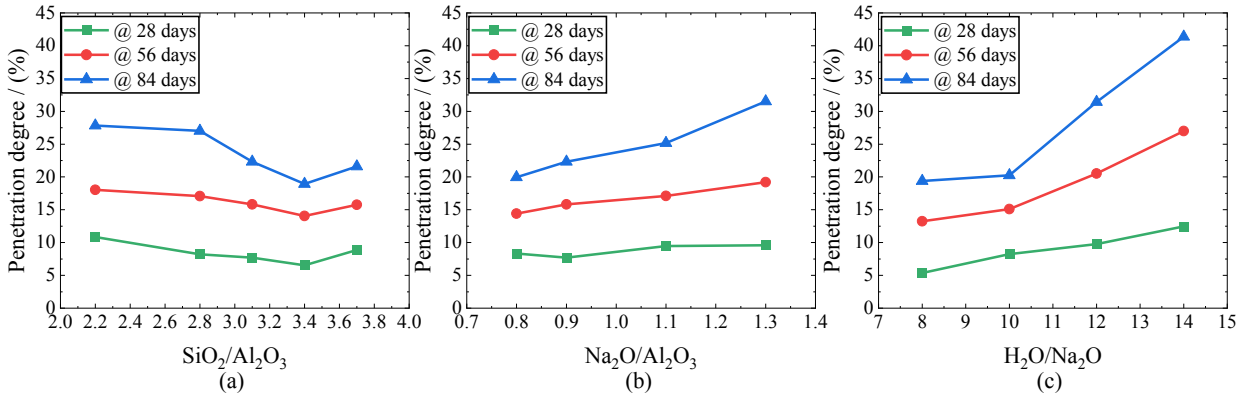


Figure 5.6 Effects of (a) $SiO_2/Al_2O_3$, (b) $Na_2O/Al_2O_3$ and (c) $H_2O/Na_2O$ ratios on acid penetration degree in geopolymers.

### 5.3.3. Changes in mass, diameter and compressive strength

The sulphuric acid attack occurring in geopolymers will replace the exchangeable metal cations and trigger the dealumination of polymerized aluminosilicate frameworks. The above process macroscopically reflects noticeable losses in mass, size and mechanical strength of geopolymers. Figure 5.7 presents the mass and diameter changes of each mix when subjected to the sulphuric acid attack for up to 12 weeks. As seen therein, raising the $SiO_2/Al_2O_3$ ratio from 2.2 to 3.4 alleviates mass and diameter losses. Any further increase beyond 3.4 is however not beneficial. Once again, this trend may be explained through the competition between the enhanced geopolymerization degree and the enlarged liquid-to-solid ratio. In this regard, when the $SiO_2/Al_2O_3$ ratio is smaller than the optimal value, i.e., 3.4 found here, the benefit led by the improved geopolymerization degree governs. Instead, the negative influence due to the increased liquid content becomes dominant. Nevertheless, it is interesting to note from Figure 5.8(a) that, the mixture made with the $SiO_2/Al_2O_3$ ratio of 3.7 registers the maximum compressive strength, even after 84 days of exposure. This is mainly due to that its initial compressive strength was significantly higher than all the other four mixes. However, by computing the difference between

the initial and the remaining values after a long exposure duration (84 days), the mixture incorporating a $SiO_2/Al_2O_3$ ratio of 3.7 is found here to have a slightly greater percentage of strength loss than the other two made with 3.1 and 3.4 respectively. This may imply that the mixture incorporating an excessive $SiO_2/Al_2O_3$ ratio is likely to experience a relatively quick strength loss as the sulphuric acid attack progresses.

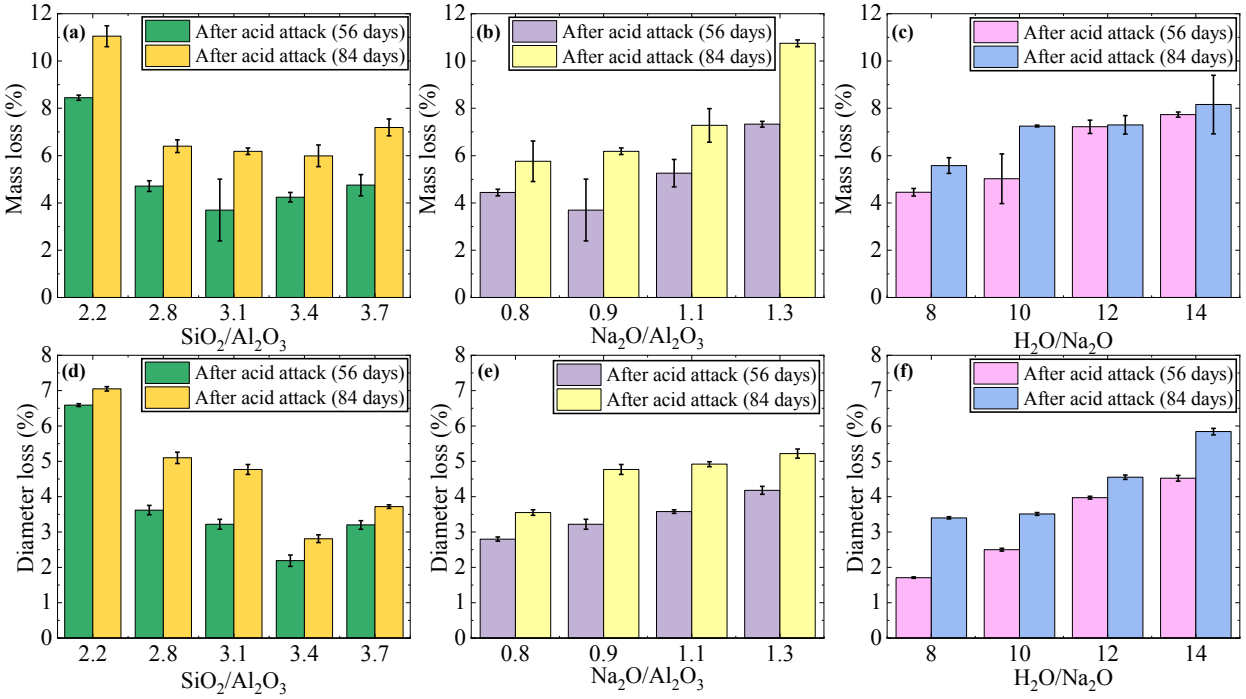


Figure 5.7 Mass and diameter losses of geopolymers after sulphuric acid attack.

As expected, an increase in either the $Na_2O/Al_2O_3$ ratio or the $H_2O/Na_2O$ ratio suffered more deterioration from the sulphuric acid attack. This is evident from the greater mass and diameter losses shown in Figure 5.7, and the lower remaining compressive strength alongside the larger reduction degree illustrated in Figure 5.8. Further, it is clear to see that when the $Na_2O/Al_2O_3$ ratio reaches up to 1.1 or the $H_2O/Na_2O$ ratio goes up to 14, the associated mixtures register significantly large percentages of loss of compressive strength. This may suggest that when served in an acidic

environment, the $Na_2O/Al_2O_3$ and $H_2O/Na_2O$ ratios must be controlled within a suitable value for N-A-S-H geopolymers, here recommended as 0.9 and 12 respectively.

As summarized above, the optimal combination of compositional ratios against sulphuric acid attack may be concluded as $SiO_2/Al_2O_3$=3.1~3.4, $Na_2O/Al_2O_3$=0.8~0.9 and $H_2O/Na_2O$=8~10. On the other hand, some numerical studies directed toward the compressive strength of intact N-A-S-H geopolymers suggested the optimized $SiO_2/Al_2O_3$, $Na_2O/Al_2O_3$ and $H_2O/Na_2O$ ratios respectively as 3.6~3.8, 1.0~1.2, and 10~11 (Aboutalebi et al., 2010).

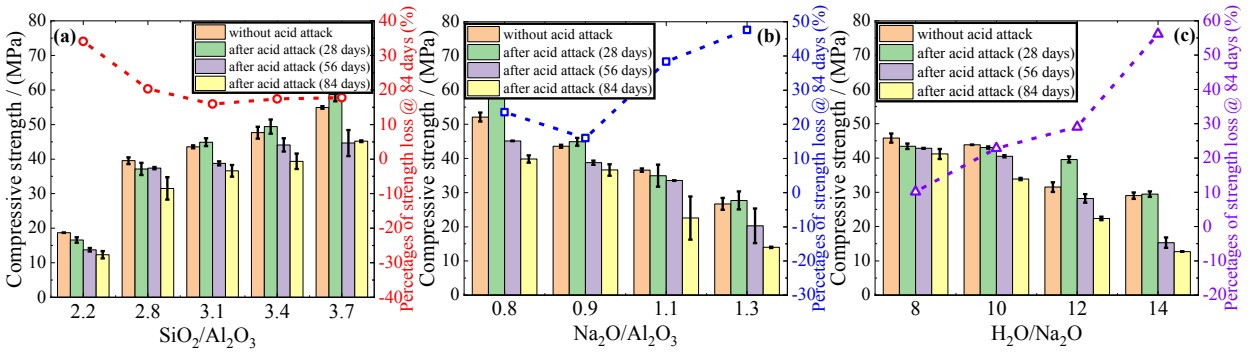


Figure 5.8 Compressive strength of geopolymers right before and after sulphuric acid attack.

### 5.3.4. Apparent volume of permeable voids

The porous character of cementitious systems determines that the associated structural members are detrimental to those aggressive ions in external environments. The external sulphuric acid attack essentially involves both physical diffusion and chemical reaction behaviours. The apparent volume of permeable voids (AVPV) indicates the capacity of cementitious materials to resist the penetration of aggressive ions from the exterior (Zhang and Zong, 2014). In the mature state but prior to the sulphuric acid exposure, geopolymers made with varying mixing proportions were tested for this parameter, as shown in Figure 5.9. Clearly, as the $SiO_2/Al_2O_3$ ratio increases through 2.2 and to 3.7, the AVPV of geopolymers experiences a noticeable drop and reaches the optimal

at the $SiO_2/Al_2O_3$ ratio of 3.4, then followed by a slight rise for the subsequent increase up to 3.7. Note here that this trend is consistent with results in terms of losses on alkalinity, mass, diameter and compressive strength presented in Figures 5.6~5.8. It is well established that the higher $SiO_2/Al_2O_3$ ratio usually corresponds to the higher polycondensation degree of N-A-S-H frameworks and accordingly the greater initial strength (De Silva et al., 2007). However, the results obtained here may suggest that the acid-induced deteriorations upon geopolymers depend on not only the degree of geopolymerization but also the evolution of the pore structure. In the case of $Na_2O/Al_2O_3$ ratio, the lowest AVPV is found for the mixture made with a value of 0.8~0.9. The mixtures incorporating a $Na_2O/Al_2O_3$ ratio beyond 1 experienced a considerable increase in the AVPA. As well, the monotonic rise in the AVPA is observed when increasing the $H_2O/Na_2O$ ratio from 8 to 14. The above phenomena are likely attributed to the enlarged liquid-to-solid ratio and water content while increasing $Na_2O/Al_2O_3$ and $H_2O/Na_2O$ ratios, as evident from Table 5.2. As well documented, the higher liquid content usually causes the worse pore structure for hardened cementitious systems (Monteiro, 2006).

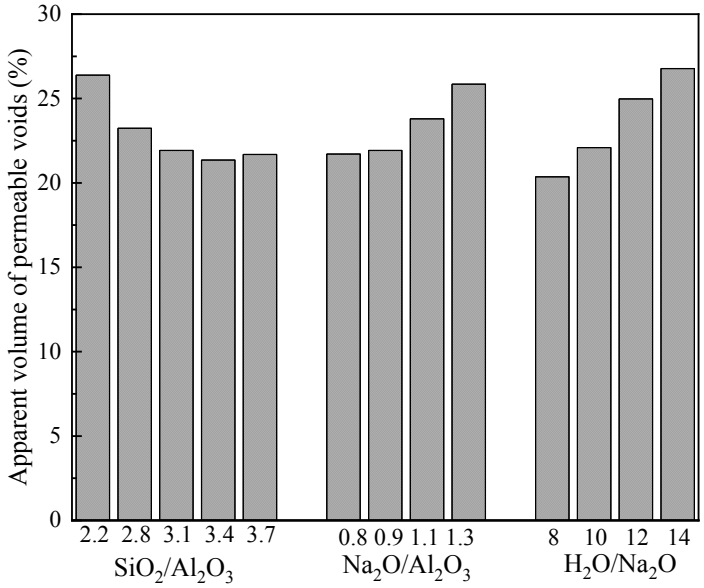


Figure 5.9 The apparent volume of permeable voids of geopolymers prior to sulphuric acid attack.

### 5.3.5. X-ray diffraction (XRD)

The XRD diffractograms of representative geopolymers right before and after the sulphuric acid attack are illustrated in Figure 5.10. According to Figure 5.10(a), the aluminosilicate precursor activated with an over-low $SiO_2/Al_2O_3$ ratio, i.e., 2.2, displays an insufficient amorphocity. This is evident firstly from numerous crystals including Faujasite (F), Anatase (A), Na-Chabazite (C), Hydroxysodalite (S) and Quartz (Q) and secondly, from the vague shape of the diffuse hump centred at about 28.5º of 2θ. As the $SiO_2/Al_2O_3$ ratio increases through 2.8 and to 3.7, the clear diffuse hump ascribed to the N-A-S-H framework evolves, alongside the obvious disappearance of the above "crystal impurities". This may be attributed to that the increasing amorphous silica boosts the formation of aluminosilicate oligomers. Figure 5.10(b and c) presents the XRD spectra for the respective exposed samples that were respectively collected at different layers. Interestingly, the diffuse hump of samples located at layer 1 all shift toward the lower end, including the mix incorporating a $SiO_2/Al_2O_3$ ratio of 2.2. More importantly, no visually detectable difference is witnessed. Taken together, it may indicate the following: (i) the geopolymer matrix suffering from the acidic environment will experience a reduction in the amorphocity, due to the dealumination of N-A-S-H networks as the attack progresses; (ii) once the aluminosilicate frameworks are depolymerized completely, any further acid exposures will no longer affect the amorphocity; (iii). zeolitic crystals formed in the case of low geopolymerization may also be susceptible to sulphuric acid attack. With regard to layer 2, the associated XRD spectra are mutually comparable. One sees from Figure 5.10(c) that, the diffuse hump for the mixture made with the higher $SiO_2/Al_2O_3$ ratio shifts toward the smaller end of 2θ with a lesser extent. This indicates that the associated mixture registered a higher remaining amorphocity. As seen from Figure 5.10(d), increasing the $Na_2O/Al_2O_3$ ratio of geopolymers from 0.8 to 1.3 reflects a prominent shift in the diffuse hump,

from 28.7º to 27.4 º in 2θ. This suggests the depressed amorphocity, and also explains the lowered compressive strength for geopolymers in their mature states without any sulphuric acid immersion (see Figure 5.8(b)). As for the exposed samples, no obvious difference is detected for the series of layer 1. Whereas, the XRD patterns captured at the deeper location are mutually comparable, see Figure 5.10(f). In this regard, as the $Na_2O/Al_2O_3$ ratio raises from 0.8 to 1.3, the center of the corresponding diffuse hump moves from 27.4º to 25.7º in 2θ. More importantly, the change in 2θ right before and after the acid attack is determined as 1.3º for the mixture of $Na_2O/Al_2O_3$ =0.8 and 1.7º for the mixture of $Na_2O/Al_2O_3$ =1.3, respectively. This may illustrate that the former lost less amorphocity than the latter within the same exposure durations. Also, the above XRD results agree with those findings reported in Figures 5.6~5.8. In Figure 5.10(g), very minor difference could be found between the unexposed samples incorporating varying $H_2O/Na_2O$ ratios. Connecting to the initial compressive strength shown in Figure 5.8(c), it suggests that varying this ratio may generate a stronger influence on other characteristics such as the pore structure, in comparison to the amorphocity. As the sulphuric acid attack progressed, the region suffering from the acid attack lost more amorphocity when a larger $H_2O/Na_2O$ ratio was designed, as evident from Figure 5.10(i).

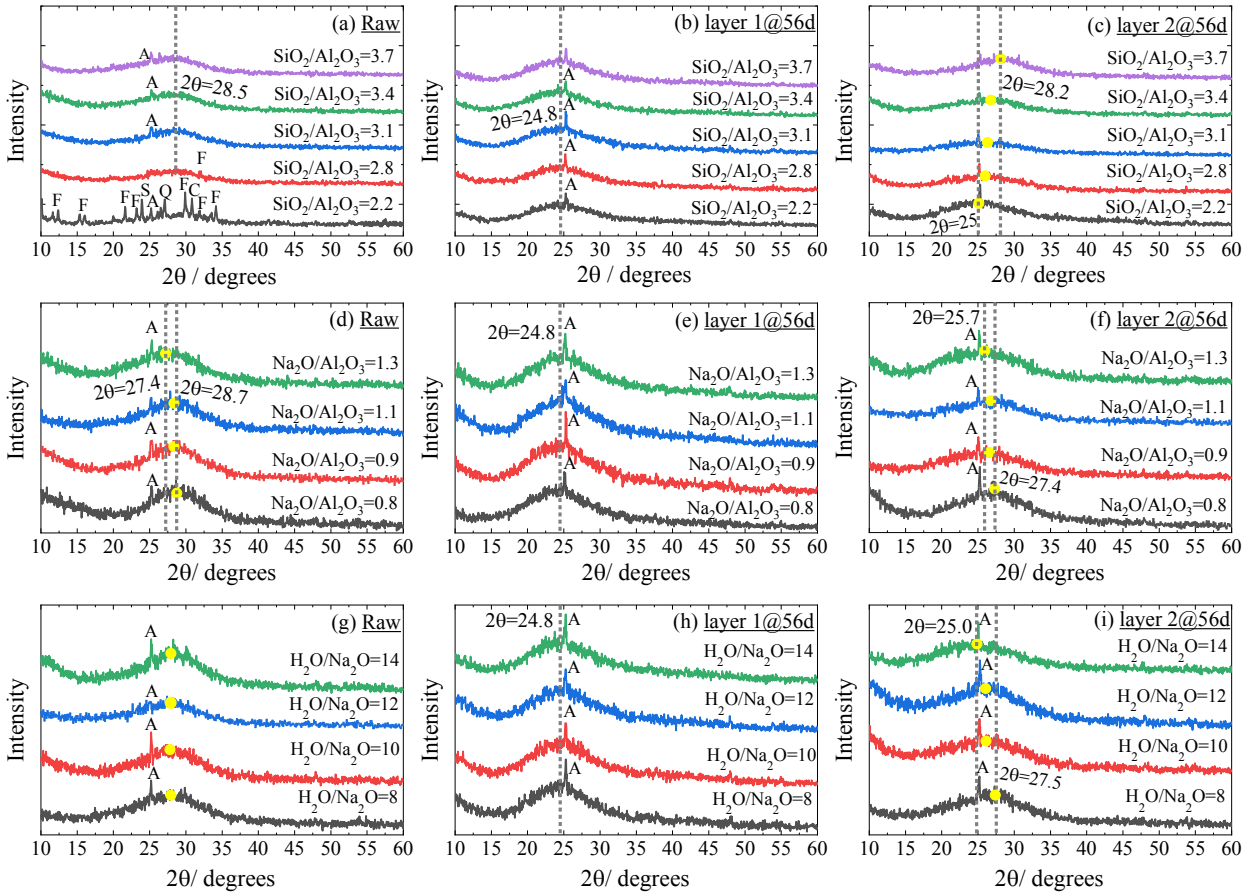


Figure 5.10 XRD outcomes for geopolymers right before and after sulphuric acid attack.

### 5.3.6. Thermogravimetric analysis (TGA)

The TGA curves of examined geopolymers right before and after sulphuric acid attack are plotted in Figure 5.11. As widely reported, the principal weight loss is usually witnessed as heating from room temperature (~22 °C) to 300 °C, due to the evaporation of free water and the chemically bound water constituting N-A-S-H frameworks (Tchakouté et al., 2017; da Silva Rocha et al., 2018). Prior to the sulphuric acid immersion, a relatively minor difference is noted among the thermalgravimetric curve of various geopolymers. As the acid attack progresses, their mutual differences appear to evolve, as evident from Figure 5.11. According to the principal chemical equation involved in the polycondensation shown in Figure 5.12 (Davidovits, 2008), the side

functional group in the aluminosilicate oligomer chain are silanes that register more hydroxyls in comparison to the intermediate tetrahedral Si and Al groups. However, as the sulphuric acid attack dealuminates the aluminosilicate framework and releases out the connected Al-OH groups, the relative proportion of hydroxyls carried in the side silanol groups increases accordingly. In addition, a part of water will be formed during the formation of the silicious framework as the sulphuric acid attack progresses. These above may together explain the intensified DTG peak witnessed between 20~300 °C after the sulphuric acid immersion. Through computing this thermal gravimetric variation, the degree of acid-induced deterioration may be compared between various geopolymers, as presented in Figure 5.13. Clearly, the mixture made with a $SiO_2/Al_2O_3$ of 3.4 once again displays the minimal variation in the respective series. This may be mutually supportable with previous XRD results. As for $Na_2O/Al_2O_3$ and $H_2O/Na_2O$ ratios, reducing their values is both noted to alleviate the thermal gravimetric variation related to the N-A-S-H framework.

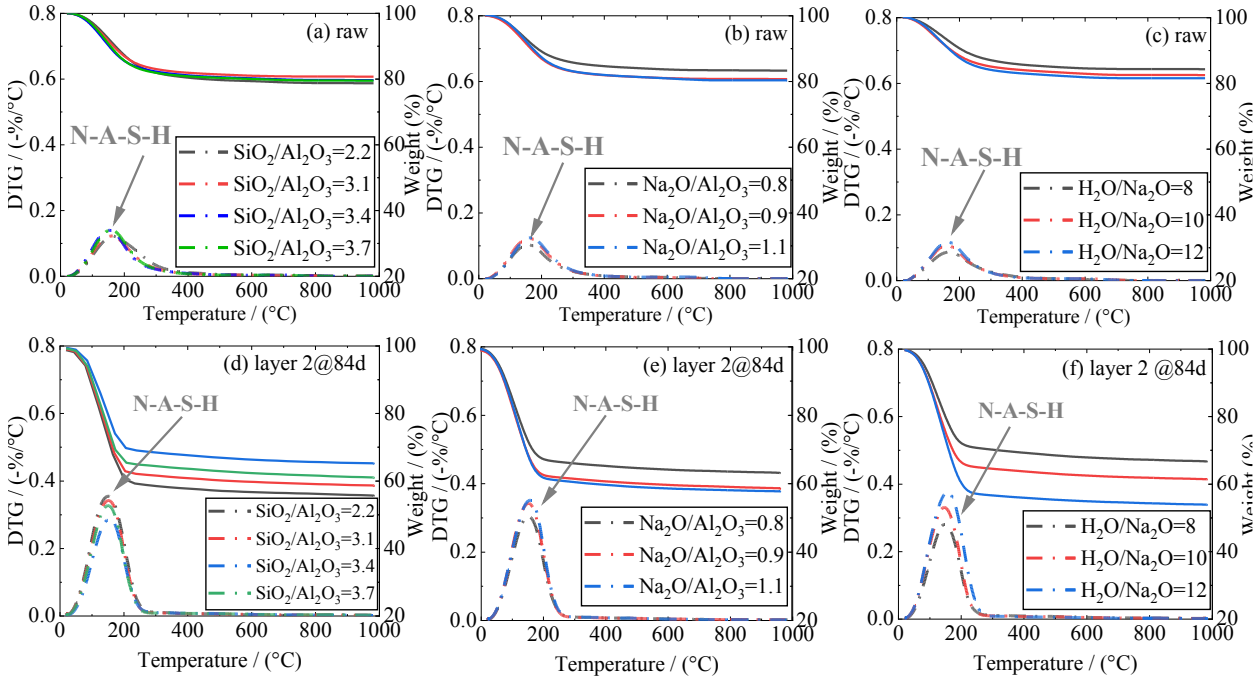


Figure 5.11 TGA outcomes for geopolymers right before and after sulphuric acid attack.

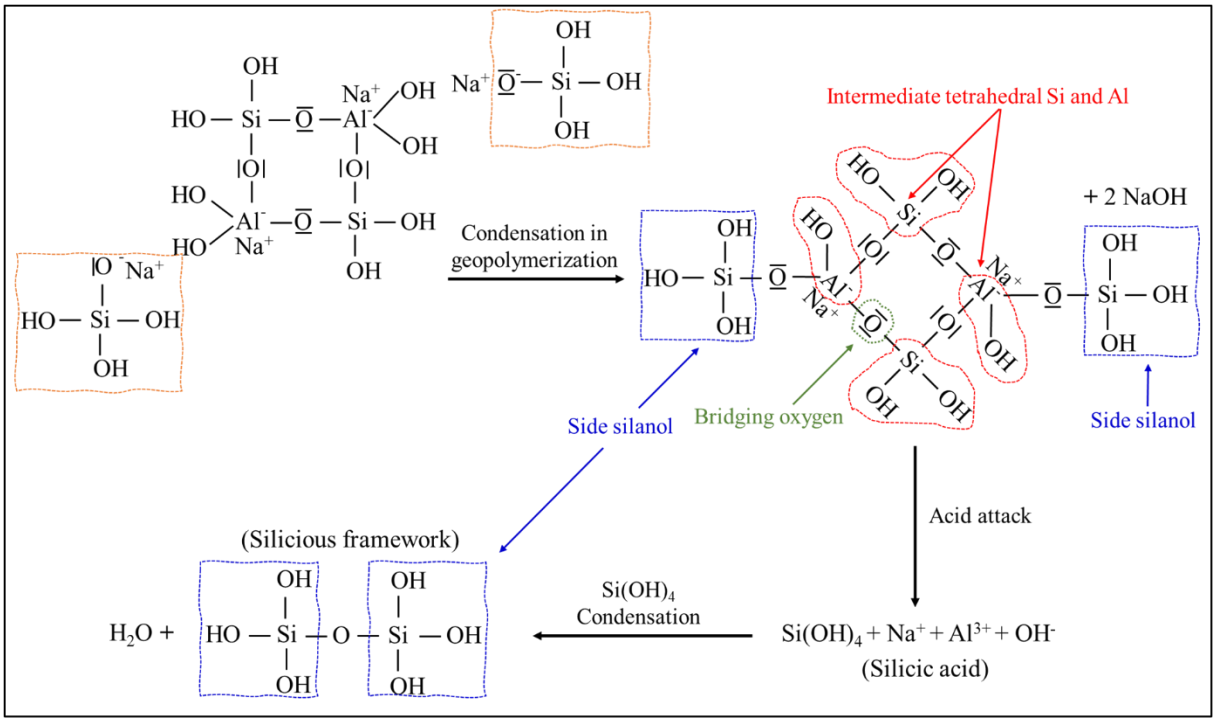


Figure 5.12 The polycondensation involved in the production of N-A-S-H geopolymers.

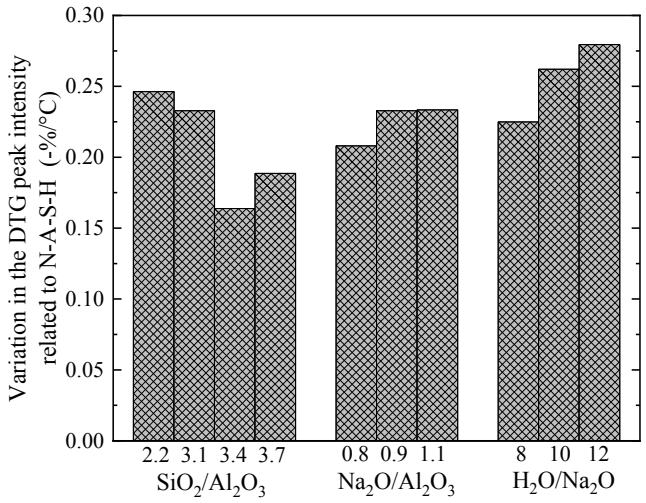


Figure 5.13 Variation in the DTG peak intensity between 20~300 °C after sulphuric acid immersion.

### 5.3.7. Fourier transform infrared spectroscopy (FTIR)

According to previous XRD results, the region near the exterior surface may be deteriorated

completely within the designed exposure duration and accordingly, no obvious difference was detected. Therefore, besides the unexposed samples, only the exposed powders collected at layer 2 were examined in the FTIR characterization. As seen in Figure 5.14, the minor band detected at 560~570 $cm^{-1}$ is ascribed to the external linkage vibrations of the $TO_4$ in the double rings of zeolite (Zhang et al., 2012). The most prominent peak is noted between 800~1300 $cm^{-1}$, connected to the asymmetric stretching vibrations of the polymerized band 'Si-O-T', (Chen et al., 2019; Li et al., 2019). Here, 'T' indicates the 4-coordinated silicon or aluminum atoms. More importantly, the degree of geopolymerization is widely recognized to be associated with the shift of this band (Li et al., 2019). Further, other minor bands positioned at ~1645 $cm^{-1}$ and ~3370 $cm^{-1}$ are attributed to the vibrations of H–O–H and –O–H, both implying the presence of chemically bound water in the reaction products (Zhang et al., 2012). Figure 5.14(a-c) illustrates the FTIR spectra for geopolymers prior to sulphuric acid immersion, while Figure 5.14(d-f) shows the respective case after sulphuric acid attack. For starters, either increasing the $SiO_2/Al_2O_3$ ratio or decreasing the $Na_2O/Al_2O_3$ ratio is seen to noticeably favour the degree of geopolymerization for unexposed specimens, as evident from the noticeable increase in the wavenumber of the principal Si-O-T band. By contrast, varying the $H_2O/Na_2O$ ratio causes a very minor difference in this regard.

The sulphuric acid attack upon geopolymers appears to trigger the dealumination upon polymerized aluminosilicate frameworks and afterwards, the aluminum atoms are mostly leached out to the exterior (Zhang et al., 2016). Also, the peak of the S-O bond locates within the range of the Si-O-T band in the FTIR spectrum. But the center of the former is about 1070 $cm^{-1}$ (Qu et al., 2021), which is slightly higher than the latter (~960-1000 $cm^{-1}$ noted here). Given the above, the overall peak assigned to the Si-O-T band was widely found to shift toward the higher end of the wavenumber after sulphuric acid immersion (Zhang et al., 2016; Wu et al., 2021). This

phenomenon was also witnessed in the present study, see Figure 5.14. The wavenumber difference in terms of the principal Si-O-T band right before and after sulphuric acid attack is computed in Figure 5.15. As expected, the mixture made with $SiO_2/Al_2O_3$=3.4 displays the smallest shift in terms of the Si-O-T band after sulphuric acid immersion. This is mutually supportable with the corresponding XRD results (in Figure 5.10), and also explains the least deterioration seen in previous physical and mechanical tests. Further, it is interesting to note that the mixture incorporating a $SiO_2/Al_2O_3$ of 2.2 experienced the second least shift across five examined specimens, ranking only behind the optimal case of 3.4. Recall earlier, the mixture made with the lowest $SiO_2/Al_2O_3$ ratio was found to contain numerous crystals and also displayed extremely low amorphocity in the previous XRD evaluation. That may imply its polymerized aluminosilicate amount was considerably less than the other four mixes. As a result, the corresponding Si-O-T band in the FTIR spectrum is likely to show a relatively small shift after sulphuric acid immersion. With regard to the two $Na_2O$-involved ratios, one sees from Figure 5.15 that increasing either of them boosts the acid-induced shift associated to the principal Si-O-T band. This justifies that the geopolymer system made with the larger $Na_2O/Al_2O_3$ or/and $H_2O/Na_2O$ ratios will deteriorate more substantially when subjected to the sulphuric acid attack. In the former case, it may be collaboratively due to the depressed degree of geopolymerization alongside the degraded pore structure. While in the latter case, the evolving deterioration is mainly attributed to the enlarged content of permeable voids.

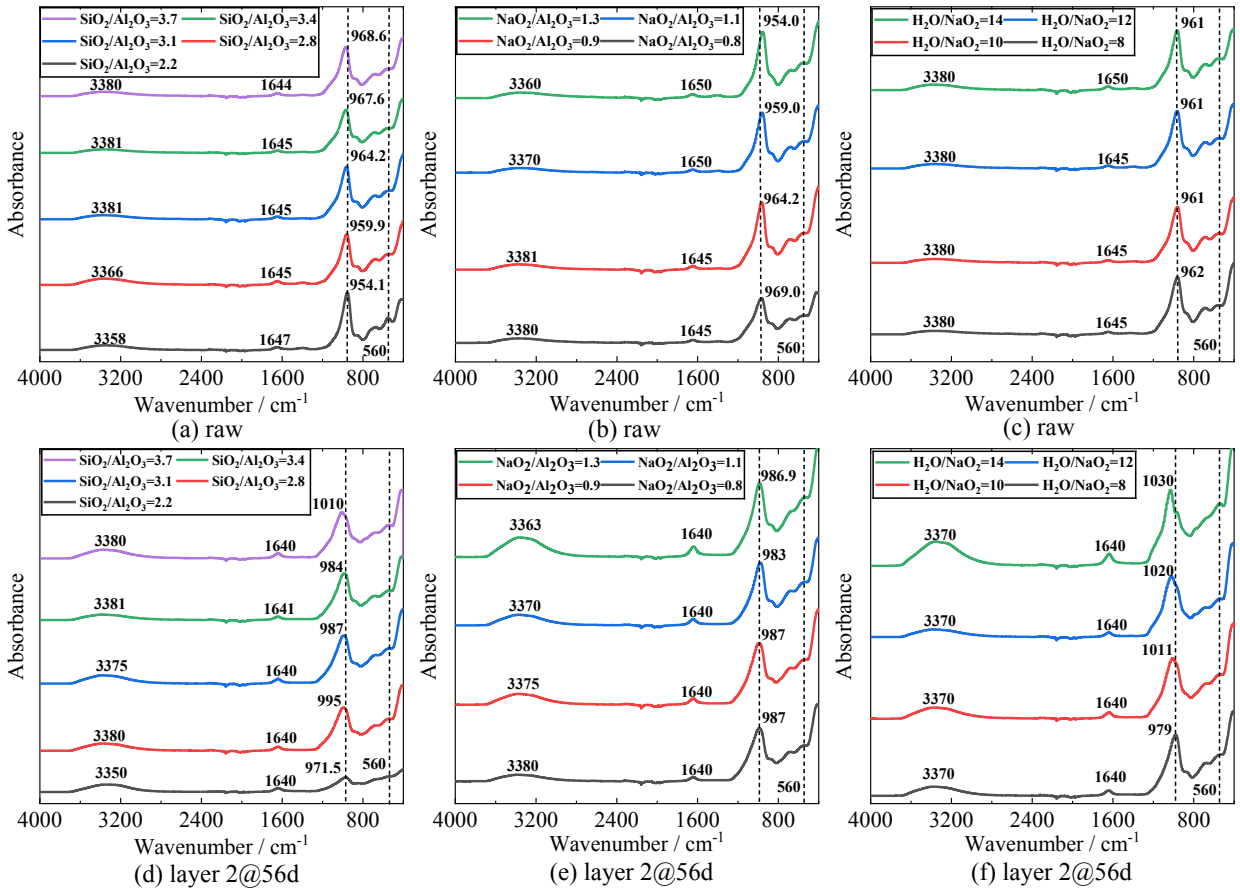


Figure 5.14 FTIR outcomes for geopolymers right before and after sulphuric acid immersion.

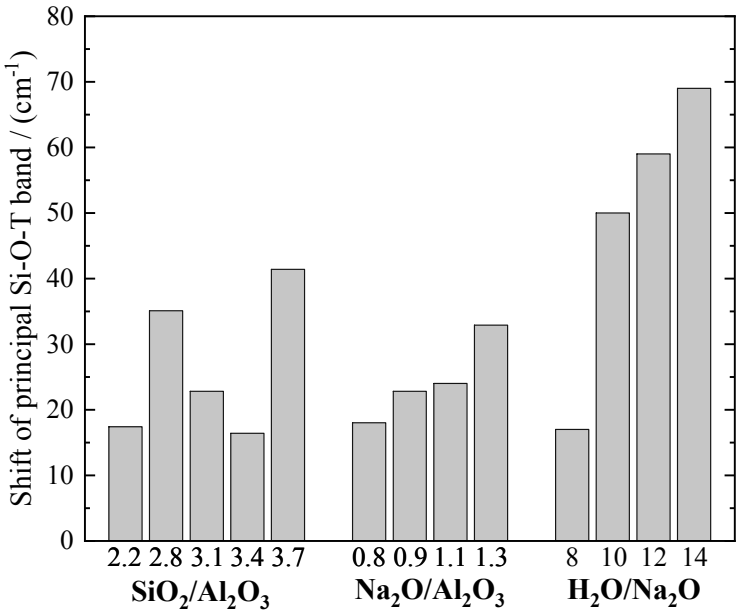


Figure 5.15 The shift of principal Si-O-T band as reported in Figure 5.14.

In order to interpret the structural changes referred above, the FTIR spectra were deconvoluted for the range of 800~1250 $cm^{-1}$ which corresponds to the polymerized Si-O-T band (Zhang et al., 2012). The associated fitting procedure was performed referring to the related literature (Cortes et al., 2021). In this manner, the following peaks are considered: Peak I (~850-860 $cm^{-1}$) to Si-OH bending; Peak II (~930 $cm^{-1}$) to Si-O-T in $Q^2$; Peak III (~960 $cm^{-1}$) to asymmetric stretching vibrations of nonbridging oxygen (NBO) sites; Peak IV (~1000 $cm^{-1}$) to Si-O-T in a 3-dimensional N-A-S-H network; Peak V (~1070-1080 $cm^{-1}$) to Si-O-Si of silica gels (also the S-O bond after sulphuric acid immersion (Qu et al., 2021)) and, Peak VI (~1150-1160 $cm^{-1}$) to Si-O-T of unreacted metakaolin. The FTIR deconvolution peaks for unexposed and exposed mixtures are now presented in Figures 5.16 and 5.17**,** respectively, with a regression coefficient $R^2$ of 0.99. Also, the relative area proportions for the aforementioned sub-peaks are quantified, as illustrated in Figure 5.18.

For geopolymers prior to sulphuric acid attack, increasing the $SiO_2/Al_2O_3$ ratio leads to a significant rise in the area proportion of Peaks IV and V, alongside a reduction in the area fraction of Peak III, see Figure 5.18(a). This is attributed to that more amorphous silica are available to promote the aluminosilicate oligomer formation as well as the chain length, and therefore, a greater degree of geopolymerization is obtained (Li et al., 2019). Moreover, it is once again confirmed here that mixtures made with the larger $Na_2O/Al_2O_3$ or $H_2O/Na_2O$ ratios register a lower polycondensation degree, as particularly evident from the smaller proportion of N-A-S-H networks (Peak IV) and the greater percentage for NBO (Peak III). Comparing Figure 5.18(a)&(b), the sulphuric acid attack upon geopolymers causes a significant rise in the relative proportion of Peak V and a considerable reduction in the relative fraction of NBO (Peak III). The increased Peak V should be collaboratively led by the penetrating $SO_4^{2-}$ and the released silicic acid during the

sulphuric acid attack. The reduced Peak III area may be attributed to that the dealuminated N-A-S-H frameworks release numerous Al-OH groups to the exterior, accompanied by the leaching of nonbridging oxygens. Although a part of silicon species may also be leached out, the corresponding amount is significantly lower than aluminum species, as experimentally confirmed in a related study (Khan et al., 2020). From the prospect of chemistry, the tetrahedral $AlO_4^-$ could only attain its stability under the strong alkaline condition, whereas the progressive acid attack significantly reduces the alkalinity inside geopolymers, which in turn transforms $AlO_4^-$ into general $Al^{3+}$ (Davidovits, 2008). These $Al^{3+}$ ions are no longer able to form aluminosilicate oligomers. Instead, the depolymerized $SiO_4$ groups are still tetrahedral due to the nature of tetravalence and, may re-link to the local geopolymer as time elapses. Furthermore, one can note from Figure 5.18(c) that in each of the independent series, the respective optimal case, i.e., $SiO_2/Al_2O_3$=3.4, $Na_2O/Al_2O_3$=0.8 and $H_2O/Na_2O$=8, displays the minimal increase in the relative proportion of Si-O-Si (Peak V) as well as the smallest reduction in the relative fraction of NBO (Peak III). This indicates they were most chemically durable against the sulphuric acid attack, across their respective series.

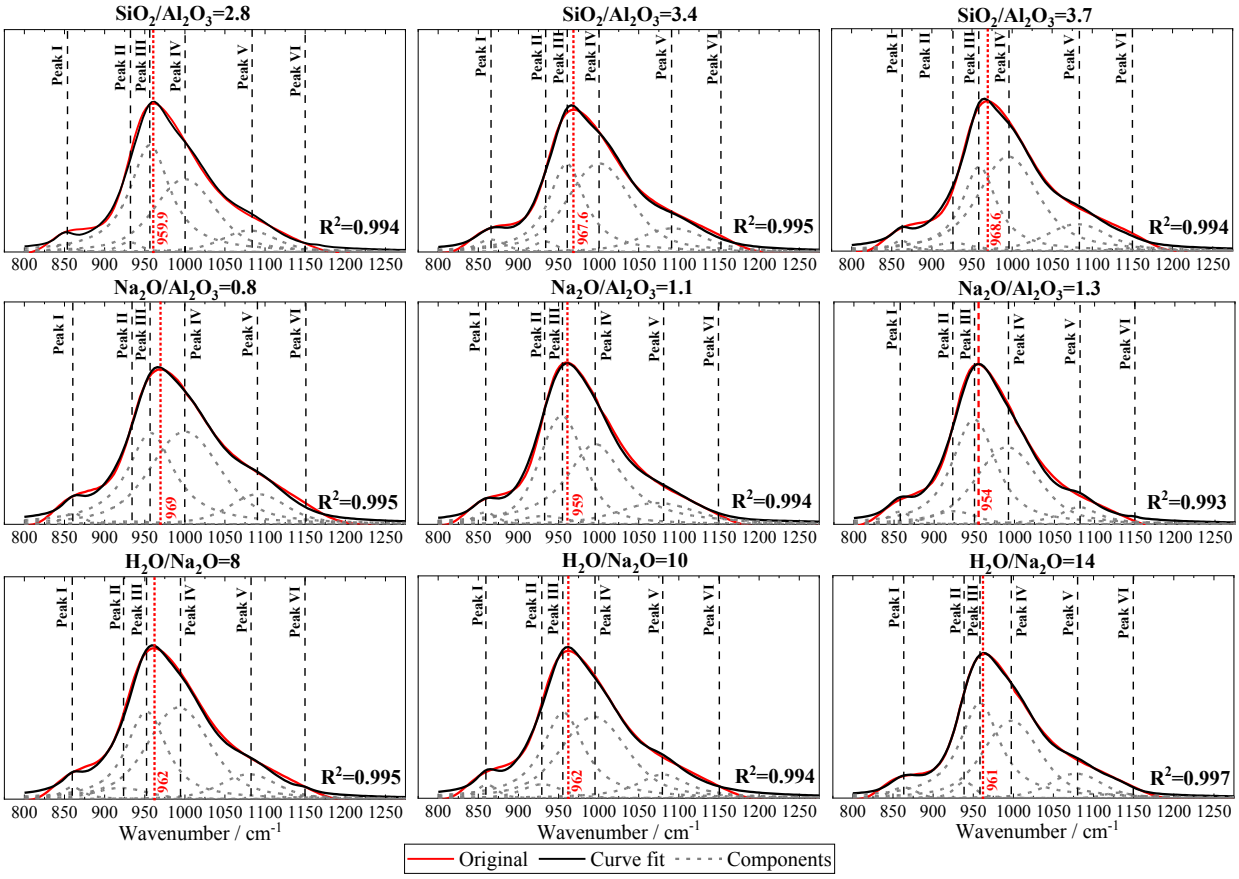


Figure 5.16 FTIR spectral deconvolutions of the main Si-O-T stretching band positioned at 800~1250 $cm^{-1}$ for geopolymers reported in Figure 5.14(a-c).

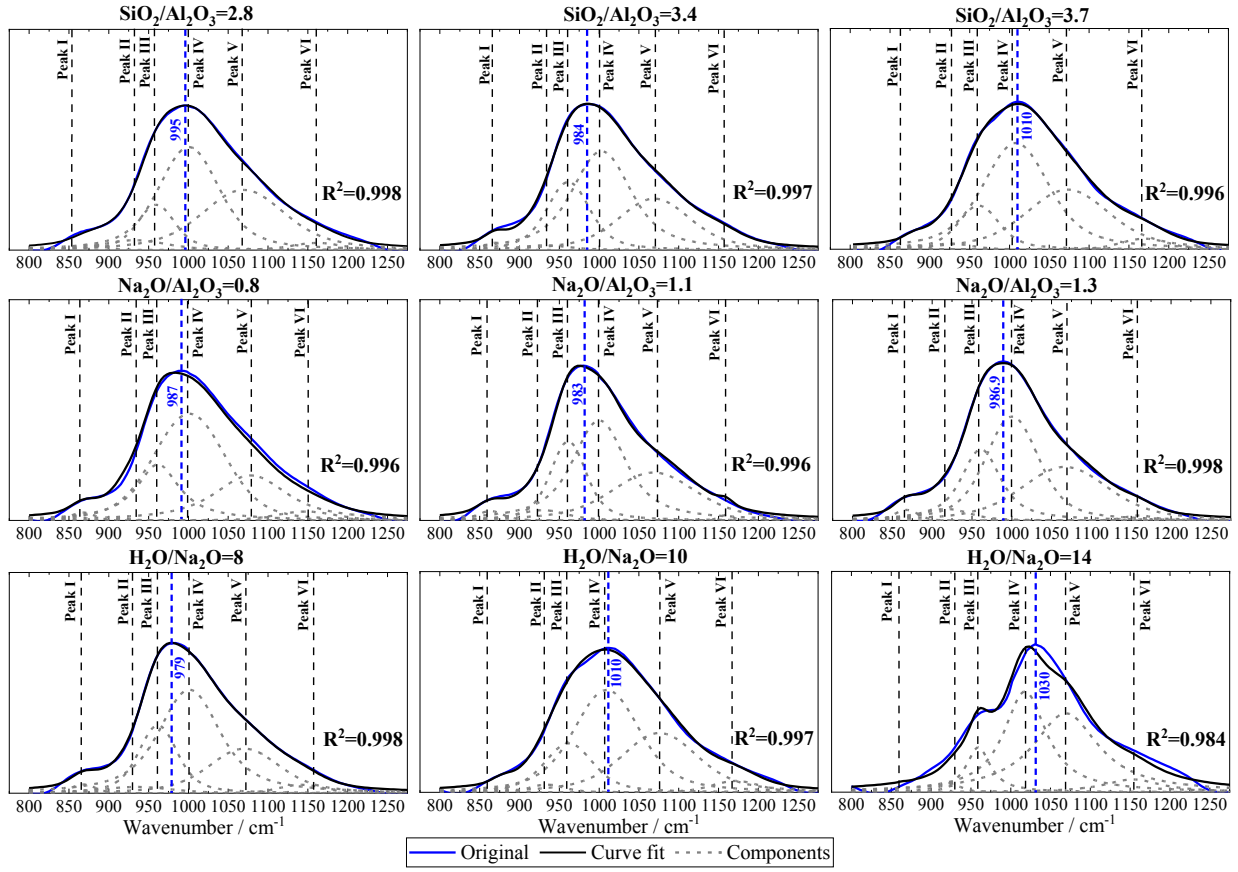


Figure 5.17 FTIR spectral deconvolutions of the main Si-O-T stretching band positioned at 800~1250 $cm^{-1}$ for geopolymers reported in Figure 5.14 (d-f).

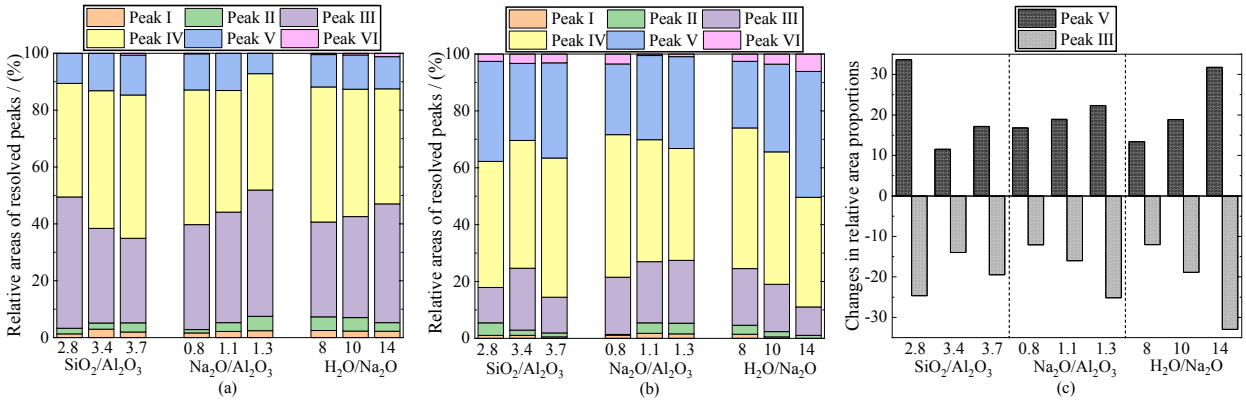


Figure 5.18 Relative area proportions of the deconvoluted sub-peaks right (a) before and (b) after sulphuric acid attack, alongside (c) the variation in the area proportion of Peaks III and V.

### 5.3.8. Scanning electron microscope and energy dispersive X-ray spectroscope (SEM-EDS)

Prior to sulphuric acid attack, the microstructure of various N-A-S-H geopolymer mixtures was evaluated under SEM at 300X and 5000X magnifications, respectively. The raw images alongside the associated binarized images are now presented in Figures 5.19~5.22. The images taken under the lower magnification visibly showed the microcracks while the other set captured under the higher magnification yielded a clear view upon the voids and compactness of examined samples. Seen from Figures 5.19(a-c) and 5.21(a-c), an increase in the $SiO_2/Al_2O_3$ ratio from 2.1 to 3.4 led to a considerable refinement in the microstructure of geopolymers. This manifested in an approximate reduction in the width of microcracks from 8 μm to 1 μm. However, the further increase in this ratio from 3.4 to 3.7 appeared to increase the size of microcracks up to about 2 μm, likely attributed to the increased liquid content and the resultant high liquid-to-solid ratio. Under the higher magnification (5000X), the mixture made with a $SiO_2/Al_2O_3$ ratio of 3.4 also displayed the densest texture across the three examined samples shown in Figures 5.20(a-c) and 5.22(a-c). This is then supported by the quantification upon the area of voids and microcracks based on the associated binarized images, see Figure 5.23. With regard to the $Na_2O/Al_2O_3$ ratio, increasing the value from 0.8 to 1.3 boosted the evolution of microcracks appearing in N-A-S-H geopolymers and loosened the associated texture. This is evident from Figures 5.19(d-f) ~5.22(d-f), alongside the quantified area of voids and cracks shown in Figure 5.23. In the case of $H_2O/Na_2O$ ratio, lowering this ratio effectively alleviated the appearance of cracks and large pores in hardened geopolymers. However, by comparing Figure 5.20(g-h), the excessively low $H_2O/Na_2O$ ratio is noted to possibly degrade the texture of formed N-A-S-H networks. This may be explained from the aspect of reaction dynamics in terms of polycondensation. Recall Figure 5.12, the polycondensation of aluminosilicate oligomers is a regeneration process of $Na^+$ and $OH^-$. The over-

low $H_2O/Na_2O$ ratio essentially corresponds to the over-high alkali concentration. Accordingly, once this ratio exceeds a certain threshold, the polycondensation may be depressed instead, and hence the texture of polymerized N-A-S-H framework is so loosened.

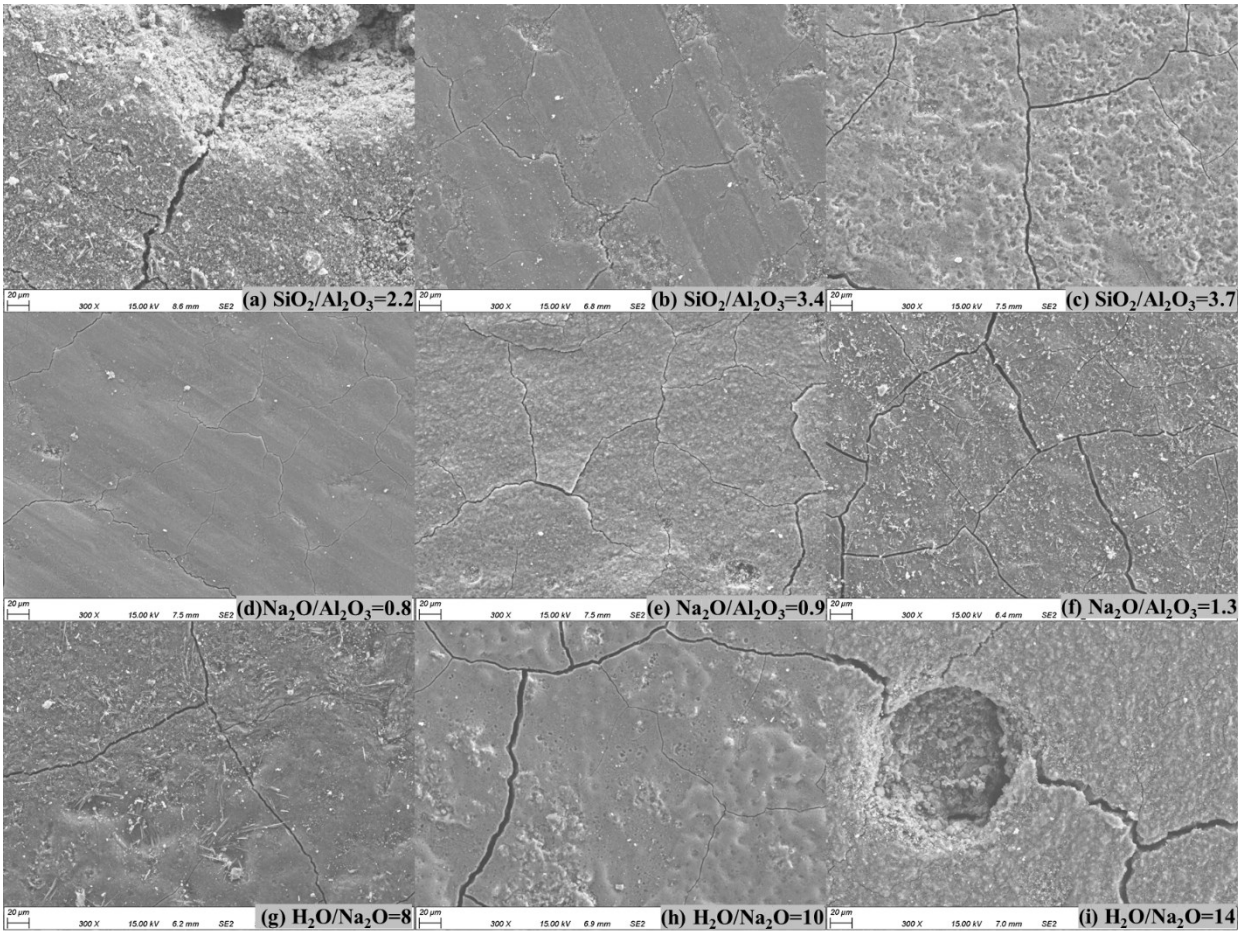


Figure 5.19 Original SEM images of unexposed geopolymer mixtures at 300X.

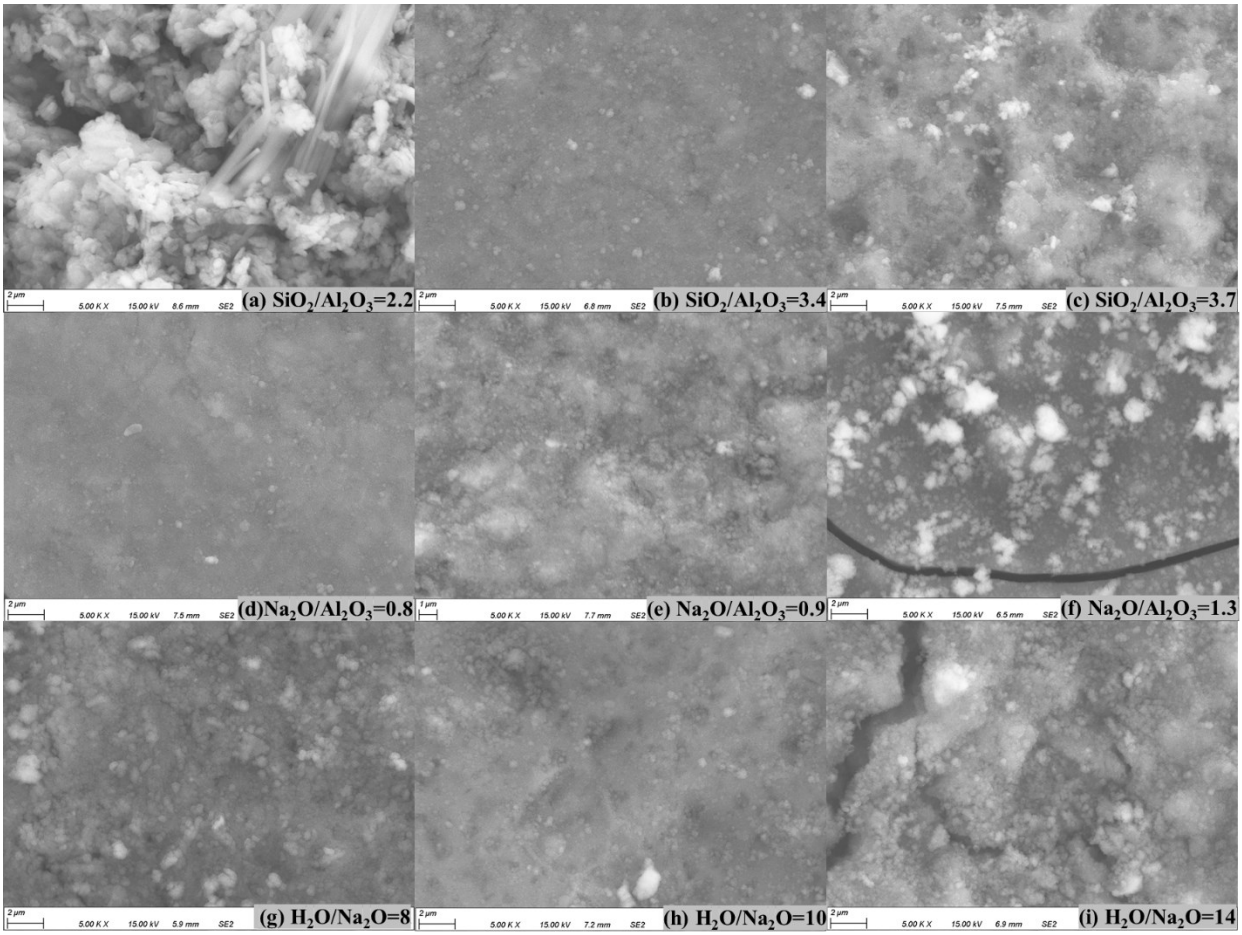


Figure 5.20 Original SEM images of unexposed geopolymer mixtures at 5000X.

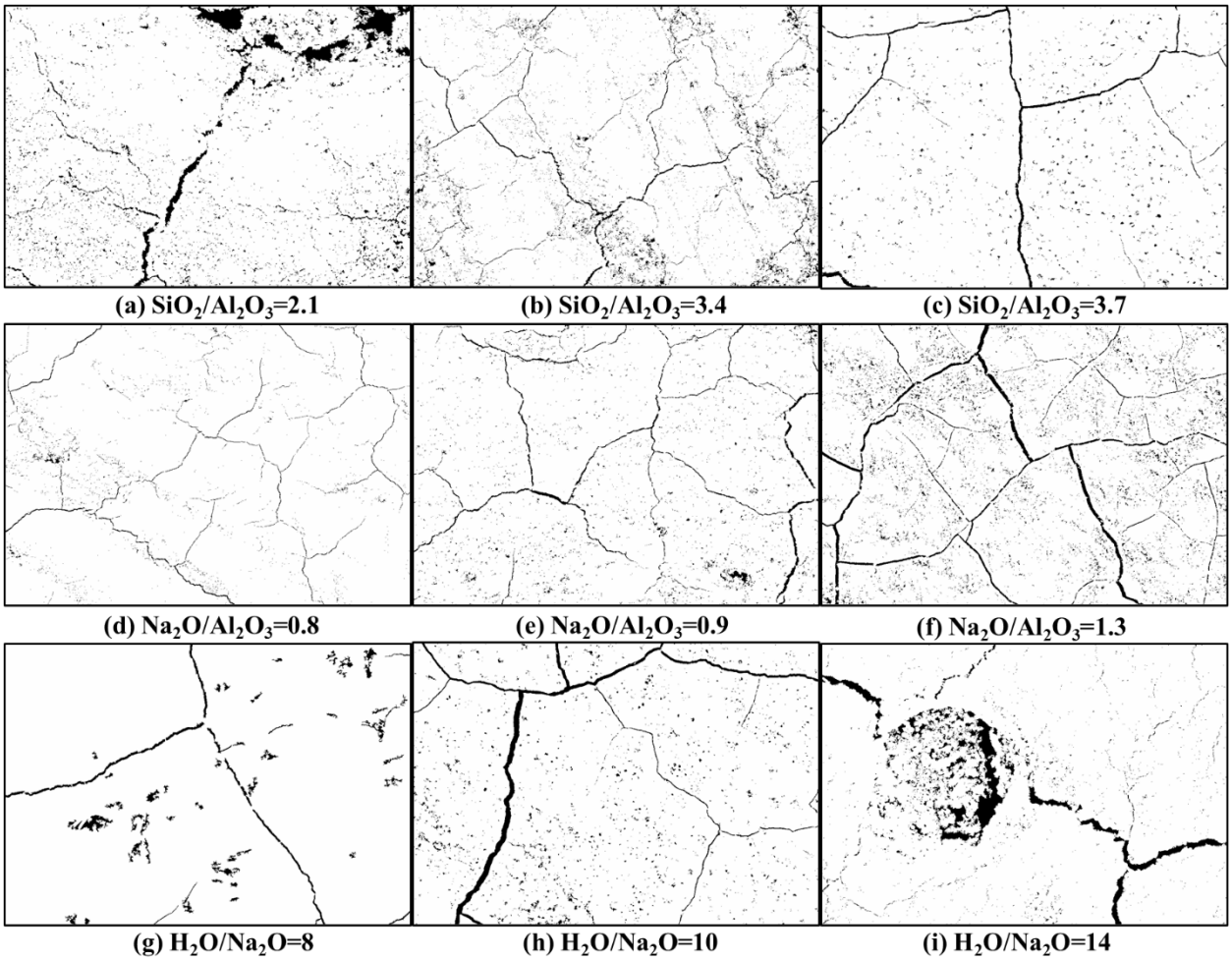


Figure 5.21 Binarized SEM images of unexposed geopolymer mixtures at 300X.

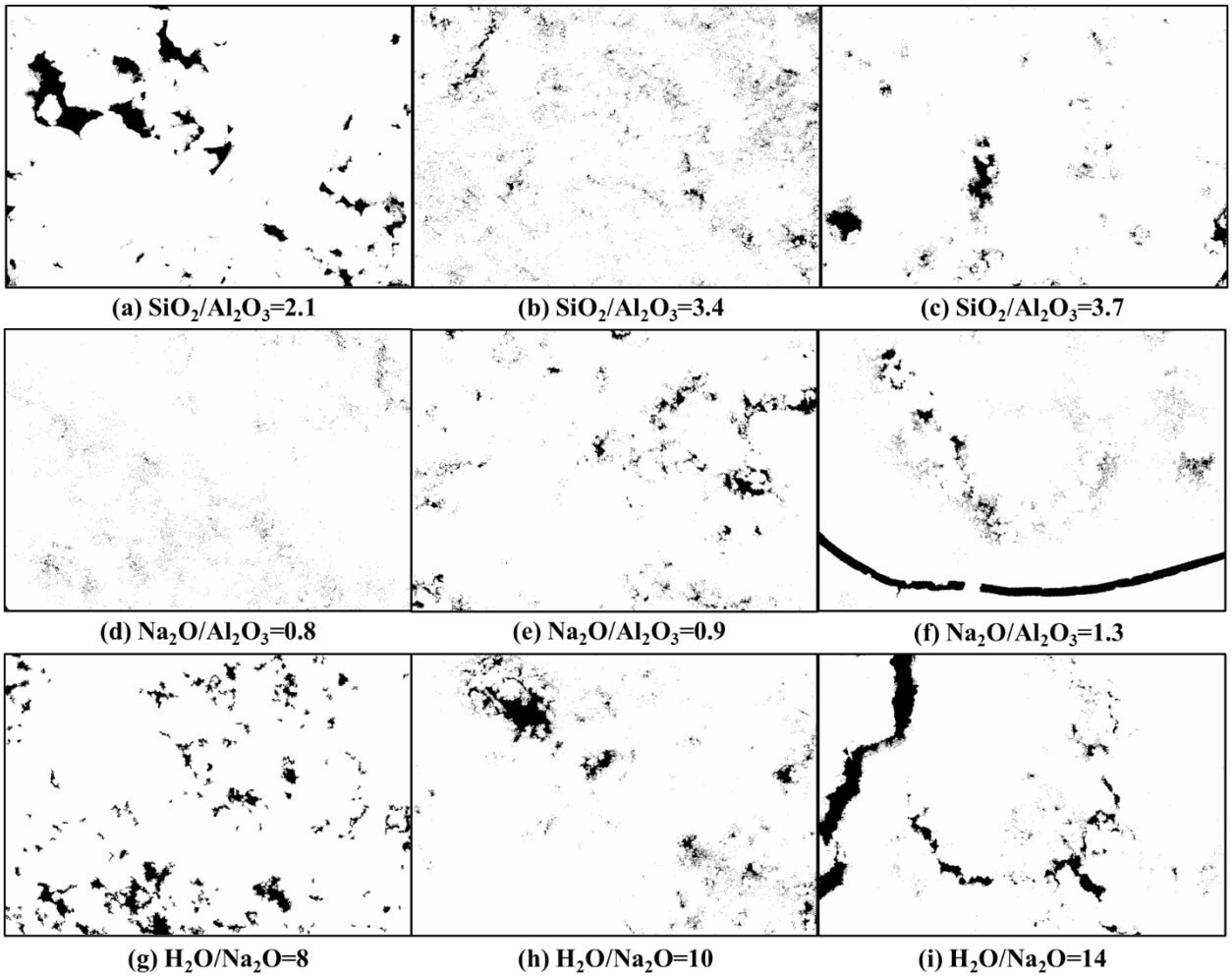


Figure 5.22 Binarized SEM images of unexposed geopolymer mixtures at 5000X.

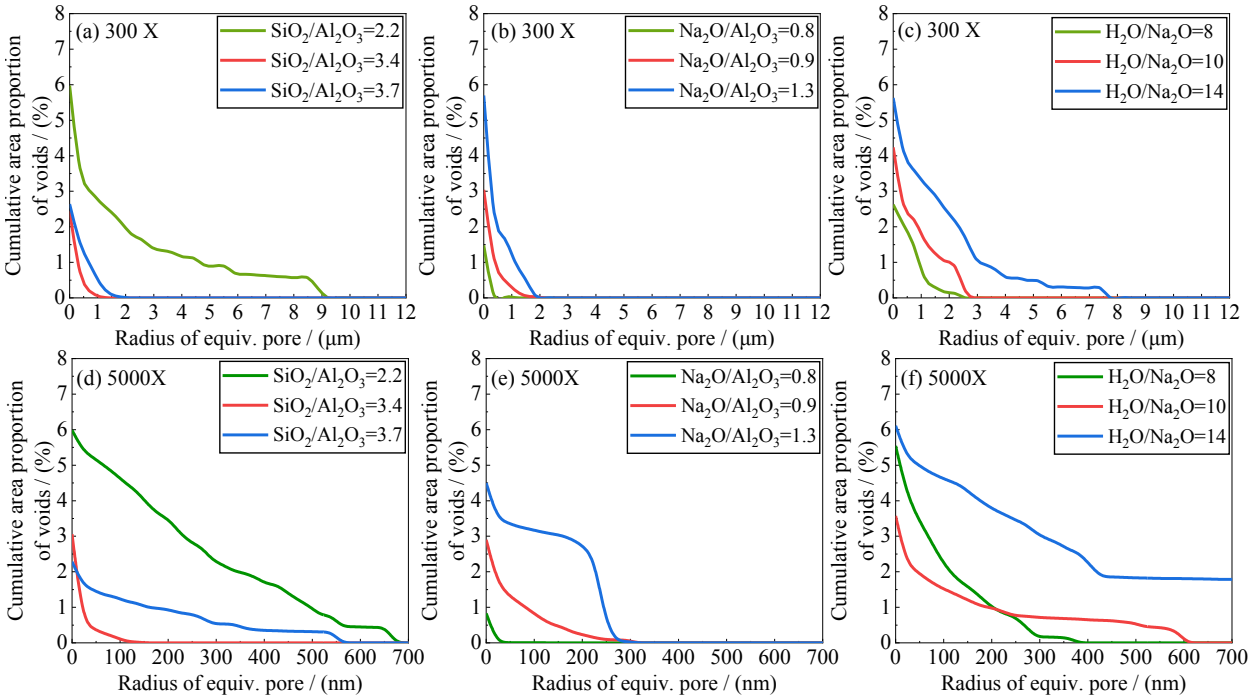


Figure 5.23 Cumulative area fraction of voids derived from images taken at (a-c) 300X and (d-f) 5000X.

For the exposed specimens, the cross-section located at the transition zone was scanned under the SEM. As highlighted in Figure 5.24, this examined area is between the severely degraded and visually intact regions. Seen from Figure 5.25 that regardless of mixture compositions, the internal microcrack evolved significantly, as compared to the respective unexposed sample (at 300X). Nevertheless, the mixtures respectively made with a $SiO_2/Al_2O_3$ ratio of 3.4 (Figure 5.25(b)), a $Na_2O/Al_2O_3$ ratio of 0.8 (Figure 5.25(d)) and a $H_2O/Na_2O$ ratio of 8 (Figure 5.25(g)) displayed the smallest acid-induced microcracks in the respective series. This phenomenon also supports their physical and mechanical performances after sulphuric acid attack.


Figure 5.24 (a) Paste species for SEM test and (b) the scanned area for exposed specimens.

Further, EDS results sourced from the cross section at 300X magnifications are presented in Figure 5.26 and Table 5.3. As widely reported, the acid-induced degradation upon geopolymers is widely reported to start with the replacement of exchangeable alkali metal ions by hydrogen ions ($H^+$) (Allahverdi and Skvara, 2005; Pyatina and Sugama, 2016). This was also confirmed in the present study. One sees that most of the mixtures experienced a noticeable reduction in the relative mass proportion of Na. On the other hand, only minor sulphur could be detected in various specimens after exposure. This is likely attributed to that the acid-induced degradation upon N-A-S-H networks is essentially led by hydrogen ions ($H^+$). However, the attendant sulphur could not form any corrosion products due to the extremely low $Ca^{2+}$ content in aluminosilicates and therefore, displayed the relatively low content. This phenomenon was confirmed elsewhere by Qu et al. (2021). Their EDS results indicated that even after 18 months of exposure to sulphuric acid, the region identified as the N-A-S-H network only registered 0.06%~0.56% sulphur, whereas this value in the area contained gypsum and AFt increased up to 5.69%~11.99% (Qu et al., 2021). Nevertheless, the Na content in the mixture with a $SiO_2/Al_2O_3$ ratio of 2.2 reduced drastically after 12 weeks of acid exposure, from 13.98% to 2.72%. Besides, it registered the most increase in the

sulphur content (5.21%), progressively followed by 0.14% for $SiO_2/Al_2O_3$=3.7 and 0.044 for $SiO_2/Al_2O_3$=3.4. This again implies the N-A-S-H geopolymer made with an excessively low $SiO_2/Al_2O_3$ ratio is extremely susceptible to the sulphuric acid environment, attributed to the low polycondensation degree and the loose microstructure. On the other hand, due to the enlarged liquid content, a continuous increase in $SiO_2/Al_2O_3$ ratio will not enhance the acid resistance monotonically. In the case of $Na_2O/Al_2O_3$ ratio, increasing its value from 0.8 to 1.3 appeared to accelerate the replacement of $Na^+$ by $H^+$. This is evident from the greatest sulphur content (3.11%) alongside the highest reduction rate in $Na^+$ content (5.07%), in the case of $Na_2O/Al_2O_3$=1.3. Similarly, the higher $H_2O/Na_2O$ ratio corresponded to the greater deterioration, manifesting chemically as more losses of $Na^+$ along with the slightly higher sulphur content after sulphuric acid attack.

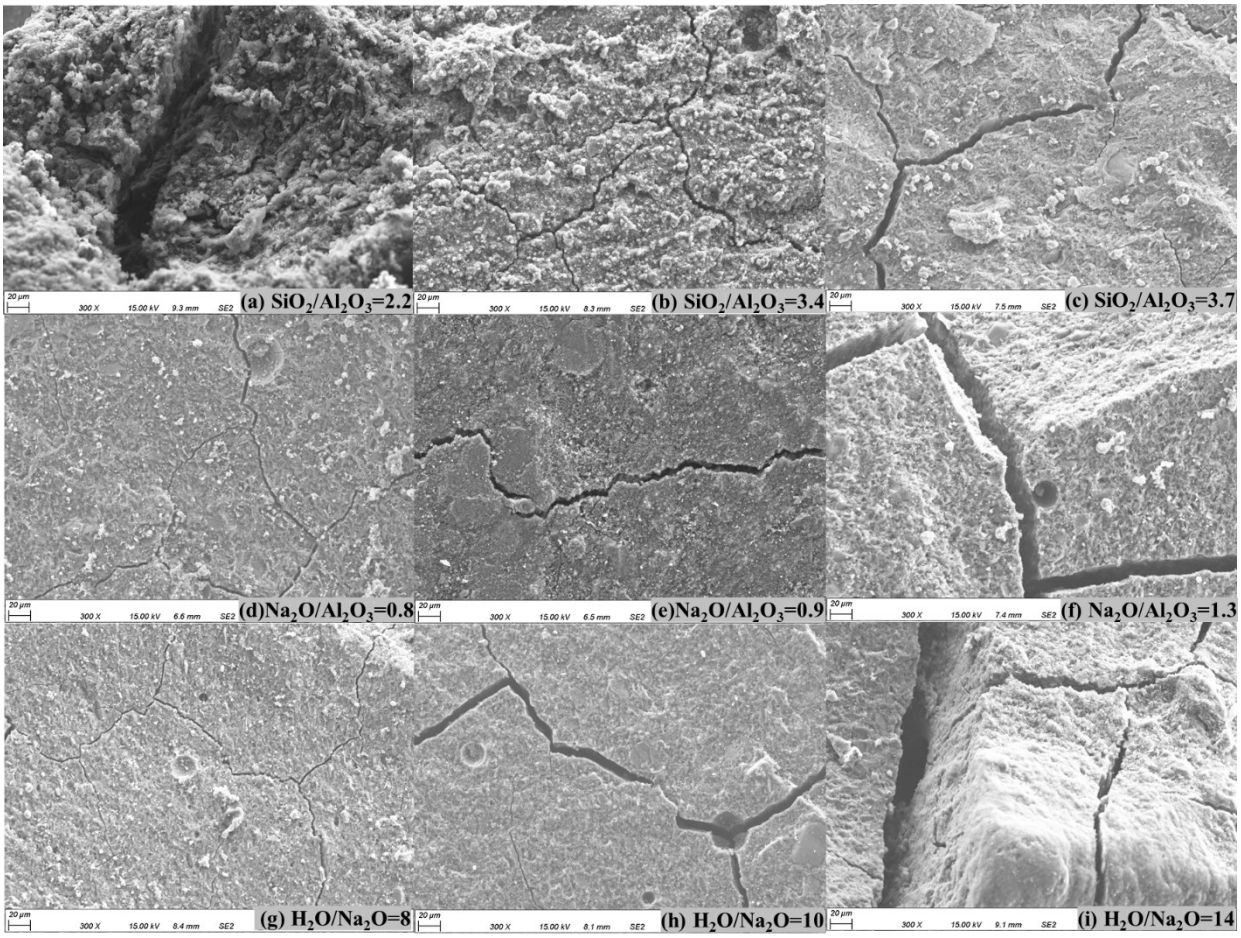


Figure 5.25 SEM images for geopolymers after 84 days of exposure (at 300X).

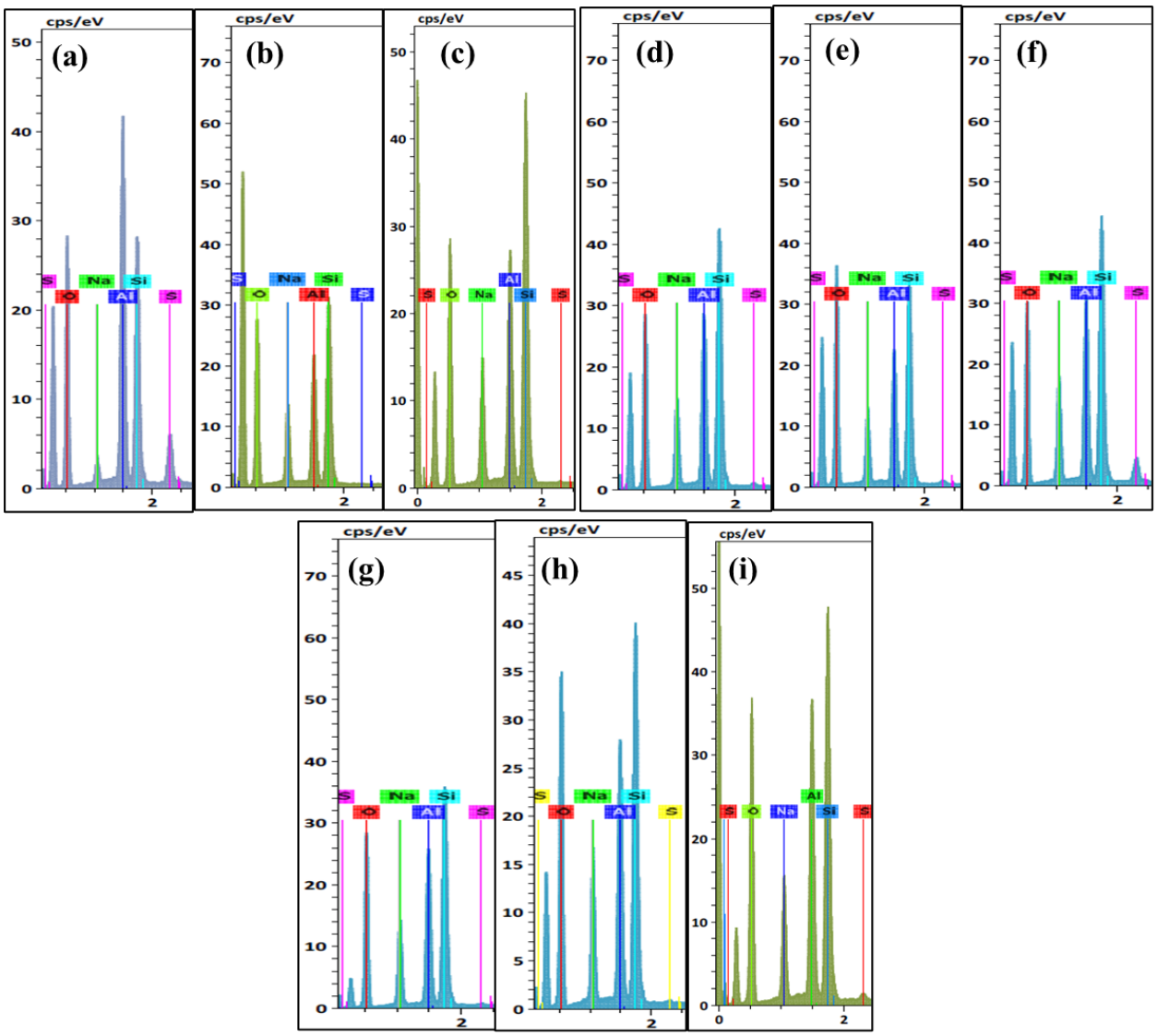


Figure 5.26 EDS results for geopolymers after 84 days of exposure, as captured from Figure 5.25.

Table 5.3 Relative mass proportion of various elements constituting N-A-S-H geopolymers.

| Mixture designations | | Oxygen (%) | Sodium (%) | Aluminum (%) | Silicon (%) | Sulphur (%) |
|---|---|---|---|---|---|---|
| $SiO_2/Al_2O_3$=2.2 | unexposed | 49.42 | 13.98 | 17.12 | 19.48 | 0 |
| | (exposed) | (43.23) | (2.72) | (26.83) | (21.81) | (5.21) |
| $SiO_2/Al_2O_3$=3.4 | unexposed | 46.96 | 11.51 | 14.81 | 26.71 | 0 |
| | (exposed) | (44.54) | (11.30) | (15.49) | (28.62) | (0.044) |
| $SiO_2/Al_2O_3$=3.7 | unexposed | 48.39 | 12.45 | 13.06 | 26.10 | 0 |
| | (exposed) | (40.56) | (11.24) | (16.07) | (31.99) | (0.14) |
| $Na_2O/Al_2O_3$=0.8 | unexposed | 47.22 | 12.28 | 15.40 | 25.09 | 0 |
| | (exposed) | (40.19) | (12.44) | (16.71) | (30.28) | (0.39) |
| $Na_2O/Al_2O_3$=0.9 | unexposed | 50.00 | 10.31 | 14.44 | 25.24 | 0 |
| | (exposed) | (48.40) | (10.03) | (14.43) | (26.45) | (0.69) |
| $Na_2O/Al_2O_3$=1.3 | unexposed | 49.62 | 18.38 | 11.88 | 20.11 | 0 |
| | (exposed) | (39.22) | (13.31) | (16.48) | (27.88) | (3.11) |
| $H_2O/Na_2O$ =8 | unexposed | 45.68 | 14.28 | 14.47 | 25.57 | 0 |
| | (exposed) | (42.54) | (12.53) | (16.89) | (27.91) | (0.13) |
| $H_2O/Na_2O$ =10 | unexposed | 49.20 | 13.47 | 13.07 | 24.25 | 0 |
| | (exposed) | (45.61) | (11.72) | (15.53) | (26.72) | (0.42) |
| $H_2O/Na_2O$ =14 | unexposed | 47.81 | 12.51 | 14.75 | 24.93 | 0 |
| | (exposed) | (42.61) | (8.70) | (17.90) | (30.15) | (0.63) |

### 5.4. Sensitivity analysis

An effective variance-based sensitivity analysis (Yi et al., 2019) was conducted as per Equations (5.3) and (5.4), to quantify the influence of compositional oxide ratios on the performance of geopolymers against sulphuric acid attack. Here, $x$ indicates the respective compositional oxide ratio and $y$ is the evaluated performance. $n$ denotes the size of the dataset and $m$ represents the median value of each factor. The data in terms of the acid penetration degree, the initial compressive strength and the associated loss at 84 days of exposure are analyzed here. The sensitivity index, $S_i$, for each factor is defined as the proportion of the effective partial variance,

$V_{ei}$, in the total effective variance, $V_{te}$. An increment coefficient, $\alpha_{ij}$, is introduced to eliminate the disturbance and to normalize the traditional variance.

$$V_{ei} = \frac{1}{n\text{-}1}\sum_{j=1}^{n}\frac{\left(y_{ij}-y_{im}\right)^2}{\alpha_{ij}} \quad \text{with} \quad \alpha_{ij} = \frac{x_{ij}-x_{im}}{x_{im}} \tag{5.3}$$

$$S_i = \frac{V_{ei}}{V_{te}} = \frac{V_{ei}}{\sum_{i=1}^{l} V_{ei}} \in [0,1] \tag{5.4}$$

The computed sensitivity indices are now illustrated in Figure 5.27, for ratios of $SiO_2/Al_2O$ (with $Na_2O/Al_2O_3$=0.9 and $H_2O/Na_2O$=11), $Na_2O/Al_2O_3$ (with $SiO_2/Al_2O$ =3.1 and $H_2O/Na_2O$=11) and $H_2O/Na_2O$ (with $SiO_2/Al_2O$ =3.1 and $Na_2O/Al_2O_3$=1). The sulphuric acid-induced deteriorations are more dependent upon the other two $Na_2O$-involved ratios. Particularly, the $H_2O/Na_2O$ ratio is noted to dominate the resistance of geopolymers to the penetration of acid ions, as evident from the highest sensitivity index, i.e., 77.6%. This is likely due to the following: (i) While a continuous increase in the $SiO_2/Al_2O_3$ ratio favours the degree of geopolymerization, an excessive ratio, i.e., a value beyond 3.4, may also degrade the associated microstructure. There accordingly exists an offset between these two attendant effects; (ii) On the other hand, raising the $Na_2O/Al_2O_3$ and $H_2O/Na_2O$ ratios depresses the geopolymerization and threatens the microstructure of geopolymers in parallel. Hence, the eventual acid-induced deterioration is intensified.

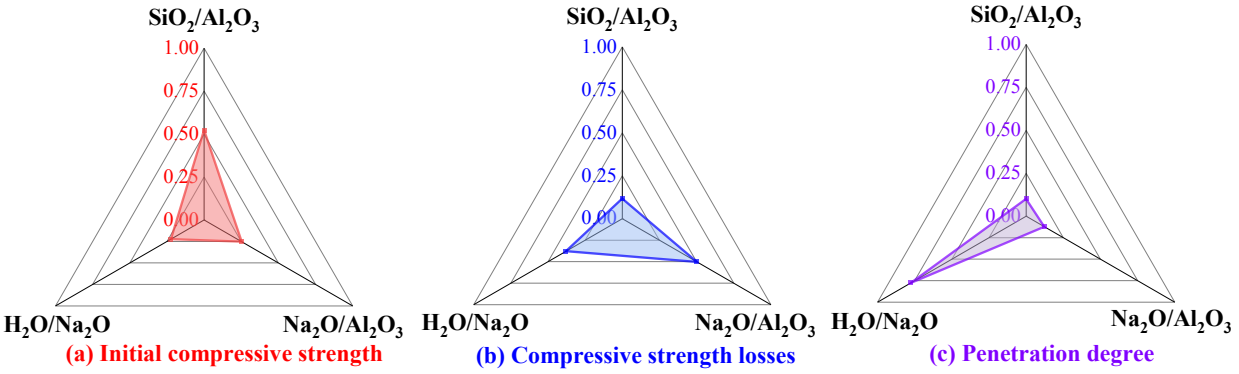

Figure 5.27 Sensitivities of initial compressive strength, strength losses and penetration degree to $SiO_2/Al_2O_3$, $Na_2O/Al_2O_3$ and $H_2O/ Na_2O$ ratios.

### 5.5. Conclusion

This Chapter investigated the effects of chief oxide ratios on the sulphuric acid attack in N-A-S-H geopolymers. A combination of macroscopic, morphological, thermalgravimetric, chemical and microscopic analyses was carried out to experimentally characterize the underlying mechanisms. Moreover, the sensitivities of the sulphuric acid resistance to principal oxide ratios are quantified by a variance-based analysis. Based on the obtained results, the following concluding remarks may be drawn:

(1) The sulphuric acid attack upon geopolymers may not only depolymerize the N-A-S-H frameworks but also transform the crystalline zeolites into their amorphous states. Nonetheless, the amorphocity of geopolymers exposed to the sulphuric acid condition reduces progressively, as evident from the shift of diffuse hump toward the lower end in XRD evaluations. Once reaching a certain value, further exposure will not affect the degree of amorphocity, which may indicate the respective region has now deteriorated completely. As the sulphuric acid attack progresses, although the structure of N-A-S-H geopolymers loses a significant amount of nonbridging oxygens, a forward shift in terms of the principal Si-O-T band is still observed in the FTIR spectrum. Simultaneously, the thermal gravimetric peak related to the N-A-S-H framework evolves in TGA analysis. This may be due to that the acid-induced dealumination leaches Al-OH groups out to the exterior, whereas the associated Si-OH groups may re-link to the intact aluminosilicate networks.

(2). Increasing the $SiO_2/Al_2O_3$ ratio indeed favours the degree of geopolymerization as well as the ensuing strength development. However, when subjected to the sulphuric acid attack, there exists an optimal value, experimentally found as 3.4, for this ratio to yield the best acid resistance. Either

a deficient or an excessive $SiO_2/Al_2O_3$ ratio is believed to magnify the acid-induced deteriorations, including mass, diameter, strength and alkalinity losses. This may be attributed to that, a continuous increase in this ratio will boost the formation and the length of aluminosilicate oligomers on the one hand but enlarge the amount of permeable voids on the other hand. The antagonism between these two effects reaches the balance at a certain point, namely $SiO_2/Al_2O_3$=3.4.

(3) Although the ideal $Na_2O/Al_2O_3$ ratio is theoretically recognized as 1.0 to achieve the equilibrium of chemical valency states, the optimal value is experimentally observed as 0.8~0.9, which is slightly lower than the theoretical value. Any further increase beyond this range will cause considerably increased damage to geopolymers when subjected to the sulphuric acid environment, due to the depressed geopolymerization degree and the enlarged L/S ratio. Increasing the $H_2O/Na_2O$ ratio will lower the activation efficiency and degrade the pore structure of geopolymers significantly, and these together weaken the acid resistance of geopolymers.

(4) As compared to the optimal ranges that were reported in the literature for initial mechanical strength, the best $SiO_2/Al_2O_3$, $Na_2O/Al_2O_3$ and $H_2O/Na_2O$ ratios all shift slightly towards the smaller end. This may be attributed to that the mechanical performance of geopolymer is predominantly controlled by the degree of geopolymerization, whereas the microstructure, particularly the permeable voids, also takes an important part. However, increasing any of these ratios will automatically enlarge the L/S ratio.

(5) The sensitivity analysis illustrates that the remaining compressive strength after sulphuric acid attack is more sensitive to $Na_2O/Al_2O_3$ and $H_2O/Na_2O$ ratios. As for the alkalinity loss, the $H_2O/Na_2O$ ratio is found to govern the degree of neutralization, as it affects the microstructure predominantly.

# Chapter 6. Potential benefits of nano silica stabilized dry water for N-A-S-H geopolymers against sulphuric acid attack

## 6.1. Introduction

Although high mechanical strength could be assured for cementitious systems during the mix design stage, structural failures are still highly possible to be witnessed in practice, particularly when subjected to some aggressive conditions (Miyamoto et al., 2014; Aiken et al., 2018). Due to the active nature of precursors, the durability of geopolymers essentially dominates the service life in such cases (Gutberlet et al., 2015). Sulphuric acid resistance is an important subset of durability. Structural members serving in sewer systems, industrial estates, mines and backfill areas are frequently exposed to sulphuric acid (Hewayde t al., 2006; Bassuoni et al., 2007; Araghi et al., 2015; Barbhuiya and Kumala, 2017; Wu et al., 2021). As well, this harsh condition may also appear on the walls of geothermal wells, through the dissolution of hydrogen sulphide (Pyatina and Sugama, 2016). So far, intensive investigations have been carried out to examine the performance of geopolymers against the sulphuric acid environment. Vafaei et al. (2018) compared the sulphuric acid resistance of OPC and geopolymer systems by exposing these specimens to the respective acid solution with a pH of 3 for 1 year. The obtained results revealed that although the geopolymer system displayed much better acid resistance than the OPC system, the associated specimens still experienced a significant strength loss after such an acid exposure, approximately corresponding to 48%. Similarly, this mechanical degradation was reported elsewhere and, explained through the replacement of alkali metal ions by hydrogen ions alongside the dealumination of the polymerized aluminosilicate framework (Bakharev et al., 2005).

Adding nanoparticles is one of the most popular means to improve the properties of cementitious systems. Due to the chemical compositions of geopolymers, nano silica has been broadly employed

in this subject. Prior studies reported that a 1%~3% addition of nano silica to geopolymer mixtures was able to improve the compressive strength by 10%~55% (Gao t al., 2013b; Gao et al., 2015; Deb et al., 2016; Rashad and Ouda, 2019). Also, the geopolymer specimen made with nano silica displayed a stronger resistance to acid attack, manifesting as the higher remaining compressive and splitting strength after various acid exposures. Moreover, the corresponding optimum dosage was reported as 1.5% (Sumesh et al., 2017). Nevertheless, it has also been attracting attention that the enhancement led by nanoparticles upon the above properties usually comes at sacrificing other equally important engineering properties, such as workability and setting time (Gao et al., 2015; Deb et al., 2016; Lo et al., 2017). This is likely attributed to the nanoscale in the size of nanoparticles and the resultant agglomeration. As such, the widespread application of nanoparticles is constrained in cementitious materials, due to the "trade-off" between various engineering properties. Nanoparticles stabilized dry water may be a promising resolution to the above issue. Dry water is a water-in-air Pickering emulsion, which is usually produced by stabilizing 90%~95% water droplets with 5%~10% predominantly hydrophobic nanoparticles under the highly shearing stirring process (Binks and Murakami, 2006; Forny et al., 2009; Yi et al., 2020). The obtained dry water will exist in the form of soft powder with the water droplet encapsulated inside. Also, the particle size of dry water could usually reach up to a few micrometres after the above physical re-organization, which is significantly larger than nanoparticles themselves. This transformation is so called as size coarsening effect. As for its potential application in geopolymers, nano silica is the most promising stabilizer to form suitable dry water powders, due to the demand for geopolymerization upon amorphous silica. However, the potential benefits of this dry water powder upon the durability (acid resistance) of N-A-S-H

geopolymers have not been examined yet and therefore, require further comprehensive investigations.

Given the above, the present study was undertaken to investigate the effect of nano silica stabilized dry water on the performance of N-A-S-H geopolymers exposed to the sulphuric acid environment. Three variants of dry water were produced in advance, and the corresponding nanoparticle dosage was set as 10%, 15% and 20%, respectively. Then, 10% (w/w) of this dry water was added to metakaolin to produce the respective geopolymer mixture. Accordingly, the overall nanoparticle content was 1.0%, 1.5% and 2% respectively, which fell into the optimum range reported in prior literature. Note further that besides a reference mixture without any nanoparticles, the other one was also prepared with the nano silica as it is. The produced geopolymer specimens aged 28 days were thereafter immersed in the sulphuric acid solution (1% w/w) for up to 12 weeks. The exposed specimens were retrieved for a suite of macroscopic tests, alongside companion microscopic characterizations including XRD, TGA, FTIR and SEM-EDS. It is the author's wish that this detailed investigation will provide an insight into the potential enhancement led by nano silica stabilized dry water upon the acid resistance of N-A-S-H geopolymers and in turn, promote the widespread applications of such alternatives to Portland cement, especially where durability against sulphuric acid attack is of importance.

## 6.2. Methodology

### 6.2.1. Materials

In this study, the aluminosilicate precursor was chosen as a commercially sourced metakaolin, which was then activated by the sodium hydroxide alongside the respective silicate solution. The chemical composition constituting the employed metakaolin has been reported earlier, see Table 5.1. Also, the adopted activator was the same as the one introduced in the previous Chapter 5,

Section 5.1. In this regard, the sodium hydroxide was in the form of solid pellets with a purity of 99%, while the sodium silicate solution was approximately composed of 60% water and 40% sodium silicate. The river sand was used for producing geopolymer mortars. This fine aggregate registered an oven-dry bulk density of 1570 kg/$m^3$, while its moisture content and water absorption were determined as 0.11% and 1.54%, respectively. Further, the acid condition was created by using a laboratory reagent-grade sulfuric acid with a purity of 95~98% $H_2SO_4$, and the mass concentration was set at 1%.

According to prior studies, only the hydrophobic nano silica could form the water-in-air Pickering emulsion (dry water powder) successfully, while the hydrophilic nano silica yielded the air-in-water Pickering emulsion (foam) instead (Binks and Murakami, 2006; Forny et al., 2009). Thus, the hydrophobic one was employed to produce the dry water powders. The physicochemical properties of this nanoparticle are presented in Table 6.1.

Table 6.1 Physicochemical properties of silica nanoparticles from the manufacturer.

| Properties | Silica nanoparticles |
|---|---|
| Average particle diameter | 7~14 nm |
| Specific surface area (BET) | 195-245 $m^2/g$ |
| Contact angle against water | 118 $^o$ |
| pH value (in 4% dispersion) | 5.5-9.0 |
| Loss on drying | $\leq$ 0.5% |
| $SiO_2$ content (based on ignited) | $\geq$ 99.8% |

### 6.2.2. Production of dry water powders

The mechanism underlying the formation of water-in-air Pickering emulsion (dry water powder) is the adsorption of solid particles under the partial wetting condition. Generally, the hydrophobic solids are easy to achieve this partial wetting status, whereas the hydrophilic particles may be

dispersed in the aqueous phase completely. This may be validated by computing the related energy of particle adhesion onto the water surface as per Equation (4.1), see Section 4.3.1, Chapter 4.

In order to form the dry water powders, the deionized water was blended with the hydrophobic nano silica in a mixer that could generate a highly shearing force with a 30,000-rpm speed. According to prior studies, the stirring time required to produce dry water powders varies from a minimum of 10 s up to a maximum of 5 mins (Forny et al., 2009). In this study, an average mixing time of 3 mins was adopted. During the mixing stage, water was firstly separated into a couple of droplets under the shearing force. Then, depending on the hydrophobic character, the silica nanoparticles gradually adsorbed onto the outer surface of each single water droplet under the partial wetting condition. This eventually resulted in well-encapsulated water droplets stabilized by a layer of silica nanoparticles, namely dry water powders. The formation of dry water is schematically plotted, see Figure 6.1(a). Also, the obtained samples alongside the observation under the optical microscope are displayed in Figure 6.1(b-c). In this study, the proportion of encapsulating nano silica was tried from 10% to 20% to produce various dry water powders, in order to capture the optimum nano dosage as reported in the literature, i.e., 1%~2%. Also, the present authors noted that 20% of nanoparticles were the upper bound to encapsulate the remaining water. Any further increase in this proportion caused a significant overplus of nano silica.

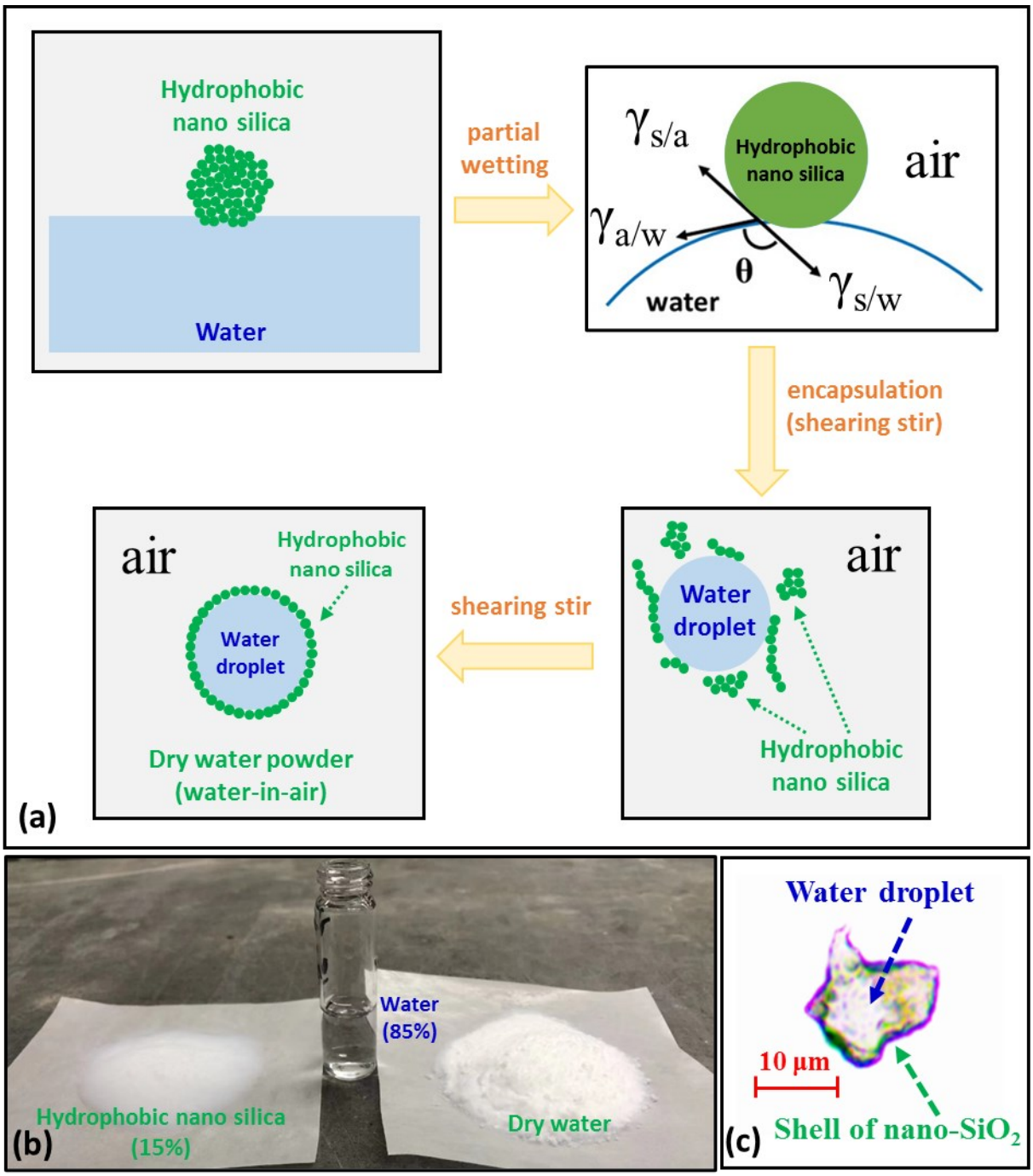


Figure 6.1 Schematic illustrations of producing dry water and the actual product with its microscopic image.

### 6.2.3. Mix proportions and specimen preparations

To avoid the disturbance from compositional ratios, the $SiO_2/Al_2O_3$, $Na_2O/Al_2O_3$ and $H_2O/Na_2O$ molar ratios were all kept constant for N-A-S-H geopolymer mixtures. Also, it should be emphasized here that since the produced three variants of dry water were composed of 80%, 85% and 90% water respectively, this part of water should be removed from the batched water during the mix design. The mixing proportions are now shown in Table 6.2. For each mix, both mortar and paste mixtures were cast. The former was used to measure physical and mechanical properties, including the compressive strength, the mass alongside dimension losses, the neutralized degree and the apparent volume of permeable voids. The latter was taken for the following characterizations, namely XRD, TGA, FTIR and the alkalinity of the geopolymer matrix.

Table 6.2 Mix proportions of N-A-S-H- geopolymers incorporating nano additives.

| Mixture Designation | Metakaolin (g) | Sodium silicate (g) | NaOH (g) | Batched water (g) | Dry water (g) | Nano silica (g) | Sand (g) |
|---|---|---|---|---|---|---|---|
| Reference | 1000 | 911.4 | 239 | 203.7 | 0 | 0 | 2000 |
| NS | 1000 | 911.4 | 239 | 203.7 | 0 | 15 | 2000 |
| DW[a] | 1000 | 911.4 | 239 | 113.7 | 100[a] | 0 | 2000 |
| DW[b] | 1000 | 911.4 | 239 | 118.7 | 100[b] | 0 | 2000 |
| DW[c] | 1000 | 911.4 | 239 | 123.7 | 100[c] | 0 | 2000 |

Note: ‘a’, ‘b’ and ‘c’ indicate the nanoparticle dosage is respectively 10%, 15% and 20%.

The alkali activator was prepared in advance by blending the solid NaOH pellets with the sodium silicate solution along with batched water. Afterwards, the cooled activator was stirred in the mixer for 1 min. Then, the pre-weighed metakaolin was added to mix constantly with the activator until the homogeneous paste mixture was witnessed. Next, the fine aggregates (for mortal only) and the nano additives (either nano silica or dry water) were added and mixed for another 3~5 mins.

Eventually, the fresh geopolymer mixture was cast into cylindrical moulds with a size of Φ50 mm × 100 mm, which were then placed on a vibrator to experience a 30s dynamic compaction. After 24 hours, the specimens, after demolding, were cured in air-tight plastic bags under ambient conditions for up to 28 days.

### 6.2.4. Test protocols

The geopolymer specimens aged 28 days were divided into two series. The first group was tested immediately for various macro-properties and characterizations, while the second group was immersed in the pre-made sulphuric acid condition (1% w/w) for up to 12 weeks. During this period, the sulphuric acid solution was weekly replenished to ensure the acidity as much as possible, and the ratio between the volume of acid solution and the area of exposed surface of specimens was fixed at 10 (Vafaei t al., 2018). The mortar specimens retrieved after 56 and 84 days were tested for mass, diameter and compressive strength changes as well as the neutralized depth. Meanwhile, the respective paste specimens were taken to collect the powder samples for XRD, TGA and FTIR characterizations. In this manner, the cylindrical paste was firstly cut into six slices, and the 4 slices close to the mid-height plane were placed in a customized mould to collect powder samples. The drilling protocol and the actual operation are the same as the previous Chapter 5, see Figure 5.2. In this regard, the first layer of powder samples was gathered from the exterior edge with a thickness of about 2 mm. The second layer was collected at a greater depth (at approximate 4 mm), wherein much less deterioration had been noticed.

The acidity of sulphuric acid solution was daily monitored using an instant-read pH meter. The acid penetration degree inside various geopolymers was visually inspected by spraying the phenolphthalein solution onto the surface of the sliced sample. Accordingly, the region with a pH value greater than 8.3 would display a perceptible red colour (Herriott, 1938; Khan et al., 2020).

Subsequently, the neutralized degree was quantified as the proportion between the colorless length and the original diameter. Further, the powder suspension method (Räsänen and Penttala, 2004; Khan et al., 2020) was adopted to determine the original and residual alkalinity at various depths in geopolymers after sulphuric acid attack. In this regard, the powder samples collected from the exposed geopolymer pastes were blended with the distilled boiling water to result in the suspension at a solid-to-liquid ratio of 1. Then, the pH value of the powder suspension was measured after 24 hours. With regard to the mechanical property, the compressive strength of geopolymers was tested conforming to ASTM C39/C39M-18 (2018).

Further characterizations were conducted to clarify the mechanisms underlying the influence of dry water on the sulphuric acid resistance of N-A-S-H geopolymers. The sulphuric acid attack essentially involves both physical diffusion and chemical reaction behaviours. Hence, the apparent volume of permeable voids (AVPV) was firstly assessed through Equation (5.1), conforming to ASTM C642-13 (2013).

The amorphicity alongside the morphology of geopolymers was examined under X-ray diffraction (XRD), using a Copper-Kα radiation beam (operated at 40kV and 44mA). The step size was constantly fixed at 5°/min, while the diffraction angle (2θ) was set from 10° to 60°. A detailed thermogravimetric analysis (TGA) was carried out within the temperature range of 20~1000°C, along with a heating rate of 10 °C/min under the nitrogen atmosphere. The Fourier-transform infrared spectroscopy (FTIR) was adopted to reveal the chemical bonds constituting N-A-S-H geopolymers. Furthermore, the obtained FTIR spectra were deconvoluted within the range of 800~1250 $cm^{-1}$ to illustrate the structural changes upon the principal Si-O-T band after sulphuric acid attack. The microstructure of various geopolymer pastes was evaluated under the Field Emission Scanning Electron Microscope (FE-SEM) at a 15 kV accelerating voltage to result in a

magnification scale ranging from 300 X to 5000 X. The generated images were binarized further to display the voids and microcracks as the black region and the solid geopolymer gel as fully white. As such, the compactness of examined samples could be quantified by counting the black pixels. Moreover, an Oxford Energy Dispersive X-ray Spectroscope (EDS) was used to analyze the elementary composition of geopolymer pastes.

## 6.3. Results and discussion

### 6.3.1. pH evolution of sulphuric acid solution

When subjected to an acid solution, the penetrating hydrogen ions in geopolymer matrix will be neutralized, which in turn manifests as an increase in the pH value of external acid solution within each immersion cycle (7 days). Now, the pH evolution during each cycle is presented in Figure 6.2. Despite the similar pH profiles at the early stage, the difference appeared to evolve after 28 days of exposure. Seen from Figure 6.2(a-c), when attacking the mixture dosed with dry water, the associated sulphuric acid solution registered a lower pH value than the other two references, namely the one with the lone nano silica and the other one without any nanoparticles. This may indicate that the neutralization progress of hydrogen ions was slower in specimens incorporating dry water. Since the pH value is essentially an exponential function of the hydrogen concentration, the quantity of consumed hydrogen ions could be quantified. Hence, the neutralization potential was computed (Khan et al., 2020), as per Equation (5.2). When exposed to this sulphuric acid solution for up to 84 days, the neutralization potential was determined as 83.8% (pH=1.49) for the group of dry water, whereas the corresponding value was found as 85.2% (pH=1.53) for the one dosed with nano silica and 87.1% (pH=1.59) for the plain mixture, respectively. This implies that adding nano silica and the associated dry water could both decelerate the degradation of the N-A-

S-H framework when subjected to the acid-rich environment. More importantly, the latter was even better than the former.

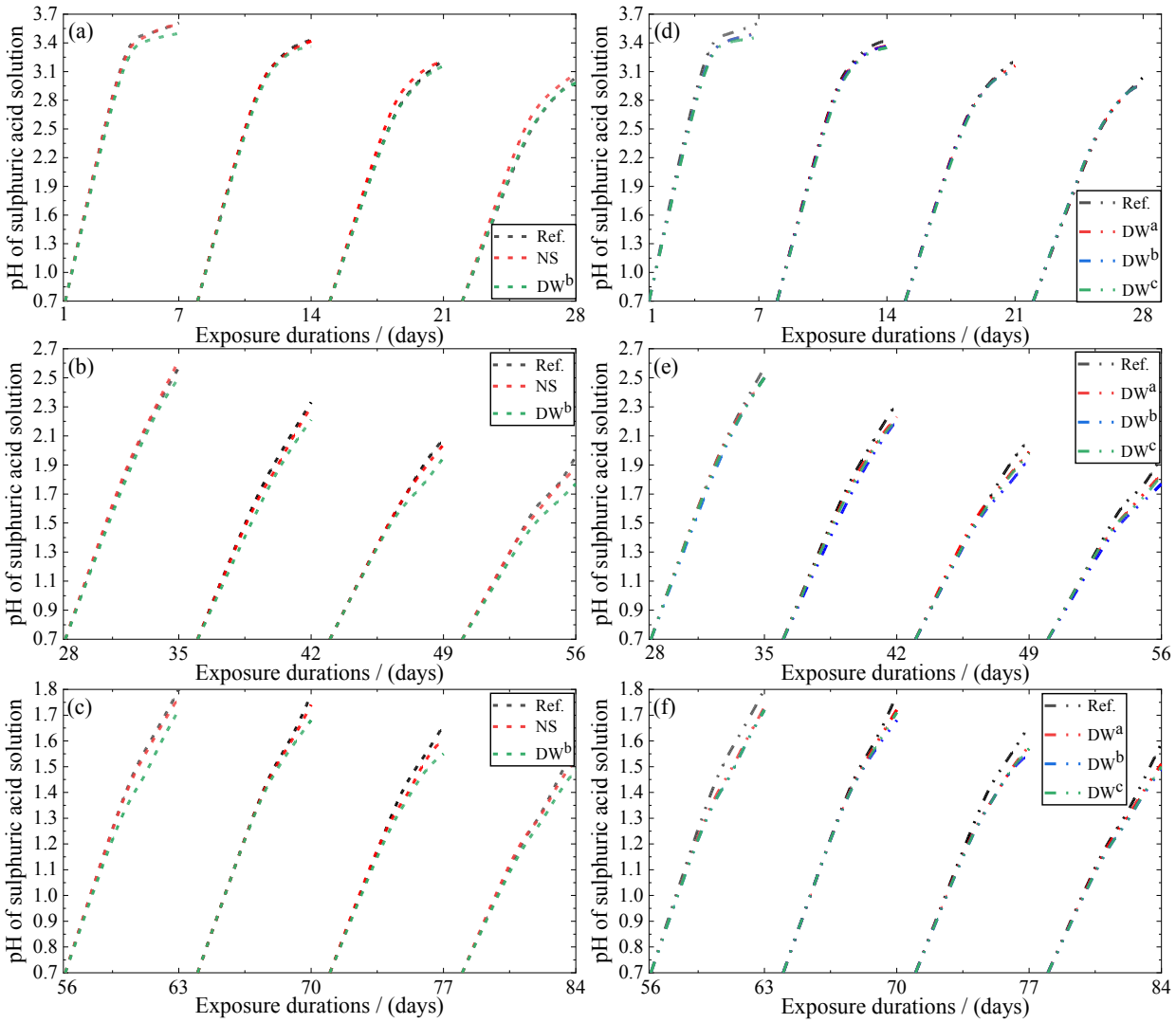


Figure 6.2 pH evolution of sulphuric acid solution.

Further, the effect of the composition of dry water was examined, as shown in Figure 6.2(d-f). Although the mixtures made with various dry water were all seen to display a slower pH evolution than the reference mixture, the mutual difference between the dry water series was relatively minor. The corresponding neutralization potential was respectively computed as 92.8% (pH=1.84),

91.5% (pH=1.77) and 92.6% (pH=1.83) at the 56th days of exposure, and 84.5% (pH=1.51), 83.8% (pH=1.49) and 84.2% (pH=1.50) at the 84th days of exposure.

### 6.3.2. Alkalinity of geopolymers after acid exposure

Besides the pH evolution of sulphuric acid solution, the acid-induced neutralization could also be evaluated by determining the alkalinity of the exposed geopolymer matrix. The alkalinity reflects the integrity of reaction products on the one hand and, prevents the embedded reinforcement from corrosion on the other hand (Garcés et al., 2005). Prior to the sulphuric acid attack, the original pH value of the geopolymer matrix was found about 12.3 for all examined mixes, using the powder suspension method. This value coincided well with the related literature (Khan et al., 2020). The powders samples collected at different layers were examined after 56 days of exposure, and the results are now presented in Table 6.3. One sees that despite the close alkalinity at layer 1, the difference between various mixtures evolved as the examined depth increased (at layer 2). All three mixtures dosed with dry water retained higher alkalinity than the NS and plain reference mixtures. Particularly, the pH of powder suspension sourced from $DW^b$ was the highest across all examined specimens. The visual inspection was also carried out by spraying the phenolphthalein solution onto the surface of geopolymer slices after the acid attack, see Figure 6.3. Figure 6.4 illustrates the neutralized degree of various geopolymers. As expected, the mixtures dosed with dry water displayed a slightly smaller neutralized degree. Also, the tendency supports the previous outcomes with respect to the pH evolution of the sulphuric acid solution and the residual alkalinity of powder suspension.

Table 6.3 pH value of powder suspension derived from varying depths.

| | Ref. | NS | DW[a] | DW[b] | DW[c] |
|---|---|---|---|---|---|
| Layer 1 | 6.34 | 6.37 | 6.39 | 6.43 | 6.45 |
| Layer 2 | 7.90 | 7.98 | 8.02 | 8.30 | 8.12 |

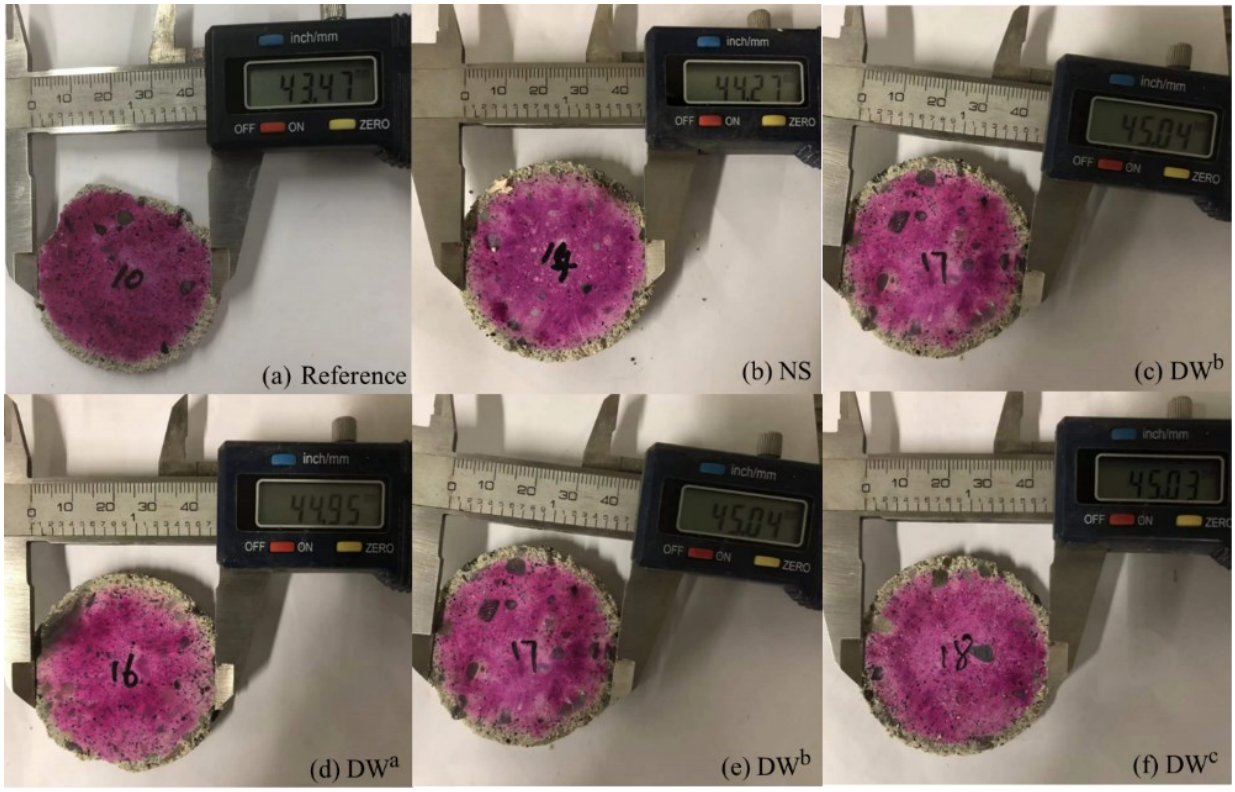


Figure 6.3 Representative images of visual inspection upon geopolymer mortars after 56 days of exposure.

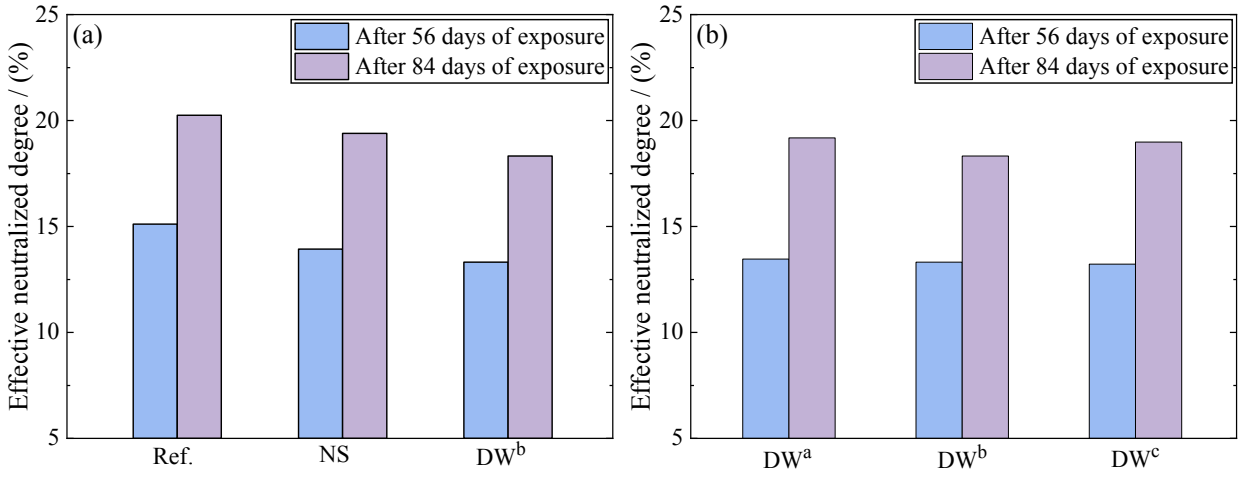


Figure 6.4 The neutralized degree of various geopolymers after sulphuric acid attack.

### 6.3.3. Changes in mass, diameter and compressive strength

Figure 6.5 illustrates the mass and diameter changes of geopolymer specimens, while Figure 6.6 presents the associated changes in compressive strength. Clearly, adding nano silica stabilized dry water reduced losses of mass, diameter and compressive strength in comparison to the plain reference mixture. This advantage was particularly obvious after relatively long exposure, i.e., 84 days. More importantly, the mixture containing dry water ($DW^b$) performed much better than the one dosed with the equivalent amount of lone nano silica (NS). This may be attributed to that besides serving as the supplementary silica source, the encapsulated water in dry water also temporarily improved the alkalinity at the early stage, which may in turn boost the dissolution alongside the subsequent geopolymerization. Among the three examined dry water, 15% nano silica together with 85% water was found as the optimum composition to impart the strongest sulphuric acid resistance to N-A-S-H geopolymers. This is particularly evident from the lowest loss on the dimension of specimens, and the highest remaining compressive strength alongside the least reduction degree after 84 days of exposure. An unexpected reduction in the remaining compressive strength of exposed specimens was noted, when increasing the nano content in dry

water from 15% to 20%. Note here that this value corresponds to 1.5% to 2.0% in the overall mixture. According to prior studies, a nanoparticle content beyond 1.5% was likely to trigger the significant appearance of weak zones in geopolymers, led by the agglomeration of nanoparticles (Sumesh et al., 2017). This in turn acted as defects in geopolymers and eventually offset the enhancement led by nano additives. Given the above, it may explain that continuous improvement was not seen while increasing the nano content of dry water through 15% and to 20%.

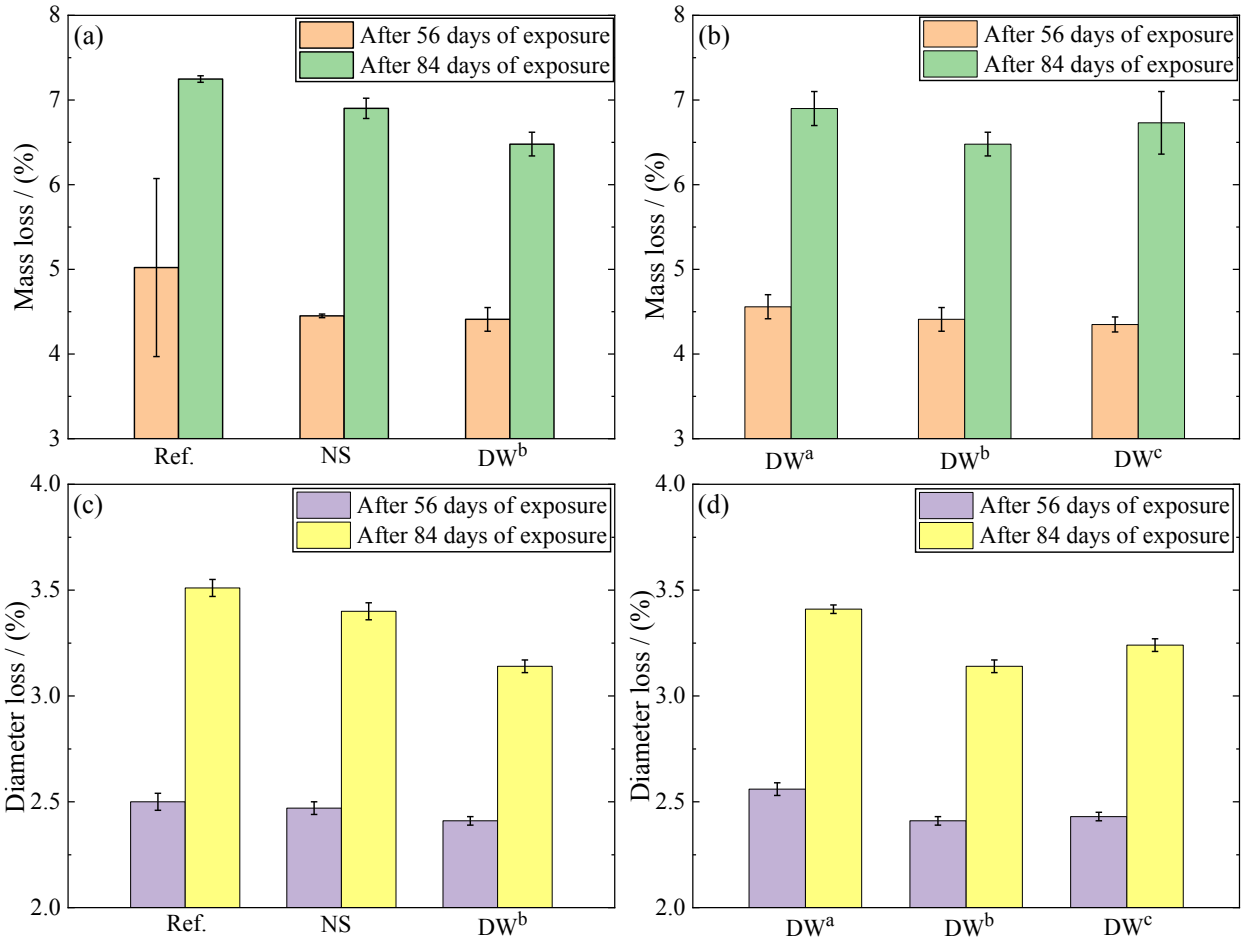


Figure 6.5 Mass and diameter losses of geopolymers after sulphuric acid attack.

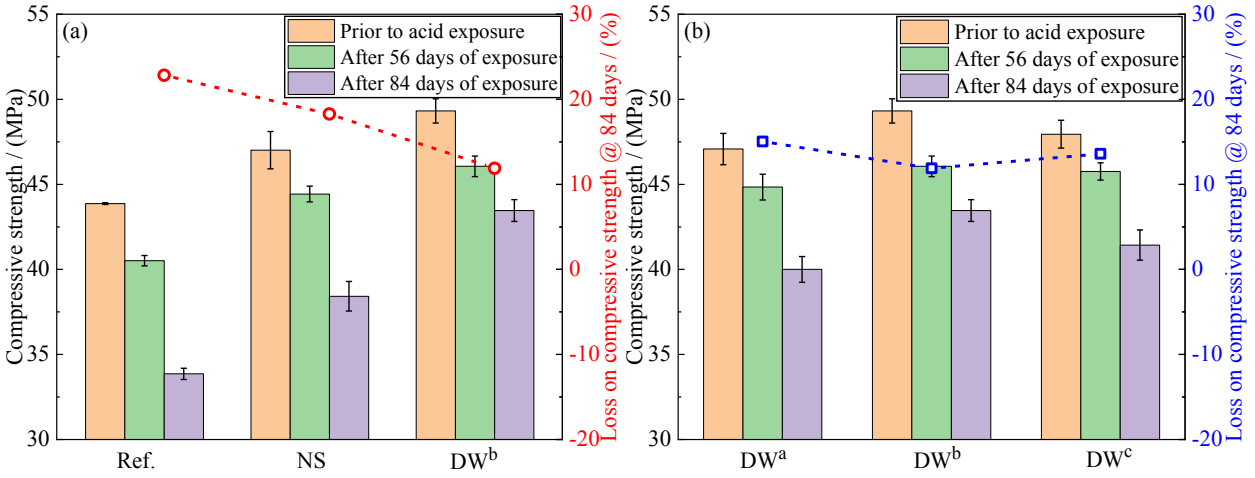


Figure 6.6 Compressive strength of geopolymers right before and after sulphuric acid attack.

### 6.3.4. Apparent volume of permeable voids

The apparent volume of permeable void is recognized as the void volume which is emptied during the specified drying and filled with water during the subsequent immersion. The porous nature of cementitious materials decides that the external deleterious reagents are transportable inside geopolymers, due to the concentration gradient, and this physical diffusion process is usually dominated by the apparent volume of permeable voids (AVPV) (Zhang and Zong, 2014). In this study, the intact geopolymer specimens aged 28 days were tested for this parameter, prior to the sulphuric acid immersion. Seen from Figure 6.7(a), the plain mixture displays the greatest AVPV, while the mixtures made with either the lone nano silica or dry water register much lower values. These two nano additives supply the additional amorphous silica to improve the $SiO_2/Al_2O_3$ ratio slightly. As a result, the aluminosilicate oligomers formed in the corresponding geopolymer may register a slightly higher polycondensation degree. Besides, the liquid-to-solid ratio was reduced in both NS and $DW^b$ mixtures, which may also play a positive part (Monteiro, 2006). Given the above, it may not be surprising to see the lower AVPV in mixtures made with either lone nano silica or dry water. Besides the benefit from nano silica, the activation efficiency was temporarily

enhanced at the early stage in the case of dry water, due to the encapsulated water. This may explain the lower AVPV in the $DW^b$ mixture, in comparison to the NS mixture. According to Figure 6.7(b), increasing the nano silica content in dry water from 10% to 15% reduces the AVPV, whereas the subsequent increase beyond 15% does not lead to the expected improvement. On the one hand, an increase in nano silica content within a range indeed refines the microstructure and compactness of hardened mixtures (Deb et al., 2016). On the other hand, a continuously increased nano content also intensifies the agglomeration of nanoparticles as well as the appearance of weak zones in hardened specimens (Sumesh et al., 2017; Radu et al., 2021), which adversely affects the evolution of pore structure. Based on the obtained results, the optimum dosage of nano silica in dry water was found here as 15%, to achieve the minimum amount of permeable voids. Note that this value corresponds to 1.5% in proportion to the precursor, which agrees with the optimum nano content reported in other related studies (Sumesh et al., 2017).

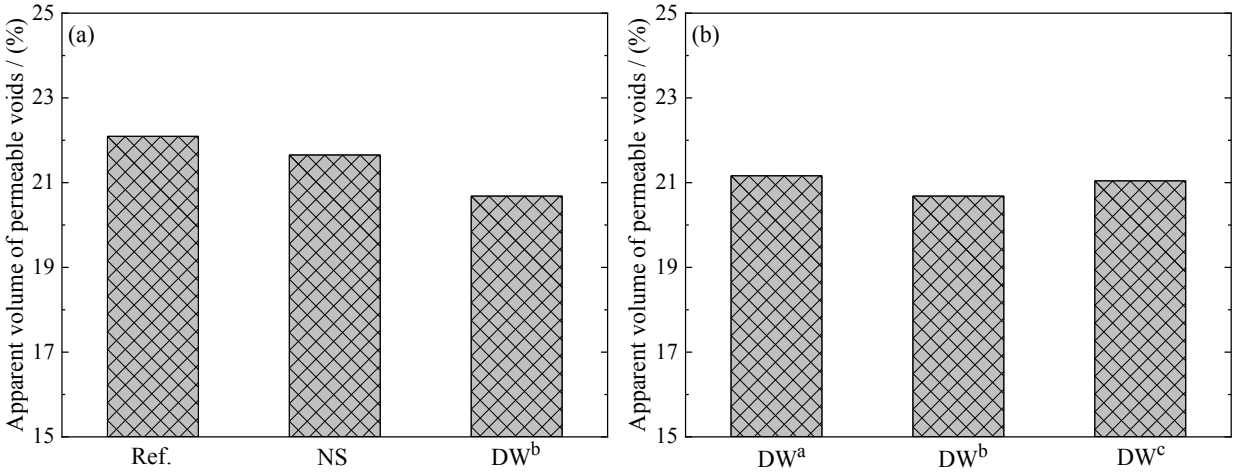


Figure 6.7 The apparent volume of permeable voids of various geopolymers.

### 6.3.5. X-ray diffraction (XRD)

Figure 6.8 maps the XRD spectra for original and exposed geopolymer pastes. A minor crystalline peak ascribed to Anatase (A) could be noted in all cases. Besides, these N-A-S-H geopolymers all display a smooth diffuse hump centred at 27.5º~28º of 2θ in XRD traces, which indicates the amorphous characteristic of N-A-S-H frameworks. Of particular note, the shift of this diffuse hump usually reflects the variation in the degree of amorphocity and in turn, affects the performance of geopolymers. For instance, Yuan et al. reported a slight reduction in 2θ from 28° to 27.8°, and this was accompanied by a noticeable decrease in the compressive strength of geopolymers (Yuan et al., 2016). Seen from Figure 6.8(a), the mixtures made with either lone nano silica or varying dry water display similar XRD spectra as the plain reference. This implies that these nano additives will not substantially change the morphology of N-A-S-H geopolymers. However, a minor shift may be noted in the centre of the diffuse hump. The plain mixture registers the smallest 2θ (~27.5º) for the centre of this diffuse hump, progressively followed by the one incorporating lone nano silica and various dry water-involved mixtures. Figure 6.8(b) reveals XRD spectra for various exposed samples collected at layer 1. Interestingly, their diffuse humps all shift toward the smaller side of the diffraction angle. As the sulphuric acid attack progresses, the penetrating hydrogen ions appear to decompose the polymerized aluminosilicate chain and then, release the tetrahedral Al groups. Therefore, such a leftward shift detected in XRD spectra may indicate a reduction in the degree of amorphocity of geopolymers when subjected to sulphuric acid attack. However, the similar spectra may imply this region was deteriorated completely by hydrogen ions. When it comes to the deeper location (layer 2), the centre of the diffuse hump in the reference mixture locates at about 2θ = 25.8º, while adding dry water dosed with 15% and 20% nano silica causes this hump to shift to 2θ =26.8º and 2θ =26.3º, respectively (see Figure 6.8(c)). This may imply that

the two dry water-involved samples registered the greater residual amorphocity than the reference mixture made without nano additives.

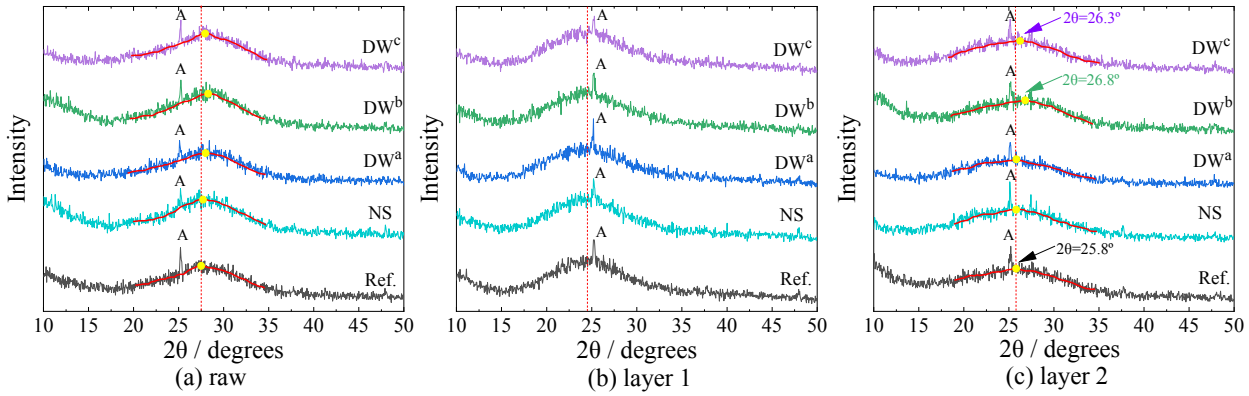


Figure 6.8 XRD outcomes for various geopolymers right before and after sulphuric acid attack.

### 6.3.6. Thermogravimetric analysis (TGA)

The TGA outcomes for various N-A-S-H geopolymers are shown in Figure 6.9. The principal weight loss is frequently witnessed in the temperature range of 20 °C~300 °C, caused by the evaporation of free water and the chemically bound water in N-A-S-H geopolymers (Tchakouté et al., 2017; da Silva Rocha et al., 2018). Seen from Figure 6.9(a), the mixtures produced with various dry water display a significantly higher DTG peak, particularly between 100~200 °C, than the one containing lone nano silica and the plain reference. This possibly indicates the enhanced polycondensation of N-A-S-H gels in dry water-involved mixtures. Figure 6.9(b) reveals the TG/DTG curves for various geopolymer samples collected at layer 2 after 56 days of acid exposure. Interestingly, the DTG peaks linked to N-A-S-H networks evolve significantly in reference and NS mixtures, from 0.111 to 0.176 (-%/°C) and from 0.122 to 0.167 (-%/°C), respectively. Despite a minor increase in the DTG peak after the sulphuric acid immersion, the three mixtures incorporating various dry water all display lower DTG peaks than the above two

mixtures. This increased DTG peak is likely an indication of deteriorations led by sulphuric acid attack upon geopolymers. The aluminosilicate oligomer in N-A-S-H geopolymers is essentially composed of tetrahedral Si and Al atoms that are mutually linked by a bridging oxygen. These Si and Al atoms positioned at different locations usually register the different amount of hydroxyl groups (Davidovits, 2008), as schematically shown in Figure 6.10. Clearly, the side functional groups in the aluminosilicate oligomers are silane which carries more hydroxyls than the intermediate tetrahedral Si and Al atoms. When subjected to the sulphuric acid attack, the polymerized aluminosilicate framework is dealuminated by hydrogen ions to release the connected Al-OH group, and the original aluminosilicate networks will then turn to the silicious framework (Bakharev, 2005). As a result, the relative proportion of hydroxyls carried by silanol groups increases after continuous immersion in the acid environment. Given this, it is reasonable to witness the evolved DTG peak after sulphuric acid attack.

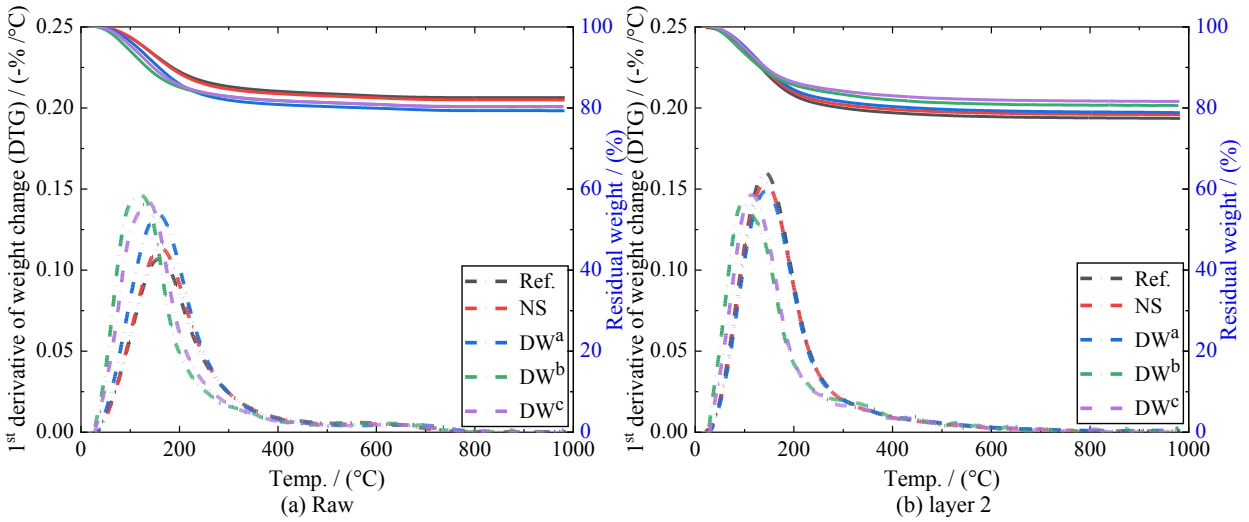


Figure 6.9 TGA outcomes for various geopolymers right before and after sulphuric acid attack.

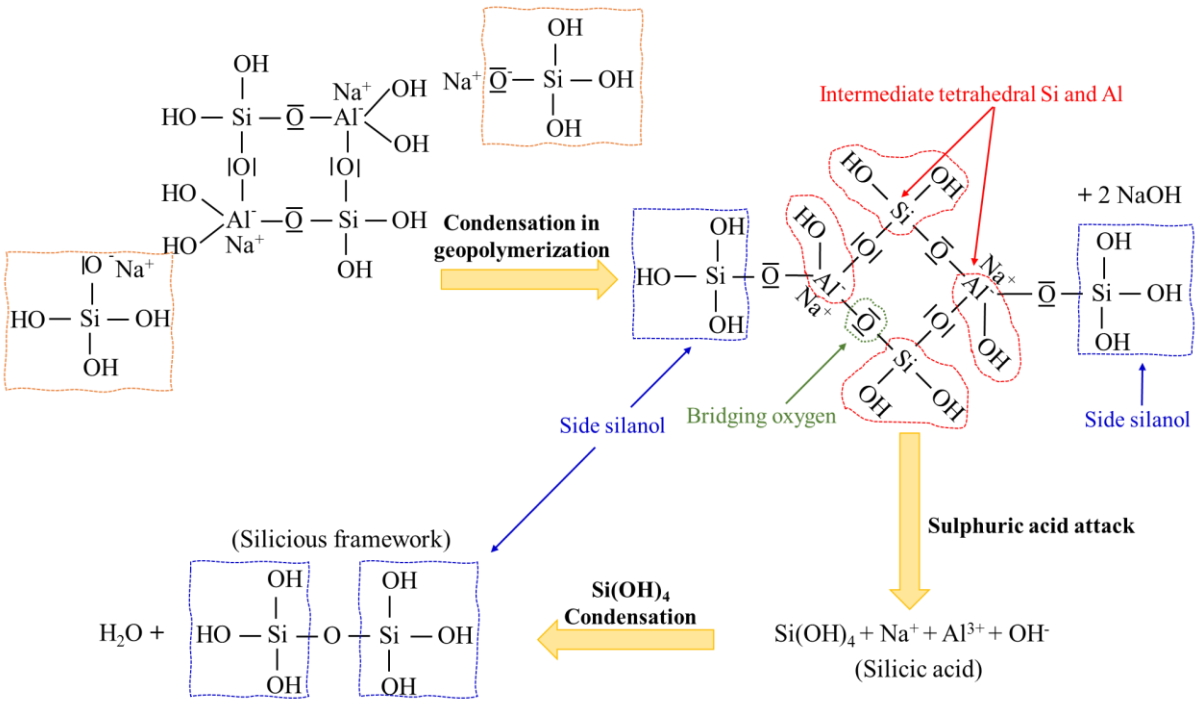


Figure 6.10 The polycondensation and the acid-induced dealumination of N-A-S-H chains.

### 6.3.7. Fourier transform infrared spectroscopy (FTIR)

Figure 6.11 illustrates the obtained FTIR spectra for both unexposed and exposed specimens. As seen therein, the most prominent peak positions at 800~1300 $cm^{-1}$, are attributed to the asymmetric stretching vibrations of 'Si-O-T' band constituting the N-A-S-H framework (Zhang et al., 2012; Chen et al., 2019; Li et al., 2019). Here, 'T' denotes tetrahedral Si or Al atoms. Of particular note, the shift of this principal band is widely recognized to connect with the variation in the degree of geopolymerization (Li et al., 2019). Further, other minor bands located at ~1645 $cm^{-1}$ and ~3370 $cm^{-1}$ are respectively ascribed to the vibrations of H–O–H and –O–H, implying the presence of chemically bound water in geopolymers (Zhang et al., 2012).

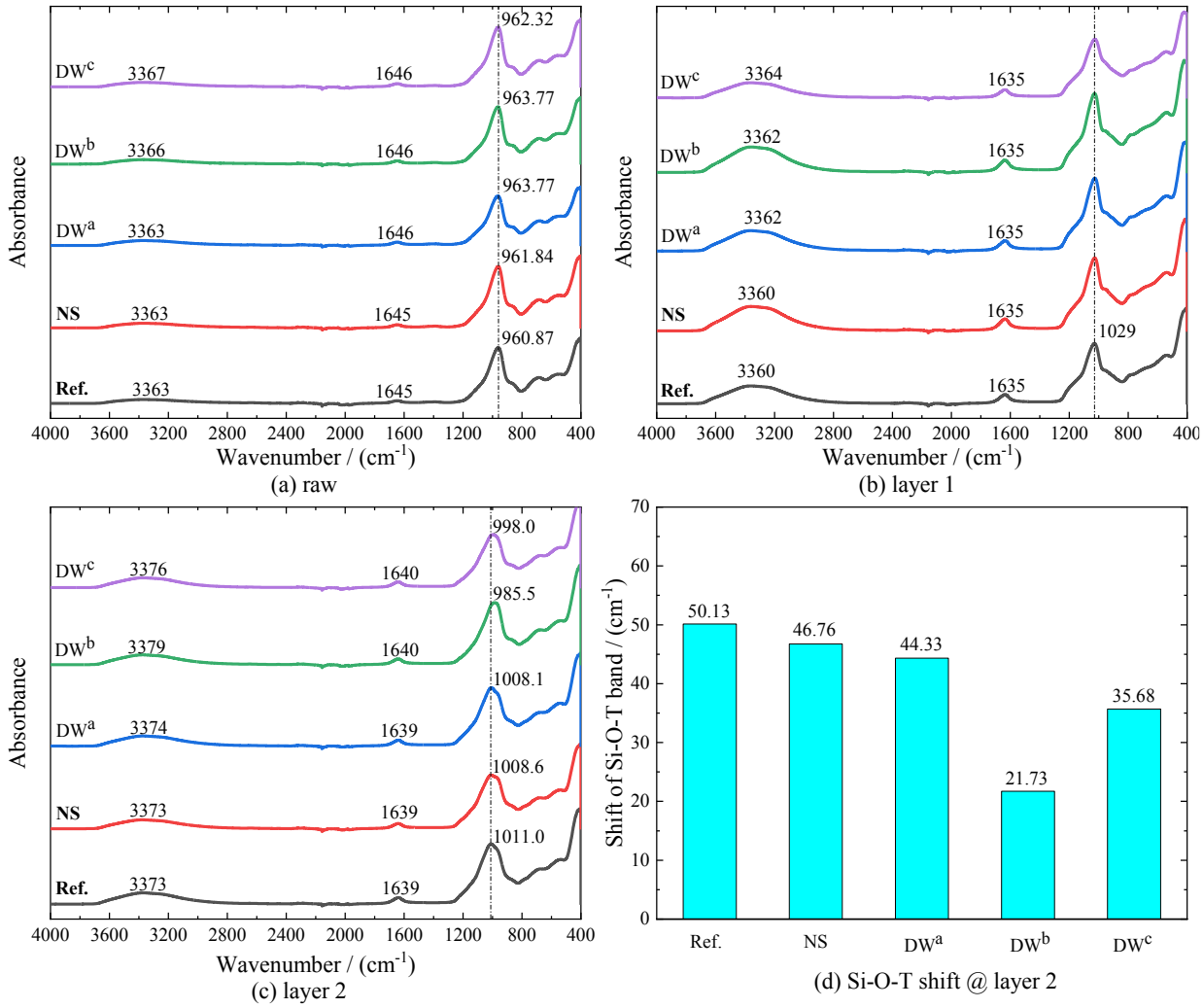


Figure 6.11 FTIR outcomes for various geopolymers right before and after sulphuric acid immersion.

Figure 6.11(a) displays the FTIR spectra for geopolymers prior to sulphuric acid immersion. One sees that despite the minor difference, the wavenumber of peak assigned to the Si-O-T band increases slightly from 960.87 $cm^{-1}$ in the plain reference to 962.32~963.77 $cm^{-1}$ in various dry water-involved mixtures. Figure 6.11(b-c) shows the FTIR spectra for the region located at layers 1 and 2 after 56 days of sulphuric acid exposure. Although all exposed samples display the FTIR spectra with the principal Si-O-T band shifted to the larger end, no obvious difference could be

found between these mixes at layer 1. This is mutually supportable with the XRD results presented in Figure 6.8(b). This again implies that the penetrating hydrogen ions may have deteriorated this area completely. However, the difference evolves as the examined depth increases. According to Figure 6.11(c-d), the paste of plain reference registered the most acid-induced damages, as evident from the largest wavenumber alongside the most shifting extent in terms of the Si-O-T band across all fives mixes. As widely reported, this leftward shift witnessed on the Si-O-T band in FTIR is essentially attributed to the dealumination of polymerized aluminosilicate networks led by hydrogen ions (Zhang et al., 2016) and the appearance of S-O bond due to $SO_4^{2-}$ (Qu et al., 2021). In this regard, the intact N-A-S-H framework gradually decomposes to the silicious framework, as the sulphuric acid attack progresses. This corresponds to an increase in the relative proportion of silicon species in the post-exposed specimens. Besides, the peak of the S-O bond is at about 1070 $cm^{-1}$ (Qu et al., 2021), which is greater than the value found for the overall Si-O-T band in unexposed specimens (~960 $cm^{-1}$). Taken together, the exposed geopolymers experienced a shift toward the larger end in FTIR spectra. Further, compared with the lone nano silica, dry water alleviates the acid-induced damages more significantly. Particularly, the one produced with 15% nano silica imparted the best acid resistance, as evident from the lowest wavenumber in Figure 6.11(c) and the smallest shift in terms of the Si-O-T band in Figure 6.11(d) after sulphuric acid attack. The above results may also explain the fewer losses of mass, diameter, alkalinity and compressive strength seen in dry water series.

Further deconvolutions were also carried out within the range of 800~1250 $cm^{-1}$, to interpret the structural changes in the polymerized Si-O-T band (Zhang et al., 2021; Cortes et al., 2021). In this manner, the following subpeaks are taken into account, as they appear in the above wavenumber range and contribute to the overall shape of the principal Si-O-T band in the FTIR spectrum: Peak

I (~860 $cm^{-1}$) to Si-OH bending; Peak II (~930 $cm^{-1}$) to Si-O-T in $Q_2$; Peak III (~960 $cm^{-1}$) to asymmetric stretching vibrations of nonbridging oxygen (NBO) sites; Peak IV (~1000 $cm^{-1}$) to Si-O-T in a 3-dimensional N-A-S-H network; Peak V (~1070-1080 $cm^{-1}$) to Si-O-Si of silica gels (also the S-O bond after sulphuric acid immersion (Qu et al., 2021)) and, Peak VI (~1150 $cm^{-1}$) to Si-O-T of unreacted metakaolin. The deconvolution with a regression coefficient $R^2$ beyond 0.99 is conducted, as now presented in Figure 6.12 and Figure 6.13. Alongside, the relative area proportion for each of the considered sub-peaks is quantified.

Comparing the FTIR deconvolution results right before and after sulphuric acid attack, one can find there is a considerable reduction in the fraction of Peak III but a significant increase in the proportion of Peak IV, see Figure 6.14. The former may be attributed to the dealumination of the aluminosilicate framework, accompanied by the loss of hydroxyls linked to tetrahedral $AlO_4^-$ groups. The latter is related to the transformation of N-A-S-H into the silicious framework when subjected to sulphuric acid attack. Accordingly, these may imply that adding dry water alleviates the acid-induced damage upon N-A-S-H geopolymers. More importantly, this enhancement was most significant in the two mixtures designated as $DW^b$ and $DW^c$, which were dosed with 15% and 20% nano silica (corresponding to 1.5% and 2.0% in proportion to the precursor), respectively.

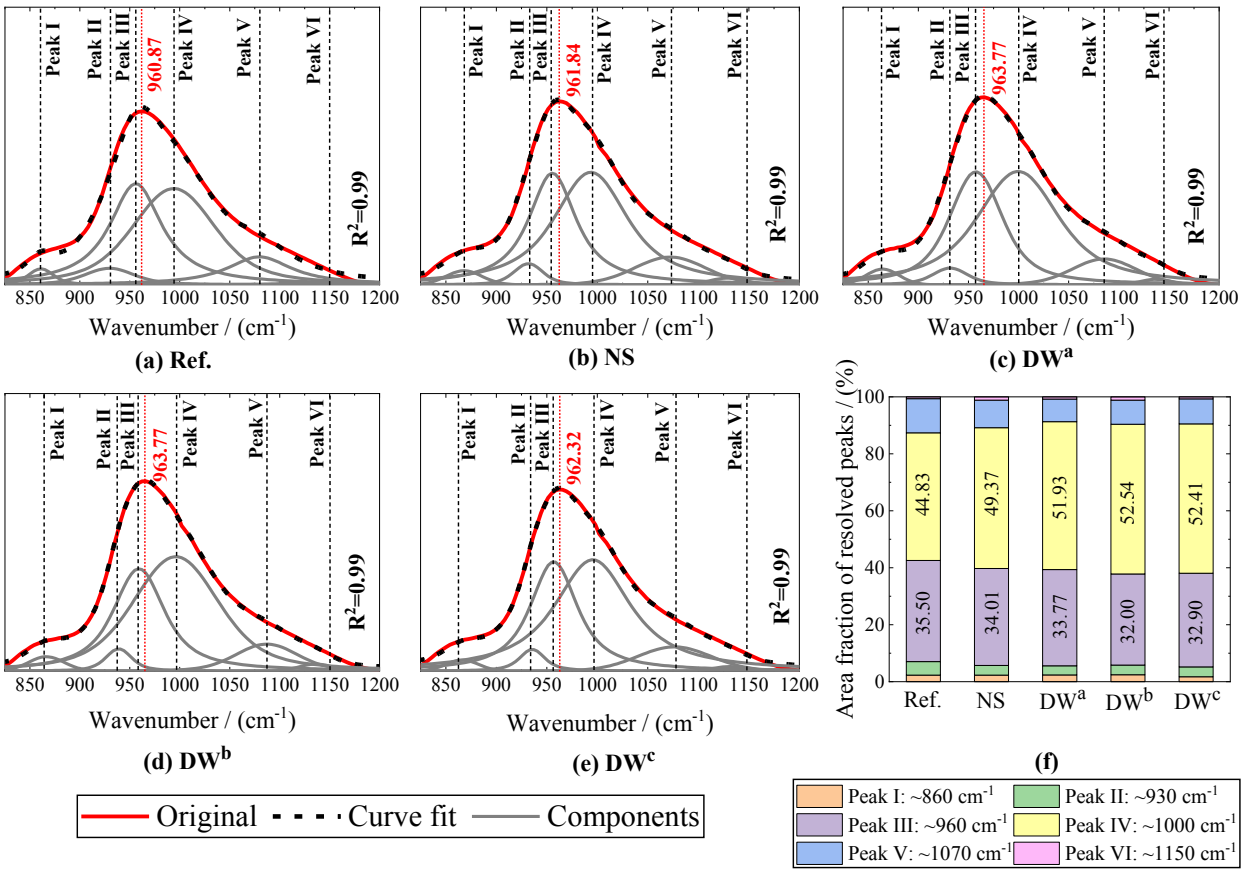


Figure 6.12 FTIR spectral deconvolutions of the main Si-O-T stretching band positioned at 800~1250 $cm^{-1}$ for geopolymers reported in Figure 6.11(a).

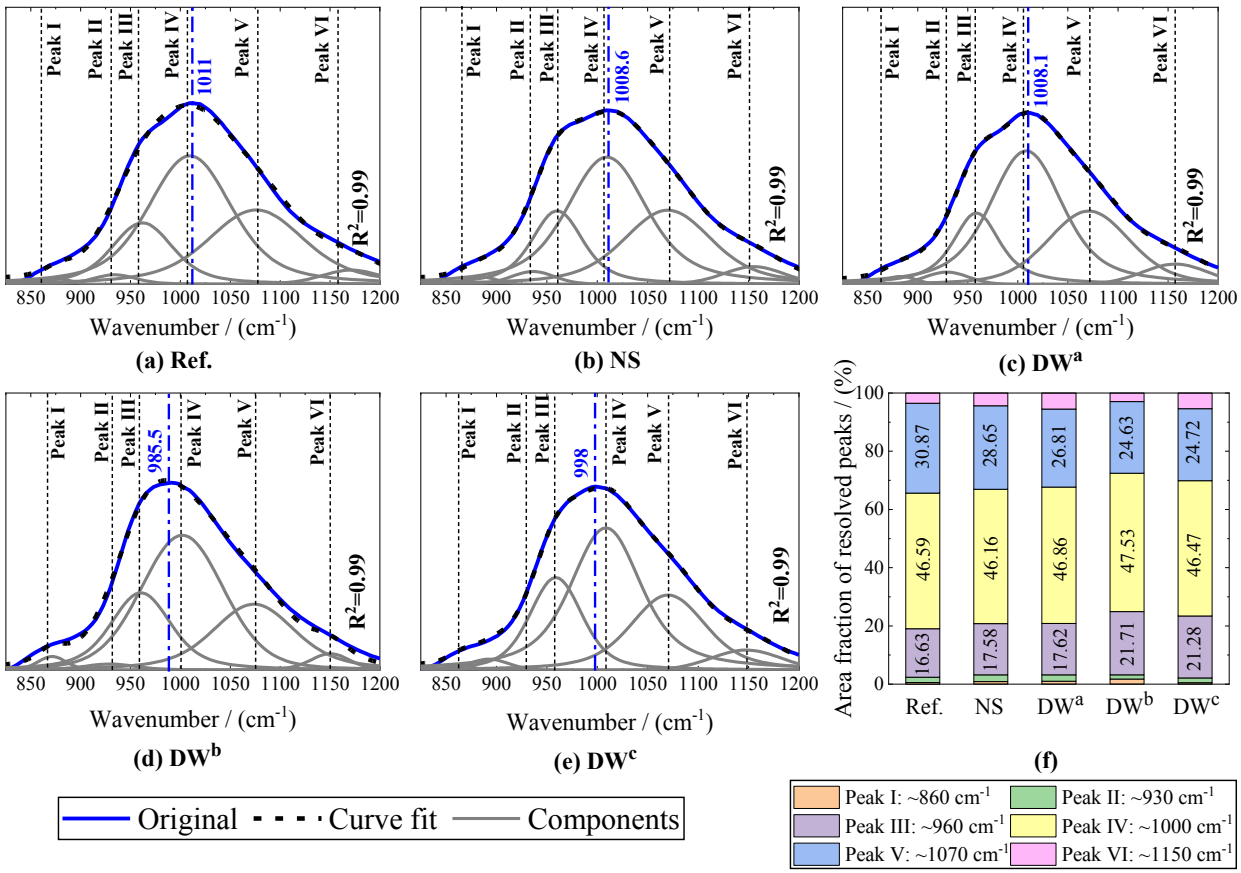


Figure 6.13 FTIR spectral deconvolutions of the main Si-O-T stretching band positioned at 800~1250 $cm^{-1}$ for geopolymers reported in Figure 6.11(c).

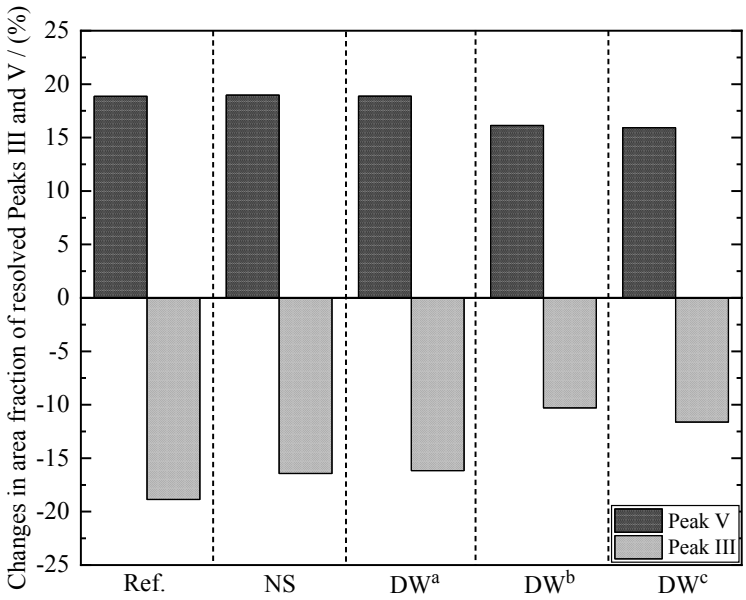

Figure 6.14 Changes in the area fraction of resolved Peaks III and V.

### 6.3.8. Scanning electron microscope and energy dispersive X-ray spectroscope (SEM-EDS)

Prior to the sulphuric acid attack, the microstructure of various geopolymer pastes was evaluated under SEM at 300X magnifications. The raw images alongside the binarized outcomes are now shown in Figure 6.15. Clearly, the widest microcracks (sized 6~7 μm) are captured in the plain reference mixture and in the meantime, visible air-entrained pores could be detected. These together led to its worst microstructure across all examined mixes. On the other hand, the width of microcracks was slightly reduced to 3~4 μm in the mixture incorporating lone nano silica (NS). With regard to the dry water series, the corresponding microstructure was variously improved, as evident from Figure 6.15(c-e). While microcracks still appeared in hardened mixtures, they were considerably smaller than both reference and NS mixtures. Particularly, the size of microcracks in the two mixtures of $DW^b$ and $DW^c$ was decreased below 1 μm.

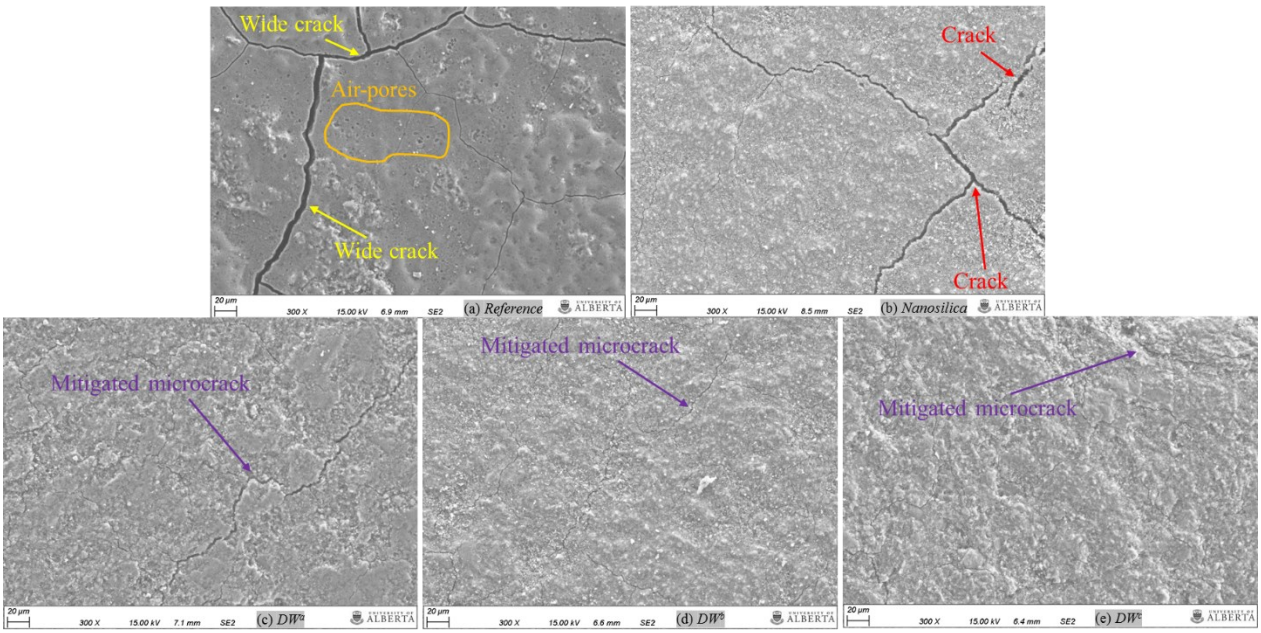


Figure 6.15 SEM images of geopolymer pastes before sulphuric acid immersion (at 300X): (a) reference, (b) NS, (c) $DW^a$, (d) $DW^b$ and (e) $DW^c$.

The microstructure of various exposed specimens was also examined under the same magnification scale, i.e., 300X. These images were generated at the transitional zone, namely the position between the severely degraded and the visually intact regions, as highlighted in Figure 5.24(b). Seen from Figure 6.16, the size of microcracks is noted to evolve after sulphuric acid attack. This is mainly attributed to the depolymerization of the N-A-S-H framework alongside the loss of water. Particularly, the reference mixture once again registered the widest microcrack, then followed by the one made with lone nano silica. On the other hand, the size of microcracks was smaller in those mixtures incorporating dry water. Moreover, the solid region captured at 300X was further magnified up to 5000X to examine the compactness of geopolymerized gels, as shown in Figure 6.17. Once again, the worst texture was found in the reference mixture. While adding lone nano silica refined the microstructure slightly, the long microcrack still showed up in the NS mixture under such a high magnification. With respect to the dry water series, the N-A-S-H networks displayed a significantly denser texture than the previous two mixtures, and no large microcrack was visibly detected.

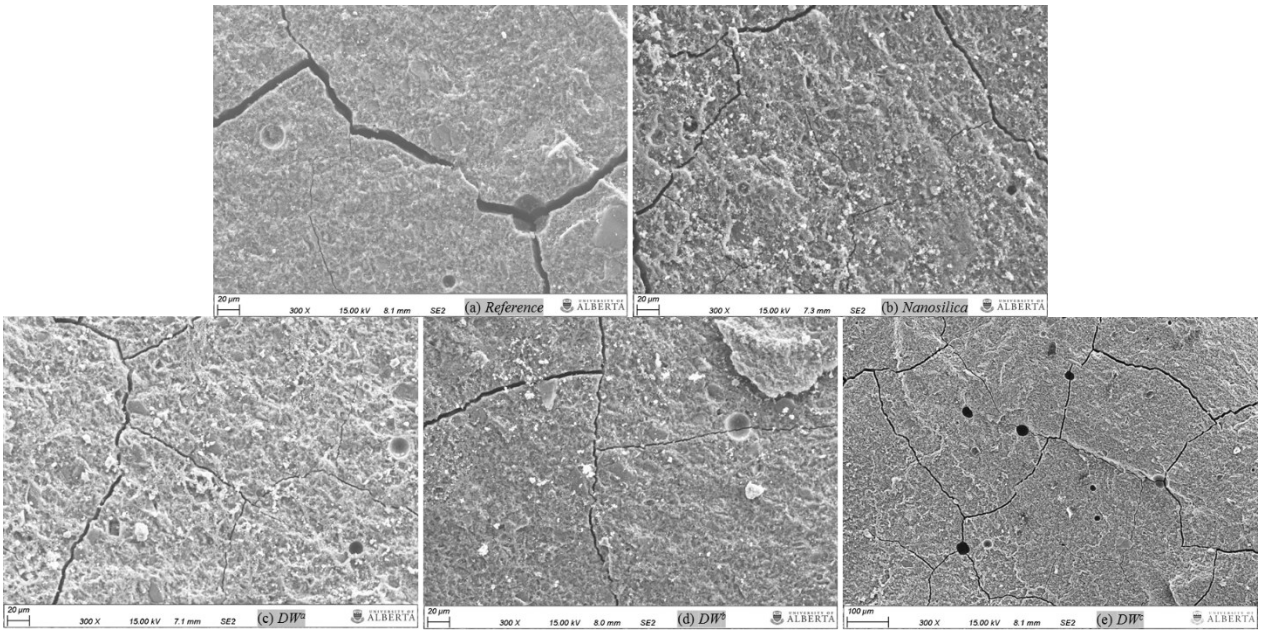

Figure 6.16 SEM images of geopolymer pastes after 12 weeks of acid immersion (at 300X): (a) reference, (b) NS, (c) $DW^a$, (d) $DW^b$ and (e) $DW^c$.

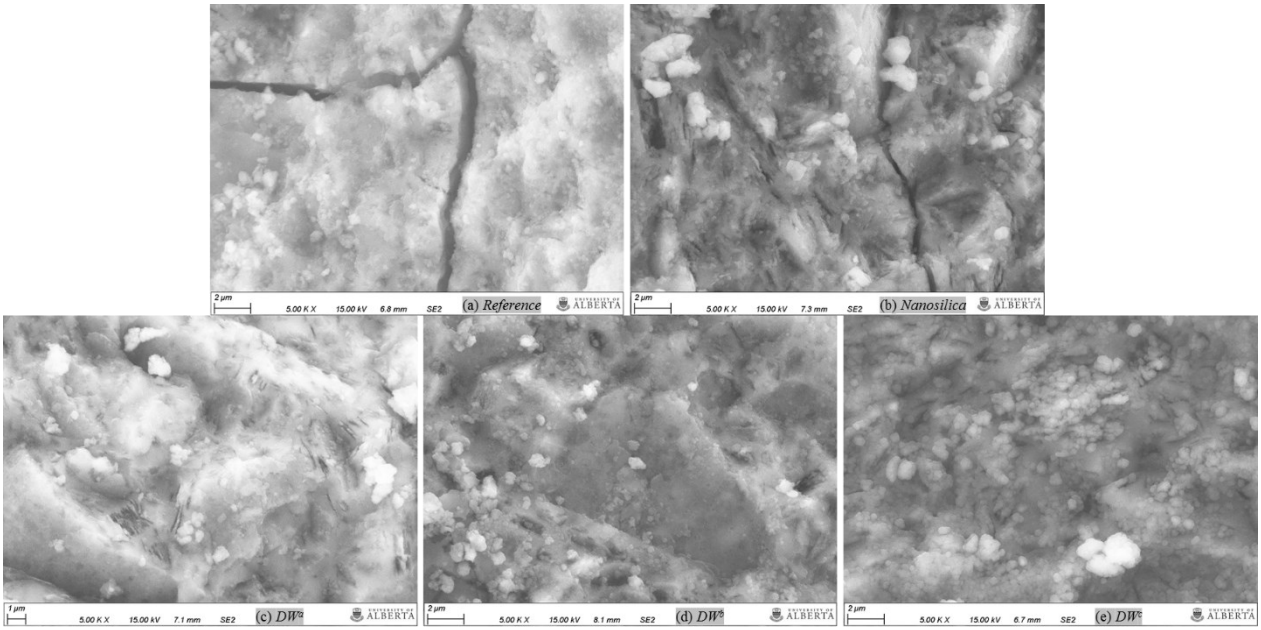


Figure 6.17 SEM images of geopolymer pastes after 12 weeks of acid immersion (at 5000X): (a) reference, (b) NS, (c) $DW^a$, (d) $DW^b$ and (e) $DW^c$.

The SEM images captured under 300X magnification were binarized to evaluate the quality of geopolymer mixtures, as shown in Figures 6.18 and 6.19. In this manner, the black pixels representing microcracks and voids were counted to compute the area fraction of these flaws. According to Figure 6.20, this parameter increased from 4.2% to 7.9% in the reference mixture, ranking first in all examined samples. This may partially explain its worst physical and mechanical performances after sulphuric acid attack. Although the microstructure of NS mixture was slightly improved, the corresponding area fraction of flaws increased to 6.5% after 84 days of exposure, second to the reference mixture. This parameter for various dry water-involved mixtures was all controlled within 6%. Particularly, the mixture of $DW^b$ displayed the minimum value across all cases, corresponding to 4.3%.

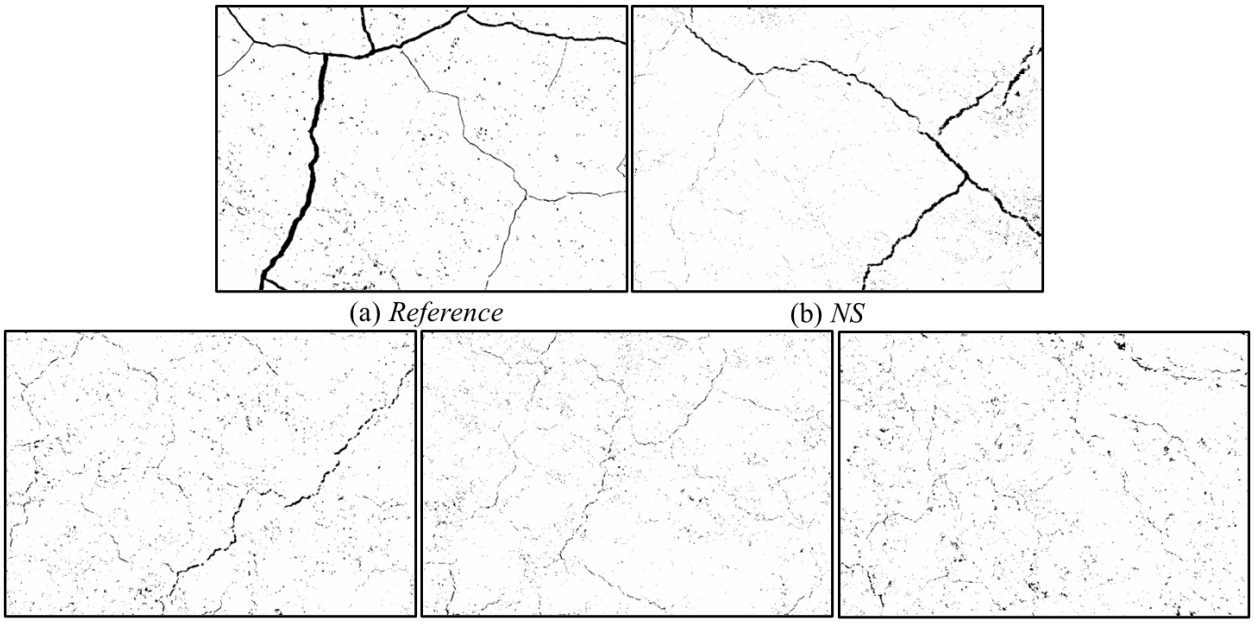


Figure 6.18 Binarized SEM images of geopolymer pastes before sulphuric acid immersion (at 300X): (a) reference, (b) NS, (c) $DW^a$, (d) $DW^b$ and (e) $DW^c$.

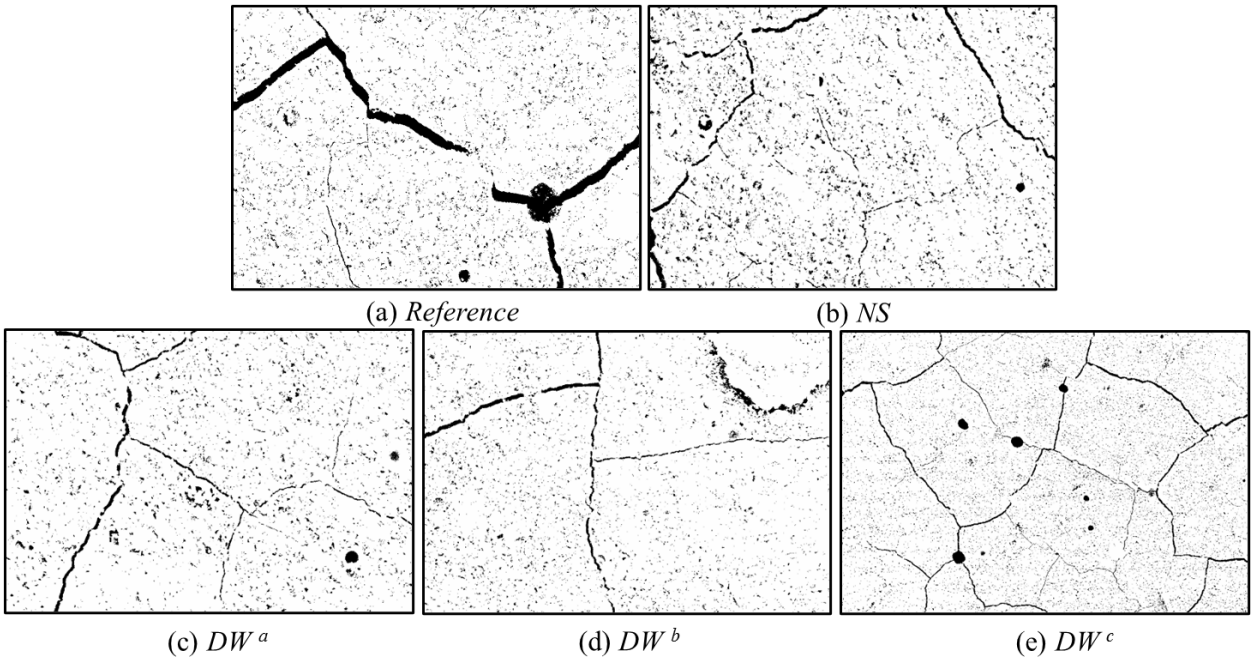


Figure 6.19 Binarized SEM images of geopolymer pastes after 12 weeks of acid immersion (at 300X): (a) reference, (b) NS, (c) $DW^a$, (d) $DW^b$ and (e) $DW^c$.

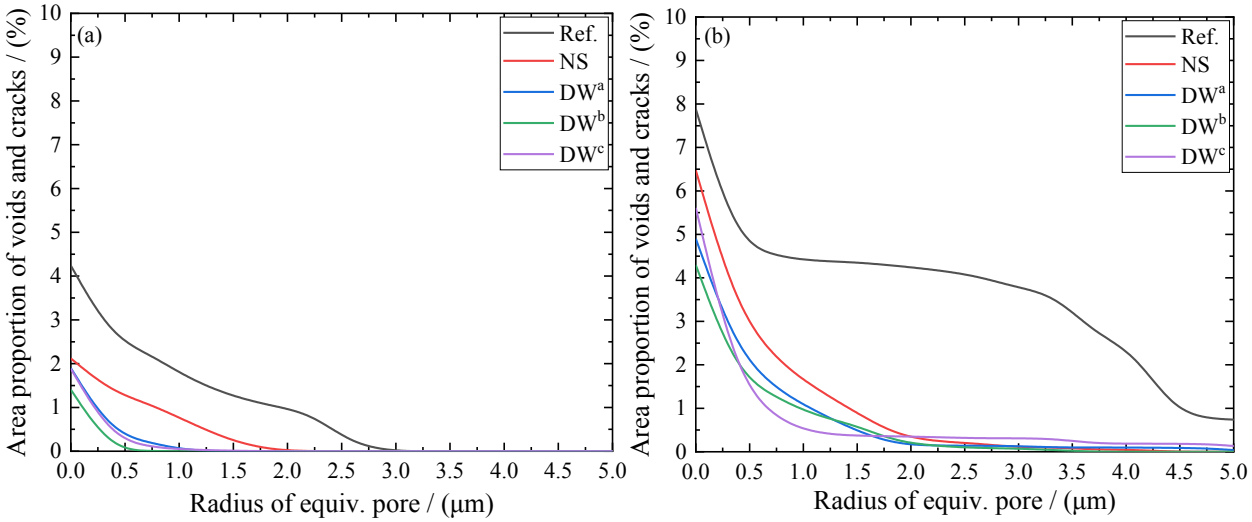


Figure 6.20 Quantified area proportion of voids and cracks in geopolymer mixtures: (a) before and (b) after acid immersion.

The entire area captured at 300X was scanned under the Energy Dispersive X-Ray Spectroscope (EDS) to analyze elementary compositions. O, Na, Al and Si are detected as four prominent elements in N-A-S-H geopolymer paste prior to sulphuric acid immersion, as presented in Table 6.4. Although the chief compositional ratios ($SiO_2/Al_2O_3$, $Na_2O/Al_2O_3$ and $H_2O/Na_2O$) were fixed for all mixes during the mix design stage, the mixtures dosed with dry water ($DW^a$, $DW^b$ and $DW^c$) displayed the highest Si and Al content (39.12%~40.74%), progressively followed by the NS mixture (38.39%) and the reference mixture (37.32%). More importantly, the mixtures made with dry water registered the Na/Al molar ratio closer to the designed value (1.0). This may imply that the dissolution rate of Al and Si from the precursor was much higher.

According to prior studies, the degradation led by acid attack upon geopolymers essentially begins with the disassociation of metal ions by hydrogen ions ($H^+$) (Bakharev, 2005; Vafaei et al., 2018). In the present study, this phenomenon was confirmed by the EDS outcomes of exposed specimens. In Table 6.4, all mixtures experienced a detectable reduction in the relative mass proportion of

alkali metal ions ($Na^+$), indicating the examined region was undergoing acid-induced degradation. The Na/Al molar ratio in the reference mixture reduced drastically from 1.21 to 0.89, equivalent to 26.4% in percentage. Then, it was followed by the NS mixture, dropping from 1.09 to 0.89 (corresponding to 18.3% in percentage). The mixtures containing dry water displayed a relatively small decrease in this ratio. Further, it deserves to emphasize here that in all mixtures, the penetrating sulphur content was found very few at the transitional region. This may be due to that there originally existed few $Ca^{2+}$ in the aluminosilicate precursor as well as the hardened N-A-S-H gel. As a result, no bound sulphate ions could be formed locally. This inference may be supported by a recent study conducted by Qu et al. (2021). For the fly ash/slag-based geopolymer, only the region with detectable gypsum and AFt displayed a noticeable sulphur content of 5.69%~11.99%, whereas the area identified as N-A-S-H gels registered 0.06%~0.56% sulphur only. Taking the above, the N-A-S-H geopolymer may be a promising choice for serving in the environment of sulphate salt, wherein the resultant deterioration is strongly dependent upon the availability of calcium. The principal reason behind the above is there almost exists no calcium in N-A-S-H geopolymer systems to react with sulphate ions and in turn to form expansive ettringite (AFt).

Table 6.4 Relative mass proportion of various elements in N-A-S-H geopolymers before and after sulphuric acid attack.

| Mixture designation | Oxygen (%) | Sodium (%) | Aluminum (%) | Silicon (%) | Sulphur (%) | Na/Al (molar ratio) |
|---|---|---|---|---|---|---|
| **Prior to sulphuric acid immersion** | | | | | | |
| Reference | 49.2 | 13.5 | 13.1 | 24.3 | - | **1.21** |
| NS | 48.3 | 13.3 | 14.3 | 24.1 | - | **1.09** |
| DW[a] | 47.8 | 13.0 | 14.8 | 24.4 | - | **1.04** |
| DW[b] | 47.6 | 12.4 | 15.6 | 24.4 | - | **0.93** |
| DW[c] | 47.0 | 12.2 | 15.4 | 25.4 | - | **0.93** |
| **After sulphuric acid immersion** | | | | | | |
| Reference | 45.6 | 11.7 | 15.5 | 26.7 | 0.4 | **0.89** |
| NS | 50.2 | 11.2 | 14.8 | 23.6 | 0.2 | **0.89** |
| DW[a] | 48.1 | 11.7 | 15.1 | 25.1 | 0.1 | **0.91** |
| DW[b] | 49.0 | 11.1 | 15.0 | 24.8 | 0.1 | **0.87** |
| DW[c] | 43.3 | 12.1 | 16.3 | 28.0 | 0.3 | **0.87** |

## 6.4. Conclusion

This study examined the potential benefits of the hydrophobic nano silica stabilized dry water in improving the acid resistance of N-A-S-H geopolymers. Three variants of dry water, differing in the relative proportion of encapsulating nano silica (10%~20%), were added at 10% to the metakaolin-based N-A-S-H geopolymer. This resulted in an overall nano dosage of 1%~2%, which fell into the optimum range of nanoparticles in literature. Also, the geopolymer mixtures reinforced by dry water were also compared with another two references, one made without any nanoparticles and the other one dosed with nano silica as is. Besides evaluating physical and mechanical properties, a combination of poromeric, morphological, thermal and chemical characterizations

was conducted to characterize the benefits led by dry water on N-A-S-H geopolymers against sulphuric acid attack. Based on the obtained results, the following specific conclusions may be drawn:

(1) The nanoparticles of silica and the associated dry water could both improve the acid resistance of N-A-S-H geopolymers, manifesting as the mitigated losses in mass, diameter, alkalinity and compressive strength. More importantly, the enhancement from hydrophobic nano silica stabilized dry water is even stronger than nano silica as is.

(2) Dry water registers a unique combination of characteristics, including size coarsening, supplementary silica source and temporary water encapsulation. When added to the geopolymer mixture, it is able to boost the activation efficiency and supplies additional amorphous silica for geopolymerization. More importantly, the associated geopolymer experiences a considerable refinement in the microstructure, as evident from the reduced amount of permeable voids and the mitigated microscopic flaws. These together mitigate the penetration of hydrogen ions as well as the replacement of alkali metal ions, and in turn relieve the deterioration of N-A-S-H geopolymers when subjected to the sulphuric acid attack.

(3). The dry water produced from 15% nano silica alongside 85% water is found as the optimum composition to yield the most durable N-A-S-H geopolymer when subjected to the sulphuric acid attack. Also, the associated benefit led by dry water is noted to evolve as the exposure duration increases.

# Chapter 7. Multi-factor models to predict the flow, final set, strength and acid penetration of N-A-S-H geopolymers

## 7.1. Introduction

In the last few decades, the alkali-activated geopolymer has attracted extensive scientific attention, due to its potential to serve as an alternative to conventional OPC systems and in turn, the advantage of reducing the carbon footprint led by cementitious materials (Davidovits et al., 1990; McLellan et al., 2011). Numerous studies have confirmed that such a novel and sustainable material displayed comparable engineering properties to OPC systems, including fair workability, quick set, high strength and excellent durability when designed with a suitable mixing proportion. Notwithstanding active studies on the fresh and hardened properties of alkali-activated geopolymer systems, there still lacks a guideline to ensure satisfactory fresh and hardened properties simultaneously. According to related studies, there exists a mutual interaction between these engineering properties (De Silva et al., 2007; Sadat et al., 2016; Yi et al., 2022). In specific, the high strength is somehow obtained for geopolymers, by sacrificing other properties such as extending the setting process and reducing the flowability. In the available literature, some researchers proposed recommended a range for each chief oxide ratio to achieve high strength. Davidovits (2008) pioneered the following range: $SiO_2/Al_2O_3$=3.5~4.5, $Na_2O/Al_2O_3$=0.8~1.2 and $H_2O/Na_2O$=10~25. More recently, some studies adopted the technique of artificial neural network to optimize the above mixing ratios and updated the optimal range (Kamalloo et al., 2010; Nazari and Torgal, 2013; Ghanbari et al., 2017; Shahmansouri et al., 2021). For instance, Kamalloo et al. (2010) optimized $SiO_2/Al_2O_3$, $M_2O/Al_2O_3$ and $H_2O/M_2O$ (M: Na or K) ratios as 3.6~3.8, 1.0~1.2, and 10~11, respectively, to achieve the maximum compressive strength, whereas the optimal combination was predicted as $SiO_2/Al_2O_3$ = 2.90, $Na_2O/Al_2O_3$ = 0.58, $H_2O/Na_2O$ = 13.75 by

Ghanbari et al. (2017). However, it must be emphasized here that these proposed ranges only considered compressive strength, and other equally important engineering properties were completely ignored. Besides, the aforementioned ratios are typically generated by a private trained network, and no explicit model is presented. This means that the practitioners are very difficult to use these outcomes to conduct and validate their mix design flexibly, particularly when the fresh and hardened properties of geopolymer are assigned with varying priorities.

From the available literature, there is very limited study that establishes the explicit model to guide the mix design for N-A-S-H geopolymers. Considering the multiple mixing oxide ratios, multi-factor modelling may be a promising means to fill this gap. In general, a multi-factor model is established and determined based on the least square method alongside the multiple regression analysis. Although no multi-factor model is found in the available literature to relate the chief oxide ratios to fresh and hardened properties of N-A-S-H geopolymers, such a technique has been maturely used in other related topics for cementitious systems. For example, Zhao et a. (2021) proposed a multi-factor model to predict the chloride penetration in cement-based systems, on the basis of a dataset comprising 12 points, and this model accounted for the water-to-cement ratio, the replacement of fly ash and the substitution of blast furnace slag. More recently, the author also contributed to the application of this concept in correlating various reaction products to the carbonation performance of alkali-activated slag systems, based on 28 experimental data (Li et al., 2022). As compared to the artificial neural network, one of the huge advantages of multi-factor modelling is the significantly reduced demand on the size of the dataset.

As summarized above, the main objective of this Chapter is to develop multi-factor models for predicting workability, final set, compressive strength and the progress of acid attack in N-A-S-H geopolymers, based on the liquid-to-solid, $SiO_2/Al_2O_3$, $Na_2O/Al_2O_3$ and $H_2O/Na_2O$ ratios. It is

wished that when serving as a potential alternative to conventional OPC systems, the outcomes generated in previous Chapters 3&5 are promising to guide the mixture design of N-A-S-H geopolymers for structural members. In the meantime, the proposed multi-factor models shall serve as an efficient predictive tool for practitioners to conduct and validate their mix design for N-A-S-H geopolymers in practice.

## 7.2. Methodology

### 7.2.1. Multiple regression model in matrix form

As introduced earlier, the principal theory behind multi-factor modelling is the regression analysis based on the least square method. In this manner, the correlation between various variables and the outcome could be detected and expressed in a mathematical way. Obviously, the effect of each examined variable could be investigated by a simple regression, separately. However, the outcomes generated in the simple regression are usually misleading, as the mutual correlations between various variables are ignored. Hence, the model established on the basis of multiple regression is more reasonable and also displays greater accuracy.

The objective of multiple regression analysis is to predict the value of a single output based on several independent variables alongside the associated weight coefficient. In general, it could be expressed in a linear model, either naturally or after transformation by variable separation, see Equation (7.1).

$$y_i = \beta_1 + \beta_2 x_{2i} + \beta_3 x_{3i} + \beta_4 x_{4i} + \cdots + \beta_k x_{ki} + \varepsilon_i \qquad (i = 1, 2 \cdots, n) \tag{7.1}$$

Here, $y$ indicates the predicted output while $x$ represents various variables. The subscript $i$ and $k$ denote the size of the dataset and the number of explanatory variables.

It should be noted here that although the above equation is written in a linear function, the considered variable, $x_{ki}$, could be either a single factor or a coupling between different factors. For example, the multi-factor model proposed by Zhao et al. (2021) is originally expressed as Equation (7.2). After transformation, i.e., variable separation, this model could be finally rewritten in a linear expression, as shown in Equation (7.3), and then simplified in Equation (7.4). The corresponding coefficient and variable vectors are illustrated in Equations (7.5).

$$D_0 = b_0(R_{W/B} + b_1)(R_{FA}^2 + b_2 R_{FA} + b_3)(R_{SG} + b_4) \tag{7.2}$$

$$\begin{aligned} D_0 = {} & b_0 R_{W/B} R_{FA}^2 R_{SG} + b_0 b_2 R_{W/B} R_{FA} R_{SG} + b_0 b_3 R_{W/B} R_{SG} \\ & + b_0 b_4 R_{W/B} R_{FA}^2 + b_0 b_2 b_4 R_{W/B} R_{FA} + b_0 b_2 b_3 R_{W/B} \\ & + b_0 b_1 R_{SG} R_{FA}^2 + b_0 b_1 b_4 R_{SG} R_{FA} + b_0 b_1 b_3 R_{SG} \\ & + b_0 b_1 b_4 R_{FA}^2 + b_0 b_1 b_2 b_4 R_{FA} + b_0 b_1 b_3 b_4 \end{aligned} \tag{7.3}$$

$$D_0 = \beta_1 + \beta_2 x_{2i} + \beta_3 x_{3i} + \beta_4 x_{4i} + \cdots + \beta_k x_{ki} \tag{7.4}$$

$$\begin{aligned} \tilde{\beta} &= \left\{ \begin{matrix} b_0 b_1 b_3 b_4, b_0, b_0 b_2, b_0 b_3, b_0 b_4, b_0 b_2 b_4, b_0 b_2 b_3, \\ b_0 b_1, b_0 b_1 b_4, b_0 b_1 b_3, b_0 b_1 b_4, b_0 b_1 b_2 b_4 \end{matrix} \right\} \\ \tilde{x} &= \left\{ \begin{matrix} 1, R_{W/B} R_{FA}^2 R_{SG}, R_{W/B} R_{FA} R_{SG}, R_{W/B} R_{SG}, R_{W/B} R_{FA}^2, \\ R_{W/B} R_{FA}, R_{W/B}, R_{SG} R_{FA}^2, R_{SG} R_{FA}, R_{SG}, R_{FA}^2, R_{FA} \end{matrix} \right\} \end{aligned} \tag{7.5}$$

For the purpose of computation and analysis, the above function in Equation (7.1) could be re-written in a matrix form, by accounting for the entire dataset:

$$Y = Xb \ , \ Y = \begin{pmatrix} Y_1 \\ Y_2 \\ \vdots \\ Y_n \end{pmatrix}, X = \begin{pmatrix} X_{11} & \cdots & X_{1k} & 1 \\ X_{21} & \cdots & X_{2k} & 1 \\ \vdots & \vdots & \vdots & \vdots \\ X_{n1} & \cdots & X_{nk} & 1 \end{pmatrix}, b = \begin{pmatrix} b_1 \\ b_2 \\ \vdots \\ b_n \end{pmatrix}, \varepsilon = \begin{pmatrix} \varepsilon_1 \\ \varepsilon_2 \\ \vdots \\ \varepsilon_n \end{pmatrix} \tag{7.6}$$

Here, $Y_n$ indicates the predicted value for the $n^{\text{th}}$ output, while $X_{nk}$ means the value of the $k^{\text{th}}$ item after variable separation sourced from the $n^{\text{th}}$ set of data. Further, the size of the coefficient vector, $b$, depends on the number of items after variable separation, $k$. $\varepsilon$ denotes the residual error.

### 7.2.2. Residual and least square criterion

As aforementioned, the coefficient vector, b, is a $n\times1$ vector of estimates of $\beta$, and $\varepsilon$ is a $n\times1$ vector of residuals when multiple data are considered. So that, the value of the residual error vector could be computed by subtracting the predicted and the actual values, see Equation (7.7).

$$\varepsilon = y - Xb \tag{7.7}$$

Then, the least square estimator, $S(\varepsilon)$, is expressed as the product between the residual error vector and its transposition, as shown in Equation (7.8). This estimator essentially means the sum of squares of the residuals. Note further that, $S(\varepsilon)$ has scalar values as $\varepsilon$ is a $n\times1$ column vector.

$$S(\varepsilon) = \sum \varepsilon_i = \varepsilon^{'}\varepsilon \tag{7.8}$$

Substituting Equation (7. 7) into Equation (7.8), the least square estimator, $S(\varepsilon)$, could be further updated as Equation (7.9), which now completely depends on the input variables, outputs and involved coefficients.

$$S(\varepsilon) = (y - Xb)^{'}(y - Xb) = y^{'}y - y^{'}Xb - b^{'}X^{'}y + b^{'}X^{'}Xb \tag{7.9}$$

### 7.2.3. Determination of coefficients for regression model

Recall that, the least square estimator, $S(\varepsilon)$, is a scalar value, indicating the residual error between the predicted value and the actual observation. In the meantime, as the value of $y$ and $X$ can be obtained from the actual experimental observation, the only unknown in Equation (7.9) is the coefficient vector, $b$. Thus, the optimum solution to the proposed multi-factor model shown in Equation (7.1) will be found when the residual error is minimum. In this manner, the first-order derivative of $S(\varepsilon)$ is taken and then set to zero, see Equation (7.10).

$$\frac{\partial S(\varepsilon)}{\partial b} = 0 \tag{7.10}$$

Note here that in Equation (7.9), the first term, $y'y$, is a scalar value as it is an output of a $1\times n$ row vector and a $n\times 1$ column vector. The second and third terms are essentially identical, as each of them eventually yields a $1\times 1$ constantly symmetric matrix. Hence, these two terms could be replaced as $2b'X'y$ or $2\,y'Xb$. With regard to the last term in Equation (7.9), it is a quadratic form in terms of coefficient vector $b$. So that, the first-order derivative of this term is a vector and could be written as $2X'Xb$. Given the above, the first-order derivative of the least square estimator, $S(\varepsilon)$, is obtained as:

$$\frac{\partial S(\varepsilon)}{\partial b} = -2X'y + 2X'Xb \tag{7.11}$$

Then, setting Equation (7.11) equal to 0, the coefficient vector, $b$, can be solved by Equation (7.12).

$$b = (X'X)^{-1}X'y \tag{7.12}$$

### 7.2.4. Proof of minimum residual

A proof that $\varepsilon$ minimizes the sum of the squares of the residuals could be validated by Equation (7.13). As seen therein, the second-order derivative of the least square estimator, $S(\varepsilon)$, equals twice of the product between $X'$ and $X$, which is determined as a positive definite matrix (also known as the Hessian matrix). Therefore, the coefficient vector, $b$, solved by Equation (7.12) indeed registers the minimum residual error.

$$\frac{\partial^2 S(\varepsilon)}{\partial^2 b} = \frac{\partial^2 S(\varepsilon)}{\partial b \partial b'} = 2X'X \tag{7.13}$$

### 7.2.5. Coefficient of determination

The error between the actual observation and the predicted value could be quantified by evaluating the corresponding coefficient of determination, $R^2$, using the following Equations (7.14) and (7.15).

$$R^2 = 1 - \frac{SSR}{SST} = 1 - \frac{\varepsilon^{'}\varepsilon}{y^{'}Ny} = \frac{b^{'}X^{'}NXb}{y^{'}Ny} \tag{7.14}$$

$$N = I - \frac{1}{n}ll^{'} \tag{7.15}$$

Here, *SST* and *SSR* respectively denote the total variation and the residual variation in $y$, $I$ is the identity matrix, $l$ is the unit vector, and $l'$ represents the inverse vector.

### 7.3. Establishment of multi-factor models

#### 7.3.1. Find relationship between variables and predicted outcomes

The multi-factor models require sufficient experimental observations first. Accordingly, together with 12 mixtures prepared in Chapter 3, over 60 mixtures were produced to establish the dataset for workability, final set and compressive strength. 85% of them, as now presented in Table 7.1, are selected randomly to establish the proposed multi-factor models. The remaining 15%, as illustrated in Table 7.2, are used later to validate the proposed models. The process to establish the multi-factor model is as follows. First, a correlation between each explanatory variable ($x_i$) and the output ($y$) is established. This study aims to investigate the effect of compositional ratios on various engineering properties of N-A-S-H type geopolymers. So that, firstly, the three compositional oxide ratios namely, $SiO_2/Al_2O_3$, $Na_2O/Al_2O_3$ and $H_2O/Na_2O$, are selected as three explanatory variables. Note also that a change in any one of the above ratios will automatically alter the liquid-to-solid ratio. Hence, it is taken here as the fourth explanatory variable when developing the corresponding multi-factor models for workability, final set, compressive strength and acid penetration.

According to the previous results and discussion in Chapter 3, the flow diameter of freshly produced N-A-S-H geopolymer increases with an increase in the amount of any of the three compositional ratios (see Figure 7.1), and an approximately linear correlation may be assumed. Hence, a preliminary model for flow diameter is described as Equation (7.16). However, this model does not account for the coupling between the selected variables. Thus, the mutual combinations between these compositional oxide ratios were now taken into account. And consequently, the multi-factor model for the flow diameter of N-A-S-H type geopolymer is updated as Equation (7.17).

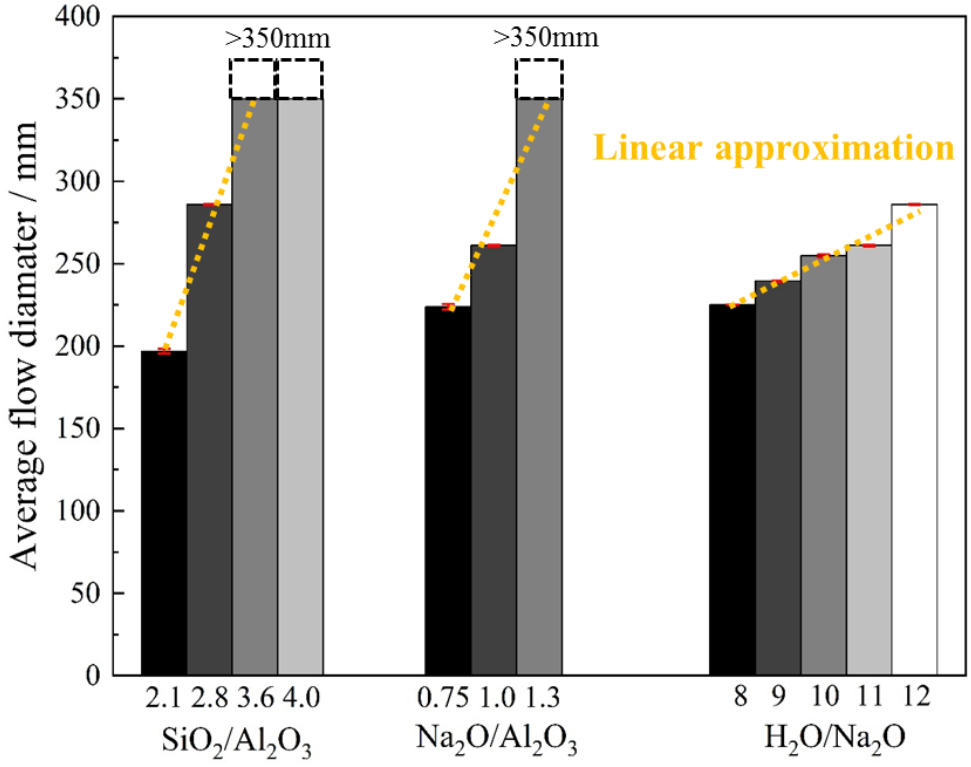


Figure 7.1 Correlation between flow diameter and various compositional oxide ratios.

$$F_{flow} = a_1 x_1 + a_2 x_2 + a_3 x_3 + a_4 x_4 + a_5 \tag{7.16}$$

$$
\begin{aligned}
&F_{flow} = f_1 + f_2 \quad with \\
&f_1 = a_1 x_1 + a_2 x_2 + a_3 x_3 + a_4 x_4 + a_5 \\
&f_2 = a_6 x_4 (x_1 + a_7 x_2 + a_8 x_3) + a_9 x_1 (x_2 + a_{10} x_3 + a_{11} x_2 x_3)
\end{aligned} \tag{7.17}
$$

Here, $x_i$ denotes the individual explanatory variable: $SiO_2/Al_2O_3$ (Si/Al), $Na_2O/Al_2O_3$ (Na/Al), $H_2O/Na_2O$ (H/Na), and the liquid-to-solid ratio when *i* increases from 1 to 4, respectively.

With regard to the final set, the actual experimental observations presented in Figure 7.2 is taken as an example here to correlate the final set with various compositional oxide ratios. It implies that there may exist optimum values within the range of examined compositional ratios to yield the quickest setting process. Based on Figure 7.2 and also other data shown in Table 7.1, the corresponding value is assumed here as 2.4~2.8 for $SiO_2/Al_2O_3$, 0.75~1.0 for $Na_2O/Al_2O_3$ and 9~10 $H_2O/Na_2O$, respectively. Accordingly, a parabolic function is adopted in this study to simulate the correlation between oxide ratios and the setting time. However, as with flow, the setting time is once again modelled using a linear Equation to capture the effect of the liquid-to-solid ratio. The uncoupled multi-factor model for the final set is shown in Equation (7.18). This first-generation model is updated further after accounting for the mutual interactions between the four explanatory variables, and is expressed in Equation (7.19).

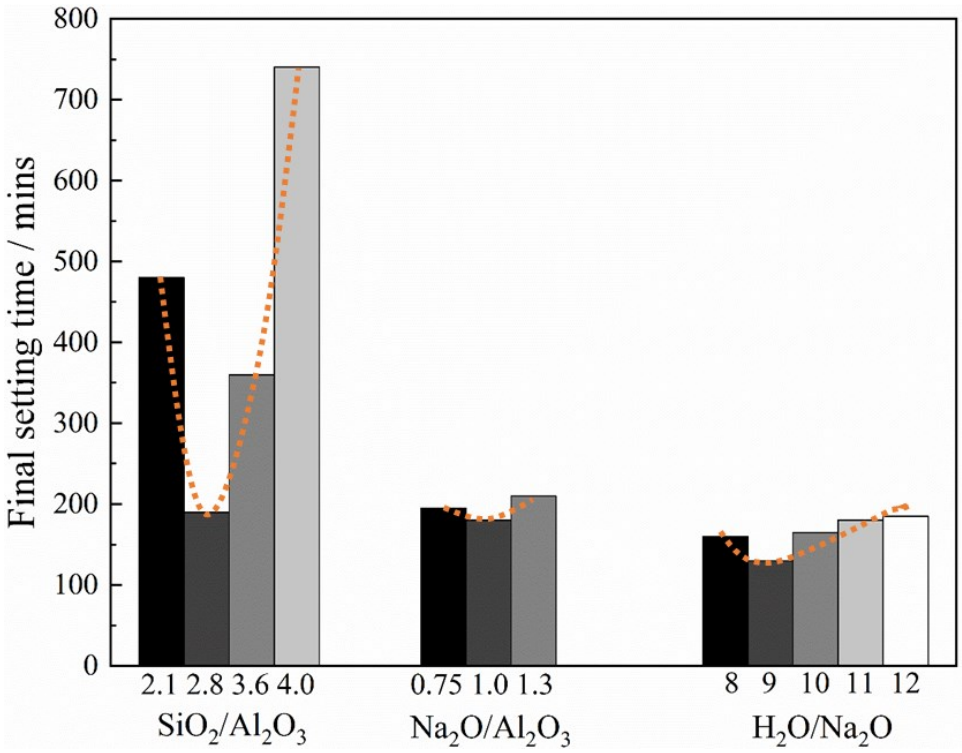


Figure 7.2 Correlation between final set and various compositional oxide ratios.

$$F_{set} = a_1(x_1 - 2.4)^2 + a_2(x_2 - 0.8)^2 + a_3(x_3 - 9)^2 + a_4 x_4 + a_5 \tag{7.18}$$

$$\begin{aligned} &F_{set} = f_1 + f_2 \quad with \\ &f_1 = a_1(x_1 - 2.4)^2 + a_2(x_2 - 0.8)^2 + a_3(x_3 - 9)^2 + a_4 x_4 + a_5 \\ &f_2 = a_6(x_1 - 2.4)(x_2 - 0.8)(x_3 - 9)(x_4 + a_7) \end{aligned} \tag{7.19}$$

As for compressive strength, an increase in the $SiO_2/Al_2O_3$ ratio or a drop in the $Na_2O/Al_2O_3$ ratio within the examined range yields a higher strength, see the representative batch shown in Figure 7.3. Again, due to their monotonic behaviour, a linear correlation is assumed for their influence on compressive strength. The optimum $H_2O/Na_2O$ is determined as 9~10 for N-A-S-H geopolymers, based on the dataset shown in Table 7.1. So that, the correlation between this ratio and the compressive strength may be approximated through a parabolic function. The multi-factor models

for compressive strength, are shown uncoupled in Equation (7.20) and, in Equation (7.21) with coupling considered.

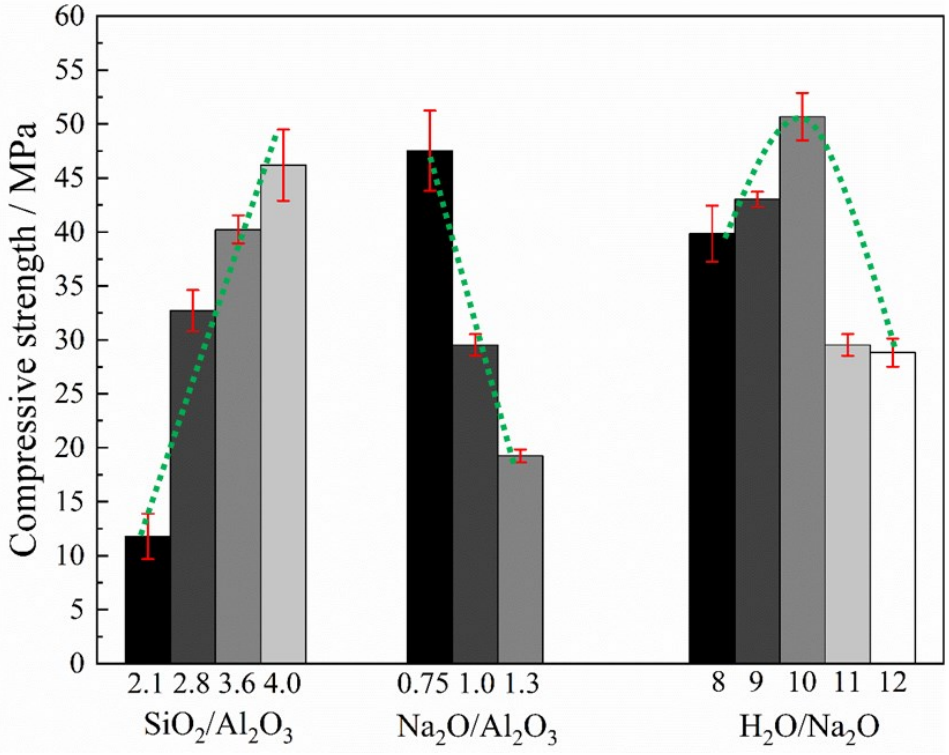


Figure 7.3 Correlation between compressive strength and various compositional oxide ratios.

$$F_{strength} = a_1 x_1 + a_2 x_2 + a_3 (x_3 - 9)^2 + a_4 x_4 + a_5 \tag{7.20}$$

$$\begin{aligned} &F_{strength} = f_1 + f_2 \quad with \\ &f_1 = a_1 x_1 + a_2 x_2 + a_3 (x_3 - 9)^2 + a_4 x_4 + a_5 \\ &f_2 = a_6 (x_1 + a_7)(x_2 + a_8)(x_4 + a_9) + a_{10} x_1 x_2 x_4 (x_3 - 9)^2 \end{aligned} \tag{7.21}$$

Table 7.1 Training dataset for fresh and hardened properties and predicted outcomes.

| $SiO_2/Al_2O_3$ | $Na_2O/Al_2O_3$ | $H_2O/Na_2O$ | L/S | Tested Flow (mm) | Predicted Flow (mm) | Tested Set (min) | Predicted Set (min) | Tested Strength (MPa) | Predicted Strength (MPa) |
|---|---|---|---|---|---|---|---|---|---|
| 2.1 | 0.75 | 11 | 0.899 | 101.5 | 107.8 | 140 | 144 | 17.3 | 17.6 |
| 2.1 | 0.95 | 11 | 1.138 | 152.3 | 167.8 | 185 | 172 | 11.6 | 12.7 |
| 2.2 | 0.75 | 11 | 0.923 | 109.3 | 126.6 | 100 | 131 | 21.3 | 22.2 |
| 2.3 | 1.00 | 9 | 1.090 | 147.1 | 154.1 | 115 | 124 | 33.0 | 27.5 |
| 2.3 | 1.00 | 10 | 1.167 | 185.5 | 188.0 | 130 | 131 | 23.8 | 23.4 |
| 2.3 | 1.00 | 12 | 1.322 | 225.4 | 231.3 | 160 | 179 | 10.3 | 14.5 |
| 2.3 | 1.00 | 14 | 1.476 | 255.7 | 241.7 | 220 | 269 | 8.9 | 6.9 |
| 2.4 | 0.75 | 11 | 0.969 | 172.9 | 160.1 | 120 | 123 | 30.8 | 30.7 |
| 2.4 | 0.95 | 11 | 1.208 | 203.5 | 210.0 | 135 | 129 | 20.6 | 24.0 |
| 2.4 | 1.15 | 11 | 1.447 | 285.9 | 280.6 | 180 | 184 | 20.2 | 17.7 |
| 2.4 | 0.80 | 11 | 1.029 | 189.6 | 170.7 | 85 | 120 | 27.5 | 29.0 |
| 2.4 | 1.00 | 11 | 1.268 | 242.7 | 225.7 | 140 | 139 | 20.3 | 22.4 |
| 2.4 | 1.20 | 11 | 1.507 | 307.3 | 301.5 | 195 | 205 | 18.7 | 16.2 |
| 2.6 | 0.88 | 11.5 | 1.210 | 247.2 | 224.2 | 120 | 136 | 30.3 | 29.8 |
| 2.7 | 0.90 | 9 | 1.086 | 157.1 | 173.9 | 90 | 128 | 39.2 | 45.2 |
| 2.7 | 0.90 | 10 | 1.149 | 180.7 | 204.6 | 110 | 126 | 43.8 | 40.5 |
| 2.7 | 0.90 | 12 | 1.288 | 215.7 | 245.5 | 165 | 155 | 29.7 | 29.4 |
| 2.7 | 0.90 | 14 | 1.427 | 238.9 | 256.9 | 235 | 227 | 15.1 | 19.8 |
| 2.8 | 0.95 | 11 | 1.302 | 257.3 | 248.2 | 165 | 149 | 30.4 | 35.6 |
| 2.8 | 1.15 | 11 | 1.540 | 285.7 | 305.2 | 190 | 171 | 32.7 | 29.4 |
| 2.8 | 0.75 | 11 | 1.063 | 223.8 | 211.9 | 195 | 172 | 47.5 | 43.9 |
| 2.8 | 0.80 | 11 | 1.122 | 232.0 | 219.0 | 155 | 162 | 43.6 | 41.7 |
| 2.8 | 1.00 | 11 | 1.361 | 261.0 | 260.6 | 180 | 150 | 29.5 | 33.9 |
| 2.8 | 1.20 | 11 | 1.600 | 321.5 | 322.7 | 195 | 184 | 28.0 | 28.2 |
| 2.8 | 1.00 | 8 | 1.129 | 225.1 | 170.8 | 160 | 182 | 39.8 | 46.0 |
| 2.8 | 1.00 | 9 | 1.207 | 239.5 | 209.0 | 130 | 162 | 43.0 | 45.2 |
| 2.8 | 1.00 | 10 | 1.284 | 254.7 | 238.9 | 165 | 151 | 50.7 | 39.4 |
| 2.8 | 1.00 | 12 | 1.439 | 285.9 | 274.0 | 185 | 160 | 28.8 | 29.1 |
| 2.9 | 0.99 | 11 | 1.368 | 287.3 | 263.7 | 145 | 167 | 39.8 | 36.8 |
| 3.1 | 0.75 | 11 | 1.133 | 224.9 | 237.1 | 315 | 267 | 53.4 | 50.8 |
| 3.1 | 0.95 | 11 | 1.372 | 261.0 | 263.3 | 240 | 221 | 32.5 | 41.7 |
| 3.2 | 0.75 | 11 | 1.156 | 227.8 | 243.0 | 380 | 310 | 49.0 | 52.6 |
| 3.2 | 0.80 | 11 | 1.216 | 235.7 | 246.7 | 350 | 293 | 49.1 | 49.8 |
| 3.2 | 0.80 | 12.7 | 1.321 | 261.0 | 271.2 | 365 | 343 | 46.5 | 38.7 |
| 3.2 | 1.00 | 11 | 1.455 | 261.0 | 274.7 | 235 | 249 | 50.6 | 41.5 |
| 3.3 | 1.02 | 10.5 | 1.466 | 253.8 | 270.8 | 260 | 296 | 48.0 | 44.9 |
| 3.3 | 0.95 | 11 | 1.418 | 271.7 | 267.1 | 290 | 297 | 37.3 | 44.6 |
| 3.3 | 1.00 | 9 | 1.323 | 232.5 | 231.6 | 305 | 339 | 50.8 | 56.8 |
| 3.3 | 1.00 | 10 | 1.401 | 241.7 | 257.4 | 295 | 309 | 59.9 | 49.3 |
| 3.5 | 1.00 | 11 | 1.482 | 293.0 | 279.8 | 350 | 383 | 50.0 | 49.3 |
| 3.6 | 0.85 | 13 | 1.501 | 285.9 | 273.3 | 520 | 527 | 40.2 | 39.0 |

| | | | | | | | | | |
|---|---|---|---|---|---|---|---|---|---|
| 3.6 | 0.85 | 10 | 1.303 | 236.9 | 236.2 | 430 | 485 | 51.5 | 58.6 |
| 3.6 | 0.95 | 11.5 | 1.525 | 289.5 | 268.2 | 415 | 445 | 41.0 | 43.9 |
| 2.4 | 1.30 | 11 | 1.626 | / | / | 260 | 255 | 11.9 | 13.2 |
| 2.8 | 1.30 | 11 | 1.720 | / | / | 210 | 218 | 19.2 | 26.1 |
| 3.2 | 1.30 | 11 | 1.813 | / | / | 265 | 267 | 41.8 | 36.2 |
| 3.6 | 1.15 | 11 | 1.727 | / | / | 360 | 407 | 40.2 | 42.9 |
| 3.8 | 0.95 | 13 | 1.682 | / | / | 555 | 558 | 40.3 | 38.7 |
| 4.0 | 1.20 | 12 | 1.973 | / | / | 475 | 533 | 42.1 | 44.4 |
| 4.0 | 1.15 | 11 | 1.885 | / | / | 740 | 621 | 46.2 | 45.3 |

Table 7.2 Predicted fresh and hardened properties for mixtures in the validating dataset.

| $SiO_2/Al_2O_3$ | $Na_2O/Al_2O_3$ | $H_2O/Na_2O$ | L/S | Tested Flow (mm) | Predicted Flow (mm) | Tested Set (min) | Predicted Set (min) | Tested Strength (MPa) | Predicted Strength (MPa) |
|---|---|---|---|---|---|---|---|---|---|
| 2.2 | 0.85 | 11 | 1.042 | 143.53 | 152.3 | 125 | 136 | 16.7 | 19.6 |
| 2.6 | 0.90 | 10 | 1.126 | 201.40 | 194.2 | 120 | 115 | 36.0 | 37.4 |
| 2.7 | 1.00 | 11 | 1.275 | 240.87 | 251.5 | 190 | 141 | 32.7 | 35.5 |
| 3.0 | 0.85 | 11 | 1.229 | 240.54 | 242.2 | 245 | 205 | 45.8 | 44.0 |
| 3.4 | 0.90 | 10 | 1.312 | 243.13 | 241.7 | 350 | 361 | 49.5 | 54.6 |
| 3.4 | 0.80 | 10 | 1.201 | 214.90 | 230.7 | 395 | 376 | 60.4 | 59.5 |
| 3.4 | 1.00 | 10 | 1.424 | 263.03 | 257.3 | 360 | 357 | 57.5 | 50.5 |
| 3.4 | 1.20 | 10 | 1.648 | 335.14 | 303.1 | 335 | 382 | 51.1 | 45.6 |
| 3.4 | 0.85 | 12 | 1.388 | 271.13 | 270.0 | 395 | 388 | 46.3 | 43.2 |
| 3.6 | 0.85 | 11 | 1.369 | 259.02 | 255.5 | 450 | 489 | 49.7 | 51.0 |

The penetration of deleterious chemicals in cementitious materials is a time-dependent behaviour (Yi et al., 2019; Woyciechowski et al., 2019). Therefore, besides the aforementioned compositional ratios, the exposure duration ($t$) is treated as an additional explanatory variable, when establishing the associated multi-factor model for acid penetration. Here, the correlation between the acid-induced penetration degree and $t$ is illustrated in Figure 7.4. As seen therein, regardless of the mix proportion, the penetration of acid ions in the N-A-S-H geopolymer increases monotonically as exposure time, and therefore, a linear approximation is adopted in this study. Further, the correlation between the acid-induced penetration and compositional ratios is illustrated in Figure 7.5. Clearly, the penetration degree evolves with an increase in either the $Na_2O/Al_2O_3$ or the $H_2O/Na_2O$ ratios, whereas there exists an optimal value for $SiO_2/Al_2O_3$ ratio

(found here as 3.4) to achieve the smallest penetrated depth. Given this, the approximate linear correlations are adopted for the first two oxide ratios and a parabolic correlation is assumed for the third oxide ratio. Besides, the linear assumption is also considered here for L/S. Eventually, a preliminary mathematic expression for the neutralized depth induced by the acid attack is given in Equation (7.22). However, this model does not account for the coupling between the selected variables. Thus, a mutual combination is tried here as the product of these explanatory variables, and the coupled multi-factor model is now updated in Equation (7.23). The dataset used to establish multi-factor models for acid penetration is summarized in Table 7.3, which was generated in the experimental program introduced earlier in Chapter 5.

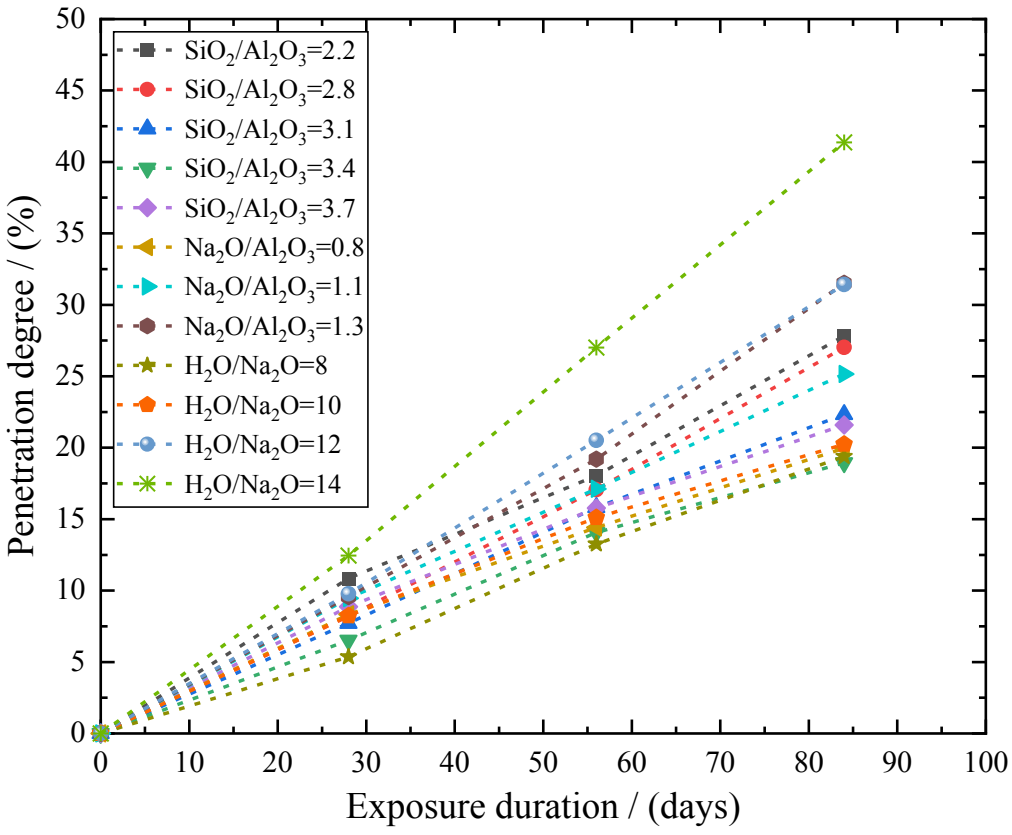


Figure 7.4 Correlation between the penetration degree and exposure time ($t$).

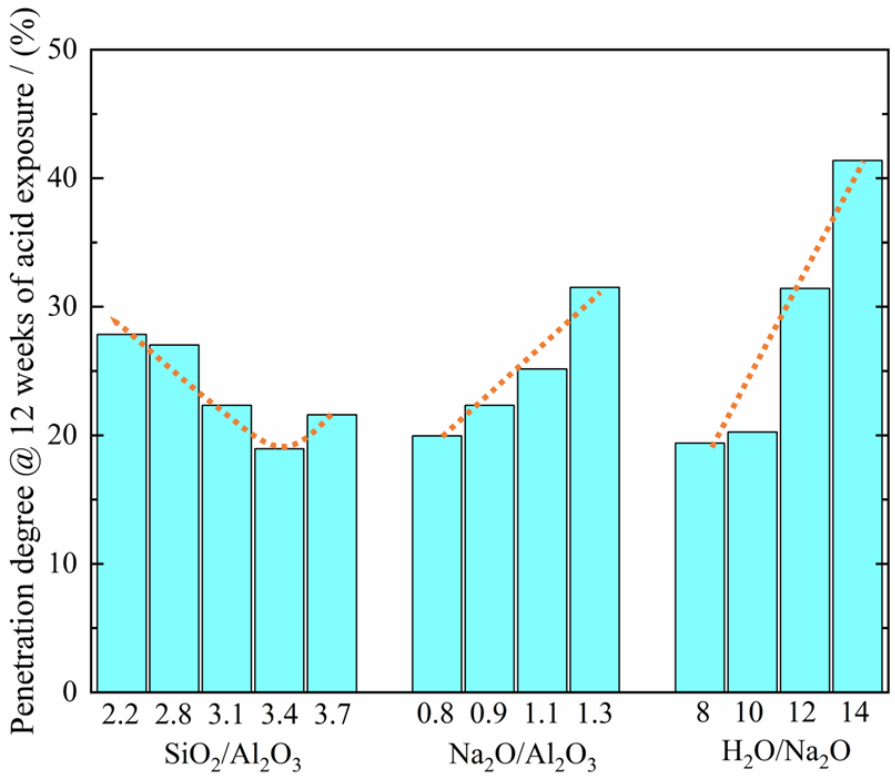


Figure 7.5 Correlation between the penetration degree and various compositional oxide ratios.

$$D_n = \left[ a_1 (x_1 - 3.4)^2 + a_2 x_2 + a_3 x_3 + a_4 x_4 \right] x_5 \tag{7.22}$$

$$D_{cn} = \left[ c_1 (x_1 - 3.4)^2 + c_2 x_2 + c_3 x_3 + c_4 x_4 + c_5 (x_1 - 3.4)^2 x_2 x_3 x_4 \right] x_5 \tag{7.23}$$

Note here, $x_i$ denotes the individual *explanatory* variable: $SiO_2/Al_2O_3$ (Si/Al), $Na_2O/Al_2O_3$ (Na/Al), $H_2O/Na_2O$ (H/Na), L/S ratios, and $t$ when the subscript $i$ increases from 1 to 5. $D_n$ and $D_{cn}$ mean the neutralized depth as predicted by the uncoupled and coupled models, respectively.

Table 7.3 Dataset for acid penetration and the predicted outcomes.

| $SiO_2$/ $Al_2O_3$ | $Na_2O$/ $Al_2O_3$ | $H_2O$/ $Na_2O$ | L/S | Exposure time (yrs) | Tested Depth (mm) | Predicted Depth, $D_n$ (mm) | Predicted Depth, $D_{cn}$ (mm) |
|---|---|---|---|---|---|---|---|
| 2.2 | 0.9 | 11 | 1.102 | 0.077 | 2.80 | 2.47 | 2.38 |
| 2.8 | 0.9 | 11 | 1.242 | 0.077 | 2.10 | 2.09 | 2.45 |
| 3.1 | 0.9 | 11 | 1.312 | 0.077 | 1.99 | 2.08 | 2.06 |
| 3.4 | 0.9 | 11 | 1.382 | 0.077 | 1.67 | 2.20 | 1.79 |
| 3.7 | 0.9 | 11 | 1.441 | 0.077 | 2.32 | 2.43 | 1.99 |
| 3.1 | 0.8 | 11 | 1.193 | 0.077 | 2.16 | 1.97 | 1.93 |
| 3.1 | 1.1 | 11 | 1.551 | 0.077 | 2.44 | 2.31 | 2.38 |
| 3.1 | 1.3 | 11 | 1.790 | 0.077 | 2.48 | 2.53 | 2.78 |
| 3.1 | 1.0 | 8 | 1.199 | 0.077 | 1.38 | 1.47 | 1.29 |
| 3.1 | 1.0 | 10 | 1.354 | 0.077 | 2.11 | 1.95 | 1.89 |
| 3.1 | 1.0 | 12 | 1.509 | 0.077 | 2.54 | 2.44 | 2.54 |
| 3.1 | 1.0 | 14 | 1.663 | 0.077 | 3.24 | 2.92 | 3.23 |
| 2.2 | 0.9 | 11 | 1.102 | 0.153 | 4.65 | 4.91 | 4.73 |
| 2.8 | 0.9 | 11 | 1.242 | 0.153 | 4.37 | 4.14 | 4.88 |
| 3.1 | 0.9 | 11 | 1.312 | 0.153 | 4.08 | 4.14 | 4.09 |
| 3.4 | 0.9 | 11 | 1.382 | 0.153 | 3.60 | 4.38 | 3.57 |
| 3.7 | 0.9 | 11 | 1.441 | 0.153 | 4.12 | 4.83 | 3.95 |
| 3.1 | 0.8 | 11 | 1.193 | 0.153 | 3.73 | 3.92 | 3.83 |
| 3.1 | 1.1 | 11 | 1.551 | 0.153 | 4.42 | 4.58 | 4.72 |
| 3.1 | 1.3 | 11 | 1.790 | 0.153 | 4.97 | 5.03 | 5.52 |
| 3.1 | 1.0 | 8 | 1.199 | 0.153 | 3.41 | 2.91 | 2.56 |
| 3.1 | 1.0 | 10 | 1.354 | 0.153 | 3.87 | 3.88 | 3.75 |
| 3.1 | 1.0 | 12 | 1.509 | 0.153 | 5.32 | 4.84 | 5.04 |
| 3.1 | 1.0 | 14 | 1.663 | 0.153 | 7.03 | 5.80 | 6.43 |
| 2.2 | 0.9 | 11 | 1.102 | 0.230 | 7.17 | 7.39 | 7.11 |
| 2.8 | 0.9 | 11 | 1.242 | 0.230 | 6.91 | 6.23 | 7.33 |
| 3.1 | 0.9 | 11 | 1.312 | 0.230 | 5.76 | 6.22 | 6.15 |
| 3.4 | 0.9 | 11 | 1.382 | 0.230 | 4.85 | 6.59 | 5.36 |
| 3.7 | 0.9 | 11 | 1.441 | 0.230 | 5.64 | 7.26 | 5.94 |
| 3.1 | 0.8 | 11 | 1.193 | 0.230 | 5.17 | 5.89 | 5.76 |
| 3.1 | 1.1 | 11 | 1.551 | 0.230 | 6.50 | 6.89 | 7.10 |
| 3.1 | 1.3 | 11 | 1.790 | 0.230 | 8.15 | 7.56 | 8.30 |
| 3.1 | 1.0 | 8 | 1.199 | 0.230 | 4.99 | 4.38 | 3.84 |
| 3.1 | 1.0 | 10 | 1.354 | 0.230 | 5.19 | 5.83 | 5.64 |
| 3.1 | 1.0 | 12 | 1.509 | 0.230 | 8.15 | 7.28 | 7.58 |
| 3.1 | 1.0 | 14 | 1.663 | 0.230 | 10.76 | 8.72 | 9.66 |

### 7.3.2. Determine regression coefficients for proposed multi-factor models

Each unknown coefficient is linearly expanded with a couple of regression coefficients, $b_i$. The size of the coefficient vector, $b$, depends on the number of items after variable separation, $z$. The expanded model may be stated as a matrix to include all $n$ sets of data. Recall that, the residual error, $\varepsilon$, between the predicted and the actual values, is computed by a $n\times1$ vector, see Equation (7.7). Based on the least square method, the optimum solution to each undetermined model will be found when the sum of the squares of the residuals is a minimum, namely setting the first order derivative of $S(\varepsilon)$ equal to zero. As a result, the corresponding coefficient vector, $b$, could be determined as per Equation (7.12).

Recall that, over 60 mixtures were produced to establish the dataset for flow diameter, final set and compressive strength. Hence, 85% of data, as shown in Table 7.1, are efficient to find the optimum estimate of coefficient vectors for each proposed multi-factor model. The proposed multi-factor models are now given below: Equations (7.24) and (7.25) for flow diameter, Equations (7.26) and (7.27) for final set, and Equations (7.28) and (7.29) for compressive strength.

$$F_{flow} = 54.5\frac{\mathrm{Si}}{\mathrm{Al}} + 183.4\frac{\mathrm{Na}}{\mathrm{Al}} + 12.9\frac{\mathrm{H}}{\mathrm{Na}} + 57.1\frac{\mathrm{L}}{\mathrm{S}} - 305.4 \tag{7.24}$$

$$\begin{aligned} F_{flow} = {} & 145.4838\frac{\mathrm{Si}}{\mathrm{Al}} - 353.055\frac{\mathrm{Na}}{\mathrm{Al}} + 17.4084\frac{\mathrm{H}}{\mathrm{Na}} + 1148.87\frac{\mathrm{L}}{\mathrm{S}} - 807.22 \\ & - 275.98\frac{\mathrm{L}}{\mathrm{S}}\left(\frac{\mathrm{Si}}{\mathrm{Al}} - 0.783\frac{\mathrm{Na}}{\mathrm{Al}} + 0.1924\frac{\mathrm{H}}{\mathrm{Na}}\right) + 7.3366\frac{\mathrm{Si}}{\mathrm{Al}}\left(\frac{\mathrm{Na}}{\mathrm{Al}} + 2.2237\frac{\mathrm{H}}{\mathrm{Na}} + 1.2745\frac{\mathrm{Na}}{\mathrm{Al}}\frac{\mathrm{H}}{\mathrm{Na}}\right) \end{aligned} \tag{7.25}$$

$$F_{set} = 194.39\left(\frac{\mathrm{Si}}{\mathrm{Al}} - 2.4\right)^2 + 266.32\left(\frac{\mathrm{Na}}{\mathrm{Al}} - 0.8\right)^2 + 4.96\left(\frac{\mathrm{H}}{\mathrm{Na}} - 9\right)^2 - 58.77\frac{\mathrm{L}}{\mathrm{S}} + 188.31 \tag{7.26}$$

$$\begin{aligned} F_{set} = {} & 275.915\left(\frac{\mathrm{Si}}{\mathrm{Al}} - 2.4\right)^2 + 592.326\left(\frac{\mathrm{Na}}{\mathrm{Al}} - 0.8\right)^2 + 5.3867\left(\frac{\mathrm{H}}{\mathrm{Na}} - 9\right)^2 - 20.936\frac{\mathrm{L}}{\mathrm{S}} + 129.88 \\ & - 24.598\left(\frac{\mathrm{Si}}{\mathrm{Al}} - 2.4\right)\left(\frac{\mathrm{Na}}{\mathrm{Al}} - 0.8\right)\left(\frac{\mathrm{H}}{\mathrm{Na}} - 9\right)\left(\frac{\mathrm{L}}{\mathrm{S}} + 6.389\right) \end{aligned} \tag{7.27}$$

$$F_{strength} = 39.3\frac{\mathrm{Si}}{\mathrm{Al}} + 58.3\frac{\mathrm{Na}}{\mathrm{Al}} - 0.02\left(\frac{\mathrm{H}}{\mathrm{Na}} - 9\right)^2 - 75.06\frac{\mathrm{L}}{\mathrm{S}} - 37.8 \tag{7.28}$$

$$F_{strength} = 101.9\frac{\mathrm{Si}}{\mathrm{Al}} + 24.3647\frac{\mathrm{Na}}{\mathrm{Al}} - 1.2137(\frac{\mathrm{H}}{\mathrm{Na}} - 9)^2 - 53.849\frac{\mathrm{L}}{\mathrm{S}} - 177.3826 \\ +44.8786(\frac{\mathrm{Si}}{\mathrm{Al}} - 2.4)(\frac{\mathrm{Na}}{\mathrm{Al}} - 2.17)(\frac{\mathrm{L}}{\mathrm{S}} - 0.1565) + 0.3367(\frac{\mathrm{Si}}{\mathrm{Al}})(\frac{\mathrm{Na}}{\mathrm{Al}})(\frac{\mathrm{L}}{\mathrm{S}})(\frac{\mathrm{H}}{\mathrm{Na}} - 9)^2 \quad (7.29)$$

Since only 36 data were generated in the experimental program of acid attack, all of them are used here to determine the optimal estimate of coefficient vectors, in order to ensure adequate accuracy. Based on the experimental dataset presented in Table 7.3, the uncoupled and coupled multi-factor models to predict acid penetration in N-A-S-H geopolymers are now determined as Equations (7.30) and (7.31)**,** respectively.

$$D_n = \left[ 9.2(\frac{\mathrm{Si}}{\mathrm{Al}} - 3.4)^2 - 27.2\frac{\mathrm{Na}}{\mathrm{Al}} + 0.44\frac{\mathrm{H}}{\mathrm{Al}} + 34.9\frac{\mathrm{L}}{\mathrm{S}} \right] t \quad (7.30)$$

$$D_{cn} = \left[ -118.4(\frac{\mathrm{Si}}{\mathrm{Al}} - 3.4)^2 + 11.9\frac{\mathrm{Na}}{\mathrm{Al}} + 3.23\frac{\mathrm{H}}{\mathrm{Al}} - 16.6\frac{\mathrm{L}}{\mathrm{S}} + 11.05(\frac{\mathrm{Si}}{\mathrm{Al}} - 3.4)^2 \frac{\mathrm{Na}}{\mathrm{Al}}\frac{\mathrm{H}}{\mathrm{Al}}\frac{\mathrm{L}}{\mathrm{S}} \right] t \quad (7.31)$$

### 7.3.3. Comparison between actual observation and predicted outcomes

Figures 7.6~7.8 compares the outcomes in terms of flow diameter, final setting time and compressive strength, which are outputted from the proposed multi-factor models and the actual experimental observations. One can see that regardless of whether these models are coupled or not, the points distribute uniformly around the linearly fitted line. The error is quantified by evaluating the corresponding coefficient of determination, $R^2$, according to Equations (7.14 and 7.15). The three uncoupled models register lower $R^2$ values: 0.79 for flow diameter, 0.87 for final set and 0.83 for compressive strength. Upon coupling, the corresponding indices improve to 0.92, 0.95 and 0.88, respectively. Note further that another subset containing 15% of 'hitherto unseen' data is employed to examine the independence of the proposed multi-factor models upon the training process. The proposed coupled models are validated against the remaining 15% of the experimental dataset, in Figure 7.9. It is seen that the predicted data set falls within ±20% of this

experimental set. As summarized above, the proposed multi-factor predictive models, even without coupling, promise guidelines for future N-A-S-H geopolymer mixture design.

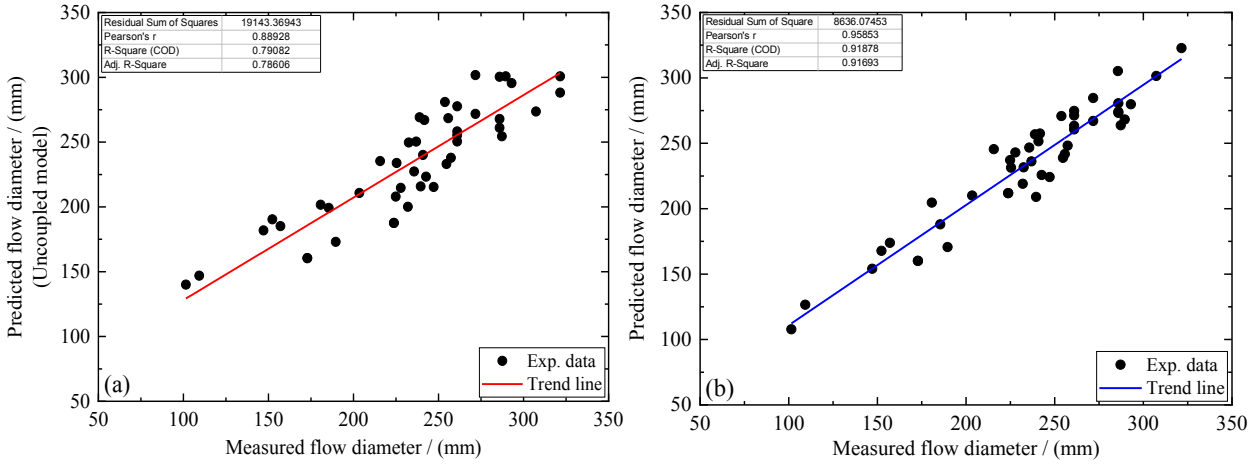


Figure 7.6 Comparing actual flow diameter with the predicted results from (a) uncoupled model and (b) coupled model.

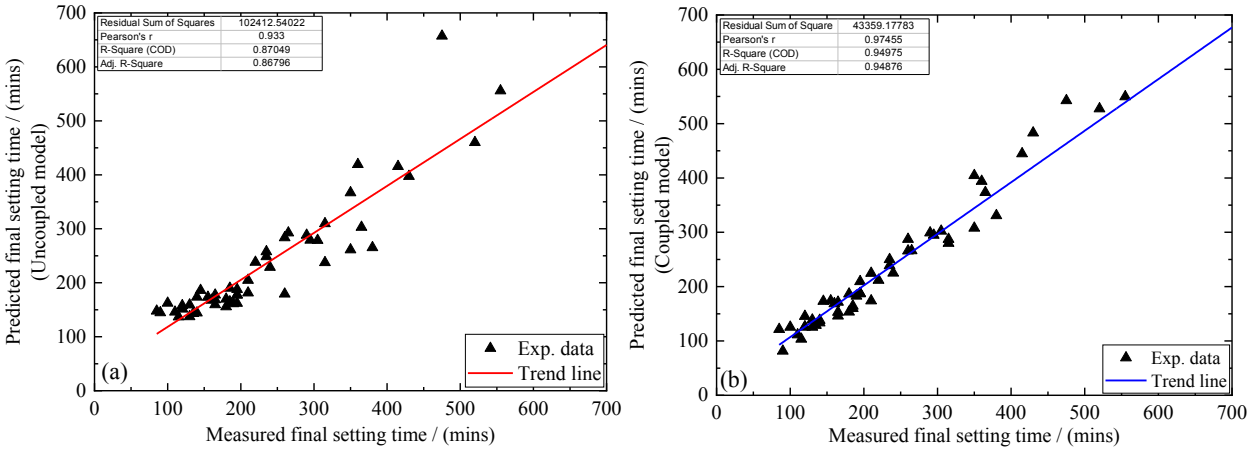


Figure 7.7 Comparing actual final setting time with the predicted results from (a) uncoupled model and (b) coupled model.

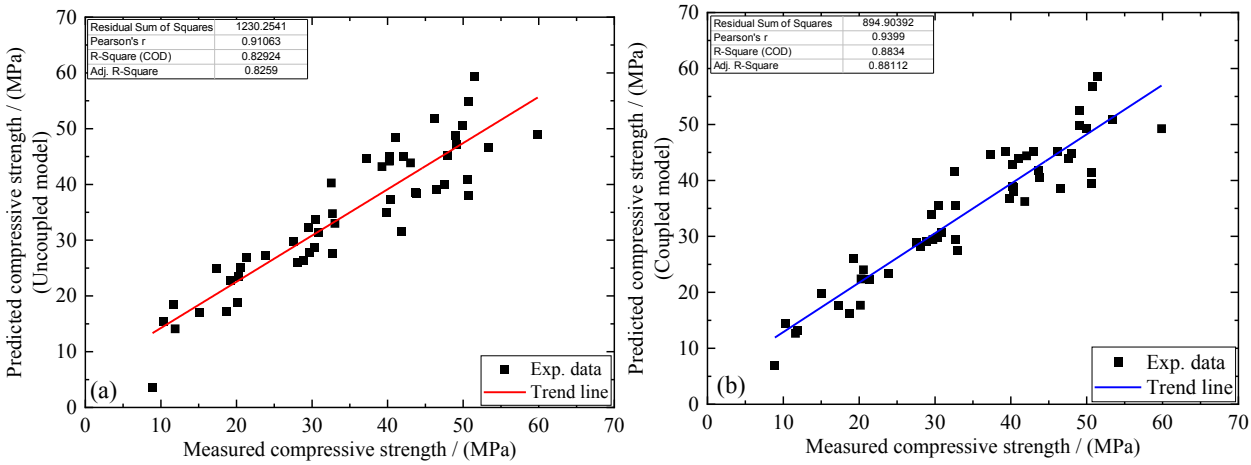


Figure 7.8 Comparing actual compressive strength with the predicted results from (a) uncoupled model and (b) coupled model.

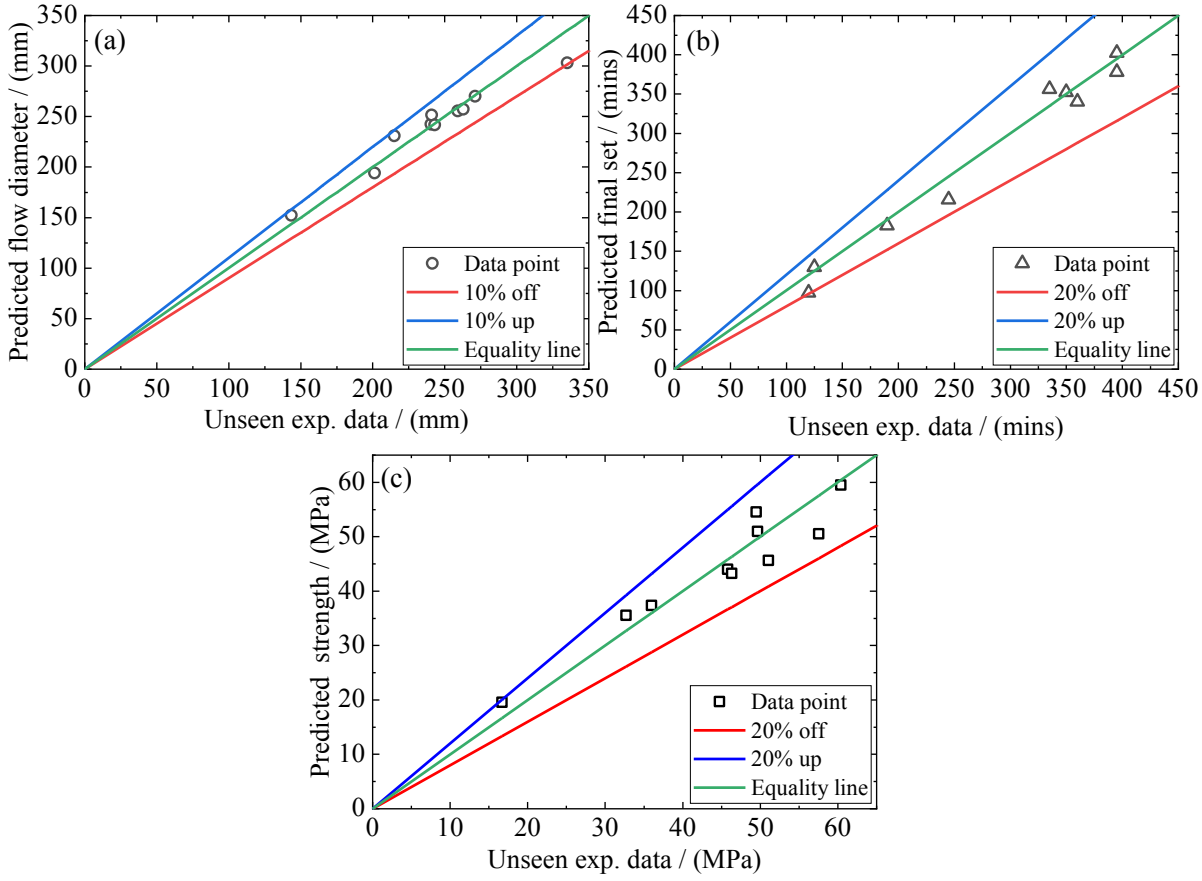


Figure 7.9 Comparing predicted results with validation dataset for (a) flow diameter, (b) final setting time, and (c) compressive strength.

Figure 7.10 compares the outcome from the proposed multi-factor models with the actual acid penetration degree. Once again, it is clear to see that even without the coupling between explanatory variables, the data points distribute uniformly around the equality line (Y=X), with a promising determination coefficient $R^2$ of 0.94. This may indicate that the employed uncoupled model is capable to describe the relationship between the acid penetration and the compositional oxide ratios. Moreover, the corresponding coupled model is found to display an improved $R^2$, from 0.94 to 0.98.

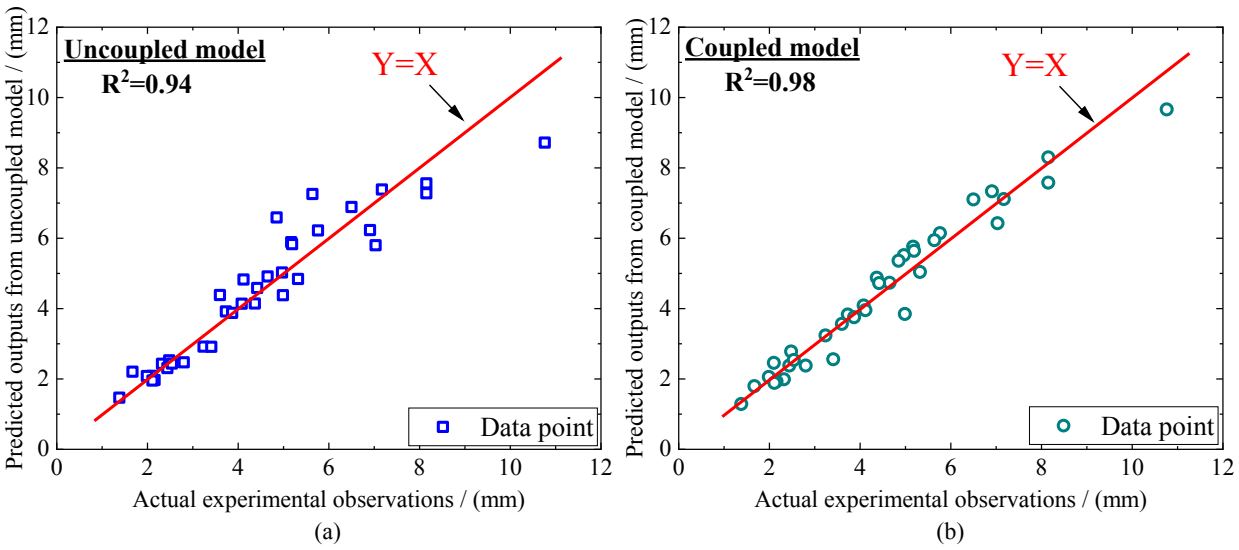


Figure 7.10 Comparing the actual acid penetration degree with the predicted results from (a) uncoupled model and (b) coupled model.

### 7.3.4. Further investigation on $D_{cn}/R$ and loss of compressive strength

Recall that, the acid penetration degree (neutralized degree) is computed as the fraction of $D_{cn}$ over the initial diameter of the specimen ($R$). In this Section, the correlation between the neutralized degree ($D_{cn}/R$) and the compressive strength loss ($CSL$) is aimed to be found. This means that, once the degree of acid-induced neutralization is determined based on the multi-factor models, the deteriorations upon mechanical strength of geopolymers could also be quantified. According to

the compressive strength results shown in Figure 5.8, Chapter 5, all geopolymer specimens appeared to experience a loss of compressive strength at and after 8 weeks of sulphuric acid immersion. So that, the strength data collected at 8 and 12 weeks are plotted against the respective $D_{cn}/R$ in the following Figure 7.11. As seen therein, an approximate polynomial function, as presented in Equation (7.32), is able to capture the correlation between the neutralized degree and the loss of compressive strength efficiently, as evident from a $R^2$ of 0.833. Note here that, the expression with the higher degree of the polynomial has also been examined during the fitting process. However, the presented quadratic Equation is found as the optimal one. This may be attributed to that the strength of N-A-S-H geopolymers is essentially a quadratic function of either the diameter or the radius of the specimen. Given the above, the correlation between the neutralized degree and the loss of compressive strength after sulphuric acid attack is expressed as Equation (7.32).

$$CSL = 0.195(\frac{D_{cn}}{R}) + 0.031(\frac{D_{cn}}{R})^2 \tag{7.32}$$

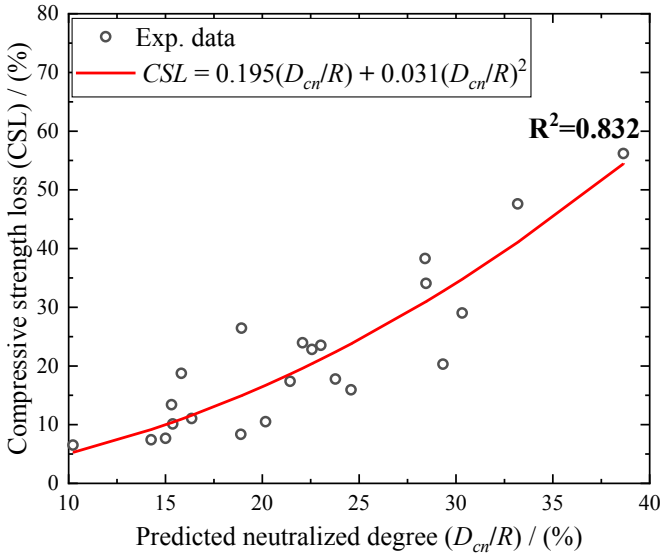


Figure 7.11 The correlation between the neutralized degree and the loss of compressive strength.

## 7.4. Conclusion

This Chapter proposed two sets of muti-factor models to predict the individual workability, final set, compressive strength and acid penetration of N-A-S-H geopolymers, based on the $SiO_2/Al_2O_3$, $Na_2O/Al_2O_3$, $H_2O/Na_2O$ and liquid-to-solid ratios. The correlation between each above property and the considered ratios was studied prior to the model establishment. Then, the associated multi-factor models were determined based on the experimental dataset generated in previous Chapters, using the least square method along with a multiple regression analysis. According to the obtained results, the main concluding remarks are drawn as follows:

(1) The proposed multi-factor models could efficiently capture the effect of each oxide component in the mixture design upon the possible flow, final setting time and compressive strength. When the mutual interactions between the different oxide ratios are considered, the coefficient of determination is improved: for flow improved from 0.79 to 0.92, for setting time, from 0.87 to 0.95 and from 0.83 to 0.88 for the compressive strength.

(2) Even without coupling, the proposed multi-factor model displays a promising efficiency and accuracy in predicting the neutralized depth of N-A-S-H geopolymers against sulphuric acid attack, as evident from a $R^2$ beyond 0.9.

(3) The loss of compressive strength shows a quadratic correlation with the neutralized depth in N-A-S-H geopolymers when subjected to sulphuric acid attack. This is very likely attributed to that the mechanical strength of geopolymer systems is essentially a quadratic function of the diameter (or radius).

(4) From the aspect of the application, these proposed models may serve as a predictive tool to conduct and validate the future mixture design for N-A-S-H geopolymers with varying priorities upon workability, final set, compressive strength and acid resistance.

# Chapter 8. Conclusion and future work

## 8.1. Conclusions

The overall target of this thesis was to develop a guideline for designing and synthesizing the workable, strong and acid-resistant N-A-S-H geopolymers and in turn, boosted the sustainability of civil engineering in Canada. To achieve the above target, firstly, numerous N-A-S-H geopolymers were prepared with varying principal compositional oxide ratios namely, $SiO_2/Al_2O_3$, $Na_2O/Al_2O_3$, $H_2O/Na_2O$, followed by subsequent measurements upon workability, final setting time, strength and acid resistance. Alongside, the multiple regression analysis coupled with the least square method was adopted to establish the associated multi-factor models, which may serve as the predictive tool for practitioners to conduct and validate the future mix design for N-A-S-H geopolymers. Secondly, the nano silica stabilized dry water was examined as an agent to potentially benefit the aforementioned fresh and hardened properties of N-A-S-H geopolymers. The findings firmly confirmed that the N-A-S-H geopolymer is a qualified alternative to conventional OPC systems. Based on the obtained results, the main concluding remarks of this thesis are summarized as follows:

(1) An increase in any of three compositional oxide ratios namely, $Na_2O/Al_2O_3$, $H_2O/Na_2O$ and $SiO_2/Al_2O_3$, automatically increased the liquid-to-solid ratio and frequently lowered the viscosity alongside the yield shear stress of fresh geopolymer mixtures. These together led to a reduced friction between inter-particles and eventually, raised the flowability of the system.

(2) Due to the dissolution and polycondensation, the synthesis of N-A-S-H geopolymers displayed an exothermic characteristic, which is essentially associated with its setting process. The sensitivity analysis revealed that the final setting time of N-A-S-H geopolymers was most sensitive to the $SiO_2/Al_2O_3$ ratio, as this ratio essentially dominated the degree of geopolymerization. By

contrast, the other two oxide ratios, i.e., $Na_2O/Al_2O_3$ and $H_2O/Na_2O$, caused a relatively minor influence on setting. When the above two ratios were fixed, the mixture made with a $SiO_2/Al_2O_3$ ratio of 2.4-2.8 was found to display the fastest setting time.

(3) A deficient $SiO_2/Al_2O_3$ ratio and an excessive $Na_2O/Al_2O_3$ ratio reduced the amorphocity and boosted the significant formation of crystalline zeolite. These, therefore, led to a depression upon the geopolymerization of N-A-S-H systems and in turn, reduced the mechanical strength and elastic modulus of hardened specimens. There may exist an optimum value for the $H_2O/Na_2O$ ratio, found as ~9-10 here, to yield the highest degree of geopolymerization as well as the best mechanical performance. This could be explained through the following: An over-low this ratio may lead to a depressed polycondensation as geopolymerization is also a regeneration process of $Na^+$ and $OH^-$, while a value exceeding the larger end will lower the activation of aluminosilicate precursor.

(4) Although a larger $SiO_2/Al_2O_3$ ratio led to a greater degree of geopolymerization as well as a higher initial strength, a continuous increase beyond a threshold did not improve the associated acid resistance permanently. In this study, the optimal value was experimentally found as 3.4 for this ratio to yield the best acid resistance. Either a deficient or an excessive $SiO_2/Al_2O_3$ ratio magnified the acid-induced deteriorations upon hardened N-A-S-H systems. This is mainly due to that, the extremely low $SiO_2/Al_2O_3$ ratio significantly depresses the polycondensation extent while the over-high value automatically introduces large liquid content into the system and in turn, appears to degrade the microstructure. Lowering the $H_2O/Na_2O$ ratio implies the increased alkalinity, which in turn enhances the potential of N-A-S-H geopolymer to neutralize the penetrating hydrogen ions and eventually, manifests as the improved acid resistance. The effect of $Na_2O/Al_2O_3$ on acid resistance follows the same trend as seen in the mechanical investigation.

Specifically, the lower this ratio, the stronger resistance to acid attack. Furthermore, the sensitivity analysis illustrates that the acid resistance of N-A-S-H geopolymers may be more sensitive to the $Na_2O/Al_2O_3$ and $H_2O/Na_2O$ ratios, in comparison to the $SiO_2/Al_2O_3$ ratio.

(5) For generally used N-A-S-H geopolymers (not serving in a harsh environment), a satisfactory combination of compositional ratios to simultaneously achieve the desired workability, final set and strength may fall within $SiO_2/Al_2O_3$ = 2.8-3.6, $Na_2O/Al_2O_3$ = 0.75-1.0 and $H_2O/Na_2O$ = 9-10. When subjected to the acid-rich environment, the $SiO_2/Al_2O_3$ ratio could be suitably narrowed to 3.1-3.4, and the $H_2O/Na_2O$ ratio could shift slightly to the lower end, i.e., 8-10.

(6) The proposed models could efficiently capture the influence of each compositional oxide ratio on the workability, final set, strength and acid penetration of N-A-S-H geopolymers. They may serve as a predictive tool for practitioners to conduct and validate the future mixture design for N-A-S-H geopolymers with varying priorities upon the aforementioned properties of N-A-S-H geopolymers. Moreover, there predominantly exists a power correlation between the compressive strength and tensile strength and also between the compressive strength and elastic modulus of N-A-S-H geopolymers.

(7) The nano silica stabilized dry water powders registered a significant increase in the particle size from the nanoscale to the microscale, after a physical reorganization under the highly shearing stirring. This size coarsening effect reduced the water demand for fresh geopolymer to achieve a constant workability. Besides, the temporary water encapsulation inside dry water enhanced the early activation efficiency by promoting the alkalinity. Also, the stabilizing nano silica boosted the subsequent reaction and the microstructure of N-A-S-H geopolymers, in the way of either joining the polycondensation due to its amorphous character or acting as the micro-fillers owing to its nano-size effect. These together improved the mechanical strength and acid resistance of N-A-S-

H geopolymers. Moreover, depending on the unique combination of characteristics of size coarsening, micro-filling, supplementary silica source and temporary water encapsulation, the nano silica stabilized dry water resolved the "trade-off" between the fresh and hardened properties when silica nanoparticles were added as an additive to geopolymer systems.

(8) In preparing the dry water, an optimal ratio was found at 15% nanoparticles-to-emulsion ratio. The resulting dry water led to the most satisfactory combination of high flow diameter, quick final set, great strength and superior acid resistance simultaneously. An excess of silica nanoparticles beyond this optimum did not further benefit these properties significantly.

### 8.2. Application of the findings from this study

As a potential alternative to conventional OPC systems, N-A-S-H geopolymers have displayed comparable workability, setting, strength and durability. In the meantime, such a novel material emits significantly less carbon dioxide and consumes considerably less energy during manufacture. Hence, its widespread application is firmly expected to boost sustainable development and alleviate the global warming tendency led by the huge carbon emission. A comprehensive combination of rheological, thermal, morphological, chemical and microstructural characterizations helps optimize the mix design and clarify the potential enhancement led by nano silica stabilized dry water on the overall behaviour of N-A-S-H geopolymers, and in turn, meet the varying engineering requirements in reality. To this end, the findings of this thesis are expected to have several applications in the development of sustainable cementitious materials in the civil engineering field, particularly when subjected to an acid-rich environment. A brief outline of the possible applications is presented below:

(1) The experimental findings presented in this thesis will be useful for understanding the mechanism of geopolymerization and the effects of principal oxide constituents ($SiO_2$, $Al_2O_3$,

$Na_2O$ and $H_2O$) alongside their mutual ratios upon the fresh, mechanical and durability properties of N-A-S-H geopolymer concrete.

(2) The recommended optimal range for each of the principal oxide ratios provides a convenient and reliable mixture design guideline to produce the qualified N-A-S-H geopolymer that registers great workability, quick final set, strong mechanical strength and excellent acid resistance, simultaneously.

(3) The sensitivity analysis regarding the aforementioned principal oxide ratios quantifies the influential extent of fresh, mechanical and durability properties of N-A-S-H geopolymers to each principal oxide constituent. This further helps the practitioners to develop their mixing design strategy, aiming at the varying engineering requirements in practical projects.

(4) The experimental data generated in this study are very valuable for developing the associated mix design dataset of N-A-S-H geopolymer, as the available literature mainly focused on the compressive strength and there currently exists very limited information to account for the workability, setting, strength and acid resistance simultaneously.

(5) Unlike conventional OPC systems, no mix design model is available presently, either from the literature or from the international standard, to guide the cast of N-A-S-H geopolymers. For the first time, this thesis proposes multi-factor models to forecast the workability, final setting time, compressive strength and acid penetration of N-A-S-H geopolymers, with any given mix proportion formulation. These models could efficiently serve as the predictive tool for practitioners to conduct and validate their mix design in practice.

(6) As the precursors are often by-products which may cause important variation in the properties of geopolymers. The current guideline of multi-factor modelling may be used as a quality control

method for correcting the amorphous oxide composition of by-products used for producing N-A-S-H geopolymers.

(7) The nano silica stabilized dry water (a water-in-air Pickering emulsion) is found to benefit the geopolymerization and more significantly the microstructure of N-A-S-H geopolymers. These subsequently manifest as an improvement in both mechanical strength and acid resistance. As a result, adding nano silica stabilized dry water is promising to promote the application of N-A-S-H geopolymers in some aggressive conditions such as the acid-rich environment.

(8) Depending on the unique combination of characteristics of size coarsening, micro-filling, supplementary silica source and temporary water encapsulation, the nano silica stabilized dry water resolves the "trade-off" between the fresh and hardened properties of geopolymers when conventional nanoparticles are added. This may promote the further application of nanoparticles as a reinforcement additive in cementitious materials.

### 8.3. Recommendations for future studies

The macro-properties of fresh and hardened N-A-S-H geopolymer mixtures were investigated and improved by optimizing the mix design and adding nano silica stabilized dry water. Also, a systematic combination of rheological, thermal, morphological, chemical and microstructural characterizations was carried out to understand the underlying mechanisms. However, there still exists a need for continued investigation, and some recommendations for future studies are outlined as follows:

(1) The N-A-S-H geopolymer is essentially made by activating the aluminosilicate precursor with the sodium-based activator, and this, therefore, determines that the main oxide constituents are $Na_2O$, $Al_2O_3$, $SiO_2$ and $H_2O$. However, there also exist some eligible precursors containing

adequate CaO, such as slag, sugarcane bagasse ash, high calcium fly ash, etc. In such cases, besides the N-A-S-H framework, other products like C-S-H and C-A-S-H may also be formed, as the geopolymerization and hydration will take place in parallel. Notwithstanding the difficulty and complexity, further scientific studies are strongly recommended for developing the mix design guideline for these hybrid alkali-activated systems on the basis of principal compositional ratios.

(2) The present study mainly focuses on the macro and micro properties of N-A-S-H geopolymer itself. However, as a potential alternative to conventional OPC concrete, it is expected to be used together with other reinforcement materials such as steel. Therefore, some scientific efforts should be directed toward the mix design for the composite of N-A-S-H geopolymer and steel.

(3) For durability, only acid attack is investigated comprehensively in this study since it is able to cause both physical and chemical degradations upon the N-A-S-H geopolymer. Also, depending upon the extremely low calcium content, the N-A-S-H geopolymer is believed to be durable against other types of chemical attacks, such as chloride attack, sulphate attack and carbonation. However, the above inference should be verified experimentally in future work. More importantly, when other precursors with a rich content of calcium oxide are employed, the aforementioned durability issues may develop into a critical threat to structural safety. Thus, some scientific efforts should be directed in this direction, in order to boost the widespread application of alkali-activated geopolymers.

(4) The potential benefit of the water-in-air Pickering emulsion (nano silica stabilized dry water powder) upon N-A-S-H geopolymers is confirmed in this study. However, due to the foamy characteristic, the air-in-water Pickering emulsion (foam) is not considered in this study. Nevertheless, depending on the similar size coarsening effect and supplementary silica source, the air-in-water Pickering emulsion may lead to a possible enhancement upon geopolymer systems

Also, depending on the stronger adsorption of hydrophilic nano silica, the floating issue of dry water while mixing with fresh geopolymer mixture may be solved effectively. Owing to the foamy characteristic of air-in-water Pickering emulsion, it is recommended to be used firstly as an agent to enhance the properties of lightweight concrete, and thereafter, conduct further investigations in normal concrete.

(5) In this study, nano silica is employed as the stabilizer to produce the associated dry water, considering the necessity of amorphous silica in geopolymerization of N-A-S-H systems. However, other types of nanomaterials may also serve as the eligible stabilizer to produce the required Pickering emulsion, which could be used to enhance the properties of cementitious systems. Therefore, some scientific efforts are recommended for future studies to investigate the associated possibility in this direction.

(6) The proposed multi-factor models capture the influence of $SiO_2/Al_2O_3$, $Na_2O/Al_2O_3$ and $H_2O/Na_2O$ ratios on the workability, final set, strength and acid penetration of N-A-S-H geopolymers. However, other factors, such as curing regime, activator type, aggregate content etc., are not taken into consideration in this study. On the basis of the present study, more efforts are needed in future studies to progressively improve the mix design model for alkali-activated geopolymer systems, by accounting for more principal factors.

(7) Shrinkage has been reported in the literature for alkali-activated systems, mainly due to the formation of calcium silicate hydrate (C-S-H) and calcium aluminosilicate hydrate (C-A-S-H). However, for N-A-S-H geopolymer systems, this concern is not a threat, which has also been visually confirmed in the present study after demolding in laboratory. Nevertheless, for other alkali-activated systems, particularly those made with precursors rich in calcium oxide, it is recommended to investigate their shrinkage behaviour.

(8) The fresh properties, mechanical performance and acid resistance of N-A-S-H geopolymers have been investigated systematically in this study. There remain other concerns, particularly with respect to durability including shrinkage, carbonation, chloride and sulphate attack. These are out of the scope of this thesis and deserve further investigation in the future to clarify the associated mixture design strategy.

## References


Aboutalebi, S. H., Ganjkhanlou, Y., Kamalloo, A., & Nuranian, H. (2010). Modeling of Compressive Strength of Metakaolin Based Geopolymers by The Use of Artificial Neural Network RESEARCH NOTE. *International Journal of Engineering*, 23(2), 145-152.

ACI Committee. (2008). Building code requirements for structural concrete (ACI 318-08) and commentary. American Concrete Institute.

Adam, A. (2009). Strength and durability properties of alkali activated slag and fly ash-based geopolymer concrete (Doctoral dissertation, RMIT University).

Aiken, T. A., Kwasny, J., Sha, W., & Soutsos, M. N. (2018). Effect of slag content and activator dosage on the resistance of fly ash geopolymer binders to sulfuric acid attack. *Cement and Concrete Research*, 111, 23-40.

Aïtcin, P. C. (2000). Cements of yesterday and today: concrete of tomorrow. *Cement and Concrete research*, 30(9), 1349-1359.

Albidah, A., Alghannam, M., Abbas, H., Almusallam, T., & Al-Salloum, Y. (2021). Characteristics of metakaolin-based geopolymer concrete for different mix design parameters. *Journal of Materials Research and Technology*, 10, 84-98.

Ali, M. B., Saidur, R., & Hossain, M. S. (2011). A review on emission analysis in cement industries. *Renewable and Sustainable Energy Reviews*, 15(5), 2252-2261.

Allahverdi, A., & Skvara, F. (2001). Nitric acid attack on hardened paste of geopolymeric cements, Part 1. *Ceramics Silikaty*, 45(3), 81-88.

Allahverdi, A., & Skvara, F. (2005). Sulfuric acid attack on hardened paste of geopolymer cements-Part 1. Mechanism of corrosion at relatively high concentrations. *Ceramics Silikaty*, 49(4), 225.

Aly, M., Hashmi, M. S. J., Olabi, A. G., Messeiry, M., Abadir, E. F., & Hussain, A. I. (2012). Effect of colloidal nano-silica on the mechanical and physical behaviour of waste-glass cement mortar. *Materials & Design*, 33, 127-135.

Araghi, H. J., Nikbin, I. M., Reskati, S. R., Rahmani, E., & Allahyari, H. (2015). An experimental investigation on the erosion resistance of concrete containing various PET particles percentages against sulfuric acid attack. *Construction and Building Materials*, 77, 461-471.

Assaedi, H., Shaikh, F. U. A., & Low, I. M. (2016). Influence of mixing methods of nano silica on the microstructural and mechanical properties of flax fabric reinforced geopolymer composites. *Construction and Building Materials*, 123, 541-552.

ASTM C150/C150M-19a (2019). Standard Specification for Portland Cement. ASTM International, West Conshohocken, PA, USA.

ASTM C191-08 (2008). Standard Test Methods for Time of Setting of Hydraulic Cement by Vicat Needle. ASTM International, West Conshohocken, PA, USA.

ASTM C230/C230M-08 (2008). Standard Specification for Flow Table for Use in Tests of Hydraulic Cement. ASTM International, West Conshohocken, PA, USA.

ASTM C39/C39M-18 (2018). Standard Test Method for Compressive Strength of Cylindrical Concrete Specimens. ASTM International, West Conshohocken, PA, USA.

ASTM C496/C496M-17 (2017). Standard Test Method for Splitting Tensile Strength of Cylindrical Concrete Specimens. ASTM International, West Conshohocken, PA, USA.

ASTM C642-13 (2013). Standard Test Method for Density, Absorption, and Voids in Hardened Concrete, ASTM International, West Conshohocken, PA, USA.

Aussillous, P., & Quéré, D. (2001). Liquid marbles. *Nature*, 411(6840), 924-927.

Aveyard, R., Binks, B. P., & Clint, J. H. (2003). Emulsions stabilised solely by colloidal particles. *Advances in Colloid and Interface Science*, 100, 503-546.

Azarsa, P., & Gupta, R. (2020). Comparative study involving effect of curing regime on elastic modulus of geopolymer concrete. *Buildings*, 10(6), 101.

Bakharev, T. (2005). Resistance of geopolymer materials to acid attack. *Cement and concrete research*, 35(4), 658-670.

Bakharev, T., Sanjayan, J. G., & Cheng, Y. B. (2003). Resistance of alkali-activated slag concrete to acid attack. *Cement and Concrete Research*, 33(10), 1607-1611.

Barbhuiya, S., & Kumala, D. (2017). Behaviour of a sustainable concrete in acidic environment. *Sustainability*, 9(9), 1556.

Barbosa, V. F., MacKenzie, K. J., & Thaumaturgo, C. (2000). Synthesis and characterisation of materials based on inorganic polymers of alumina and silica: sodium polysialate polymers. *International Journal of Inorganic Materials*, 2(4), 309-317.

Bassuoni, M. T., & Nehdi, M. L. (2007). Resistance of self-consolidating concrete to sulfuric acid attack with consecutive pH reduction. *Cement and Concrete Research*, 37(7), 1070-1084.

Berger, S., Frizon, F., & Joussot-Dubien, C. (2009). Formulation of caesium based and caesium containing geopolymers. *Advances in Applied Ceramics*, 108(7), 412-417

Bindiganavile, V., & Hoseini, M. (2019). Foamed concrete. In *Developments in the Formulation and Reinforcement of Concrete* (pp. 365-390). Woodhead Publishing.

Binks, B. P. (2002). Particles as surfactants—similarities and differences. *Current opinion in colloid & interface science*, 7(1-2), 21-41.

Binks, B. P., & Horozov, T. S. (Eds.). (2006). Colloidal particles at liquid interfaces. Cambridge University Press.

Binks, B. P., & Murakami, R. (2006). Phase inversion of particle-stabilized materials from foams to dry water. *Nature materials*, 5(11), 865-869.

Bouguermouh, K., Bouzidi, N., Mahtout, L., Pérez-Villarejo, L., & Martínez-Cartas, M. L. (2017). Effect of acid attack on microstructure and composition of metakaolin-based geopolymers: The role of alkaline activator. *Journal of Non-Crystalline Solids*, 463, 128-137.

Çevik, A., Alzeebaree, R., Humur, G., Niş, A., & Gülşan, M. E. (2018). Effect of nano-silica on the chemical durability and mechanical performance of fly ash based geopolymer concrete. *Ceramics International*, 44(11), 12253-12264.

Chang, C. F., & Chen, J. W. (2006). The experimental investigation of concrete carbonation depth. *Cement and Concrete Research*, 36(9), 1760-1767.

Chen, L., Wang, Z., Wang, Y., & Feng, J. (2016). Preparation and properties of alkali activated metakaolin-based geopolymer. *Materials*, 9(9), 767.

Chen, X., Wang, J., Zhu, G. R., Ding, S., Zhang, H. Y., & Xia, F. Y. (2019). Mechanical Properties and Mechanisms of Polyacrylamide-Modified Granulated Blast Furnace Slag–Based Geopolymer. *Journal of Materials in Civil Engineering*, 31(1), 04018347.

Chevalier, Y., & Bolzinger, M. A. (2013). Emulsions stabilized with solid nanoparticles: Pickering emulsions. *Colloids and Surfaces A: Physicochemical and Engineering Aspects*, 439, 23-34.

Chindaprasirt, P., Chareerat, T., & Sirivivatnanon, V. (2007). Workability and strength of coarse high calcium fly ash geopolymer. *Cement and concrete composites*, 29(3), 224-229.

Chindaprasirt, P., Jaturapitakkul, C., Chalee, W., & Rattanasak, U. (2009). Comparative study on the characteristics of fly ash and bottom ash geopolymers. *Waste management*, 29(2), 539-543.

Cortes, P. P., Luna, K. C., & Garcia, J. I. E. (2021). Alkali-activated limestone/metakaolin cements exposed to high temperatures: Structural changes. *Cement and Concrete Composites*, 104147.

Cundy, C. S., & Cox, P. A. (2003). The hydrothermal synthesis of zeolites: history and development from the earliest days to the present time. *Chemical reviews*, 103(3), 663-702.

da Silva Rocha, T., Dias, D. P., França, F. C. C., de Salles Guerra, R. R., & de Oliveira, L. R. D. C. (2018). Metakaolin-based geopolymer mortars with different alkaline activators ($Na^+$ and $K^+$). *Construction and Building Materials*, 178, 453-461.

Damtoft, J. S., Lukasik, J., Herfort, D., Sorrentino, D., & Gartner, E. M. (2008). Sustainable development and climate change initiatives. *Cement and concrete research*, 38(2), 115-127.

Davidovits, J. (1988, June). Geopolymer chemistry and properties. In *Geopolymer* (Vol. 88, No. 1, pp. 25-48).

Davidovits, J. (2008). Geopolymer Chemistry and Applications. Geopolymer Institute: Saint-Quentin, France.

Davidovits, J., Comrie, D. C., Paterson, J. H., & Ritcey, D. J. (1990). Geopolymeric concretes for environmental protection. *Concrete International*, 12(7), 30-40.

Davidovits, J., Davidovits, M., Davidovits, N. (1994). U.S. Patent No. 5,342,595. Washington, DC: U.S. Patent and Trademark Office.

De Silva, P., Sagoe-Crenstil, K., & Sirivivatnanon, V. (2007). Kinetics of geopolymerization: role of $Al_2O_3$ and $SiO_2$. *Cement and Concrete Research*, 37(4), 512-518.

Deb, P. S., Sarker, P. K., & Barbhuiya, S. (2016). Sorptivity and acid resistance of ambient-cured geopolymer mortars containing nano-silica. *Cement and Concrete Composites*, 72, 235-245.

Diamond, S. (2000). Mercury porosimetry: An inappropriate method for the measurement of pore size distributions in cement-based materials. *Cement and concrete research*, 30(10), 1517-1525.

Dieter, S., Franz-Theo, S., & Helmut, B. (1968). U.S. Patent No. 3,393,155. Washington, DC: U.S. Patent and Trademark Office.

Duan, P., Yan, C., Luo, W., & Zhou, W. (2016). Effects of adding nano-$TiO_2$ on compressive strength, drying shrinkage, carbonation and microstructure of fluidized bed fly ash based geopolymer paste. *Construction and Building Materials*, 106, 115-125.

Duxson, P. S. W. M., Mallicoat, S. W., Lukey, G. C., Kriven, W. M., & Van Deventer, J. S. J. (2007). The effect of alkali and Si/Al ratio on the development of mechanical properties of metakaolin-based geopolymers. *Colloids and Surfaces A: Physicochemical and Engineering Aspects*, 292(1), 8-20.

Duxson, P., Provis, J. L., Lukey, G. C., Mallicoat, S. W., Kriven, W. M., & Van Deventer, J. S. (2005). Understanding the relationship between geopolymer composition, microstructure and mechanical properties. *Colloids and Surfaces A: Physicochemical and Engineering Aspects*, 269(1-3), 47-58.

El-Sayed, H. A., Abo, E. E. S., Khater, H. M., & Hasanein, S. A. (2011). Resistance of alkali activated water-cooled slag geopolymer to sulphate attack. *Ceramics-Silikáty*, 55(2), 153-160.

Fernando, P. T., João, C. G., & Said, J. (2010). Durability and environmental performance of alkali-activated tungsten mine waste mud mortars. *Journal of materials in civil engineering*, 22(9), 897-904.

Forny, L., Saleh, K., Pezron, I., Komunjer, L., & Guigon, P. (2009). Influence of mixing characteristics for water encapsulation by self-assembling hydrophobic silica nanoparticles. *Powder technology*, 189(2), 263-269.

Gao, K., Lin, K. L., Wang, D., Hwang, C. L., Shiu, H. S., Chang, Y. M., & Cheng, T. W. (2014). Effects $SiO_2/Na_2O$ molar ratio on mechanical properties and the microstructure of nano-SiO2 metakaolin-based geopolymers. *Construction and Building Materials*, 53, 503-510.

Gao, X. X., Michaud, P., Joussein, E., & Rossignol, S. (2013a). Behavior of metakaolin-based potassium geopolymers in acidic solutions. *Journal of non-crystalline solids*, 380, 95-102.

Gao, K., Lin, K. L., Wang, D., Shiu, H. S., Hwang, C. L., & Cheng, T. W. (2013b). Effects of nano-$SiO_2$ on setting time and compressive strength of alkaliactivated metakaolin-based geopolymer. *The Open Civil Engineering Journal*, 7(1).

Gao, X., Yu, Q. L., & Brouwers, H. J. H. (2015). Characterization of alkali activated slag–fly ash blends containing nano-silica. *Construction and Building Materials*, 98, 397-406.

Garcés, P., Andrade, M. C., Sáez, A., & Alonso, M. C. (2005). Corrosion of reinforcing steel in neutral and acid solutions simulating the electrolytic environments in the micropores of concrete in the propagation period. *Corrosion Science*, 47(2), 289-306.

Gartner, E. (2004). Industrially interesting approaches to "low-$CO_2$" cements. *Cement and Concrete research*, 34(9), 1489-1498.

Ghanbari, M., Hadian, A. M., Nourbakhsh, A. A., & MacKenzie, K. J. D. (2017). Modeling and optimization of compressive strength and bulk density of metakaolin-based geopolymer

using central composite design: A numerical and experimental study. *Ceramics International*, 43(1), 324-335.

Ghosh, K., & Ghosh, P. (2012a). Effect of $Na_2O/Al_2O_3$, $SiO_2/Al_2O_3$ and w/b ratio on setting time and workability of fly ash based geopolymer. *International Journal of Engineering Research and Applications*, 2, 2142-2147.

Ghosh, K., & Ghosh, P. (2012b). Effect of synthesizing parameters on compressive strength of flyash based geopolymer paste. *Int J Struct Civ Eng*, 1(8), 1-11.

Glover, TJ, 1995, Pocket Ref. Sequoia Publishing, ISBN 978-1885071002.

Glukhovsky, V. D. (1981). Slag-alkali concretes produced from fine-grained aggregate. *Kiev: Vishcha Shkolay*.

Gutberlet, T., Hilbig, H., & Beddoe, R. E. (2015). Acid attack on hydrated cement—Effect of mineral acids on the degradation process. *Cement and Concrete Research*, 74, 35-43.

Habert, G., De Lacaillerie, J. D. E., & Roussel, N. (2011). An environmental evaluation of geopolymer based concrete production: reviewing current research trends. *Journal of cleaner production*, 19(11), 1229-1238.

Hajimohammadi, A., Provis, J. L., & Van Deventer, J. S. (2008). One-part geopolymer mixes from geothermal silica and sodium aluminate. *Industrial & Engineering Chemistry Research*, 47(23), 9396-9405.

Hardjito, D., & Fung, S. S. (2009). Fly ash-based geopolymer mortar incorporating bottom ash. *Modern applied science*, 4(1), 44.

Hardjito, D., Wallah, S. E., Sumajouw, D. M., & Rangan, B. V. (2004a). Factors influencing the compressive strength of fly ash-based geopolymer concrete. *civil engineering dimension*, 6(2), pp-88.

Hardjito, D., Wallah, S. E., Sumajouw, D. M. J., & Rangan, B. V. (2004b). The stress-strain behaviour of fly ash-based geopolymer concrete. *Development in Mechanics of Structures and Materials*, 35, 831-834.

He, P., Wang, M., Fu, S., Jia, D., Yan, S., Yuan, J., ... & Zhou, Y. (2016). Effects of Si/Al ratio on the structure and properties of metakaolin based geopolymer. *Ceramics international*, 42(13), 14416-14422.

Heah, C. Y., Kamarudin, H., Bakri, A. M., Binhussain, M., Luqman, M., Nizar, I. K., ... & Liew, Y. M. (2013). Influence of oxide molar ratios on kaolin geopolymers. *Advanced Science Letters*, 19(12), 3588-3591.

Herriott, R. M. (1938). Isolation, crystallization, and properties of swine pepsinogen. *The Journal of General Physiology*, 21(4), 501-540.

Hewayde, E., Nehdi, M., Allouche, E., & Nakhla, G. (2006). Effect of geopolymer cement on microstructure, compressive strength and sulphuric acid resistance of concrete. *Magazine of Concrete Research*, 58(5), 321-331.

Horňáková, M., & Lehner, P. (2022). Analysis of measured parameters in relation to the amount of fibre in lightweight red ceramic waste aggregate concrete. *Mathematics*, 10(2), 229.

Hrabova, K., Teply, B., & Vymazal, T. (2020). Sustainability assessment of concrete mixes. In *IOP Conference Series: Earth and Environmental Science* (Vol. 444, No. 1, p. 012021). IOP Publishing.

Hu, W., Nie, Q., Huang, B., Shu, X., & He, Q. (2018). Mechanical and microstructural characterization of geopolymers derived from red mud and fly ashes. *Journal of Cleaner Production*, 186, 799-806.

Huseien, G. F., Mirza, J., Ismail, M., & Hussin, M. W. (2016). Influence of different curing temperatures and alkali activators on properties of GBFS geopolymer mortars containing fly ash and palm-oil fuel ash. *Construction and building materials*, 125, 1229-1240.

Juenger, M. C. G., Winnefeld, F., Provis, J. L., & Ideker, J. H. (2011). Advances in alternative cementitious binders. *Cement and concrete research*, 41(12), 1232-1243.

Juengsuwattananon, K., Winnefeld, F., Chindaprasirt, P., & Pimraksa, K. (2019). Correlation between initial $SiO_2/Al_2O_3$, $Na_2O/ Al_2O_3$, $Na_2O/ SiO_2$ and $H_2O/ Na_2O$ ratios on phase and microstructure of reaction products of metakaolin-rice husk ash geopolymer. *Construction and Building Materials*, 226, 406-417

Kani, E. N., & Allahverdi, A. (2009). Effect of chemical composition on basic engineering properties of inorganic polymeric binder based on natural pozzolan. *Ceramics-Silikaty*, 53(3), 195-204.

Khale, D., & Chaudhary, R. (2007). Mechanism of geopolymerization and factors influencing its development: a review. *Journal of materials science*, 42(3), 729-746.

Khan, H. A., Castel, A., & Khan, M. S. (2020). Corrosion investigation of fly ash based geopolymer mortar in natural sewer environment and sulphuric acid solution. *Corrosion Science*, 168, 108586.

Kirschner, A., & Harmuth, H. (2004). Investigation of geopolymer binders with respect to their application for building materials. *Ceramics Silikáty*, 48(11), 7-20.

Kong, D. L., Sanjayan, J. G., & Sagoe-Crentsil, K. (2007). Comparative performance of geopolymers made with metakaolin and fly ash after exposure to elevated temperatures. *Cement and concrete research*, 37(12), 1583-1589.

Kovalchuk, G., Fernández-Jiménez, A., & Palomo, A. (2008). Alkali-activated fly ash. Relationship between mechanical strength gains and initial ash chemistry. *Materiales de construccion*, 58(291), 35-52.

Kumar, S., & Kumar, R. (2014). Geopolymer: Cement for low carbon economy. *Indian Concr. J*, 88, 29-37.

Lahoti, M., Narang, P., Tan, K. H., & Yang, E. H. (2017). Mix design factors and strength prediction of metakaolin-based geopolymer. *Ceramics International*, 43(14), 11433-11441.

Lee, N. K., & Lee, H. K. (2016). Influence of the slag content on the chloride and sulfuric acid resistances of alkali-activated fly ash/slag paste. *Cement and concrete composites*, 72, 168-179.

Lei, D. Y., Guo, L. P., Sun, W., Liu, J., Shu, X., & Guo, X. L. (2016). A new dispersing method on silica fume and its influence on the performance of cement-based materials. *Construction and Building Materials*, 115, 716-726.

Li, C., Sun, H., & Li, L. (2010). A review: The comparison between alkali-activated slag (Si+ Ca) and metakaolin (Si+ Al) cements. *Cement and concrete research*, 40(9), 1341-1349.

Li, J., Yi, C., Chen, Z., Cao, W., Yin, S., Huang, H., ... & Yu, Q. (2022). Relationships between reaction products and carbonation performance of alkali-activated slag with similar pore structure. *Journal of Building Engineering*, 45, 103605.

Li, Z., Zhang, S., Zuo, Y., Chen, W., & Ye, G. (2019). Chemical deformation of metakaolin based geopolymer. *Cement and Concrete Research*, 120, 108-118.

Liew, Y. M., Heah, C. Y., & Kamarudin, H. (2016). Structure and properties of clay-based geopolymer cements: A review. *Progress in Materials Science*, 83, 595-629.

Lo, K. W., Lin, K. L., Cheng, T. W., Chang, Y. M., & Lan, J. Y. (2017). Effect of nano-$SiO_2$ on the alkali-activated characteristics of spent catalyst metakaolin-based geopolymers. *Construction and Building Materials*, 143, 455-463.

Luo, H. L., Lin, D. F., & Chen, S. C. (2017). Improving the properties of geopolymer containing oil-contaminated clay, metakaolin, and blast furnace slag by applying nano-$SiO_2$. *Environmental Technology*, 38(13-14), 1619-1628.

MacKenzie, K. J., Bradley, S., Hanna, J. V., & Smith, M. E. (2013). Magnesium analogues of aluminosilicate inorganic polymers (geopolymers) from magnesium minerals. *Journal of Materials Science*, 48(4), 1787-1793.

McLellan, B. C., Williams, R. P., Lay, J., Van Riessen, A., & Corder, G. D. (2011). Costs and carbon emissions for geopolymer pastes in comparison to ordinary portland cement. *Journal of cleaner production*, 19(9-10), 1080-1090.

Meng, W., Kumar, A., & Khayat, K. H. (2019). Effect of silica fume and slump-retaining polycarboxylate-based dispersant on the development of properties of portland cement paste. *Cement and Concrete Composites*, 99, 181-190.

Miyamoto, S., Minagawa, H., & Hisada, M. (2014). Deterioration rate of hardened cement caused by high concentrated mixed acid attack. *Construction and Building Materials*, 67, 47-54.

Monteiro, P. (2006). Concrete: microstructure, properties, and materials. McGraw-Hill Publishing.

Moudio, A. M. N., Tchakoute, H. K., Ngnintedem, D. L. V., Andreola, F., Kamseu, E., Nanseu-Njiki, C. P., ... & Rüscher, C. H. (2021). Influence of the synthetic calcium aluminate hydrate and the mixture of calcium aluminate and silicate hydrates on the compressive strengths and the microstructure of metakaolin-based geopolymer cements. *Materials Chemistry and Physics*, 264, 124459.

Mozumder, R. A., & Laskar, A. I. (2015). Prediction of unconfined compressive strength of geopolymer stabilized clayey soil using artificial neural network. *Computers and Geotechnics*, 69, 291-300.

Mu, S., Liu, J., Lin, W., Wang, Y., Liu, J., Shi, L., & Jiang, Q. (2017). Property and microstructure of aluminosilicate inorganic coating for concrete: Role of water to solid ratio. *Construction and Building Materials*, 148, 846-856.

Nath, S. K., & Kumar, S. (2020). Role of particle fineness on engineering properties and microstructure of fly ash derived geopolymer. *Construction and Building Materials*, 233, 117294.

Nazari, A. and Riahi, S. The effects of $SiO_2$ nanoparticles on physical and mechanical properties of high strength compacting concrete. *Composites, Part B*. 42 (2011) 570-578.

Nazari, A., & Torgal, F. P. (2013). Predicting compressive strength of different geopolymers by artificial neural networks. *Ceramics International*, 39(3), 2247-2257.

Noll, W. (2012). Chemistry and technology of silicones. Elsevier.

Nuaklong, P., Sata, V., Wongsa, A., Srinavin, K., & Chindaprasirt, P. (2018). Recycled aggregate high calcium fly ash geopolymer concrete with inclusion of OPC and nano-$SiO_2$. *Construction and Building Materials*, 174, 244-252.

Ogundare, J. O. (2018). Understanding least squares estimation and geomatics data analysis. John Wiley & Sons.

Olivia, M., & Nikraz, H. (2012). Properties of fly ash geopolymer concrete designed by Taguchi method. *Materials & Design (1980-2015)*, 36, 191-198.

Pacheco-Torgal, F., Castro-Gomes, J., & Jalali, S. (2008a). Alkali-activated binders: A review: Part 1. Historical background, terminology, reaction mechanisms and hydration products. *Construction and Building Materials*, 22(7), 1305-1314.

Pacheco-Torgal, F., Castro-Gomes, J., & Jalali, S. (2008b). Alkali-activated binders: A review. Part 2. About materials and binders manufacture. *Construction and Building Materials*, 22(7), 1315-1322.

Palomo, A., & Glasser, F. P. (1992). Chemically-bonded cementitious materials based on metakaolin. British ceramic. *Transactions and journal*, 91(4), 107-112.

Panagiotopoulou, C., Tsivilis, S., & Kakali, G. (2015). Application of the Taguchi approach for the composition optimization of alkali activated fly ash binders. *Construction and Building Materials*, 91, 17-22.

Phoo-ngernkham, T., Chindaprasirt, P., Sata, V., Hanjitsuwan, S., & Hatanaka, S. (2014). The effect of adding nano-$SiO_2$ and nano-$Al_2O_3$ on properties of high calcium fly ash geopolymer cured at ambient temperature. *Materials & Design*, 55, 58-65.

Provis, J. L., & Van Deventer, J. S. J. (2007). Geopolymerisation kinetics. 2. Reaction kinetic modelling. *Chemical Engineering Science*, 62(9), 2318-2329.

Pyatina, T., & Sugama, T. (2016). Acid resistance of calcium aluminate cement–fly ash F blends. *Advances in Cement Research*, 28(7), 433-457.

Qu, F., Li, W., Wang, K., Zhang, S., & Sheng, D. (2021). Performance deterioration of fly ash/slag-based geopolymer composites subjected to coupled cyclic preloading and sulfuric acid attack. *Journal of Cleaner Production*, 321, 128942.

Radu, E. R., Panaitescu, D. M., Andrei, L., Ciuprina, F., Nicolae, C. A., Gabor, A. R., & Truşcă, R. (2021). Properties of polysiloxane/nanosilica nanodielectrics for wearable electronic devices. *Nanomaterials*, 12(1), 95.

Rahier, H., Simons, W., Van Mele, B., & Biesemans, M. (1997). Low-temperature synthesized aluminosilicate glasses: Part III Influence of the composition of the silicate solution on production, structure and properties. *Journal of Materials Science*, 32(9), 2237-2247.

Ramezanianpour, A. A., & Moeini, M. A. (2018). Mechanical and durability properties of alkali activated slag coating mortars containing nanosilica and silica fume. *Construction and Building Materials*, 163, 611-621.

Räsänen, V., & Penttala, V. (2004). The pH measurement of concrete and smoothing mortar using a concrete powder suspension. *Cement and Concrete Research*, 34(5), 813-820.

Rashad, A. M. (2019). Effect of nanoparticles on the properties of geopolymer materials. *Magazine of Concrete Research*, 71(24), 1283-1301.

Rashad, A. M., & Ouda, A. S. (2019). Thermal resistance of alkali-activated metakaolin pastes containing nano-silica particles. *Journal of Thermal Analysis and Calorimetry*, 136(2), 609-620.

Rattanasak, U., & Chindaprasirt, P. (2009). Influence of NaOH solution on the synthesis of fly ash geopolymer. *Minerals Engineering*, 22(12), 1073-1078.

Rovnaník, P. (2010). Effect of curing temperature on the development of hard structure of metakaolin-based geopolymer. *Construction and building materials*, 24(7), 1176-1183.

Sadat, M. R., Bringuier, S., Muralidharan, K., Runge, K., Asaduzzaman, A., & Zhang, L. (2016). An atomistic characterization of the interplay between composition, structure and

mechanical properties of amorphous geopolymer binders. *Journal of Non-Crystalline Solids*, 434, 53-61.

Saidi, N., Samet, B., & Baklouti, S. (2013). Effect of composition on structure and mechanical properties of metakaolin based PSS-Geopolymer. *Int. J. Mater. Sci*, 3(4), 145-151.

Sathonsaowaphak, A., Chindaprasirt, P., & Pimraksa, K. (2009). Workability and strength of lignite bottom ash geopolymer mortar. *Journal of Hazardous Materials*, 168(1), 44-50.

Shahmansouri, A. A., Yazdani, M., Ghanbari, S., Bengar, H. A., Jafari, A., & Ghatte, H. F. (2021). Artificial neural network model to predict the compressive strength of eco-friendly geopolymer concrete incorporating silica fume and natural zeolite. *Journal of Cleaner Production*, 279, 123697.

Shahrajabian, F., & Behfarnia, K. (2018). The effects of nano particles on freeze and thaw resistance of alkali-activated slag concrete. *Construction and Building Materials*, 176, 172-178.

Shi, C., & Stegemann, J. A. (2000). Acid corrosion resistance of different cementing materials. *Cement and Concrete Research*, 30(5), 803-808.

Standard, AS 3600 (2009). Concrete structures. Australia. Strathfield, Australia: Standards Australia.

Steveson, M., & Sagoe-Crentsil, K. (2005). Relationships between composition, structure and strength of inorganic polymers. *Journal of materials science*, 40(16), 4247-4259.

Šulc, R. (2009). Effect of Water Ratio in Fly-Ash Concrete on the Process of Alkali Activation.

Sumesh, M., Alengaram, U. J., Jumaat, M. Z., Mo, K. H., & Alnahhal, M. F. (2017). Incorporation of nano-materials in cement composite and geopolymer based paste and mortar–A review. *Construction and Building Materials*, 148, 62-84.

Tajunnisa, Y., Sugimoto, M., Sato, T., & Shigeishi, M. (2017). A Study on Factors Affecting Geopolymerization of Low Calcium Fly Ash. *International Journal of GEOMATE*, 13(36), 100-107.

Taylor, M., Tam, C., & Gielen, D. (2006). Energy efficiency and $CO_2$ emissions from the global cement industry. *Korea*, 50(2.2), 61-7.

Tchakouté, H. K., Rüscher, C. H., Kong, S., Kamseu, E., & Leonelli, C. (2017). Thermal behavior of metakaolin-based geopolymer cements using sodium waterglass from rice husk ash and waste glass as alternative activators. *Waste and biomass valorization*, 8(3), 573-584.

Temuujin, J., van Riessen, A., & MacKenzie, K. J. D. (2010). Preparation and characterisation of fly ash based geopolymer mortars. *Construction and Building Materials*, 24(10), 1906-1910.

Thakur, R. N., & Ghosh, S. (2009). Effect of mix composition on compressive strength and microstructure of fly ash based geopolymer composites. *ARPN journal of engineering and applied sciences*, 4(4), 68-74.

Thokchom, S., Ghosh, P., & Ghosh, S. (2009). Effect of water absorption, porosity and sorptivity on durability of geopolymer mortars. *ARPN Journal of engineering and Applied Sciences*, 4(7), 28-32.

Thomas, R. J., & Peethamparan, S. (2015). Alkali-activated concrete: Engineering properties and stress–strain behavior. *Construction and building materials*, 93, 49-56.

Vafaei, M., Allahverdi, A., Dong, P., & Bassim, N. (2018). Acid attack on geopolymer cement mortar based on waste-glass powder and calcium aluminate cement at mild concentration. *Construction and Building Materials*, 193, 363-372.

Van Jaarsveld, J. G. S., Van Deventer, J. S. J., & Lorenzen, L. (1997). The potential use of geopolymeric materials to immobilise toxic metals: Part I. Theory and applications. *Minerals engineering*, 10(7), 659-669.

Villa, C., Pecina, E. T., Torres, R., & Gómez, L. (2010). Geopolymer synthesis using alkaline activation of natural zeolite. *Construction and Building Materials*, 24(11), 2084-2090.

Vogt, O., Ukrainczyk, N., & Koenders, E. (2021). Effect of Silica Fume on Metakaolin Geopolymers' Sulfuric Acid Resistance. *Materials*, 14(18), 5396.

Wang, Y., Zhu, G., Chai, G., Zhou, Y., Chen, C., & Zhang, W. (2021). Experimental study on the effect of release pressure on the extinguishing efficiency of dry water. *Case Studies in Thermal Engineering*, 26, 101177.

Williams, R. P., Hart, R. D., & Van Riessen, A. (2011). Quantification of the extent of reaction of metakaolin-based geopolymers using X-ray diffraction, scanning electron microscopy, and energy-dispersive spectroscopy. *Journal of the American Ceramic Society*, 94(8), 2663-2670.

Woyciechowski, P., Woliński, P., & Adamczewski, G. (2019). Prediction of carbonation progress in concrete containing calcareous fly ash co-binder. *Materials*, 12(17), 2665.

Wu, L., Huang, G., & Liu, W. V. (2021). Effects of calcium aluminate cement on the acid resistance of metakaolin-based geopolymer. *Advances in Cement Research*, 33(10), 423-435.

Xu, H., & Van Deventer, J. S. J. (2000). The geopolymerisation of alumino-silicate minerals. *International journal of mineral processing*, 59(3), 247-266.

Yang, Y., Fang, Z., Chen, X., Zhang, W., Xie, Y., Chen, Y., ... & Yuan, W. (2017). An overview of Pickering emulsions: solid-particle materials, classification, morphology, and applications. *Frontiers in pharmacology*, 8, 287.

Yi, C., Boluk, Y., & Bindiganavile, V. (2020). Enhancing Alkali-Activation of Metakaolin-Based Geopolymers using Dry Water. *Journal of Cleaner Production*, 120676.

Yi, C., Boluk, Y., & Bindiganavile, V. (2022). Experimental Characterization and Multi-Factor Modelling to Achieve Desired Flow, Set and Strength of NASH Geopolymers. *Materials*, 15(16), 5634.

Yi, C., Chen, Z., & Bindiganavile, V. (2019). Crack growth prediction of cement-based systems subjected to two-dimensional sulphate attack. *Construction and Building Materials*, 222, 814-828.

Yuan, J., He, P., Jia, D., Yang, C., Yan, S., Yang, Z., ... & Zhou, Y. (2016). Effect of curing temperature and $SiO_2/K_2O$ molar ratio on the performance of metakaolin-based geopolymers. *Ceramics International*, 42(14), 16184-16190.

Yunsheng, Z., Wei, S., & Zongjin, L. (2010). Composition design and microstructural characterization of calcined kaolin-based geopolymer cement. *Applied Clay Science*, 47(3-4), 271-275.

Yusuf, M. O., Johari, M. A. M., Ahmad, Z. A., & Maslehuddin, M. (2014). Effects of H2O/Na2O molar ratio on the strength of alkaline activated ground blast furnace slag-ultrafine palm oil fuel ash based concrete. *Materials & Design (1980-2015)*, 56, 158-164.

Zakka, W. P., Lim, N. H. A. S., & Khun, M. C. (2021). A scientometric review of geopolymer concrete. *Journal of Cleaner Production*, 280, 124353.

Zhang, M., Zhao, M., Zhang, G., Mann, D., Lumsden, K., & Tao, M. (2016). Durability of red mud-fly ash based geopolymer and leaching behavior of heavy metals in sulfuric acid solutions and deionized water. *Construction and Building Materials*, 124, 373-382.

Zhang, S. P., & Zong, L. (2014). Evaluation of relationship between water absorption and durability of concrete materials. *Advances in Materials Science and Engineering*, 2014.

Zhang, Z., Provis, J. L., Wang, H., Bullen, F., & Reid, A. (2013). Quantitative kinetic and structural analysis of geopolymers. Part 2. Thermodynamics of sodium silicate activation of metakaolin. *Thermochimica acta*, 565, 163-171.

Zhang, Z., Wang, H., & Provis, J. L. (2012). Quantitative study of the reactivity of fly ash in geopolymerization by FTIR. *Journal of Sustainable Cement-Based Materials*, 1(4), 154-166.

Zhang, Z., Wang, H., Zhu, Y., Reid, A., Provis, J. L., & Bullen, F. (2014). Using fly ash to partially substitute metakaolin in geopolymer synthesis. *Applied Clay Science*, 88, 194-201.

Zhao, J., Fan, Z., Xiong, J., Zhang, D., & Wu, Q. (2021, February). Experiment research on multi-factor model for chloride migration coefficient within concrete. In *IOP Conference Series: Earth and Environmental Science* (Vol. 676, No. 1, p. 012108). IOP Publishing.

Zheng, G., Cui, X., Huang, D., Pang, J., Mo, G., Yu, S., & Tong, Z. (2015). Alkali-activation reactivity of chemosynthetic $Al_2O_3$–$2SiO_2$ powders and their $^{27}Al$ and $^{29}Si$ magic-angle spinning nuclear magnetic resonance spectra. *Particuology*, 22, 151-156.

Zhuang, X. Y., Chen, L., Komarneni, S., Zhou, C. H., Tong, D. S., Yang, H. M., ... & Wang, H. (2016). Fly ash-based geopolymer: clean production, properties and applications. *Journal of Cleaner Production*, 125, 253-267.

# Appendix

Table A.1 Data of compressive strength and flow diameter for various N-A-S-H geopolymers (related to Figure 3.13(a) and Figure 3.15).

| $SiO_2$/ $Al_2O_3$ | $Na_2O$/ $Al_2O_3$ | $H_2O$/ $Na_2O$ | CS 1 (MPa) | CS 2 (MPa) | CS 3 (MPa) | Mean | Error |
|---|---|---|---|---|---|---|---|
| 2.1 | 1.15 | 11 | 13.88 | 8.93 | 12.54 | 11.78 | 2.1 |
| 2.8 | 1.15 | 11 | 34.61 | 30.10 | 33.42 | 32.71 | 1.9 |
| 3.6 | 1.15 | 11 | 41.53 | 38.45 | 40.70 | 40.23 | 1.3 |
| 4.0 | 1.15 | 11 | 49.51 | 41.69 | 47.38 | 46.19 | 3.3 |
| 2.8 | 0.75 | 11 | 51.21 | 42.51 | 48.89 | 47.54 | 3.7 |
| 2.8 | 1.00 | 11 | 30.52 | 28.15 | 29.92 | 29.53 | 1.0 |
| 2.8 | 1.30 | 11 | 19.79 | 18.45 | 19.47 | 19.24 | 0.6 |
| 2.8 | 1.00 | 8 | 42.42 | 36.29 | 40.78 | 39.83 | 2.6 |
| 2.8 | 1.00 | 9 | 43.71 | 42.09 | 43.29 | 43.03 | 0.7 |
| 2.8 | 1.00 | 10 | 52.89 | 47.69 | 51.46 | 50.68 | 2.2 |
| 2.8 | 1.00 | 12 | 30.11 | 27.02 | 29.28 | 28.80 | 1.3 |
| $SiO_2$/ $Al_2O_3$ | $Na_2O$/ $Al_2O_3$ | $H_2O$/ $Na_2O$ | Flow 1 (mm) | Flow 2 (mm) | Flow 3 (mm) | Mean | Error |
| 2.1 | 1.15 | 11 | 195.4 | 196.4 | 198.9 | 196.9 | 1.5 |
| 2.8 | 1.15 | 11 | 285.7 | 285.8 | 286.2 | 285.9 | 0.2 |
| 3.6 | 1.15 | 11 | >350 | >350 | >350 | / | / |
| 4.0 | 1.15 | 11 | >350 | >350 | >350 | / | / |
| 2.8 | 0.75 | 11 | 222.2 | 223.2 | 226.0 | 223.8 | 1.6 |
| 2.8 | 1.00 | 11 | 260.5 | 260.8 | 261.7 | 261.0 | 0.5 |
| 2.8 | 1.30 | 11 | >350 | >350 | >350 | / | / |
| 2.8 | 1.00 | 8 | 224.9 | 225.0 | 225.4 | 225.1 | 0.2 |
| 2.8 | 1.00 | 9 | 239.2 | 239.4 | 239.9 | 239.5 | 0.3 |
| 2.8 | 1.00 | 10 | 253.8 | 254.4 | 255.9 | 254.7 | 0.9 |
| 2.8 | 1.00 | 12 | 285.7 | 285.8 | 286.2 | 285.9 | 0.2 |

Table A.2 Data of splitting tensile strength for various N-A-S-H geopolymers (related to Figure 3.16).

| $SiO_2$/ $Al_2O_3$ | $Na_2O$/ $Al_2O_3$ | $H_2O$/ $Na_2O$ | STS 1 (MPa) | STS 2 (MPa) | STS 3 (MPa) | Mean | Error |
|---|---|---|---|---|---|---|---|
| 2.1 | 1.15 | 11 | 1.558 | 1.583 | 1.653 | 1.598 | 0.04 |
| 2.8 | 1.15 | 11 | 3.367 | 3.058 | 3.277 | 3.234 | 0.13 |
| 3.6 | 1.15 | 11 | 3.744 | 3.676 | 3.734 | 3.718 | 0.03 |
| 4.0 | 1.15 | 11 | 4.053 | 3.837 | 3.984 | 3.958 | 0.09 |
| 2.8 | 0.75 | 11 | 4.245 | 3.911 | 4.144 | 4.100 | 0.14 |
| 2.8 | 1.00 | 11 | 3.527 | 3.432 | 3.502 | 3.487 | 0.04 |
| 2.8 | 1.30 | 11 | 1.520 | 1.424 | 1.490 | 1.478 | 0.04 |
| 2.8 | 1.00 | 8 | 3.766 | 3.791 | 3.882 | 3.813 | 0.05 |
| 2.8 | 1.00 | 9 | 4.051 | 4.111 | 4.309 | 4.157 | 0.11 |
| 2.8 | 1.00 | 10 | 4.435 | 4.248 | 4.394 | 4.359 | 0.08 |
| 2.8 | 1.00 | 12 | 3.462 | 3.154 | 3.380 | 3.332 | 0.13 |
| 2.8 | 1.00 | 14 | 2.137 | 1.948 | 2.086 | 2.057 | 0.08 |

Table A.3 Data of compressive strength and flow diameter for various N-A-S-H geopolymers made with dry water and lone nano silica (related to Figure 4.7 and Figure 4.9 (a&b)).

| Mixtures | CS 1 (MPa) | CS 2 (MPa) | CS 3 (MPa) | Mean | Error |
|---|---|---|---|---|---|
| Ref. | 41.35 | 43.28 | 46.47 | 43.70 | 2.11 |
| Hydrophobic | 46.14 | 42.24 | 45.15 | 44.51 | 1.66 |
| Hydrophilic | 51.59 | 39.84 | 48.46 | 46.63 | 4.97 |
| Dry Water | 52.76 | 48.66 | 51.67 | 51.03 | 1.73 |
| Ref. (0%) | 36.55 | 38.58 | 44.12 | 39.75 | 3.20 |
| 10% | 56.37 | 58.56 | 64.53 | 59.82 | 3.45 |
| 15% | 59.81 | 62.08 | 68.28 | 63.39 | 3.58 |
| 20% | 59.95 | 62.04 | 67.73 | 63.24 | 3.29 |
| Mixtures | Flow 1 (mm) | Flow 2 (mm) | Flow 3 (mm) | Mean | Error |
| Ref. | 254.0 | 252.0 | 257.8 | 254.6 | 2.37 |
| Hydrophobic | 250.9 | 249.2 | 255.3 | 251.8 | 2.58 |
| Hydrophilic | 250.1 | 247.2 | 254.8 | 250.7 | 3.12 |
| Dry Water | 258.2 | 255.9 | 261.7 | 258.6 | 2.37 |
| Ref. (0%) | 244.8 | 246.0 | 249.2 | 246.65 | 1.88 |
| 10% | 252.9 | 253.4 | 254.7 | 253.68 | 0.78 |
| 15% | 251.4 | 252.0 | 253.5 | 252.30 | 0.88 |
| 20% | 253.1 | 253.9 | 256.0 | 254.36 | 1.23 |

Table A.4 Data of compressive strength for various N-A-S-H geopolymers after sulphuric acid attack (related to Figure 5.8).

| $SiO_2$/ $Al_2O_3$ | $Na_2O$/ $Al_2O_3$ | $H_2O$/ $Na_2O$ | CS 1 (MPa) | CS 2 (MPa) | CS 3 (MPa) | Mean | Error |
|---|---|---|---|---|---|---|---|
| Original | | | | | | | |
| 2.2 | 0.9 | 11 | 18.68 | 18.65 | 18.77 | 18.70 | 0.05 |
| 2.8 | 0.9 | 11 | 39.18 | 38.57 | 40.87 | 39.54 | 0.97 |
| 3.1 | 0.9 | 11 | 43.01 | 43.72 | 43.98 | 43.57 | 0.41 |
| 3.4 | 0.9 | 11 | 47.01 | 45.91 | 50.00 | 47.64 | 1.73 |
| 3.7 | 0.9 | 11 | 54.44 | 55.06 | 55.29 | 54.93 | 0.36 |
| 3.1 | 0.8 | 11 | 51.62 | 50.80 | 53.88 | 52.10 | 1.30 |
| 3.1 | 1.1 | 11 | 36.42 | 36.13 | 37.22 | 36.59 | 0.46 |
| 3.1 | 1.3 | 11 | 26.07 | 24.97 | 29.06 | 26.70 | 1.73 |
| 3.1 | 1.0 | 8 | 45.16 | 44.62 | 47.65 | 45.81 | 1.32 |
| 3.1 | 1.0 | 10 | 43.80 | 43.90 | 43.91 | 43.87 | 0.05 |
| 3.1 | 1.0 | 12 | 29.61 | 32.02 | 32.93 | 31.52 | 1.40 |
| 3.1 | 1.0 | 14 | 27.74 | 29.35 | 29.97 | 29.02 | 0.94 |
| After immersion for 28 days | | | | | | | |
| 2.2 | 0.9 | 11 | 16.89 | 15.53 | 17.41 | 16.61 | 0.79 |
| 2.8 | 0.9 | 11 | 37.78 | 34.74 | 38.93 | 37.15 | 1.77 |
| 3.1 | 0.9 | 11 | 45.31 | 43.33 | 46.03 | 44.89 | 1.14 |
| 3.4 | 0.9 | 11 | 50.13 | 46.57 | 51.44 | 49.38 | 2.06 |
| 3.7 | 0.9 | 11 | 59.47 | 56.01 | 60.71 | 58.73 | 1.99 |
| 3.1 | 0.8 | 11 | 59.04 | 58.08 | 59.43 | 58.85 | 0.57 |
| 3.1 | 1.1 | 11 | 36.13 | 30.58 | 38.17 | 34.96 | 3.21 |
| 3.1 | 1.3 | 11 | 28.68 | 24.14 | 30.34 | 27.72 | 2.62 |
| 3.1 | 1.0 | 8 | 43.73 | 42.35 | 44.24 | 43.44 | 0.80 |
| 3.1 | 1.0 | 10 | 43.15 | 42.59 | 43.35 | 43.03 | 0.32 |
| 3.1 | 1.0 | 12 | 39.89 | 38.37 | 40.45 | 39.57 | 0.88 |
| 3.1 | 1.0 | 14 | 29.77 | 28.40 | 30.27 | 29.48 | 0.79 |
| After immersion for 56 days | | | | | | | |
| 2.2 | 0.9 | 11 | 13.25 | 13.57 | 14.46 | 13.76 | 0.51 |
| 2.8 | 0.9 | 11 | 37.71 | 36.98 | 37.51 | 37.40 | 0.31 |
| 3.1 | 0.9 | 11 | 38.17 | 38.52 | 39.56 | 38.75 | 0.59 |
| 3.4 | 0.9 | 11 | 46.01 | 41.49 | 44.80 | 44.10 | 1.91 |
| 3.7 | 0.9 | 11 | 44.64 | 40.05 | 49.23 | 44.64 | 3.75 |
| 3.1 | 0.8 | 11 | 45.04 | 45.09 | 45.23 | 45.12 | 0.08 |
| 3.1 | 1.1 | 11 | 33.43 | 33.49 | 33.67 | 33.53 | 0.10 |
| 3.1 | 1.3 | 11 | 25.38 | 13.38 | 22.17 | 20.31 | 5.07 |
| 3.1 | 1.0 | 8 | 42.70 | 42.78 | 43.01 | 42.83 | 0.13 |

| | | | | | | | |
|---|---|---|---|---|---|---|---|
| 3.1 | 1.0 | 10 | 40.20 | 40.40 | 40.93 | 40.51 | 0.31 |
| 3.1 | 1.0 | 12 | 29.45 | 26.49 | 28.66 | 28.20 | 1.25 |
| 3.1 | 1.0 | 14 | 13.81 | 14.76 | 17.36 | 15.31 | 1.50 |
| After immersion for 84 days | | | | | | | |
| 2.2 | 0.9 | 11 | 13.40 | 10.87 | 12.72 | 12.33 | 1.07 |
| 2.8 | 0.9 | 11 | 34.75 | 27.09 | 32.72 | 31.52 | 3.24 |
| 3.1 | 0.9 | 11 | 38.32 | 34.32 | 37.22 | 36.62 | 1.69 |
| 3.4 | 0.9 | 11 | 37.15 | 38.53 | 42.40 | 39.36 | 2.22 |
| 3.7 | 0.9 | 11 | 45.40 | 44.86 | 45.25 | 45.17 | 0.23 |
| 3.1 | 0.8 | 11 | 40.92 | 38.39 | 40.24 | 39.85 | 1.07 |
| 3.1 | 1.1 | 11 | 16.25 | 20.26 | 31.20 | 22.57 | 6.32 |
| 3.1 | 1.3 | 11 | 13.81 | 13.92 | 14.24 | 13.99 | 0.18 |
| 3.1 | 1.0 | 8 | 41.17 | 39.38 | 42.96 | 41.17 | 1.46 |
| 3.1 | 1.0 | 10 | 34.19 | 33.41 | 33.98 | 33.86 | 0.33 |
| 3.1 | 1.0 | 12 | 22.88 | 21.67 | 22.56 | 22.37 | 0.51 |
| 3.1 | 1.0 | 14 | 12.64 | 12.67 | 12.82 | 12.71 | 0.08 |

Table A.5 Data of mass and dimension losses for various N-A-S-H geopolymers after sulphuric acid attack (related to Figure 5.7).

| $SiO_2$/ $Al_2O_3$ | $Na_2O$/ $Al_2O_3$ | $H_2O$/ $Na_2O$ | ML 1 (%) | ML 2 (%) | ML 3 (%) | Mean | Error |
|---|---|---|---|---|---|---|---|
| After immersion for 56 days | | | | | | | |
| 2.2 | 0.9 | 11 | 8.44 | 8.32 | 8.59 | 8.45 | 0.11 |
| 2.8 | 0.9 | 11 | 4.48 | 4.63 | 5.02 | 4.71 | 0.23 |
| 3.1 | 0.9 | 11 | 5.01 | 1.91 | 4.18 | 3.70 | 1.31 |
| 3.4 | 0.9 | 11 | 4.26 | 3.99 | 4.47 | 4.24 | 0.20 |
| 3.7 | 0.9 | 11 | 4.70 | 4.23 | 5.32 | 4.75 | 0.45 |
| 3.1 | 0.8 | 11 | 4.30 | 4.39 | 4.63 | 4.44 | 0.14 |
| 3.1 | 1.1 | 11 | 5.32 | 4.52 | 5.94 | 5.26 | 0.58 |
| 3.1 | 1.3 | 11 | 7.32 | 7.19 | 7.48 | 7.33 | 0.12 |
| 3.1 | 1.0 | 8 | 4.29 | 4.39 | 4.67 | 4.45 | 0.16 |
| 3.1 | 1.0 | 10 | 6.07 | 3.59 | 5.40 | 5.02 | 1.05 |
| 3.1 | 1.0 | 12 | 7.50 | 6.84 | 7.32 | 7.22 | 0.28 |
| 3.1 | 1.0 | 14 | 7.71 | 7.61 | 7.87 | 7.73 | 0.11 |
| After immersion for 84 days | | | | | | | |
| 2.2 | 0.9 | 11 | 11.09 | 10.49 | 11.57 | 11.05 | 0.44 |
| 2.8 | 0.9 | 11 | 6.14 | 6.29 | 6.77 | 6.40 | 0.27 |
| 3.1 | 0.9 | 11 | 6.04 | 6.13 | 6.37 | 6.18 | 0.14 |
| 3.4 | 0.9 | 11 | 6.03 | 5.41 | 6.53 | 5.99 | 0.46 |
| 3.7 | 0.9 | 11 | 6.83 | 7.06 | 7.68 | 7.19 | 0.36 |

| 3.1 | 0.8 | 11 | 5.84 | 4.67 | 6.77 | 5.76 | 0.86 |
|---|---|---|---|---|---|---|---|
| 3.1 | 1.1 | 11 | 7.21 | 6.45 | 8.18 | 7.28 | 0.71 |
| 3.1 | 1.3 | 11 | 10.61 | 10.70 | 10.94 | 10.75 | 0.14 |
| 3.1 | 1.0 | 8 | 5.25 | 5.46 | 6.03 | 5.58 | 0.33 |
| 3.1 | 1.0 | 10 | 7.29 | 7.20 | 7.26 | 7.25 | 0.04 |
| 3.1 | 1.0 | 12 | 7.26 | 6.84 | 7.80 | 7.30 | 0.39 |
| 3.1 | 1.0 | 14 | 6.91 | 7.72 | 9.85 | 8.16 | 1.24 |
| $SiO_2$/ $Al_2O_3$ | $Na_2O$/ $Al_2O_3$ | $H_2O$/ $Na_2O$ | DL 1 (%) | DL 2 (%) | DL 3 (%) | Mean | Error |
| After immersion for 56 days | | | | | | | |
| 2.2 | 0.9 | 11 | 6.57 | 6.55 | 6.65 | 6.59 | 0.04 |
| 2.8 | 0.9 | 11 | 3.61 | 3.47 | 3.78 | 3.62 | 0.13 |
| 3.1 | 0.9 | 11 | 3.20 | 3.06 | 3.40 | 3.22 | 0.14 |
| 3.4 | 0.9 | 11 | 2.17 | 2.00 | 2.40 | 2.19 | 0.16 |
| 3.7 | 0.9 | 11 | 3.16 | 3.08 | 3.36 | 3.20 | 0.12 |
| 3.1 | 0.8 | 11 | 2.82 | 2.72 | 2.86 | 2.80 | 0.06 |
| 3.1 | 1.1 | 11 | 3.53 | 3.56 | 3.65 | 3.58 | 0.05 |
| 3.1 | 1.3 | 11 | 4.11 | 4.09 | 4.34 | 4.18 | 0.11 |
| 3.1 | 1.0 | 8 | 1.70 | 1.69 | 1.74 | 1.71 | 0.02 |
| 3.1 | 1.0 | 10 | 2.49 | 2.46 | 2.55 | 2.50 | 0.04 |
| 3.1 | 1.0 | 12 | 3.94 | 3.94 | 4.03 | 3.97 | 0.04 |
| 3.1 | 1.0 | 14 | 4.49 | 4.44 | 4.63 | 4.52 | 0.08 |
| After immersion for 84 days | | | | | | | |
| 2.2 | 0.9 | 11 | 7.02 | 7.00 | 7.13 | 7.05 | 0.06 |
| 2.8 | 0.9 | 11 | 5.03 | 4.95 | 5.32 | 5.10 | 0.16 |
| 3.1 | 0.9 | 11 | 4.67 | 4.67 | 4.97 | 4.77 | 0.14 |
| 3.4 | 0.9 | 11 | 2.77 | 2.70 | 2.96 | 2.81 | 0.11 |
| 3.7 | 0.9 | 11 | 3.68 | 3.69 | 3.79 | 3.72 | 0.05 |
| 3.1 | 0.8 | 11 | 3.52 | 3.47 | 3.66 | 3.55 | 0.08 |
| 3.1 | 1.1 | 11 | 4.88 | 4.86 | 5.02 | 4.92 | 0.07 |
| 3.1 | 1.3 | 11 | 5.19 | 5.08 | 5.39 | 5.22 | 0.13 |
| 3.1 | 1.0 | 8 | 3.39 | 3.37 | 3.44 | 3.40 | 0.03 |
| 3.1 | 1.0 | 10 | 3.49 | 3.47 | 3.57 | 3.51 | 0.04 |
| 3.1 | 1.0 | 12 | 4.52 | 4.50 | 4.63 | 4.55 | 0.06 |
| 3.1 | 1.0 | 14 | 5.82 | 5.74 | 5.96 | 5.84 | 0.09 |

Table A.6 Data of compressive strength for nano silica and dry water involved N-A-S-H geopolymers after sulphuric acid attack (related to Figure 6.6).

| Mixtures | CS 1 (MPa) | CS 2 (MPa) | CS 3 (MPa) | Mean | Error |
|---|---|---|---|---|---|
| Original | | | | | |
| Ref | 43.80 | 43.90 | 43.91 | 43.87 | 0.05 |
| NS | 45.50 | 47.44 | 48.09 | 47.01 | 1.10 |
| DW[a] | 48.03 | 45.84 | 47.37 | 47.08 | 0.92 |
| DW[b] | 49.06 | 48.61 | 50.29 | 49.32 | 0.71 |
| DW[c] | 46.83 | 48.25 | 48.77 | 47.95 | 0.82 |
| After immersion for 56 days | | | | | |
| Ref | 40.20 | 40.40 | 40.93 | 40.51 | 0.31 |
| NS | 44.89 | 43.80 | 44.60 | 44.43 | 0.46 |
| DW[a] | 45.61 | 43.81 | 45.10 | 44.84 | 0.76 |
| DW[b] | 46.68 | 45.23 | 46.27 | 46.06 | 0.61 |
| DW[c] | 45.25 | 45.57 | 46.46 | 45.76 | 0.51 |
| After immersion for 84 days | | | | | |
| Ref | 34.19 | 33.41 | 33.98 | 33.86 | 0.33 |
| NS | 39.29 | 37.23 | 38.74 | 38.42 | 0.87 |
| DW[a] | 40.12 | 39.02 | 40.86 | 40.00 | 0.76 |
| DW[b] | 43.19 | 42.85 | 44.34 | 43.46 | 0.64 |
| DW[c] | 41.43 | 40.34 | 42.52 | 41.43 | 0.89 |

Table A.7 Data of mass and dimension losses for nano silica and dry water involved N-A-S-H geopolymers after sulphuric acid attack (related to Figure 6.5).

| Mixtures | ML 1 (%) | ML 2 (%) | ML 3 (%) | Mean | Error |
|---|---|---|---|---|---|
| After immersion for 56 days | | | | | |
| Ref | 6.07 | 3.59 | 5.40 | 5.02 | 1.05 |
| NS | 4.47 | 4.42 | 4.46 | 4.45 | 0.02 |
| DW[a] | 4.42 | 4.51 | 4.75 | 4.56 | 0.14 |
| DW[b] | 4.27 | 4.36 | 4.60 | 4.41 | 0.14 |
| DW[c] | 4.44 | 4.23 | 4.38 | 4.35 | 0.09 |
| After immersion for 84 days | | | | | |
| Ref | 7.29 | 7.20 | 7.26 | 7.25 | 0.04 |
| NS | 6.88 | 6.76 | 7.06 | 6.90 | 0.12 |
| DW[a] | 6.70 | 6.83 | 7.17 | 6.90 | 0.20 |
| DW[b] | 6.48 | 6.31 | 6.65 | 6.48 | 0.14 |
| DW[c] | 6.73 | 6.28 | 7.18 | 6.73 | 0.37 |
| Mixtures | DL 1 (%) | DL 2 (%) | DL 3 (%) | Mean | Error |

| | | | | | |
|---|---|---|---|---|---|
| After immersion for 56 days | | | | | |
| Ref | 2.49 | 2.46 | 2.55 | 2.50 | 0.04 |
| NS | 2.47 | 2.43 | 2.51 | 2.47 | 0.03 |
| DW[a] | 2.53 | 2.55 | 2.60 | 2.56 | 0.03 |
| DW[b] | 2.40 | 2.39 | 2.44 | 2.41 | 0.02 |
| DW[c] | 2.42 | 2.41 | 2.46 | 2.43 | 0.02 |
| After immersion for 84 days | | | | | |
| Ref | 3.49 | 3.47 | 3.57 | 3.51 | 0.04 |
| NS | 3.41 | 3.35 | 3.44 | 3.40 | 0.04 |
| DW[a] | 3.41 | 3.39 | 3.43 | 3.41 | 0.02 |
| DW[b] | 3.13 | 3.11 | 3.18 | 3.14 | 0.03 |
| DW[c] | 3.21 | 3.23 | 3.28 | 3.24 | 0.03 |

Figure A.1 Fracture types of some representative N-A-S-H geopolymer mortars collected from compression test in Chapter 3.